AD-A042 144 AEROSPACE CORP EL SEGUNDO CALIF CHEMISTRY AND PHYSICS LAB F/G 20/8
INFRARED EMISSIVITIES OF MICRON-SIZED PARTICLES OF C, MGO, AL S--ETC(U)
APR 77 J M DOWLING , C M RANDALL F04701-76-C-0077
UNCLASSIFIED TR-0077(2641)-1 AFRPL-TR-77-14 NL

1 OF 3
ADA042144

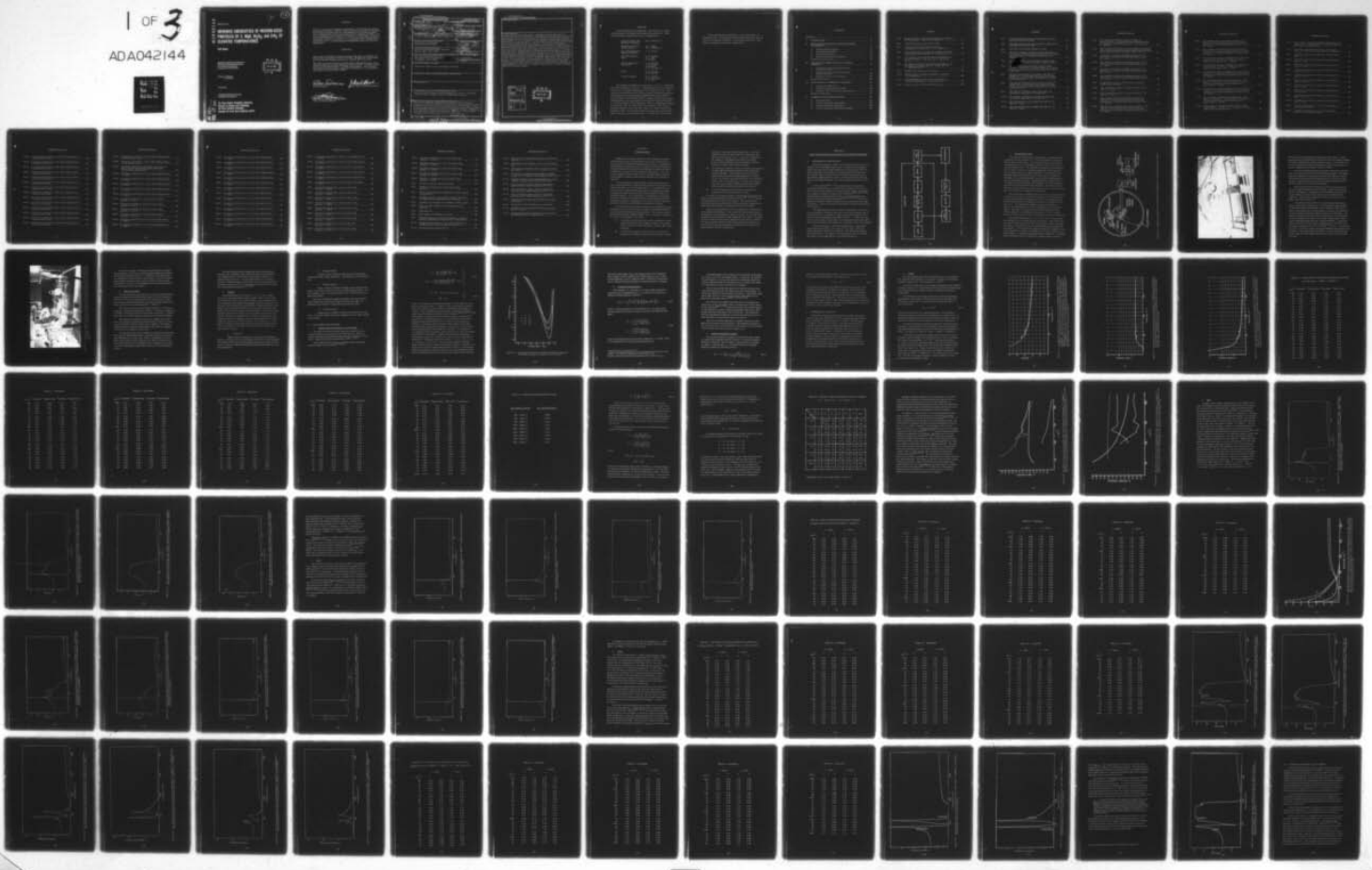

AFRPL-TR-77-14

INFRARED EMISSIVITIES OF MICRON-SIZED PARTICLES OF C, MgO, Al_2O_3, and ZrO_2 AT ELEVATED TEMPERATURES

Final Report

Chemistry and Physics Laboratory
The Ivan A. Getting Laboratories
The Aerospace Corporation
El Segundo, California 90245

Authors: J. M. Dowling
C. M. Randall

30 April 1977

Air Force Rocket Propulsion Laboratory
Director of Science and Technology
Air Force Systems Command
Edwards Air Force Base California 93523

NOTICES

When U. S. Government drawings, specifications, or other data are used for any purpose other than a definitely related government procurement operation, the Government thereby incurs no responsibility nor any obligation whatsoever, and the fact that the Government may have formulated, furnished, or in any way supplied the said drawings, specifications or other data, is not to be regarded by implication or otherwise, or in any manner licensing the holder or any other person or corporation, or conveying any rights or permission to manufacture, use, or sell any patented invention that may in any way be related thereto.

FOREWORD

This report was submitted by The Aerospace Corporation, El Segundo, CA 90245, under Contract No. F04701-76-C-0077, Job Order No. 2641, with the Air Force Rocket Propulsion Laboratory, Edwards AFB, CA 93523.

This report has been reviewed by the Information Office/DOZ and is releasable to the National Technical Information Service (NTIS). At NTIS it will be available to the general public, including foreign nations. This technical report has been reviewed and is approved for publication; it is unclassified and suitable for general public release.

William A. Danne

WILLIAM A. DANNE, 1st Lt, USAF
Project Manager

J. Daniel Stewart

J. DANIEL STEWART
Chief, Plume Technology Section

WILLIAM F. MORRIS, Colonel, USAF
Chief, Technology Division

UNCLASSIFIED

SECURITY CLASSIFICATION OF THIS PAGE *(When Data Entered)*

REPORT DOCUMENTATION PAGE	READ INSTRUCTIONS BEFORE COMPLETING FORM
1. REPORT NUMBER AFRPL-TR-77-14	2. GOVT ACCESSION NO. 3. RECIPIENT'S CATALOG NUMBER
4. TITLE (and Subtitle) INFRARED EMISSIVITIES OF MICRON-SIZED PARTICLES OF C, MgO, Al_2O_3, AND ZrO	5. TYPE OF REPORT & PERIOD COVERED Final rept.
	6. PERFORMING ORG. REPORT NUMBER TR-0077(2641)-1
7. AUTHOR(s) Jerome M. Dowling and Charles M. Randall	8. CONTRACT OR GRANT NUMBER(s) F04701-76-C-0077
9. PERFORMING ORGANIZATION NAME AND ADDRESS The Aerospace Corporation El Segundo, Calif. 90245	10. PROGRAM ELEMENT, PROJECT, TASK AREA & WORK UNIT NUMBERS P.E. 62302F Project 3059, Task 11
11. CONTROLLING OFFICE NAME AND ADDRESS Air Force Rocket Propulsion Laboratory Edwards AFB, Calif. 93523	12. REPORT DATE 30 April 1977 13. NUMBER OF PAGES<br~~322~~ 226
14. MONITORING AGENCY NAME & ADDRESS *(if different from Controlling Office)* Space and Missile Systems Organiz Los Angeles Air Force Station Los Angeles, Calif. 90009	15. SECURITY CLASS. *(of this report)* Unclassified 15a. DECLASSIFICATION/DOWNGRADING SCHEDULE

16. DISTRIBUTION STATEMENT *(of this Report)*

Approved for public release; distribution unlimited.

17. DISTRIBUTION STATEMENT *(of the abstract entered in Block 20, if different from Report)*

18. SUPPLEMENTARY NOTES

19. KEY WORDS *(Continue on reverse side if necessary and identify by block number)*

Optical Constants, Kramers-Kronig Analysis, Mie Theory, Emissivity, Levitation, Laser Heating, Fourier Transform Spectroscopy.

20. ABSTRACT *(Continue on reverse side if necessary and identify by block number)*

The Particle Optical Properties Measurements (POPM) Program is designed to assess the reliability of computing the infrared emissivity of hot particles from refractive index values measured on bulk samples. An experimental apparatus to observe the thermal radiation from a single particle electrostatically levitated and heated by 1.06 μm Nd:YAG laser radiation has been constructed and has demonstrated the capability of simultaneously levitating and irradiating single micron sized particles.

MICRO METER

DD FORM 1473 (FACSIMILE)

409 383

UNCLASSIFIED

SECURITY CLASSIFICATION OF THIS PAGE *(When Data Entered)*

19. KEY WORDS (Continued)

20. ABSTRACT (Continued)

Because little refractive index data is available for high temperatures a reflectometer has been constructed. This instrument and associated analytical techniques have been used to determine the complex refractive index between 400 and 2200 cm^{-1} (25 to 4.5 μm) of large samples of Al_2O_3, MgO and ZrO_2 at 600-700°K, as well as at 300°K. The refractive index of carbon at 300°K in the same spectral range has also been obtained. The expected emissivity of micron sized particles of all of the above materials has been computed for the spectral interval from 400 to 1800 cm^{-1} (5.5 to 25 μm) for a variety of particle sizes and based on the measured complex refractive index values. The emissivity spectrum is found to depend critically on particle size and the refractive index spectrum. Emissivities greater than unity due to resonnances between vibration modes of theparticles and the radiation are found. For particles large in size compared with the radiation wavelength, small values of the extinction coefficient (10^{-2} and smaller) lead to significant values of the calculated emissivity. Since small values of this parameter are difficult to measure experimentally and will probably change radically between the bulk and commonly occurring particle states of the material, it is concluded that the emissivity of small particles can not always be reliably computed from refractive index data obtained from large samples.

PREFACE

In an undertaking of this magnitude, many people in the Chemistry and Physics Laboratory made significant contributions. They are listed below along with their area of responsibility.

Literature Search and Handbook Compilation	M. E. Whitson, Jr.
Sample Procurement and Preparation	G. C. Light M. E. Whitson, Jr.
Bulk Index Experiment Engineering Design	L. F. Lemke
Bulk Index Measurements	J. M. Dowling R. T. Hall A. Pluchino
Particle Emissivity Experiment	L. A. Darnton J. M. Dowling A. Pluchino M. E. Whitson, Jr.
Theory	J. M. Dowling B. R. Johnson
Technical Support	R. G. Aurandt A. K. Maruyama T. E. Mott

The principal investigators on this project were D. C. Cartwright (inception to September 1974), R. T. Hall (September 1974 to September 1975), and J. M. Dowling (September 1975 to September 1976). The contract was monitored by the Air Force Rocket Propulsion Laboratory. This program was jointly funded by SAMSO/ABRES and the AFRPL. Current support is provided by AFOSR Aerospace Sciences Directorate. Helpful guidance and encouragement were provided from AFRPL by Dr. J. D. Stewart and the Project Engineers, Capt. W. Rothschild (inception to July 1974), Capt. W. Hanna (July 1974 to January 1975), Capt. D. Banasiak (January 1975 to July 1975), and Lt. W. Danne (July 1975 to September 1976). Overall administration and supervision at The Aerospace Corporation were provided by R. J. McNeal and C. M. Randall.

This report has been compiled by J. M. Dowling and C. M. Randall from the contributions of all participants presently connected with The Aerospace Corporation. The excellent work of Ms. Fran Plotnik in typing the manuscript is appreciated.

CONTENTS

PREFACE 1

I. INTRODUCTION 15

II. HIGH TEMPERATURE BULK REFRACTIVE INDEX EXPERIMENT 17

A. Experimental Description 17

B. Data Reduction Methods 26

C. Experimental Results 31

D. Summary and General Conclusions 92

Section I and II References 94

III. THEORETICAL COMPUTATION OF PARTICLE EMISSIVITY 97

A. Derivation of Theoretical Formulas for Particle Emissivity 97

B. Calculations of the Emissivity of Small Spherical Particles 101

C. Summary and General Conclusions 141

Section III References 154

IV. SINGLE PARTICLE EMISSIVITY EXPERIMENT 155

A. Experimental Approach 155

B. Emissivity Experiment Description 160

C. Summary, Discussion and Recommendations 214

Section IV References 217

V. SUMMARY AND RECOMMENDATIONS 219

A. Bulk Experiment 219

B. Particle Emissivity Computations 221

C. Particle Emissivity Experiment 222

D. General Conclusions and Recommendations 223

TABLES

II-1.	Measured Index of Refraction and Extinction Coefficient for Carbon from ν = 400 cm^{-1} to 2200 cm^{-1}	36
II-2.	Reflectivity Measurement Errors (rms)	42
II-3.	Errors in n and k as a Function of n and k, Assuming $\Delta R = \pm 0.015$, $\Delta\Psi = \pm 1.1^{\circ}$, and $\Delta\theta = 0$	45
II-4.	Index of Refraction and Extinction Coefficient for MgO at 300°K and 573°K from 400 cm^{-1} to 2200 cm^{-1}	59
II-5.	The Refractive Index (n) and Extinction Coefficient (k) for ZrO_2 between ν = 400 cm-1 for T = 300°K and 573°K	72
II-6.	The Refractive Index (n) and Extinction Coefficient (k) for Al_2O_3 in the Region 400 cm^{-1} to 2200 cm^{-1} at T = 300°K and 678°K	83
IV-1.	Pinhole Probe Data of Laser Intensity	177
IV-2.	Results of Laser Heating Calculations, Assuming a 77°K Background	186
IV-3.	Computed Signal-to-Noise for 0.5 μm Particle at Various Temperatures (ν = 400 to 412 cm^{-1})	195
IV-4.	Error in ϵ_p for a One Percent Error in T_p	203

FIGURES

II-1.	Schematic diagram of the experimental procedure for obtaining bulk measurements	18
II-2.	Schematic diagram of the experimental arrangement for obtaining bulk measurements	20
II-3.	The inside of the vacuum chamber is shown	21
II-4.	The vacuum chamber is shown on theleft and the interferometer with collection optics and detector on the right; the beam displacer is mounted in between for easy alignment	23
II-5.	Computed reflectance as a function of incidence angle for different values of complex refractive index	28
II-6.	The reflectivity spectrum (solid curve) of carbon (graphite) from 400 cm^{-1} (25 μm) to 2000 cm^{-1} (5.0 μm) measure at room temperature and an angle of incidence of 45 degrees	33
II-7.	The index of refraction (n) of carbon, from 400 cm^{-1} to 2000 cm^{-1} as determined from a Kramers-Kronig analysis of the experimental reflectivity data is shown as the solid curve.	34
II-8.	The extinction coefficient (k) of carbon from 400 cm^{-1} to 2000 cm^{-1} as determined from a Kramers-Kronig analysis of the experimental reflectivity data is shown as the solid curve.	35
II-9.	The index of refraction of carbon materials in the wavenumber region 400 cm^{-1} to 2200 cm^{-1}	47
II-10.	The extinction coefficient of carbon materials in the wavenumber region 400 cm^{-1} to 2200 cm^{-1}	48
II-11.	The reflectivity spectrum of MgO in the 400 cm^{-1} to 2000 cm^{-1} region	50
II-12.	The reflectivity spectrum of MgO in the 400 cm^{-1} to 2000 cm^{-1} region	51

FIGURES (Continued)

II-13. The calculated reflectance spectrum of MgO as determined from a classical dispersion analysis fitted to the reflectance data of Figure II-11 (θ = 45 degrees and T = 300°K) 52

II-14. The calculated reflectance spectrum of MgO as determined from a classical dispersion analysis fitted to the reflectance data of Figure II-12 (θ = 45 degrees and T = 573°K) 53

II-15. The index of refraction (n) of MgO from 400 cm^{-1} to 2000 cm^{-1} as derived by classical dispersion analysis (T = 300°K) 55

II-16. The extinction coefficient (k) of MgO from 400 cm^{-1} to 2000 cm^{-1} as derived by classical dispersion analysis (T = 300°K) 56

II-17. The index of refraction (n) of MgO from 400 cm^{-1} to 2000 cm^{-1} as derived by classical dispersion analysis (T = 573°K) 57

II-18. The extinction coefficient (k) of MgO from 400 cm^{-1} to 2000 cm^{-1} as derived by classical dispersion analysis (T = 573°K) 58

II-19. Comparison of index of refraction (n) and extinction coefficients (k) for MgO 64

II-20. The reflectivity spectrum of ZrO_2 in the 400 cm^{-1} to 2000 cm^{-1} region 65

II-21. The reflectivity spectrum of ZrO_2 in the 400 cm^{-1} to 2000 cm^{-1} region 66

II-22. The refractive index (n) of ZrO_2 from 400 cm^{-1} to 2000 cm^{-1} as determined from a Kramers-Kronig analysis of the reflectivity data shown in Figure II-20 (T = 300°K) 67

II-23. The extinction coefficient (k) of ZrO_2 from 400 cm^{-1} to 2000 cm^{-1} as determined from a Kramers-Kronig analysis of the reflectivity data shown in Figure II-20 (T = 300°K) 68

FIGURES (Continued)

II-24. The refractive index (n) of ZrO_2 from 400 cm^{-1} to 2000 cm^{-1} as determined from a Kramers-Kronig analysis of the reflectivity data shown in Figure II-21 (T = 573°K) 69

II-25. The extinction coefficient (k) of ZrO_2 from 400 cm^{-1} to 2000 cm^{-1} as determined from a Kramers-Kronig analysis of the reflectivity data shown in Figure II-21 (T = 573°K 70

II-26. The reflectivity spectrum of Al_2O_3 in the wavenumber region 400 cm^{-1} to 2200 cm^{-1} ($E\perp$) at an angle of incidence of 45 degrees and T = 300°K. 77

II-27. The reflectivity spectrum of Al_2O_3 in the wavenumber region 400 cm^{-1} to 2200 cm^{-1} ($E\perp$) at an angle of incidence of 45 degrees and T = 678°K 78

II-28. The refractive index (n) of Al_2O_3 in the region 400 cm^{-1} to 2200 cm^{-1} as determined from a Kramers-Kronig analysis of the reflectivity data shown in Figure II-26 (T = 300°K) 79

II-29. The extinction coefficient (k) of Al_2O_3 in the region 400 cm^{-1} to 2200 cm^{-1} as determined from a Kramers-Kronig analysis of the reflectivity data shown in Figure II-26 (T = 300°K) 80

II-30. The refractive index (n) of Al_2O_3 in the region 400 cm^{-1} to 2200 cm^{-1} as determined from a Kramers-Kronig analysis of the reflectivity data shown in Figure II-27 (T = 678°K). 81

II-31. The extinction coefficient (k) of Al_2O_3 in the region 400 cm^{-1} to 2200 cm^{-1} as determined from a Kramers-Kronig analysis of the reflectivity data shown in Figure II-27 (T = 678°K) 82

II-32. Representative values of refractive index (n) in the region 100 cm^{-1} to 2000 cm^{-1} as compiled by Whitson (Ref. II-17) from the literature 88

FIGURES (Continued)

II-33. Representative values of extinction coefficient (k) in the region 100 cm^{-1} to 2000 cm^{-1} as compiled by Whitson (Ref. II-17) from the literature 89

II-34. Calculated reflectivity at 45 degrees incidence for Al_2O_3 ($T \simeq 300^{\circ}K$) in the region 100 cm^{-1} to 2000 cm^{-1} 91

III-1. Calculated emissivity of a spherical carbon particle, radius = 0.5 μm 103

III-2. Calculated emissivity of a spherical carbon particle, radius = 1.0 μm 103

III-3. Calculated emissivity of a spherical carbon particle, radius = 2.0 μm 104

III-4. Calculated emissivity of a spherical carbon particle, radius = 3.0 μm 104

III-5. Calculated emissivity of a spherical carbon particle, radius = 5.0 μm 105

III-6. Calculated emissivity of a spherical carbon particle, radius = 10.0 μm 105

III-7. Caclulated emissivity of a spherical carbon particle, radius = 20 μm 106

III-8. Calculated emissivity of a spherical carbon particle, radius = 20 μm 106

III-9. Calculated emissivity of a spherical carbon particle, radius = 30 μm 107

III-10. Calculated emissivity of a spherical carbon particle, radius = 50 μm 107

III-11. Calculated emissivity for a 0.5 μm radius Al_2O_3, n and k literature values 109

III-12. Calculated emissivity for a 0.5 μm radius Al_2O_3 particle, n and k present results 109

FIGURES (Continued)

III-13. Calculated emissivity for a 1 μm radius Al_2O_3 particle, n and k literature values. 110

III-14. Calculated emissivity for a 1 μm radius Al_2O_3 particle, n and k present results 110

III-15. Calculated emissivity for a 2 μm radius Al_2O_3 particle, n and k literature values 111

III-16. Calculated emissivity for a 2 μm radius Al_2O_3 particle, n and k present results 111

III-17. Calculated emissivity for a 3 μm radius Al_2O_3 particle, n and k literature values 112

III-18. Calculated emissivity for a 3 μm radius Al_2O_3 particle, n and k present results 112

III-19. Calculated emissivity for a 5 μm radius Al_2O_3 particle, n and k literature values. 113

III-20. Calculated emissivity for a 5 μm radius Al_2O_3 particle, n and k present results 113

III-21. Calculated emissivity for a 10 μm radius Al_2O_3 particle, n and k literature values 114

III-22. Calculated emissivity for a 10 μm radius Al_2O_3 particle, n and k present results 114

III-23. Calculated emissivity for a 20 μm radius Al_2O_3 particle, n and k literature values 115

III-24. Calculated emissivity for a 20 μm radius Al_2O_3 particle, n and k present results 115

III-25. Calculated emissivity for a 30 μm radius Al_2O_3 particle, n and k literature values 116

III-26. Calculated emissivity for a 30 μm radius Al_2O_3 particle, n and k present results 116

FIGURES (Continued)

III-27. Calculated emissivity for a 50 μm radius Al_2O_3 particle, n and k literature values 117

III-28. Calculated emissivity for a 50 μm radius Al_2O_3 particle, n and k present results 117

III-29. Calculated emissivity of an infinitely thick sample of Al_2O_3 using the data from Ref. III-5 and formula represented by equation III-20 120

III-30. Calculated emissivity for a 0.5 μm radius Al_2O_3 particle, T = 678°K 121

III-31. Calculated emissivity for a 1.0 μm radius Al_2O_3 particle, T = 678°K 122

III-32. Calculated emissivity for a 2.0 μm radius Al_2O_3 particle, T = 678°K 123

III-33. Calculated emissivity for a 3.0 μm radius Al_2O_3 particle, T = 678°K 124

III-34. Calculated emissivity for a 5.0 μm radius Al_2O_3 particle, T = 678°K 125

III-35. Calculated emissivity for a 10.0 μm radius Al_2O_3 particle, T = 678°K 126

III-36. Calculated emissivity for a 20.0 μm radius Al_2O_3 particle, T = 678°K 126

III-37. Calculated emissivity for a 30.0 μm radius Al_2O_3 particle, T = 678°K 127

III-38. Calculated emissivity for a 50.0 μm radius Al_2O_3 particle, T = 678°K 127

III-39. Calculated emissivity for a 0.5 μm radius MgO particle, T = 300°K 128

III-40. Calculated emissivity for a 1.0 μm radius MgO particle, T = 300°K 129

FIGURES (Continued)

III-41. Calculated emissivity for a 2.0 μm radius MgO particle, T = 300°K 130

III-42. Calculated emissivity for a 3.0 μm radius MgO particle, T = 300°K 131

III-43. Calculated emissivity for a 5.0 μm radius MgO particle, T = 300°K 132

III-44. Calculated emissivity for a 10.0 μm radius MgO particle, T = 300°K 132

III-45. Calculated emissivity for a 20.0 μm radius MgO particle, T = 300°K 133

III-46. Calculated emissivity for a 30.0 μm radius MgO particle, T = 300°K 133

III-47. Calculated emissivity for a 50.0 μm radius MgO particle, T = 300°K 134

III-48. Calculated emissivity for a 0.5 μm radius MgO particle, T = 573°K 134

III-49. Calculated emissivity for a 1.0 μm radius MgO particle, T = 573°K 135

III-50. Calculated emissivity for a 2.0 μm radius MgO particle, T = 573°K 136

III-51. Calculated emissivity for a 3.0 μm radius MgO particle, T = 573°K 137

III-52. Calculated emissivity for a 5.0 μm radius MgO particle, T = 573°K 138

III-53. Calculated emissivity for a 10.0 μm radius MgO particle, T = 573°K 138

III-54. Calculated emissivity for a 20.0 μm radius MgO particle, T = 573°K 139

FIGURES (Continued)

III-55. Calculated emissivity for a 30.0 μm radius MgO particle, T = 573°K 139

III-56. Calculated emissivity for a 50.0 μm radius MgO particle, T = 573°K 140

III-57. Calculated emissivity for a 0.5 μm radius ZrO_2 particle, T = 300°K 143

III-58. Calculated emissivity for a 1.0 μm radius ZrO_2 particle, T = 300°K 143

III-59. Calculated emissivity for a 2.0 μm radius ZrO_2 particle, T = 300°K 144

III-60. Calculated emissivity for a 3.0 μm radius ZrO particle, T = 300°K 145

III-61. Calculated emissivity for a 5.0 μm radius ZrO_2 particle, T = 300°K 146

III-62. Calculated emissivity for a 10.0 μm radius ZrO_2 particle, T = 300°K 146

III-63. Calculated emissivity for a 20.0 μm radius ZrO_2 particle, T = 300°K 147

III-64. Calculated emissivity for a 30.0 μm radius ZrO_2 particle, T = 300°K 147

III-65. Calculated emissivity for a 50.0 μm radius ZrO_2 particle, T = 300°K 148

III-66. Calculated emissivity for a 0.5 μm radius ZrO_2 particle, T = 573°K 148

III-67. Calculated emissivity for a 1.0 μm radius ZrO_2 particle, T = 573°K 149

III-68. Calculated emissivity for a 2.0 μm radius ZrO particle, T = 573°K. 149

III-69. Calculated emissivity for a 3.0 μm radius ZrO_2 particle, T = 573°K 150

FIGURES (Continued)

III-70. Calculated emissivity for a 5.0 μm radius ZrO_2 particle, T = 573°K 151

III-71. Calculated emissivity for a 10.0 μm radius ZrO_2 particle, T = 573°K 152

III-72. Calculated emissivty for a 20.0 μm radius ZrO_2 particle, T = 573°K 152

III-73. Calculated emissivity for a 30.0 μm radius ZrO_2 particle, T = 573°K 153

III-74. Calculated emissivity for 50.0 μm radius ZrO_2 particle, T = 573°K 153

IV-1. Particle emissivity experimental setup 156

IV-2. Equilibrium temperature of laser-heated Al_2O_3 particles 157

IV-3. Time to attain equilibrium temperature for laser-heated Al_2O_3 particles 158

IV-4. Schematic diagram of the particle emission experiment as modified for two opposing lasers for heating 161

IV-5. Apparatus for levitating and irradiating a single particle . . . 162

IV-6. Close-up of the levitation cell, focusing lenses and telescope 163

IV-7. Scattering cell 164

IV-8. Block diagram of levitation electronics 166

IV-9. Schematic diagram of possible conditions for irradiated particle equilibrium in an opposed laser configuration 170

IV-10. Computed acceleration of a 5 μm carbon particle due to radiation pressure and neglecting all drag forces. 172

IV-11. The Gaussian flux density surface 173

FIGURES (Continued)

IV-12. Schematic of focused heating laser flux measurement apparatus 176

IV-13. Heating laser beam diameter σ versus d from pinhole data 178

IV-14. Heat capacity of aluminum oxide, Al_2O_3 (from Lange, Ref. IV-2) 182

IV-15. Emissivity as a function of wavelength for sapphire (Al_2O_3) of 5mm thickness (from Mergerian, Ref. IV-3) 183

IV-16. Computed efficiency factor for absorption of 1.06 μm radiation by Al_2O_3 as a function of temperature 184

IV-17. Time-temperature history of laser-heated Al_2O_3 particles with an initial temperature of 77°K 187

IV-18. Time-temperature history of laser-heated Al_2O_3 particles with an initial temperature of 77°K 188

IV-19. Time-temperature history of laser-heated Al_2O_3 particles with an initial temperature of 77°K 189

IV-20. Particle and background spectral fluxes for various temperatures 197

IV-21. The function $xe^x/(e^x-1)$ plotted as a function of x 202

IV-22. Amorphous carbon particles with diameter ranging from 1.5 to 8 μm 212

IV-23. Aluminum oxide particles that have been spherisized by melting powders in a plasma spray 215

SECTION I

INTRODUCTION

Scattering and thermal emission of electromagnetic radiation from particles of various compositions have taken on significance in several areas of technology during the past few years. In addition to the importance of these processes in certain environmental problems, emission, absorption and scattering of radiation from particles plays a crucial role in certain Air Force Systems applications. The interactions of particles with energy sources can significantly change the electromagnetic radiation field from that expected in the absence of particles.

To our knowledge, at the beginning of the present study there were no measurements of single particle emissivity in the infrared at room temperature or elevated temperatures. To compound the problem of a lack of experimental data, there were apparent discrepancies between visible emissivity measurements based on bulk and on particulate matter. As a consequence, the reliability of using bulk refractive index data to calculate particle emissivity in the infrared was open to question. Furthermore, there was a dearth of high temperature bulk refractive index data for materials of interest.

The Particle Optical Properties Measurements (POPM) Program was proposed to, and jointly funded by AFRPL and SAMSO/ABRES, to attempt to provide answers to these questions. The program agreed upon between AFRPL, SAMSO/ABRES, and The Aerospace Corporation in June of 1974 consisted of four tasks:

(1) To perform an exhaustive and critical compilation of existing measurements of bulk refractive index at room temperature and above for four materials: Carbon, MgO, ZrO_2 and Al_2O_3.

(2) To fabricate an apparatus and procedures for the determination of the infrared complex refractive index of "bulk"

samples of materials at high temperatures. (By "bulk" samples we mean samples which have dimensions such that a polished surface ~ 3.2 x 7.6cm can be prepared on the sample.) This apparatus was then to be used to measure high temperature infrared complex refractive indices for carbon, MgO, ZrO_2 and Al_2O_3.

(3) To design and construct a device to measure the emissivity of single spherical particles heated to high temperature by laser radiation. This apparatus was to be used to determine the emissivity of single particles of various sizes in the micron range formed from the four materials: carbon, MgO, ZrO_2 and Al_2O_3. The observed emissivities were to be compared with the emissivities computed from the high temperature bulk refractive indices.

(4) To use the apparatus built for Task 3 to measure the emissivity of particles provided by AFRPL.

The first of these tasks has been completed and the results published in a combined AFRPL/Aerospace report.[Ref. II-17] This task will not be discussed further in this report. The fourth task was deleted by mutual agreement when sufficient quantities of particles to make both bulk and particle measurements were not available.

Tasks 2 and particularly 3 involve combinations of state-of-the-art measurement techniques. This report discusses the procedures developed and results obtained on these two tasks. The second section discusses the bulk refractive index experiment and results. The third section provides the theory and computed particle emissivity based on Mie theory and the refractive index results presented in Section II. Section IV discusses the techniques and apparatus developed for the single particle emissivity experiment.

SECTION II

HIGH TEMPERATURE BULK REFRACTIVE INDEX EXPERIMENT

A. EXPERIMENTAL DESCRIPTION

The optical constants, n and k, of the materials of interest were obtained in the wavelength range 4.5μm to 25.0μm, and the measurements were made with sample temperatures of 300°K and ~ 600°K for all the materials except carbon, which was measured at 300°K only. The complex index of refraction was extracted from the reflectance spectrum by applying what has come to be known as Kramers-Kronig analysis and, when necessary, the classical dispersion model calculation.

In 1952 Robinson[Ref. II-1] first applied the K-K analysis to reflectance spectra that were obtained from normally incident radiation. Since then the technique has been extended to make it applicable for all angles of incidence between 0 and 90 degrees,[Ref. II-2 - II-6] provided linearly polarized light is used. The classical dispersion model is also a time-honored technique[Refs. II-7 and II-8] and can be applied to reflectance spectra obtained with any polarization and angle of incidence. These two theories are presented in detail in Section II-B of this report.

The experimental procedure, shown schematically in Figure II-1, for measuring the reflectance spectrum is to chop the radiation flux of an infrared source, collimate it, linearly polarize the light with the electric field perpendicular to the plane of incidence, reflect the radiation from the surface of the sample, spectrally modulate the light with a fast scanning Michelson interferometer, and finally, collect the radiation.

In this investigation ~ 1600 interferograms were obtained and coherently added to improve the signal-to-noise ratio. For each sample, calibration spectra were obtained. The calibration standard was a gold mirror. The sequence of measurement was: Run calibration spectra; run sample spectra; run calibration spectra.

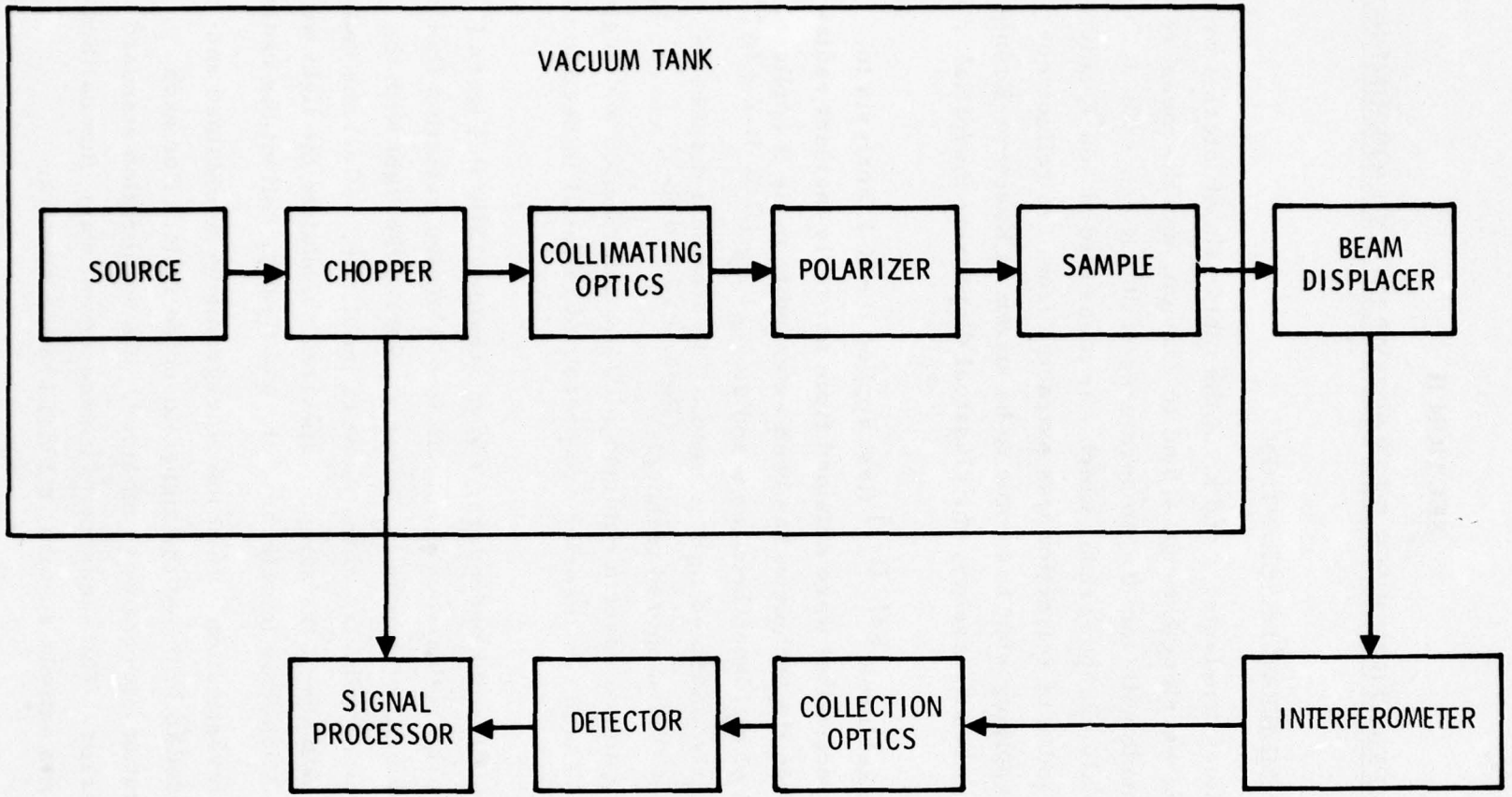

Figure II-1. Schematic diagram of the experimental procedure for obtaining bulk measurements.

1. Experimental Layout

The experimental layout for the bulk index of refraction measurements is shown in Figure II-2. The path of radiation within the tank is shown in Figure II-3. The infrared radiation is provided by an Opperman source, Perkin-Elmer 457-0244, which is a ceramic coated resistance wire. The radiation is chopped by a small mirror, 0.2 x 0.3cm, mounted on a torsional tuning fork, Bulova type L45, tuned to 10kHz, having an angular amplitude of two degrees peak to peak and which has been placed close to the source exit aperture. The light is then rendered parallel by a 31cm focal length spherical mirror used slightly off-axis. The parallel beam from the source is then folded and passed through a Perkin-Elmer wire grid polarizer, a gold wire grid deposited on silver bromide. The efficiency of this polarizer is about 98 percent at 2μm and increases to more than 99.8 percent at 10μm; the transmission is 20 percent.

The source beam, polarized with its electric field perpendicular to the plane of incidence, and with a diameter of 2.2cm, strikes the surface of the sample at an angle of 2α relative to the optical axis of the interferometer and is reflected along that axis; the angle of incidence is α. The equipment is designed to provide a range in α between 25 and 80 degrees with some vignetting at the very largest angles. The angle α is measured with a digital angular encoder (Norden Model 5-36 BCDE360L) to an accuracy of ~ 0.05 degrees. For the measurements presented in this report α was set at 45 degrees.

The sample dimensions are 7.6 x 3.2 x 1.3cm. The front and rear surfaces are cut so that they are not parallel. This insures that the radiation reflected from the back surface does not enter the interferometer. The sample has an electrical heater pressed against the rear surface. The mount for the sample and heater is designed to serve as a heat shield; it is made of tantalum and surrounds all but the front of the sample. To minimize heat losses due to conduction, the sample holder is mounted with low-conductivity ceramic parts; convective

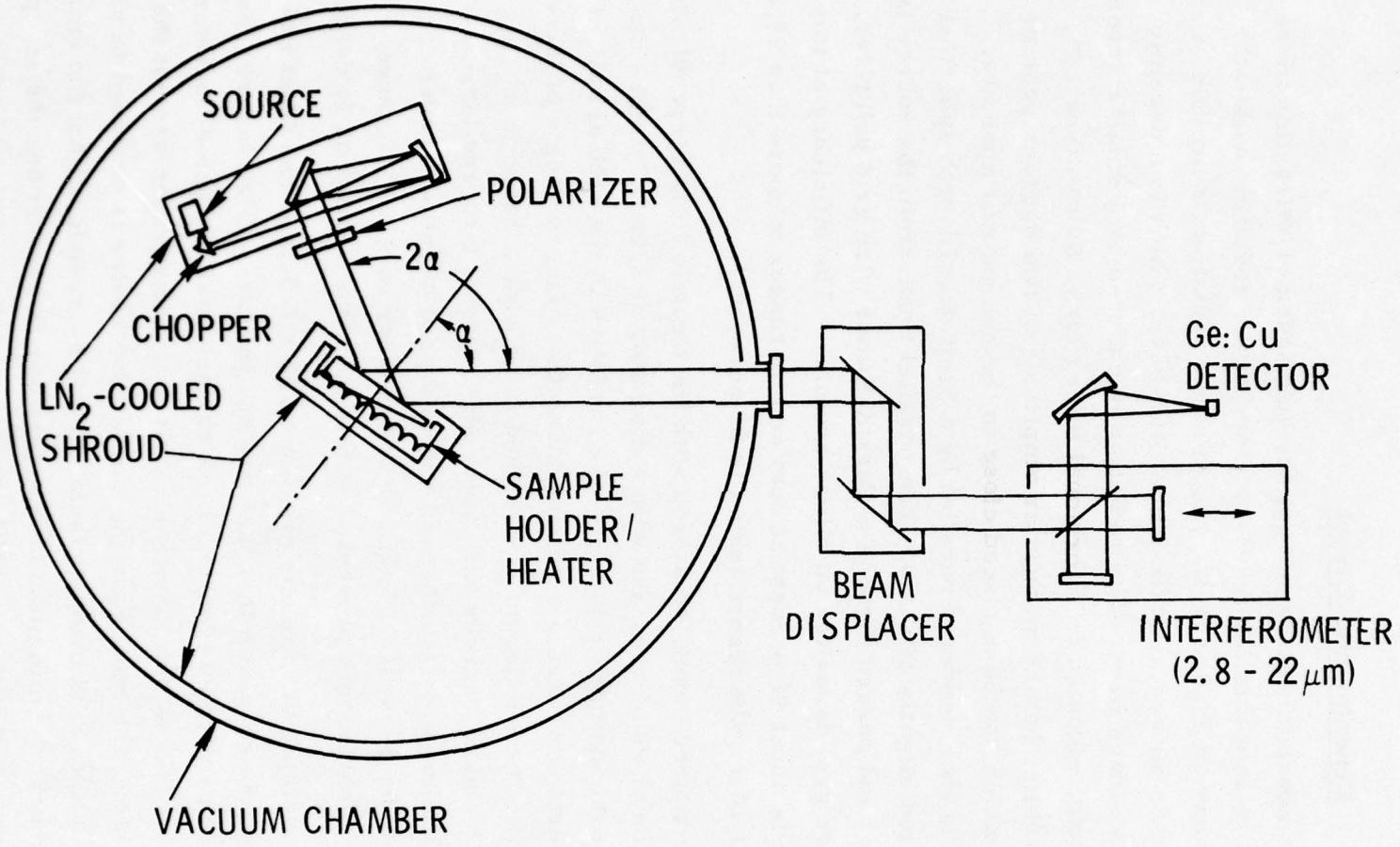

Figure II-2. Schematic diagram of the experimental arrangement for obtaining bulk measurements.

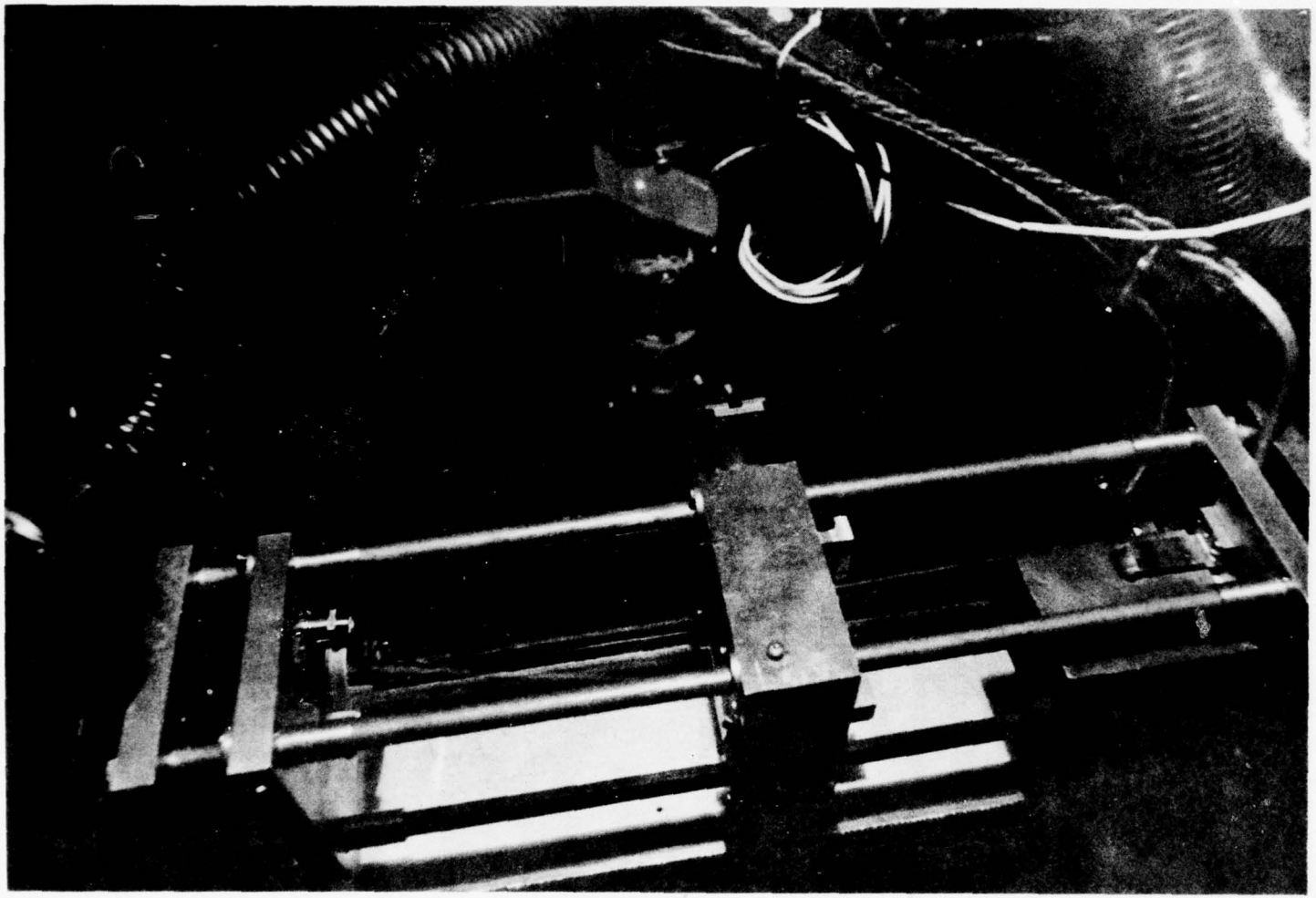

Figure II-3. The inside of the vacuum chamber is shown. A laser beam traces the optical path from the source, lower right of the photograph, to the exit from the chamber, upper left. The flexible tubing is used to fill and vent the liquid nitrogen reservoir, at the bottom of the photograph, which cools the source optics.

heat losses are eliminated by evacuating the whole system. Surface temperatures of up to 700°K have been reached by this method; attempts for higher temperatures resulted in heater failure. A new heater system is now being tested which is designed to allow the attainment of surface temperatures up to and in excess of 1000°K.

An array of spring-loaded thermocouples touching the front surface of the sample was used to detect thermal gradients. The largest difference observed on the surface was about four degrees at 600°K. During data acquisition the thermocouple array is not used; the temperature is then monitored with a thermocouple touching the surface out of the field-of-view of the interferometer.

After reflection from the sample, the source beam leaves the vacuum chamber through an Irtran 6 window. Light emerging from the vacuum chamber is brought into the interferometer by means of a beam displacer inserted in the optical train for convenience in alignment. These optical components outside the vacuum tank are shown in the left of Figure II-4.

The Digilab 296 fast scan Fourier transform interferometer, shown in the center of Figure II-4, is of the Michelson type modified so that double-sided interferograms can be obtained. Since double-sided interferograms do not require phase correction, the possibility of errors being introduced by a phase correction is eliminated. The radiation leaving the interferometer is collected by a 10cm diameter, 76cm focal length mirror and is detected by a liquid helium-cooled, copper doped germanium detector, Raytheon QKN1546. The detector characteristics are: KRS-5 entrance window, $7.85 \times 10^{-3} cm^2$ area, five degrees field-of-view, $6.8 \times 10^{-12} WHz^{-1/2}$ N.E.P. To limit the bandpass, a cold filter, Spectrum Systems 54958X, was mounted inside the dewar. The transmission of the filter is greater than 60 percent in the 2.8μm to 22.0μm range and less than 0.5 percent from 0.4μm to 2.0μm.

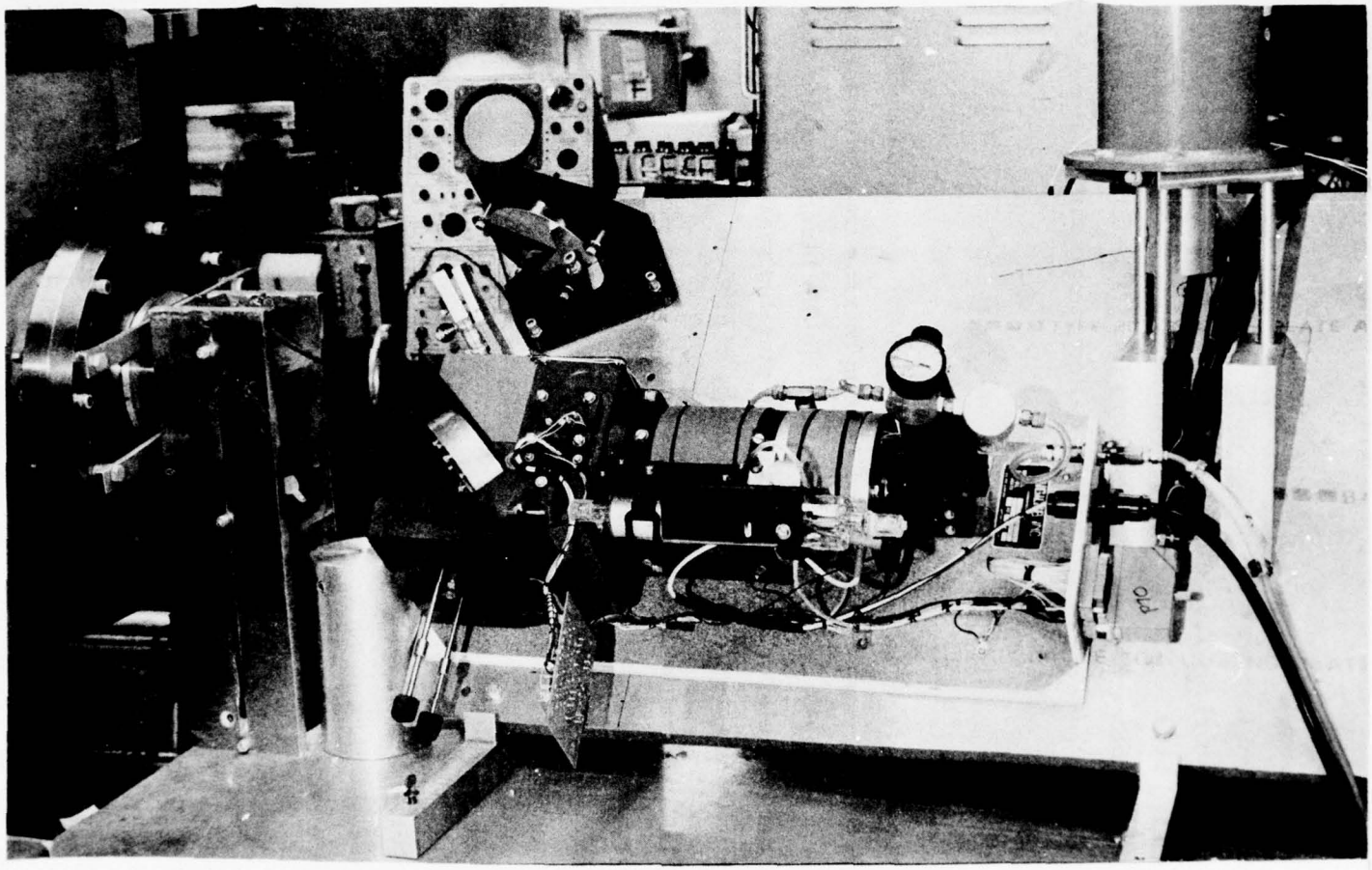

Figure II-4. The vacuum chamber is shown on the left and the interferometer with collection optics and detector on the right; the beam displacer is mounted in between for easy alignment. The interferometer is tipped at 45 degrees to compensate for polarization of the beam splitter.

The source housing, collimating and folding optics are liquid nitrogen-cooled to lower the unwanted thermal background radiation, which might overload the detector. In addition, the chamber walls are shielded by a liquid nitrogen-cooled shroud. Near the end of the experimental measurements the vacuum integrity of this chamber shroud failed. However, little degradation of experimental performance was observed after this failure.

2. Signal Processing

The interferogram was sampled when the optical path difference between the stationary mirror and moving mirror was increased by 0.63299×10^{-4}cm, the wavelength of the He-Ne laser line; for this rate of data acquisition sampling theory dictates that the largest wavenumber with non-zero intensity should be $\sim 7900\text{cm}^{-1}$.

The scan velocity of the interferometer mirror is ~ 0.5cm/sec, therefore, our largest wavenumber, 7900cm^{-1}, results in a frequency of 3950Hz. (This means that a monochromatic beam with $\nu = 7900\text{cm}^{-1}$ would have as its interferogram a cosine wave of frequency 3950Hz.)

The signal that reaches the detector is a 10kHz carrier wave (due to the chopper) modulated by lower frequencies (due to the interferometer) with the highest of these being ~ 3950Hz. This signal is amplified and then synchronously detected with a Princeton Applied Research lock-in amplifier, model 124A.

The last stage of the lock-in amplifier, which provides the final filtering of the demodulated signal, has a high frequency cutoff less than 3950Hz and so it is not used. Instead, a bandpass filter with a 6kHz cutoff frequency and an attenuation of -40dB at 10kHz has been built from commercial active bandpass filter components and is used to filter the demodulated signal before being fed to the data handling system.

The data handling system samples the filtered analog signal from the lock-in amplifier when commanded by the interferometer. The sampled signal is converted to a 12-bit digital number in an analog to digital converter. The resulting number is recorded on computer compatible tape for subsequent Fourier transformation and processing of the spectra by the Aerospace Control Data 7600 computers using standard techniques.[Ref. II-9]

3. Samples

Bulk samples had to be at least 3.2 x 7.6 x 1.3cm, of high purity and, when appropriate, single crystals. Since this last condition could not be met for all of the materials, sources and methods were sought that could produce bulk samples from pure powders. The surfaces of the samples were polished with a compound made of 0.3μm Al_2O_3 particles and distilled water, and Linde type A polishing compound. They were then cleaned with an ultrasonic cleaner and different solvents; acetone was first used, then a detergent and ammonia combination, and finally, distilled water. Impurity contamination of the samples is felt to be negligible, however, the physical process of polishing and cleaning can affect the surface of the samples (i.e., introduction of strains) and thus may affect the reflectivity measurements. This is discussed in more detail in the section on the experimental observations on Al_2O_3.

a. Carbon (C)

Single crystals of graphite can be produced synthetically. However, available sizes are not large enough to use in this experiment. The sample we have used is CEP graphite, produced by Union Carbide. This is a mixture of lamp black and binder pressed and baked at a very high temperature.

b. Magnesia (MgO)

A single crystal of MgO was obtained from the ROC/RIC Corporation of Sun Valley, California. This material is 99.99 percent pure.

c. Zirconia (ZrO_2)

Single crystals of zirconium dioxide, large enough for our needs, do not occur in nature and are not synthetically produced. The only available choice was a polycrystalline piece formed by hot pressing ZrO_2 powder.

The Cerac Corporation supplied Aerospace with a hot pressed ZrO_2 sample that is 98 percent ZrO_2 plus two percent HfO_2, an impurity which cannot be economically removed from ZrO_2.

d. Alumina (Al_2O_3)

Synthetic pure crystals of alumina were found to be available. The Union Carbide Corporation supplied us with a single crystal of pure Al_2O_3.

B. DATA REDUCTION METHODS

1. Angular Reflectance Analysis, Avery Method

The index of refraction and the extinction coefficient can be determined from a measurement of the reflectance R_{11} and/or $R_{\perp}$ (radiant flux polarized parallel and perpendicular to the plane of incidence, respectively) by the method of Avery.[Ref. II-10]

This method is based on the generalized Fresnel reflectance equations which can be written[Ref. II-11]

$$R_{\perp} = \frac{(Q - \cos\theta)^2 + P^2}{(Q + \cos\theta)^2 + P^2}, \text{ and}$$

$$R_{11} = R_{\perp} \frac{(Q - \sin\theta \tan\theta)^2 + P^2}{(Q + \sin\theta \tan\theta)^2 + P^2}, \text{ where} \qquad \text{(II-1)}$$

$$Q^2 - P^2 = n^2 - k^2 - \sin^2\theta, \text{ and}$$

$$QP = nk, \qquad \text{(II-2)}$$

where n is the index of refraction (real part), k is the extinction coefficient, and θ is the angle of incidence. Thus in principle, a measurement of $R_{\perp}$ and/or R_{11} as a function of θ will allow determination of n and k. A direct method for inverting these equations to determine n and k has been discussed recently in the literature.[Refs. II-11 - II-13] Unfortunately, when the reflectance data for Al_2O_3 were analyzed by this method, the equations proved to be ill-conditioned under certain conditions and unreasonable values of n and/or k were sometimes obtained. Invariably in these situations, small changes in the input reflectance data produced large changes in n and/or k. The reason for this ill-conditioning is not too difficult to discover. For instance, if n is small ($\lesssim 1$) and k large ($\gtrsim 7$), both $R_{\perp}$ and R_{11} are > 0.8, and change little with θ or increasing k. Another example of ill-conditioning is illustrated in Figure II-5. Plotted is R_{11} as a function of the angle of incidence $\theta = 45$ degrees for the three cases: $n = 3.5$, $k = 3.0$; $n = 4.5$, $k = 3.0$; and $n = 5.5$, $k = 2.0$. The curves do not appreciably differ from each other until θ is greater than about 72 degrees. Beyond $\theta = 75$ degrees the curves are significantly different, however, measurements at these large angles of incidence require very large samples (because of the foreshortening effect), and very accurate angular measurements,

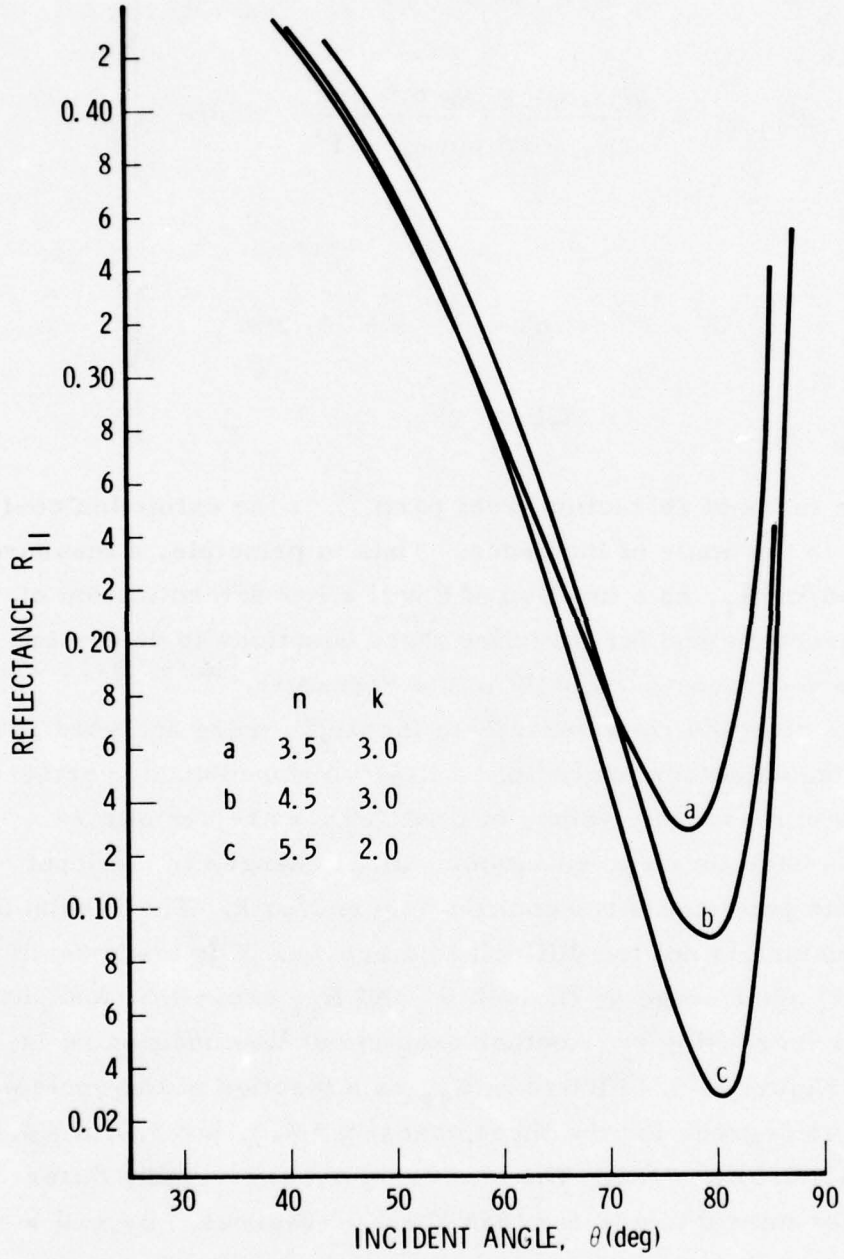

Figure II-5. Computed reflectance as a function of incidence angle for three different values of complex refractive index.

due to the rapid change of R_{11} with respect to θ for $\theta \gtrsim 75$ degrees. Since neither of these conditions are readily achieved in our experimental apparatus, we have employed either a Kramers-Kronig analysis or a classical dispersion analysis to obtain the optical constants.

2. Kramers-Kronig Analysis

The amplitude, $R_\perp$, and phase, ψ, of the complex reflectivity coefficient are not independent but can, in general, be related by a Kramers-Kronig dispersion relation.*

$$\psi(\nu_c) = \frac{1}{\pi} \int_0^\infty \ln\left|\frac{\nu + \nu_c}{\nu - \nu_c}\right| \frac{d}{d\nu}\left[\ln\left|R_\perp(\nu)\right|^{1/2}\right] d\nu \qquad \text{(II-3)}$$

where ν is the wavenumber of the reflected wave. The generalized Fresnel equations can then be written in terms of this amplitude and phase,

$$Q = \frac{(1 - R_\perp)\cos\theta}{1 + R_\perp - 2\sqrt{R_\perp}\cos\psi}, \qquad \text{(II-4)}$$

$$P = \frac{-2\sqrt{R_\perp}\cos\theta\sin\psi}{1 + R_\perp - 2\sqrt{R_\perp}\cos\psi},$$

where the quantities have their previous definitions.** Finally, n and k are obtained from P and Q by solving equation II-2.

---

*Kramers-Kronig analyses have been treated extensively in the literature. The analysis outlined here follows Ref. II-2.

**Similar but more complicated equations can be written for R_{11}.

The disadvantage of this analysis is that ψ depends on the behavior of $R_\perp(\nu)$ over all of wavenumber space. In practice, the reflectivity is measured over only a finite portion of wavenumber space and realistic approximations for the behavior of $R_\perp(\nu)$ outside this region are required for accurate evaluation of the integral.

Most of the methods discussed in the literature assume some simple functional form for the reflectivity in the outside region. In some cases the form of the function is justified by a theoretical model and in other cases it is just a simple function which behaves in a physically reasonable manner.[Refs. II-14 and II-16]

We did not use any special functional form to extrapolate the reflectivity curves, but rather tried to incorporate as much as possible any published[Ref. II-17] experimental data in the outside regions. In some cases the results of classical dispersion theory were incorporated and this is discussed in the next section. The reflectivity was then extrapolated graphically to fit these data points and to join them smoothly to our measured reflectivity spectra.

This curve was then digitized for computer calculation of the phase by the Kramers-Kronig integral. The amplitude and phase of the reflectance were used to obtain P and Q (equation II-4) and finally n and k determined from solutions of equation II-2.

3. Classical Dispersion Analysis

The classical dispersion analysis of reflectivity data is based on a model which approximates the material as a system of damped harmonic oscillators. Each oscillator is described by its strength ρ_j, width γ_j, and frequency ν_j. The expression for the complex dielectric constant (ϵ) from this model is

$$\epsilon(\nu) = \epsilon_\infty + \sum_j \frac{4\pi\rho_j}{1 - (\nu/\nu_j)^2 - i(\nu/\nu_j)(\gamma_j/\nu_j)} \qquad \text{(II-5)}$$

where ϵ_∞ is the high frequency limit. The index of refraction, n, and the coefficient of extinction, k, are related to ϵ by

$$n + ik = \sqrt{\epsilon} \qquad \text{(II-6)}$$

The reflectivity can then be calculated from Fresnel's equation if the constants in equation II-5 are known or assumed. These constants are called the dispersion parameters and the process of determining them is dispersion analysis. The parameters are varied until agreement is obtained with experiment. The criteria used was to minimize the sum of the square errors. This was accomplished with a non-linear least squares fitting computer program which systematically varied the parameters until a best fit was obtained.

C. EXPERIMENTAL RESULTS

The Kramers-Kronig analysis was used to reduce the data for carbon, Al_2O_3, and ZrO_2 where we felt we could adequately extrapolate the reflectance data to the lower ($\nu < 400cm^{-1}$) and the higher ($\nu > 2200cm^{-1}$) wavenumber regions. The MgO data was reduced using the classical dispersion analysis method where we felt we could not safely extrapolate the reflectance data to the lower ($\nu < 400cm^{-1}$) wavenumber region. In general, we feel the Kramers-Kronig method of analysis is superior to the classical dispersion method of analysis, since the former is independent of any model assumptions concerning the behavior of the optical parameters (n and k) of the material, where as the latter assumes the behavior of the optical parameters of the material may be modeled as a system of damped harmonic oscillators.

1. Carbon

The room temperature reflectivity spectrum of a microcrystalline, polished slab of graphite, at an angle of incidence of 45 degrees, is shown in Figure II-6. The resolution is $\sim 15\text{cm}^{-1}$.

The observed reflectance was smoothly extrapolated below 400cm^{-1}, as shown in Figure II-6, and a Kramers-Kronig analysis was performed. The resulting values of n and k are shown in Figures II-7 and II-8, respectively.

The variations of the observed reflectivity about the generally smooth trend of the graphite reflectivity spectra are consistent with the expected noise level. It was discovered, empirically, that a curve of the form

$$R_{\perp} = A + B\nu^{-1} \qquad \text{(II-7)}$$

could very accurately fit our experimental data. This smoothed reflectance spectrum is shown as the dashed curve in Figure II-6. A Kramers-Kronig analysis was performed and the resulting n and k are shown as the dashed curves in Figures II-7 and II-8, respectively.

For some situations the scaling in Figures II-7 and II-8 may be too coarse, and therefore n and k (as deduced from the experimental data and the smoothed data) are given as a function of wavenumber, in 12cm^{-1} increments, in Table II-1, from $\nu = 400\text{cm}^{-1}$ to 2200cm^{-1}.

In an effort to ascertain the experimental errors in our measurements, and to estimate the resulting errors in n and k, the following analysis was performed. At $\sim 12\text{cm}^{-1}$ intervals the quantity $\Delta = |R_{\perp}(s) - R_{\perp}(e)|$ was calculated where $R_{\perp}(e)$ is the experimentally measured reflectance (Figure II-6), and $R_{\perp}(s)$ is the smoothed reflectance from Figure II-6. These Δs were then used to estimate the error made in measuring reflectivity in two hundred wavenumber intervals from 400cm^{-1} to 2200cm^{-1}. The results are given in Table II-2. The ΔRs, the reflectivity errors, were calculated in a root-mean-square (rms) fashion, that is

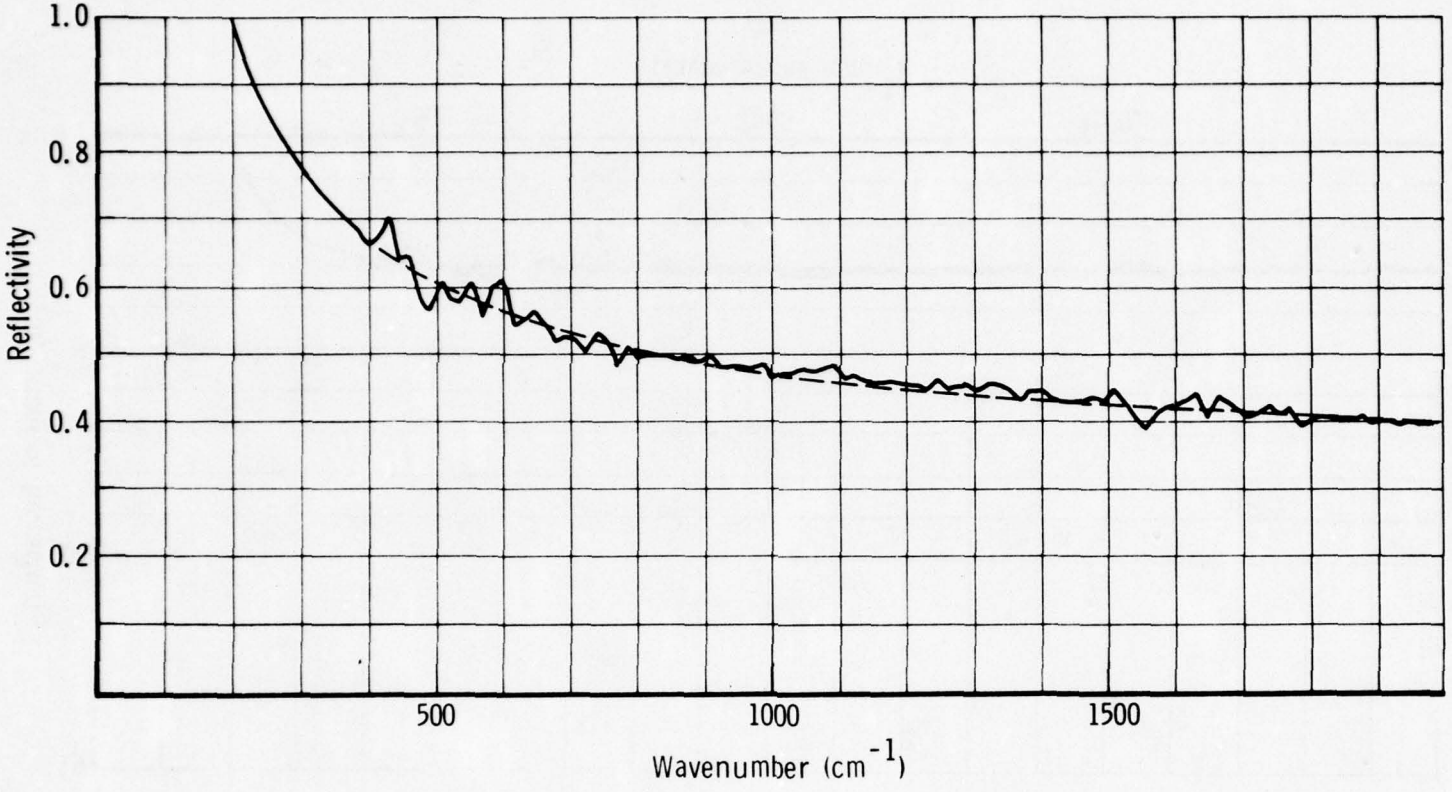

Figure II-6. The reflectivity spectrum (solid curve) of carbon (graphite) from 400cm^{-1} (25μm) to 2000cm^{-1} (5.0μm) measured at room temperature and an angle of incidence of 45 degrees. The structure in the spectrum may not be real, and in fact is the expected variation due to noise in these measurements. Values below 400cm^{-1} are extrapolated. The dashed curve was obtained by fitting the experimental data to an equation of the form $R = A + B\nu^{-1}$ and is called the smoothed reflectance spectrum of carbon. See text for further details.

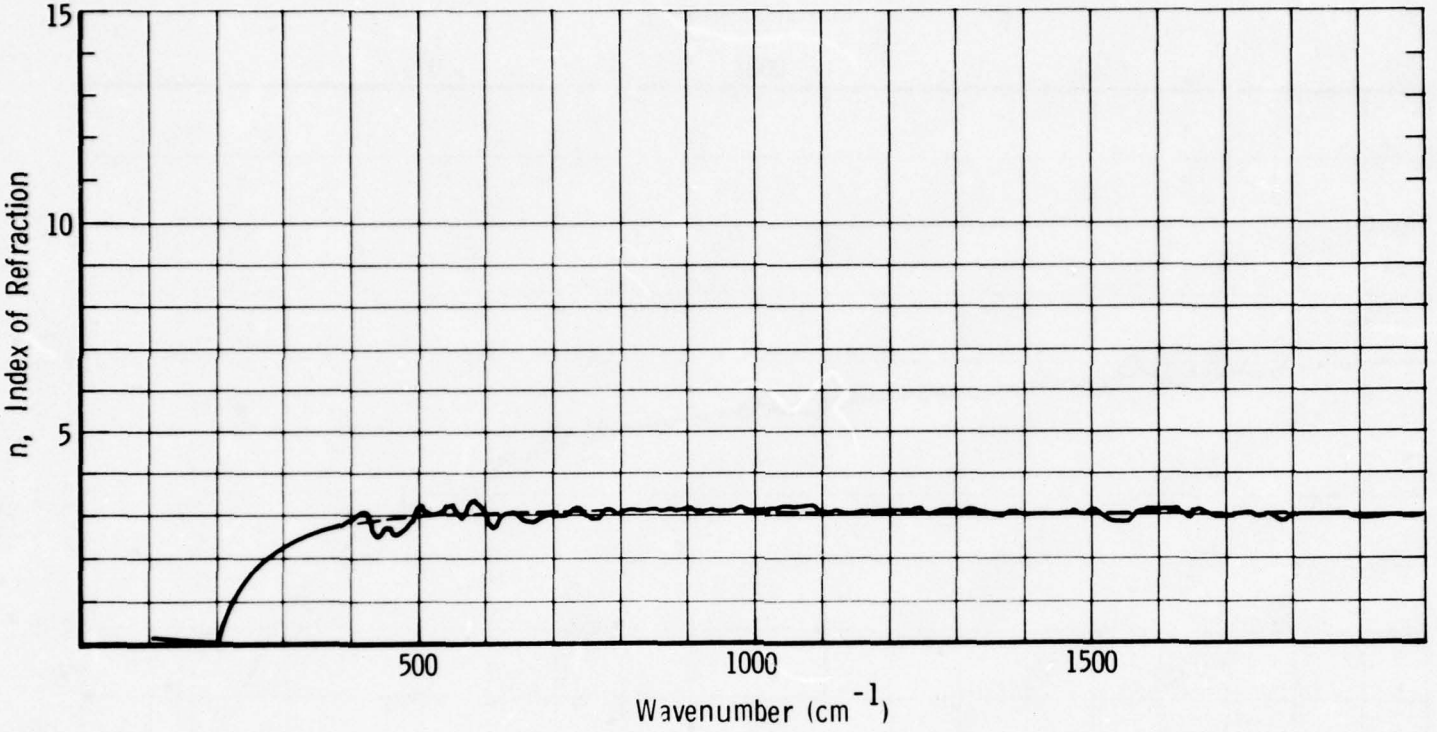

Figure II-7. The index of refraction (n) of carbon, from 400cm^{-1} to 2000cm^{-1} as determined from a Kramers-Kronig analysis of the experimental reflectivity data is shown as the solid curve. The dashed curve is n as determined from a Kramers-Kronig analysis of the smoothed reflectivity data.

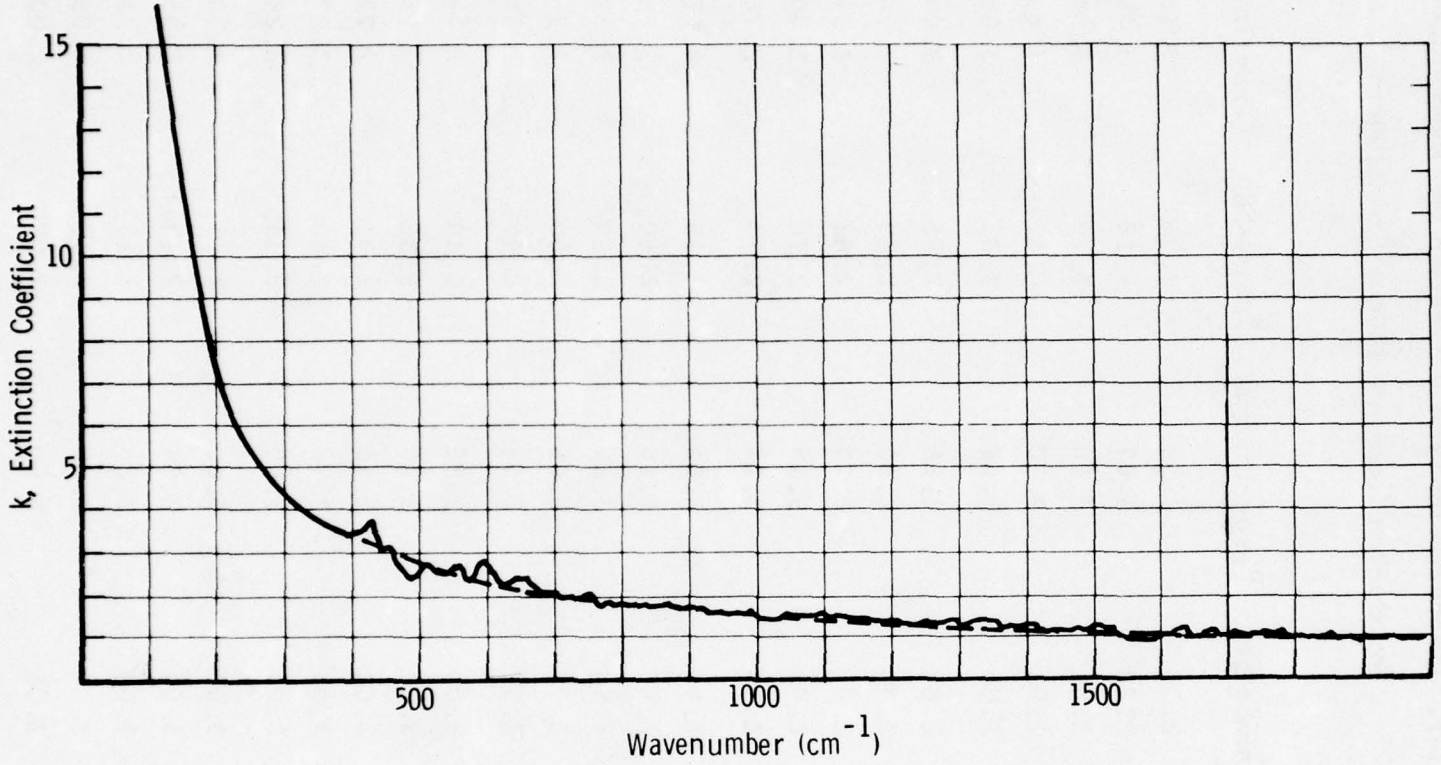

Figure II-8. The extinction coefficient (k) of carbon from 400cm^{-1} to 2000cm^{-1} as determined from a Kramers-Kronig analysis of the experimental reflectivity data is shown as the solid curve. The dashed curve is k as determined from a Kramers-Kronig analysis of the smoothed reflectivity data.

Table II-1. Measured Index of Refraction and Extinction Coefficient for Carbon from $\nu = 400 cm^{-1}$ to $2200 cm^{-1}$.

ν (cm^{-1})	$n_{smoothed}$	$n_{experimental}$	$k_{smoothed}$	$k_{experimental}$
400	2.75	2.92	3.36	3.32
12	2.78	3.07	3.28	3.43
24	2.81	3.00	3.19	3.64
36	2.83	2.50	3.11	3.48
48	2.85	2.64	3.03	3.05
60	2.88	2.66	2.96	3.09
72	2.90	2.55	2.89	2.76
84	2.91	2.77	2.82	2.51
96	2.93	3.13	2.76	2.40
508	2.95	3.21	2.70	2.76
20	2.96	3.01	2.65	2.62
32	2.97	3.10	2.60	2.52
44	2.98	3.26	2.55	2.55
56	2.98	3.06	2.50	2.76
68	2.99	2.99	2.45	2.38
80	3.00	3.36	2.40	2.49
92	3.01	3.20	2.36	2.75
604	3.02	2.78	2.31	2.73
16	3.03	2.76	2.28	2.27
28	3.03	3.00	2.24	2.23
40	3.03	3.08	2.21	2.30
52	3.04	2.94	2.17	2.35
64	3.04	2.86	2.13	2.23
76	3.04	2.86	2.10	2.05
88	3.05	3.00	2.07	2.00

Table II-1. (Continued)

ν (cm^{-1})	$n_{smoothed}$	$n_{experimental}$	$k_{smoothed}$	$k_{experimental}$
700	3.05	3.00	2.04	2.01
12	3.05	2.98	2.01	1.97
24	3.06	3.03	1.98	1.84
36	3.06	3.19	1.95	1.96
48	3.06	3.03	1.92	2.03
60	3.06	2.90	1.90	1.92
72	3.06	2.98	1.87	1.66
84	3.07	3.17	1.85	1.78
96	3.07	3.05	1.83	1.79
808	3.06	3.12	1.80	1.71
20	3.07	3.12	1.77	1.75
32	3.07	3.11	1.75	1.71
44	3.07	3.15	1.73	1.71
56	3.07	3.12	1.72	1.70
68	3.07	3.16	1.69	1.67
80	3.07	3.15	1.67	1.72
92	3.07	3.10	1.65	1.66
904	3.07	3.17	1.63	1.66
16	3.07	3.07	1.62	1.69
28	3.07	3.08	1.60	1.57
40	3.07	3.13	1.58	1.58
52	3.07	3.12	1.56	1.57
64	3.07	3.11	1.55	1.55
76	3.07	3.15	1.53	1.52
88	3.07	3.12	1.52	1.61

Table II-1. (Continued)

ν (cm^{-1})	$n_{smoothed}$	$n_{experimental}$	$k_{smoothed}$	$k_{experimental}$
1000	3.07	3.04	1.50	1.50
12	3.07	3.12	1.49	1.44
24	3.07	3.15	1.47	1.45
36	3.07	3.18	1.46	1.44
48	3.07	3.20	1.45	1.48
60	3.07	3.16	1.43	1.48
72	3.06	3.17	1.42	1.46
84	3.06	3.20	1.40	1.48
96	3.06	3.15	1.39	1.57
1108	3.07	3.04	1.38	1.48
20	3.06	3.10	1.36	1.43
32	3.07	3.07	1.35	1.44
44	4.06	3.06	1.34	1.40
56	3.06	3.06	1.33	1.36
68	3.06	3.09	1.32	1.35
80	3.06	3.09	1.30	1.35
92	3.06	3.09	1.29	1.35
1204	3.06	3.08	1.28	1.33
16	3.06	3.09	1.27	1.33
28	3.06	3.07	1.26	1.30
40	3.06	3.13	1.25	1.28
52	3.06	3.10	1.24	1.36
64	3.05	3.04	1.23	1.29
76	3.06	3.09	1.22	1.26
88	3.06	3.12	1.21	1.28

Table II-1. (Continued)

ν (cm^{-1})	$n_{smoothed}$	$n_{experimental}$	$k_{smoothed}$	$k_{experimental}$
1300	3.06	3.08	1.21	1.31
12	3.05	3.08	1.20	1.24
24	3.05	3.14	1.19	1.28
36	3.05	3.08	1.18	1.33
48	3.05	3.03	1.17	1.32
60	3.05	2.98	1.16	1.29
72	3.05	2.96	1.15	1.19
84	3.05	3.07	1.14	1.18
96	3.05	3.05	1.13	1.24
1408	3.05	3.01	1.13	1.25
20	3.05	2.97	1.12	1.21
32	3.04	2.96	1.11	1.16
44	3.04	3.00	1.10	1.12
56	3.04	3.02	1.10	1.13
68	3.04	3.04	1.09	1.11
80	3.04	3.06	1.08	1.15
92	3.04	3.01	1.07	1.14
1504	3.04	3.10	1.07	1.15
16	3.04	2.99	1.06	1.29
28	3.04	2.86	1.05	1.23
40	3.04	2.78	1.04	1.11
52	3.04	2.79	1.04	0.97
64	3.04	2.92	1.03	0.84
76	3.03	3.04	1.03	0.88
88	3.03	3.09	1.02	0.93

Table II-1. (Continued)

ν (cm^{-1})	$n_{smoothed}$	$n_{experimental}$	$k_{smoothed}$	$k_{experimental}$
1600	3.03	3.10	1.01	0.96
12	3.03	3.13	1.01	0.99
24	3.03	3.15	1.00	1.04
36	3.03	3.08	1.00	1.20
48	3.03	2.90	0.99	1.04
60	3.03	3.10	0.98	0.96
72	3.03	3.08	0.98	1.11
84	3.03	2.98	0.97	1.11
96	3.03	2.92	0.97	1.05
1708	3.03	2.94	0.96	0.98
20	3.02	2.98	0.95	0.95
32	3.02	3.03	0.95	0.96
44	3.03	3.03	0.95	1.04
56	3.02	2.95	0.94	1.01
68	3.02	2.99	0.93	0.99
80	3.02	2.88	0.93	1.04
92	3.02	2.87	0.93	0.88
1804	3.02	2.96	0.92	0.87
16	3.02	2.98	0.91	0.89
28	3.02	2.98	0.91	0.90
40	3.02	2.98	0.90	0.90
52	3.02	2.97	0.90	0.89
64	3.02	2.97	0.89	0.88
76	3.01	3.00	0.89	0.88
88	3.01	2.96	0.89	0.90

Table II-1. (Concluded)

ν (cm^{-1})	$n_{smoothed}$	$n_{experimental}$	$k_{smoothed}$	$k_{experimental}$
1900	3.01	2.96	0.88	0.84
12	3.01	2.99	0.87	0.84
24	3.01	2.98	0.87	0.85
36	3.01	2.95	0.86	0.83
48	3.01	3.01	0.86	0.74
60	3.01	3.10	0.86	0.84
72	3.01	3.04	0.85	0.85
84	3.01	3.07	0.85	0.85
96	3.01	3.05	0.84	0.91
2008	3.01	3.02	0.84	0.91
20	3.01	3.00	0.84	0.92
32	3.01	2.94	0.83	0.90
44	3.00	2.96	0.83	0.85
56	3.00	2.97	0.82	0.87
68	3.00	2.94	0.82	0.90
80	3.00	2.86	0.82	0.85
92	3.00	2.85	0.81	0.75
2104	3.00	2.97	0.81	0.66
16	3.00	3.03	0.80	0.79
28	3.00	2.96	0.80	0.76
40	3.00	3.04	0.80	0.76
52	3.00	3.00	0.79	0.83
64	3.00	2.94	0.79	0.81
76	3.00	2.92	0.79	0.70
88	2.99	3.04	0.79	0.74
2200	2.99	3.00	0.78	0.77

Table II-2. Reflectivity Measurement Errors (rms)

Wave Number Interval	ΔR, Reflectivity Error
400 - 600cm^{-1}	0.028
600 - 800cm^{-1}	0.020
800 - 1000cm^{-1}	0.007
1000 - 1200cm^{-1}	0.011
1200 - 1400cm^{-1}	0.011
1400 - 1600cm^{-1}	0.015
1600 - 1800cm^{-1}	0.013
1800 - 2000cm^{-1}	0.008
2000 - 2200cm^{-1}	0.011

$$\Delta R = \left[\sum_{i-1}^{n} (\Delta_i^2) \right]^{1/2} \Big/ n \qquad \text{(II-8)}$$

There is no a priori reason for assuming the reflectivity of carbon should be smooth as a function of wave number, or that it have the particular dependence as assumed in equation II-7. However, the ΔRs given in Table II-1 are about what would be expected when detector sensitivity, instrumental response and atmospheric absorption are taken into consideration. In a sense this method of determining reflectivity errors is conservative, since all deviations from the smoothed curve are treated as errors, whereas some of the larger deviations may be real.

As discussed previously, n and k are determined from the generalized Fresnel equations,

$$Q = \frac{(1 - R_\perp) \cos\theta}{1 + R_\perp - 2\sqrt{R_\perp} \cos\psi} ,$$

$$P = \frac{-2\sqrt{R_\perp} \cos\theta \sin\psi}{1 + R_\perp - 2\sqrt{R_\perp} \cos\psi} ,$$

where

$$Q^2 - P^2 = n^2 - k^2 - \sin^2\theta, \text{ and}$$

$$QP = nk,$$

and R is the reflectivity, θ the angle of incidence, ψ the phase change on reflection (obtained by Kramers-Kronig analysis), and n and k the desired optical constants. Q and P, and therefore n and k, are determined by three quantities; $R_\perp$, ψ and θ, and therefore, errors in these quantities will determine the probable error in n and k. The angle of

incidence, θ, is very well known experimentally and analysis has shown that the error in the measurement of $\theta(\lesssim 0.2^\circ)$ is negligible in comparison to the errors in R and ψ. The error in R, ΔR, was assumed to be

$$\Delta R = \pm 0.015,$$

and is representative of the errors given in Table II-2. The errors in ψ were determined by examining the Kramers-Kronig data for the experimental and smoothed data, in a manner analogous to the analysis for ΔR, with the result:

$$\Delta\psi = 1.10 \text{ degrees.}$$

A computer program was written to calculate n and k given ψ and R, and then four calculations were carried out, setting

$$R = R + \Delta R, \text{ and } \psi = \psi + \Delta\psi;$$
$$R = R + \Delta R, \text{ and } \psi = \psi - \Delta\psi;$$
$$R = R - \Delta R, \text{ and } \psi = \psi + \Delta\psi;$$
$$R = R - \Delta R, \text{ and } \psi = \psi - \Delta\psi;$$

to determine n and k. The two extrema (+ and - about the input value) were then selected and their difference from the input value was called the error in n and k. The results are shown in Table II-3, for a range of n and k from zero to ten. The table is in matrix form, where the top number is the error in n and the bottom number is the error in k. As an example, suppose n was measured to be 3.0 and k 2.0, then Table II-3, gives the error in n as $\pm$ 0.20 and the error in k as $\pm$ 0.17. Intermediate cases can be obtained by interpolation.

Table II-3. Errors in n and k as a Function of n and k, Assuming $\Delta R = \pm 0.015$, $\Delta\psi = \pm 1.1^{\circ}$, and $\Delta\theta = 0$.

n \ k	0.0	1.0	2.0	3.0	5.0	7.0	10.0
1.0		$\Delta n =$ $\pm .05$*	.09	.15	.29	.48	.85
		$\Delta k =$ $\pm .05$	.09	.17	.40	.75	1.42
2.0	.07	.08	.12	.21	.42	.66	1.12
	.04	.09	.10	.18	.43	.80	1.58
3.0	.11	.17	.20	.26	.52	.83	1.37
	.12	.17	.17	.17	.44	.83	1.64
5.0	.22	.34	.44	.53	.73	1.10	1.81
	.36	.40	.44	.44	.40	.80	1.67
7.0	.37	.55	.71	.86	1.12	1.45	2.18
	.72	.74	.80	.83	.78	.75	1.58
10.0	.66	.92	1.17	1.41	1.85	2.26	3.06
	1.52	1.55	1.53	1.59	1.62	1.54	1.53

*Top figure is error in n, lower figure is error in k.

Although a definitive analysis was not performed, the calculations from which Table II-3 was derived indicated that the errors in n and k were more sensitive to the error in R as opposed to ψ. Approximate scaling should therefore go as the size of ΔR (Table II-2), although it should be kept in mind that the Fresnel equations are non-linear in n and k and extreme extrapolation may be erroneous.

The optical constants (n and k) of carbon type materials (coals, ashes, graphite, etc.) are the subject of a vast literature and the reader is referred to a review by Twitty and Weinman[Ref. II-18]. In order to illustrate the wide variance in the experimental results, the present data is compared with three previous investigations in Figure II-9, for n the index of refraction, and in Figure II-10, for k the extinction coefficient. In each figure the dashed curves are the results obtained by Foster and Howarth[Ref. II-19] for polycrystalline graphite (method of preparation not discussed). The dotted curves are the results of Lenham and Treherne[Ref. II-20] for pyrolytic graphite (deposited at 2280°C and annealed at 3200°C) from reflectivity measurements with the electric field vector polarized perpendicular to the (presumably oriented) optic axis of the graphite crystal(s). The solid curve is the present results and the dot-dashed curve is for pressed carbon soot (obtained for an oil furnace process, fixed carbon percentage = 98.5 percent, particle size $\approx$ 0.023 μm) as reported by Foster and Howarth[Ref. II-19]. The results shown in these two figures were chosen to illustrate the wide difference in results obtained for carbon materials. The reader is referred to Ref. II-18 for a more complete comparison. Some of the differences are probably due to experimental error, but it is probable, especially from the investigations of Foster and Howarth[Ref. II-19], that most of the apparent disagreement is real and due to such factors as source of the raw material, and method of preparation of the samples.

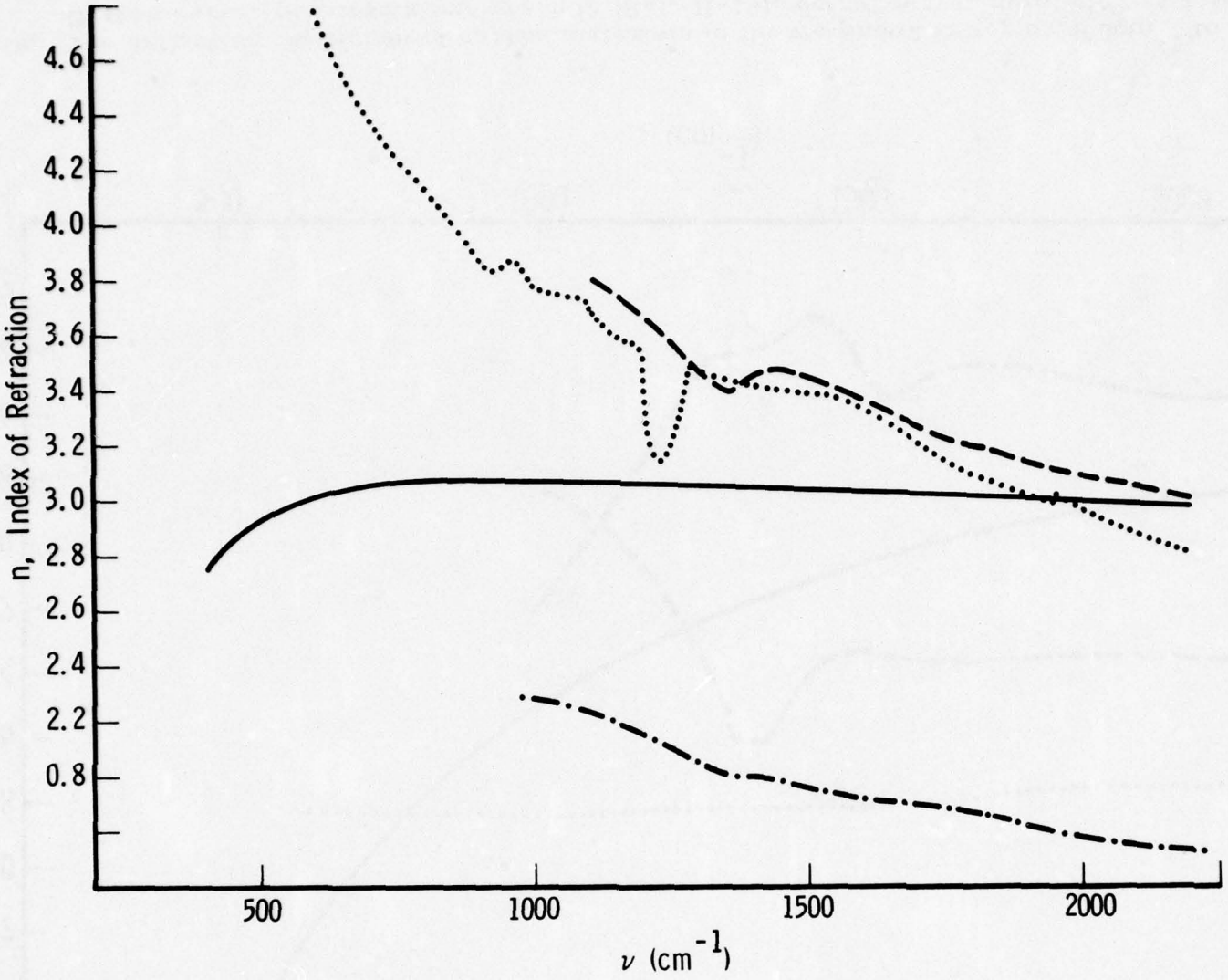

Figure II-9. The index of refraction of carbon materials in the wavenumber region 400cm^{-1} to 2200cm^{-1}. Dashed curve, polycrystalline graphite (Ref. II-19), dotted curve, pyrolytic graphite (Ref. II-20), solid curve, present results, and dot-dashed curve, pressed carbon soot (Ref. II-19).

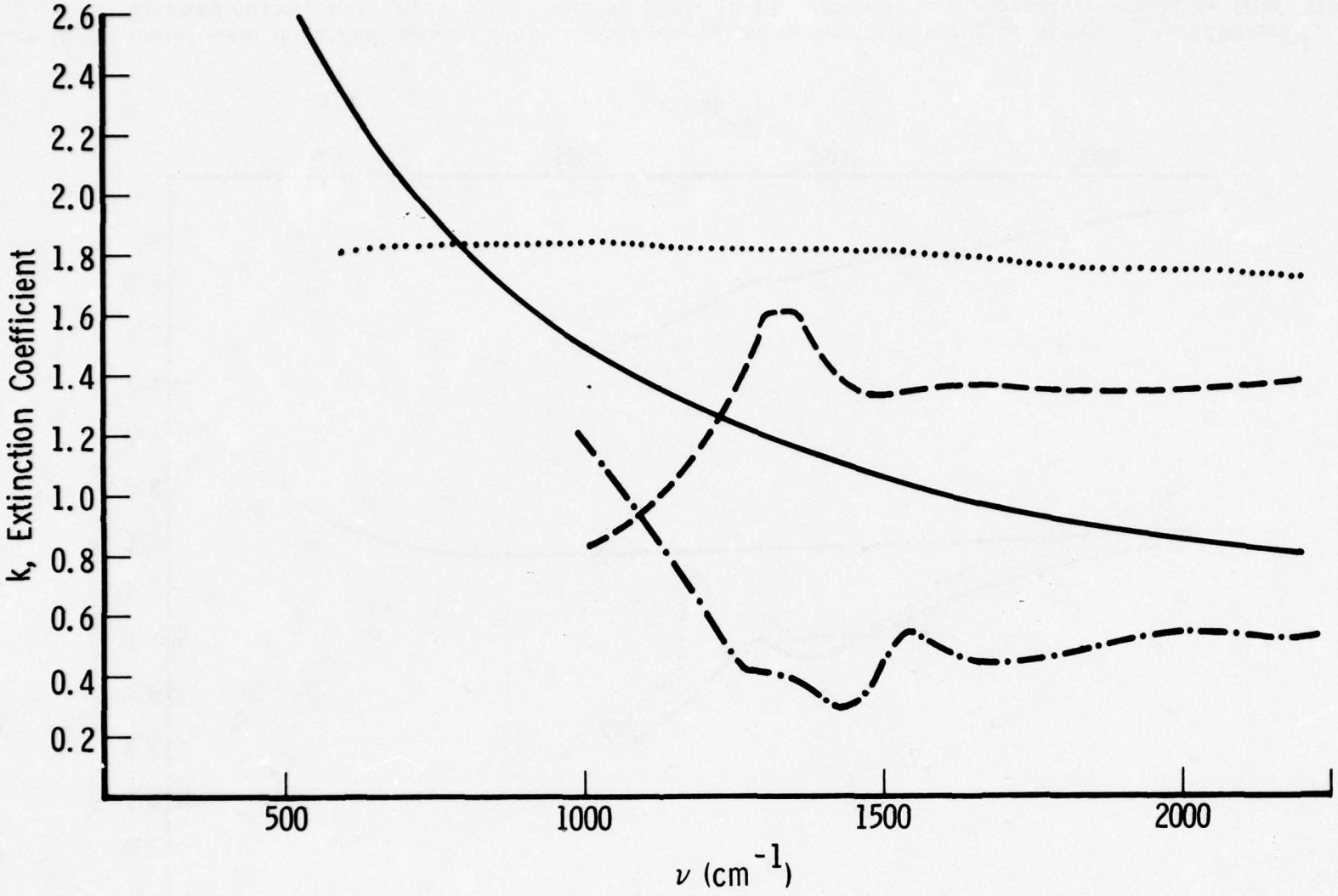

Figure II-10. The extinction coefficient of carbon materials in the wavenumber region 400cm^{-1} to 2200cm^{-1}. Dashed curve, polycrystalline graphite (Ref. II-19), dotted curve, pyrolytic graphite (Ref. II-20), solid curve, present results, and dot-dashed curve, pressed carbon soot (Ref. II-19).

2. MgO

A single crystal of MgO, approximately 7.6cm long by 3.2cm wide, was wedged to prevent internally reflected rays from entering the interferometer, and polished flat. Reflectivity measurements were made at temperatures of 300°K and 573°K. The reflectance spectra are shown in Figures II-11 and II-12, respectively. The peak in the 300°K data at $\sim 420 cm^{-1}$ (one data point) appears to be spurious. The reflectivity curves are very similar, but do differ in two details. First, the reflectance of the hotter case is in general lower than that for the cooler case in the region of $400 cm^{-1}$ to $\sim 800 cm^{-1}$. Second, the slope of the curve at about $\nu = 800 cm^{-1}$ is somewhat steeper for the cooler measurement compared to the warmer measurement. This is in agreement with what has been observed previously.[Ref. II-21] From the literature and our data, the reflectance changes of MgO below $400 cm^{-1}$ appear to be significant, and indeed the infrared allowed vibrational mode of MgO does lie below $400 cm^{-1}$. Rather than extrapolate our reflectance data, or try to use literature reflectance data for the wavenumber region below $400 cm^{-1}$ for a Kramers-Kronig analysis, we analyzed the MgO reflectance data using classical dispersion analysis. The initial values of the three dispersion parameters (ρ_j, ν_j and γ_j) were taken from the literature. The resulting best fit curves to the input reflectance data using a single oscillator are shown in Figures II-13 and II-14, and are to be compared with Figures II-11 and II-12, respectively. The dispersion parameters found for the 300°K data are $\nu = 389 cm^{-1}$, $\gamma = 71.3 cm^{-1}$ and $4\pi\rho = 5.63$. The parameters for the 573°K data are $\nu = 389 cm^{-1}$, $\gamma = 128.2 cm^{-1}$ and $4\pi\rho = 5.94$. For both temperatures $\epsilon_\infty = 2.3$.

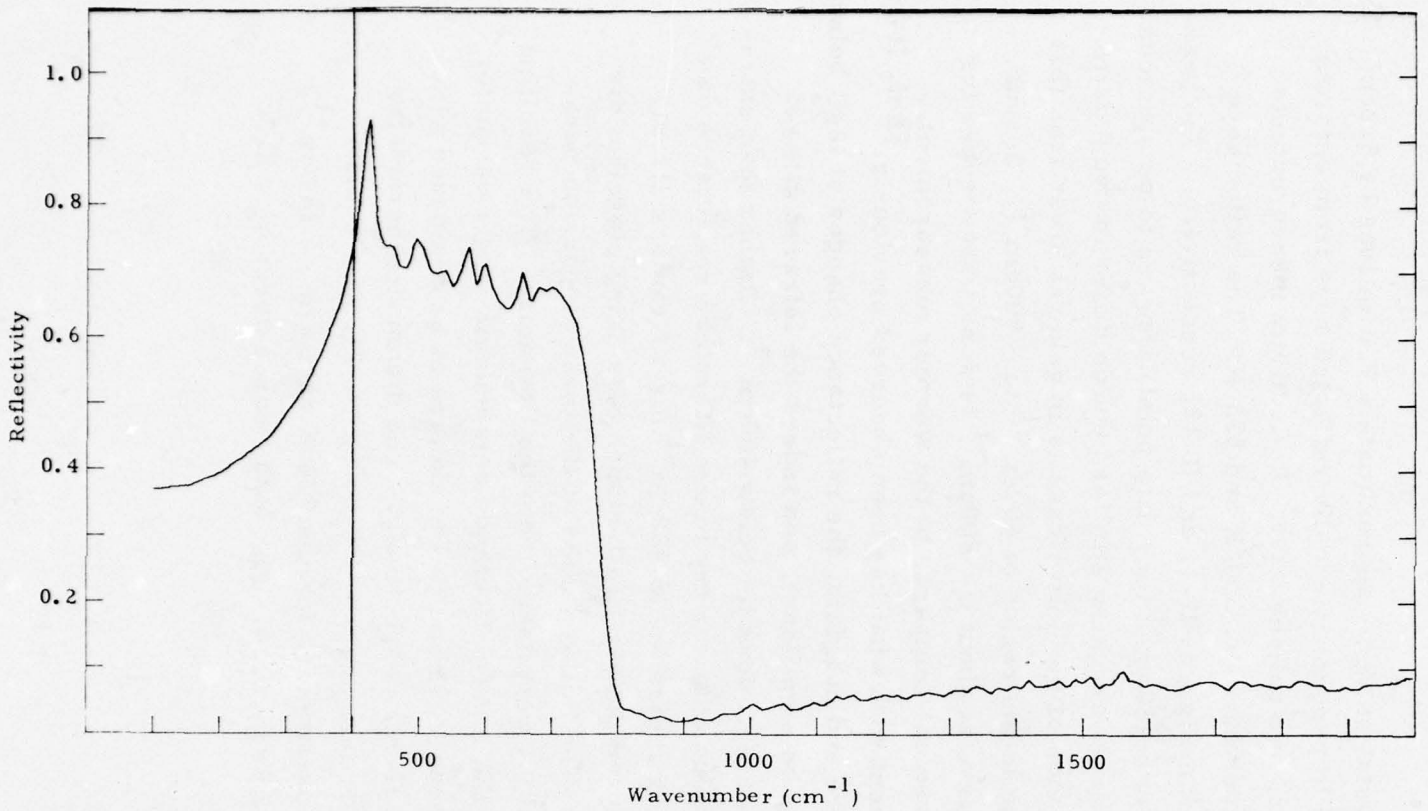

Figure II-11. The reflectivity spectrum of MgO in the 400cm^{-1} to 2000cm^{-1} region. The data were obtained at an angle of incidence of 45 degrees and at a temperature of 300°K. Values below 400cm^{-1} are extrapolated.

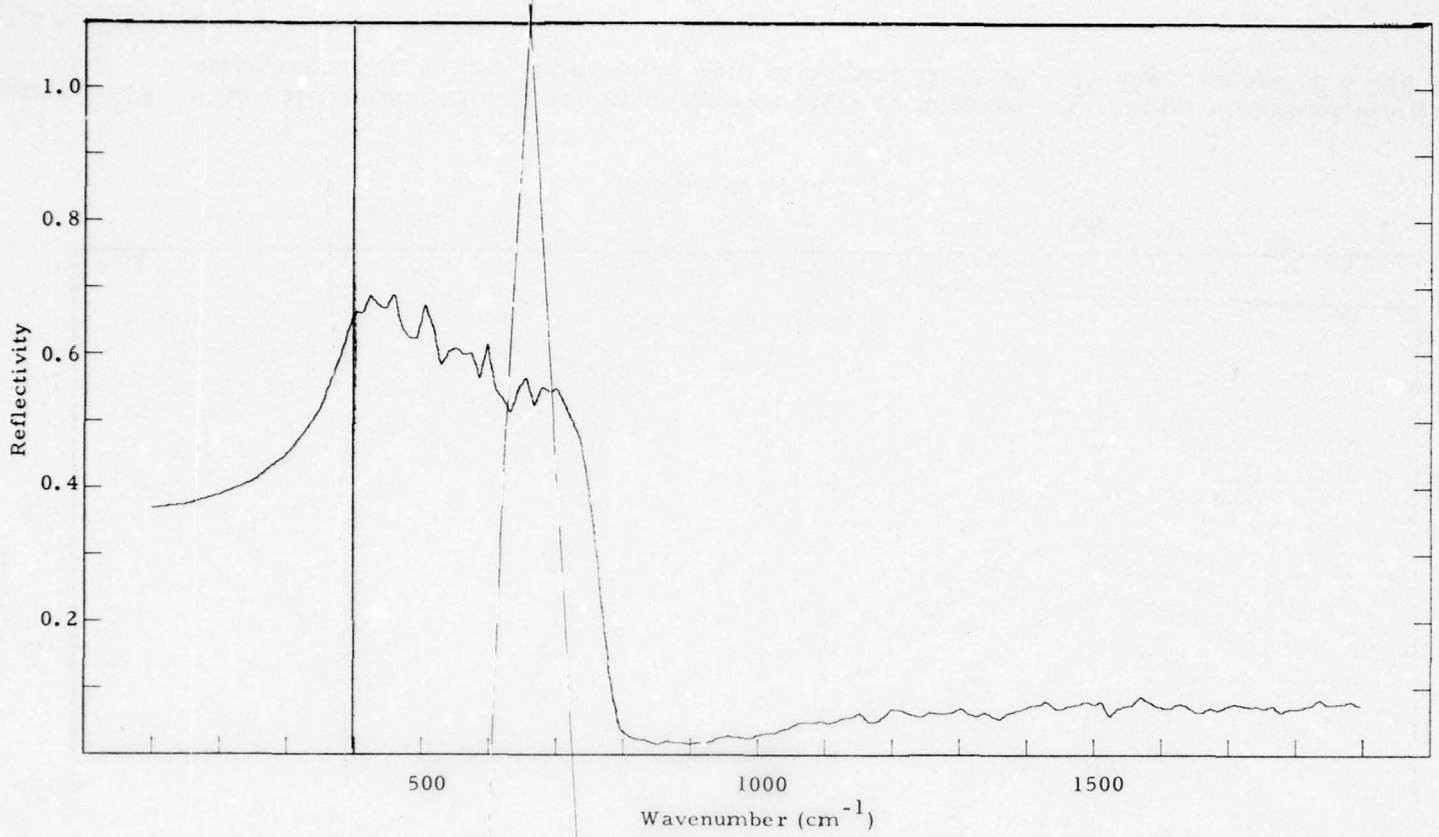

Figure II-12. The reflectivity spectrum of MgO in the 400cm^{-1} to 2000cm^{-1} region. The data were obtained at an angle of incidence of 45 degrees and at a temperature of 573°K. Values below 400cm^{-1} are extrapolated.

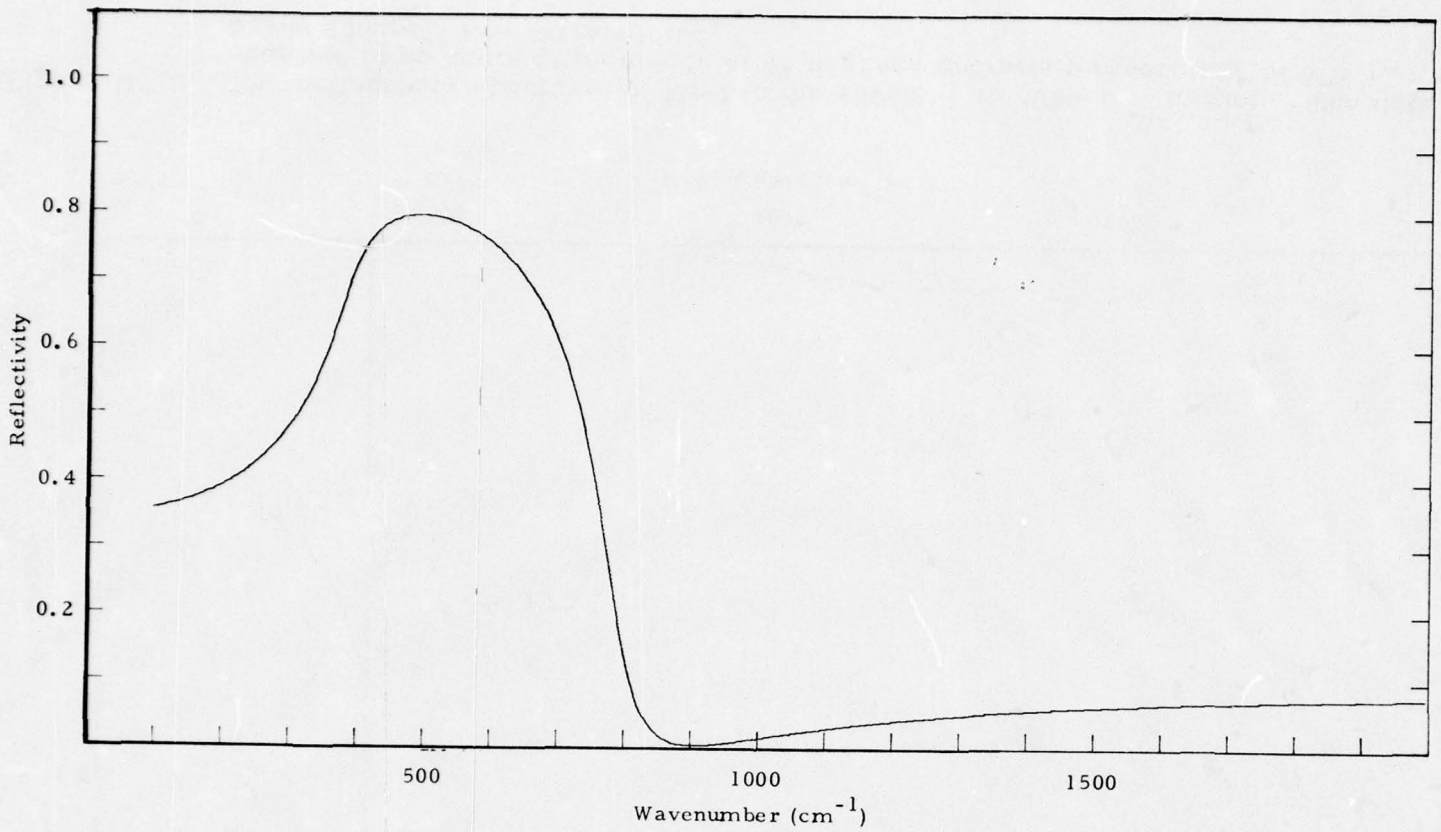

Figure II-13. The calculated reflectance spectrum of MgO as determined from a classical dispersion analysis fitted to the reflectance data of Figure II-11 (θ = 45 degrees and T = 300°K).

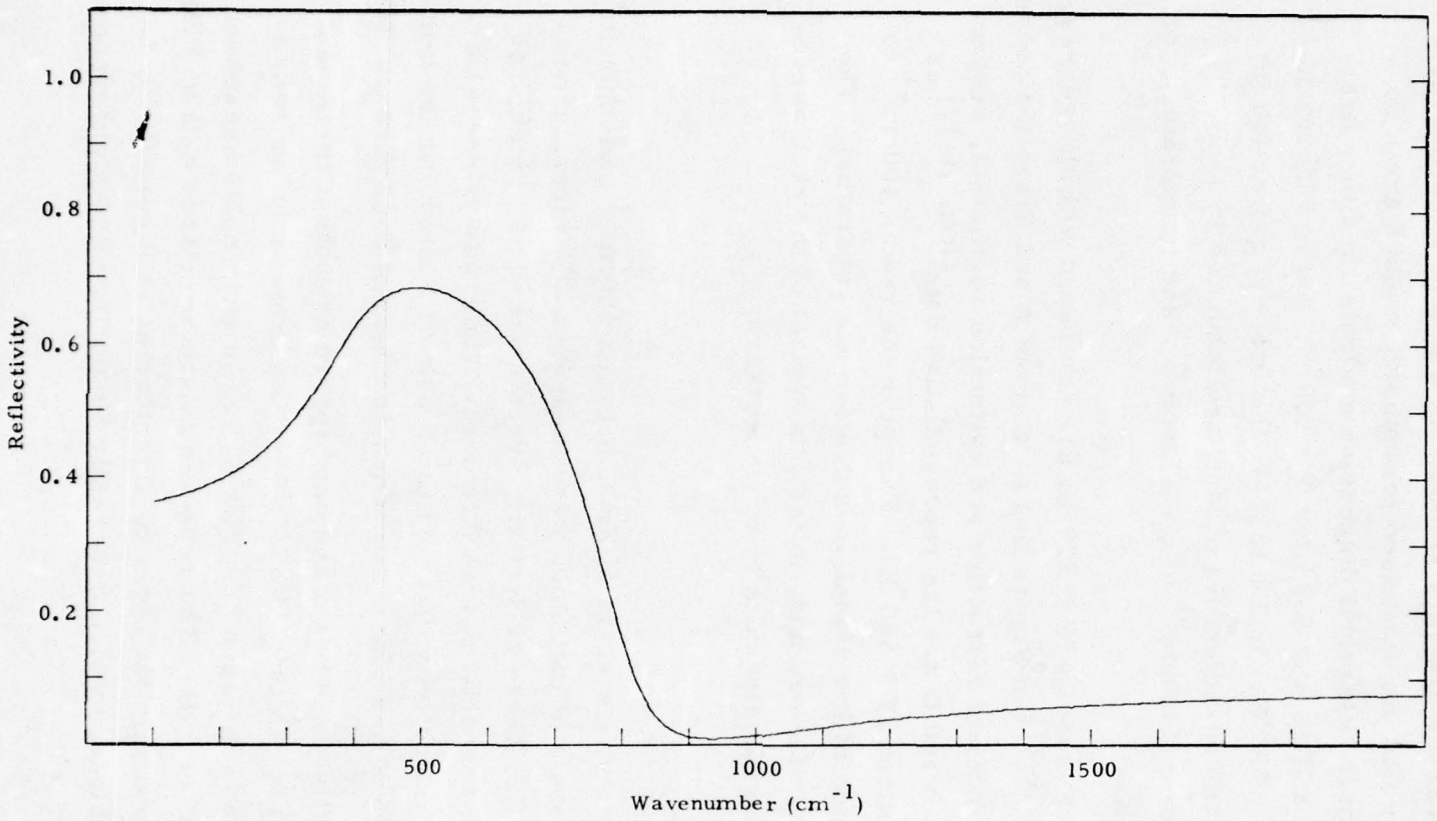

Figure II-14. The calculated reflectance spectrum of MgO as determined from a classical dispersion analysis fitted to the reflectance data of Figure II-12 (θ = 45 degrees and T = 573 °K).

The calculated curves are very smooth, as would be expected for a three parameter fit. As discussed previously, n and k are also determined from the classical dispersion analysis, and they are shown in Figures II-15 and II-16 for T = 300°K, and in Figures II-17 and II-18 for T = 573°K. In Table II-4, the index of refraction (n) and the extinction coefficient (k) of MgO are tabulated in $15cm^{-1}$ increments from $\nu = 400cm^{-1}$ to $\nu = 2200cm^{-1}$, and temperatures of 300°K and 573°K.

The present results ($T \simeq 300°K$) are compared with the representative data[Ref. II-17] in Figure II-19. Curves A and C are the present results for the index of refraction and extinction coefficient, respectively. Curves B and D are the representative data[Ref. II-17] as compiled by Whitson ($T \simeq 300°K$). Except in the region $400cm^{-1}$ to $500cm^{-1}$ (a region of low signal-to-noise for our apparatus). The agreement is satisfactory and, in fact, is typical of the good agreement between previous results by other workers.

3. ZrO_2

The reflectivity spectra of ZrO_2 between $400cm^{-1}$ and $2200cm^{-1}$, at a 45 degree angle of incidence were measured at temperatures of 300°K and 573°K. These reflectivity spectra are shown in Figures II-20 and II-21, respectively. A Kramers-Kronig analysis was performed on this reflectivity data and the resulting n and k for the temperatures of 300°K and 573°K are shown in Figures II-22 through II-25.

No refractive index data and only sparse extinction coefficient data were found by Whitson.[Ref. II-17] The representative reflectance data given by Whitson (T = 300°K) are in reasonable agreement with the present results. The representative reflectance data of Piriou [Ref. II-22] shows similar spectral structure as in Figure II-20, but are in general higher, which may easily be attributed to a difference in samples.

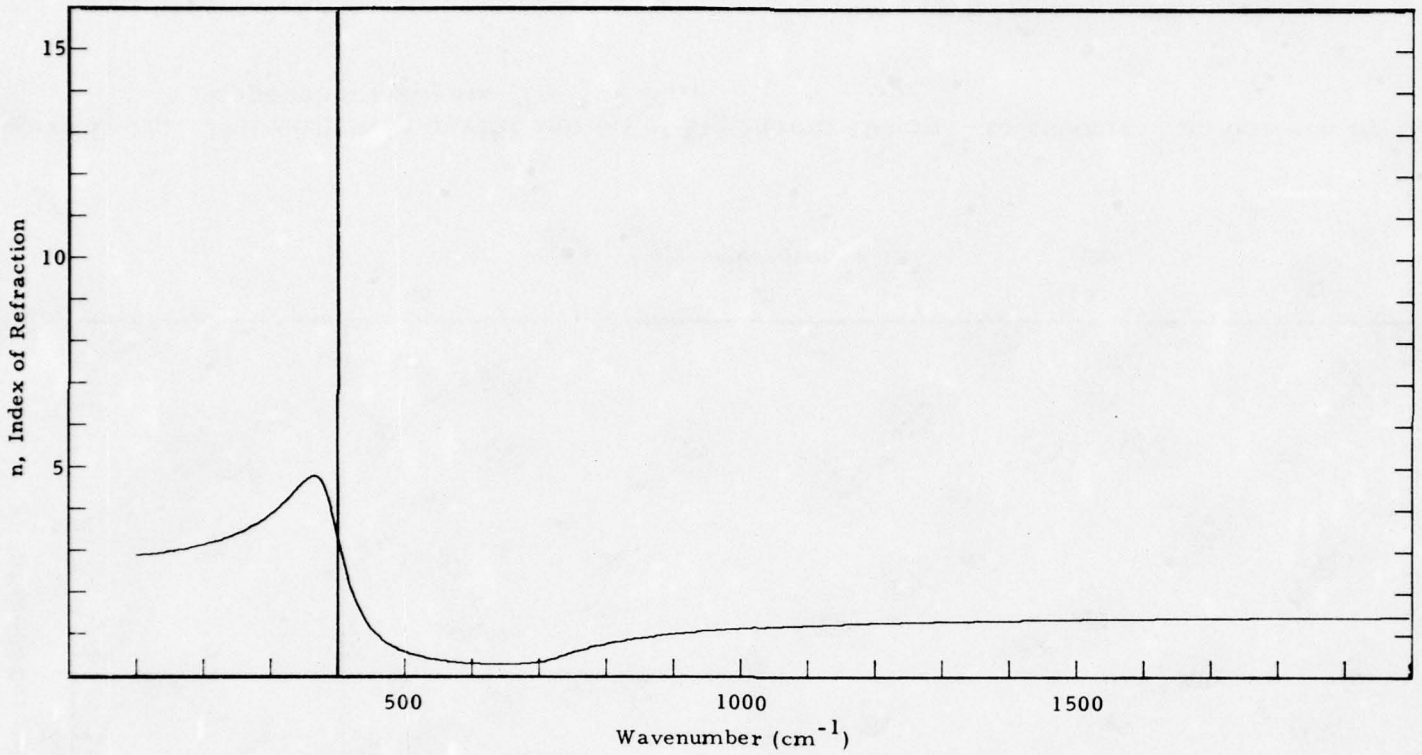

Figure II-15. The index of refraction (n) of MgO from 400cm^{-1} to 2000cm^{-1} as derived by classical dispersion analysis (T = 300°K).

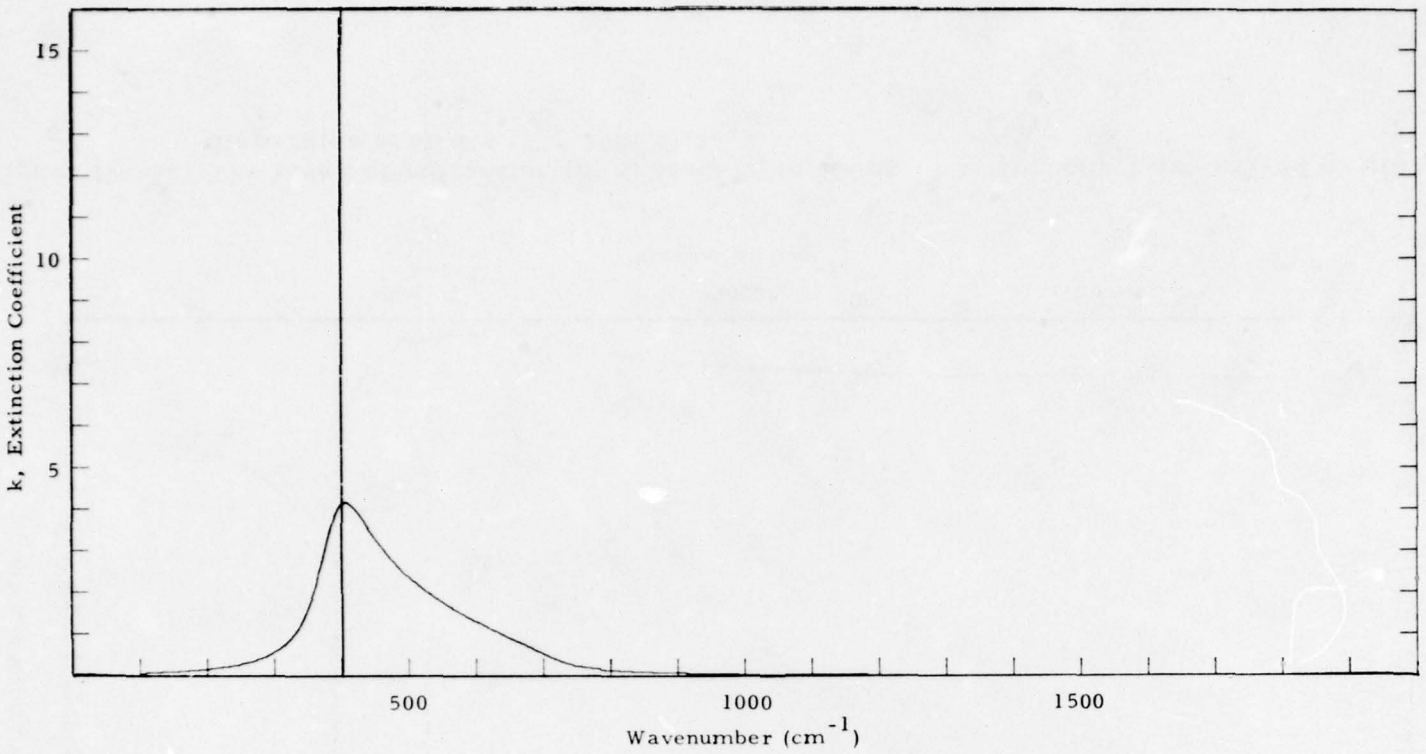

Figure II-16. The extinction coefficient (k) of MgO from 400cm^{-1} to 2000cm^{-1} as derived by classical dispersion analysis (T = 300°K).

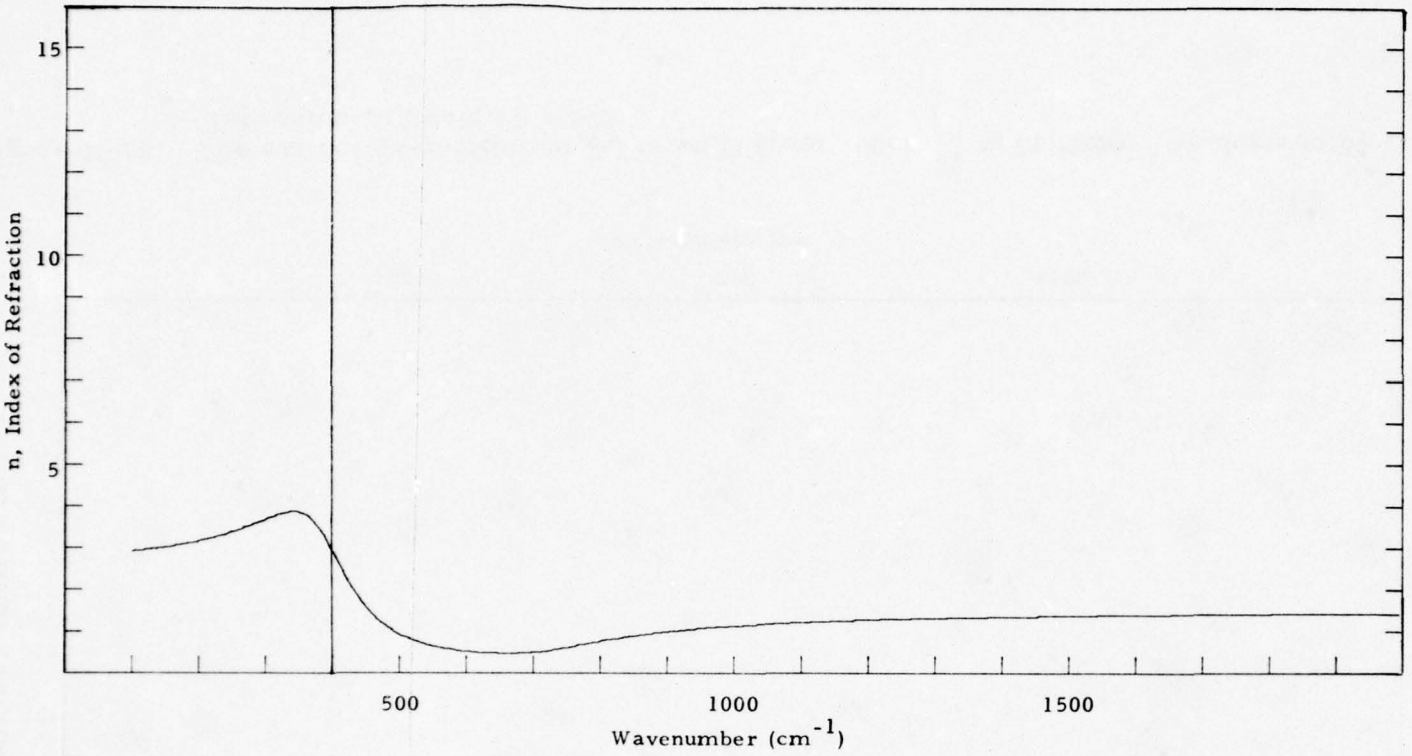

Figure II-17. The index of refraction (n) of MgO from 400cm^{-1} to 2000cm^{-1} as derived by classical dispersion analysis (T = 573 °K).

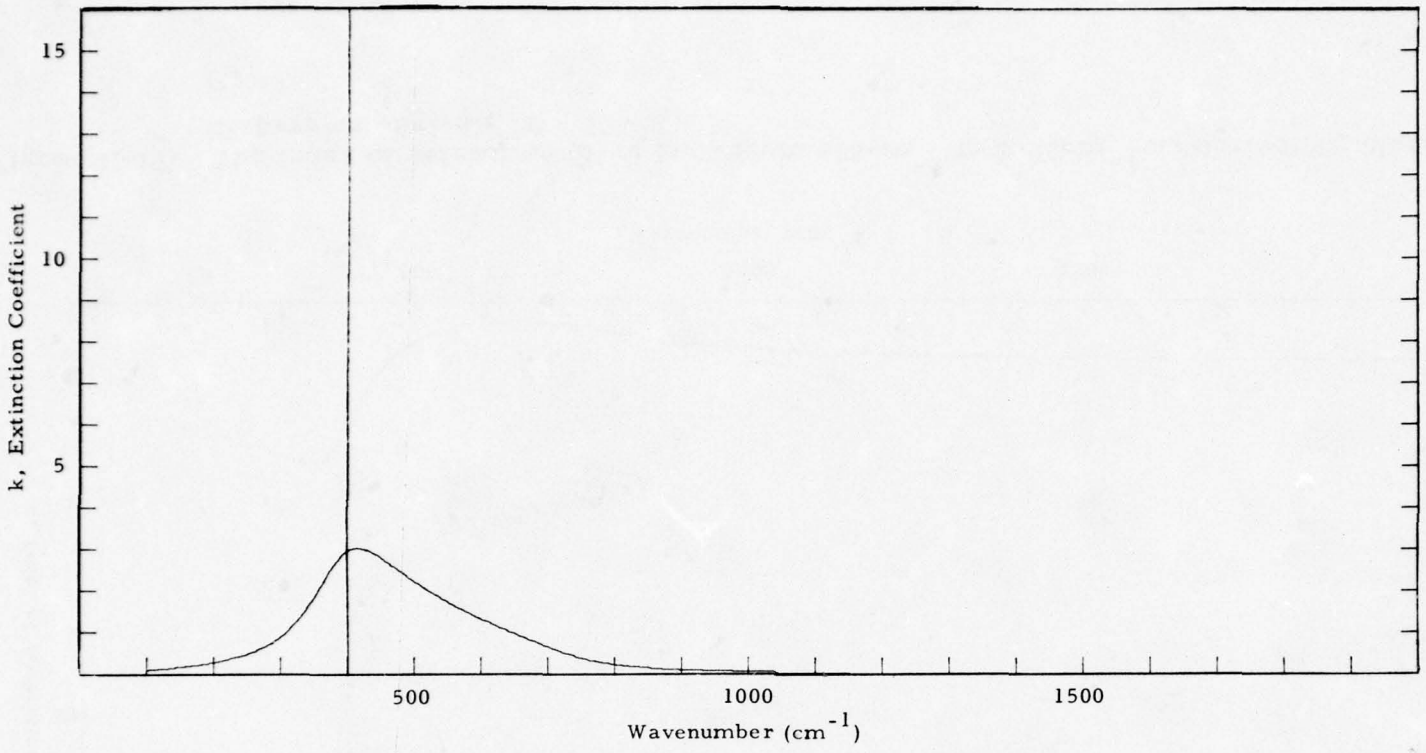

Figure II-18. The extinction coefficient (k) of MgO from 400cm^{-1} to 2000cm^{-1} as derived by classical dispersion analysis (T = 573°K).

Table II-4. Index of Refraction and Extinction Coefficient for MgO at 300°K and 573°K from 400cm^{-1} to 2200cm^{-1}.

	T = 300°K		T = 573°K	
ν (cm^{-1})	n	k	n	k
400	3.31	4.12	2.88	2.97
15	2.35	4.09	2.42	3.04
30	1.67	3.78	2.00	2.99
45	1.24	3.42	1.66	2.86
60	0.96	3.09	1.39	2.70
75	0.78	2.79	1.18	2.52
90	0.65	2.53	1.02	2.35
505	0.55	2.31	0.90	2.18
20	0.48	2.11	0.80	2.03
35	0.43	1.93	0.72	1.88
50	0.39	1.77	0.66	1.74
65	0.36	1.62	0.61	1.61
80	0.33	1.48	0.57	1.49
95	0.31	1.35	0.54	1.37
610	0.30	1.23	0.51	1.26
25	0.29	1.11	0.49	1.15
40	0.29	0.99	0.48	1.05
55	0.29	0.88	0.47	0.95
70	0.29	0.76	0.48	0.85
85	0.31	0.64	0.48	0.75
700	0.34	0.53	0.50	0.66
15	0.39	0.42	0.52	0.57
30	0.46	0.32	0.56	0.49
45	0.54	0.25	0.60	0.42
60	0.61	0.20	0.65	0.36

Table II-4. (Continued)

ν (cm^{-1})	T = 300°K		T = 573°K	
	n	k	n	k
775	0.68	0.17	0.69	0.30
90	0.74	0.14	0.74	0.26
805	0.79	0.12	0.78	0.23
20	0.83	0.11	0.82	0.20
35	0.88	0.10	0.86	0.18
50	0.91	0.09	0.90	0.16
65	0.95	0.08	0.93	0.15
80	0.98	0.07	0.96	0.13
95	1.00	0.06	0.99	0.12
910	1.03	0.06	1.01	0.11
25	1.05	0.05	1.03	0.10
40	1.07	0.05	1.05	0.09
55	1.09	0.05	1.07	0.09
70	1.11	0.04	1.09	0.08
85	1.13	0.04	1.11	0.07
1000	1.14	0.04	1.13	0.07
15	1.16	0.03	1.14	0.07
30	1.17	0.03	1.16	0.06
45	1.18	0.03	1.17	0.06
60	1.20	0.03	1.18	0.05
75	1.21	0.03	1.19	0.05
90	1.22	0.03	1.20	0.05
1105	1.23	0.02	1.21	0.05
20	1.24	0.02	1.22	0.04
35	1.25	0.02	1.23	0.04

Table II-4. (Continued)

ν (cm^{-1})	T = 300 °K		T = 573 °K	
	n	k	n	k
1150	1.26	0.02	1.24	0.04
65	1.26	0.02	1.25	0.04
80	1.27	0.02	1.26	0.04
95	1.28	0.02	1.27	0.03
1210	1.29	0.02	1.27	0.03
25	1.29	0.02	1.28	0.03
40	1.30	0.02	1.29	0.03
55	1.31	0.01	1.29	0.03
70	1.31	0.01	1.30	0.03
85	1.32	0.01	1.31	0.02
1300	1.32	0.01	1.31	0.02
15	1.33	0.01	1.32	0.02
30	1.33	0.01	1.32	0.02
45	1.34	0.01	1.33	0.02
60	1.34	0.01	1.33	0.02
75	1.35	0.01	1.34	0.02
90	1.35	0.01	1.34	0.02
1405	1.35	0.01	1.35	0.02
20	1.36	0.01	1.35	0.02
35	1.36	0.01	1.35	0.02
50	1.37	0.01	1.36	0.02
65	1.37	0.01	1.36	0.02
80	1.37	0.01	1.36	0.02
95	1.38	0.01	1.37	0.02
1510	1.38	0.01	1.37	0.02

Table II-4. (Continued)

ν (cm^{-1})	T = 300°K n	T = 300°K k	T = 573°K n	T = 573°K k
1525	1.38	0.01	1.37	0.02
40	1.38	0.01	1.38	0.02
55	1.39	0.01	1.38	0.02
70	1.39	0.01	1.38	0.02
85	1.39	0.01	1.39	0.01
1600	1.40	0.01	1.39	0.01
15	1.40	0.01	1.39	0.01
30	1.40	0.01	1.39	0.01
45	1.40	0.01	1.40	0.01
60	1.40	0.01	1.40	0.01
75	1.41	0.01	1.40	0.01
90	1.41	0.00	1.40	0.01
1705	1.41	0.00	1.41	0.01
20	1.41	0.00	1.41	0.01
35	1.42	0.00	1.41	0.01
1750	1.42	0.00	1.41	0.01
65	1.42	0.00	1.41	0.01
80	1.42	0.00	1.42	0.01
95	1.42	0.00	1.42	0.01
1810	1.42	0.00	1.42	0.01
25	1.43	0.00	1.42	0.01
40	1.43	0.00	1.42	0.01
55	1.43	0.00	1.42	0.01
70	1.43	0.00	1.43	0.01
85	1.43	0.00	1.43	0.01

Table II-4. (Concluded)

ν (cm^{-1})	T = 300 °K		T = 573 °K	
	n	k	n	k
1900	1.43	0.00	1.43	0.01
15	1.43	0.00	1.43	0.01
30	1.44	0.00	1.43	0.01
45	1.44	0.00	1.43	0.01
60	1.44	0.00	1.43	0.01
75	1.44	0.00	1.44	0.01
90	1.44	0.00	1.44	0.01
2005	1.44	0.00	1.44	0.01
20	1.44	0.00	1.44	0.01
35	1.44	0.00	1.44	0.01
50	1.45	0.00	1.44	0.00
65	1.45	0.00	1.44	0.00
80	1.45	0.00	1.44	0.00
95	1.45	0.00	1.45	0.00
2110	1.45	0.00	1.45	0.00
25	1.45	0.00	1.45	0.00
40	1.45	0.00	1.45	0.00
55	1.45	0.00	1.45	0.00
70	1.45	0.00	1.45	0.00
85	1.45	0.00	1.45	0.00
2200	1.46	0.00	1.45	0.00

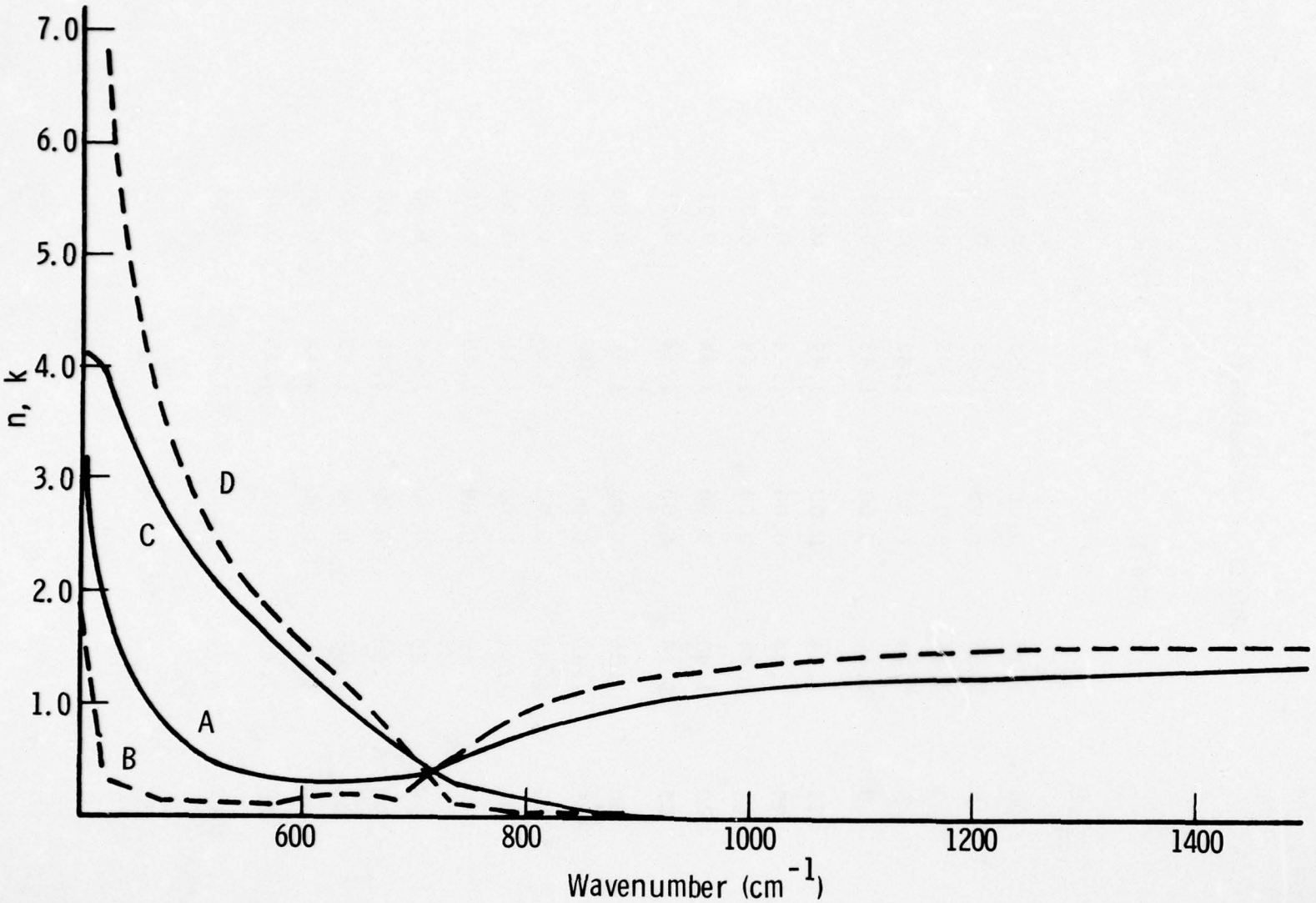

Figure II-19. Comparison of index of refraction (n) and extinction coefficients (k) for MgO. Curve A, index of refraction, present results; curve B, index of refraction, representative data (Ref. II-17); curve C, extinction coefficient, present results; curve D, extinction coefficient, representative data (Ref. II-17).

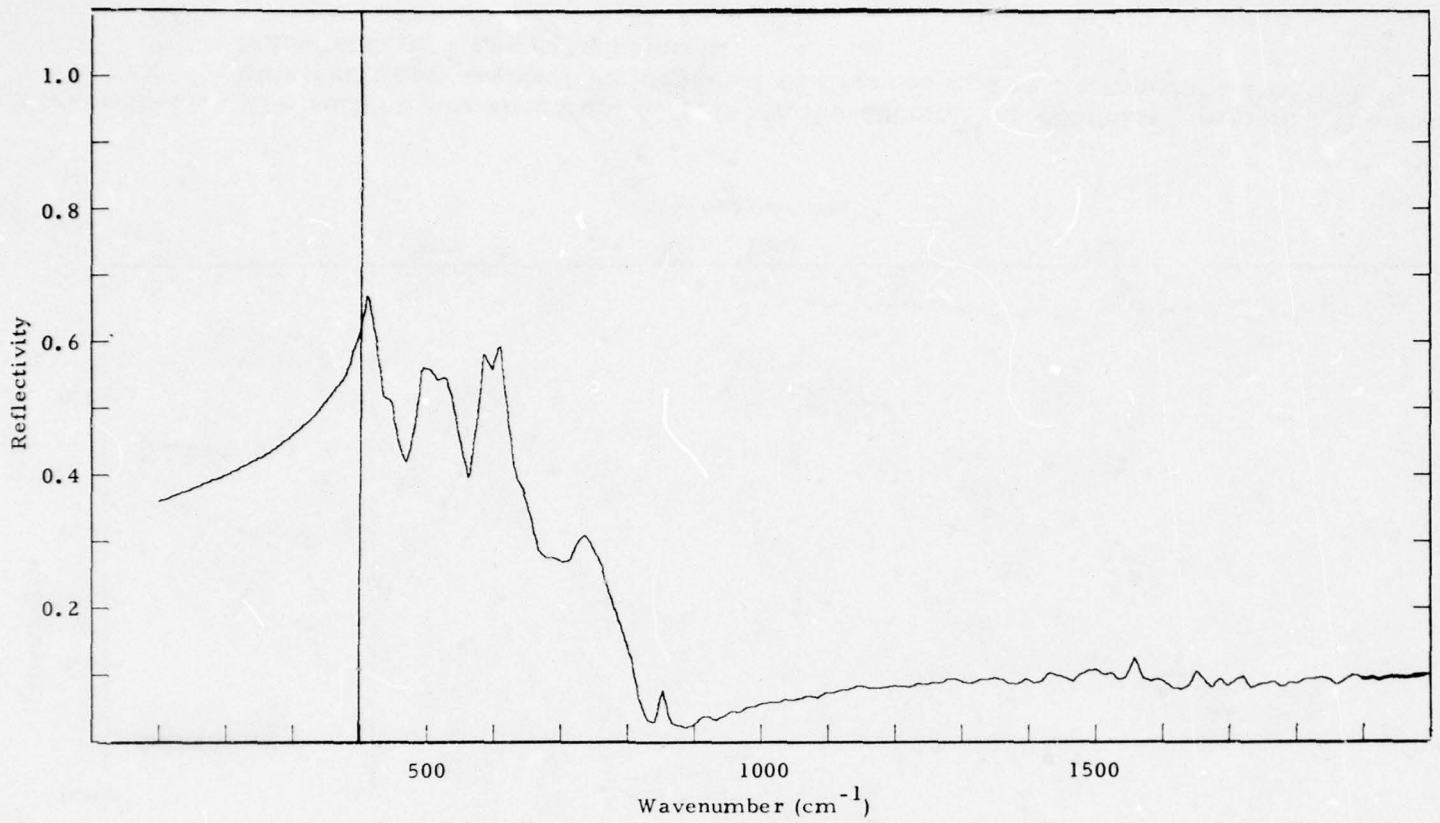

Figure II-20. The reflectivity spectrum of ZrO_2 in the 400cm^{-1} to 2000cm^{-1} region. The data were obtained at an angle of incidence of 45 degrees and at a temperature of 300°K. Values below 400cm^{-1} are extrapolated.

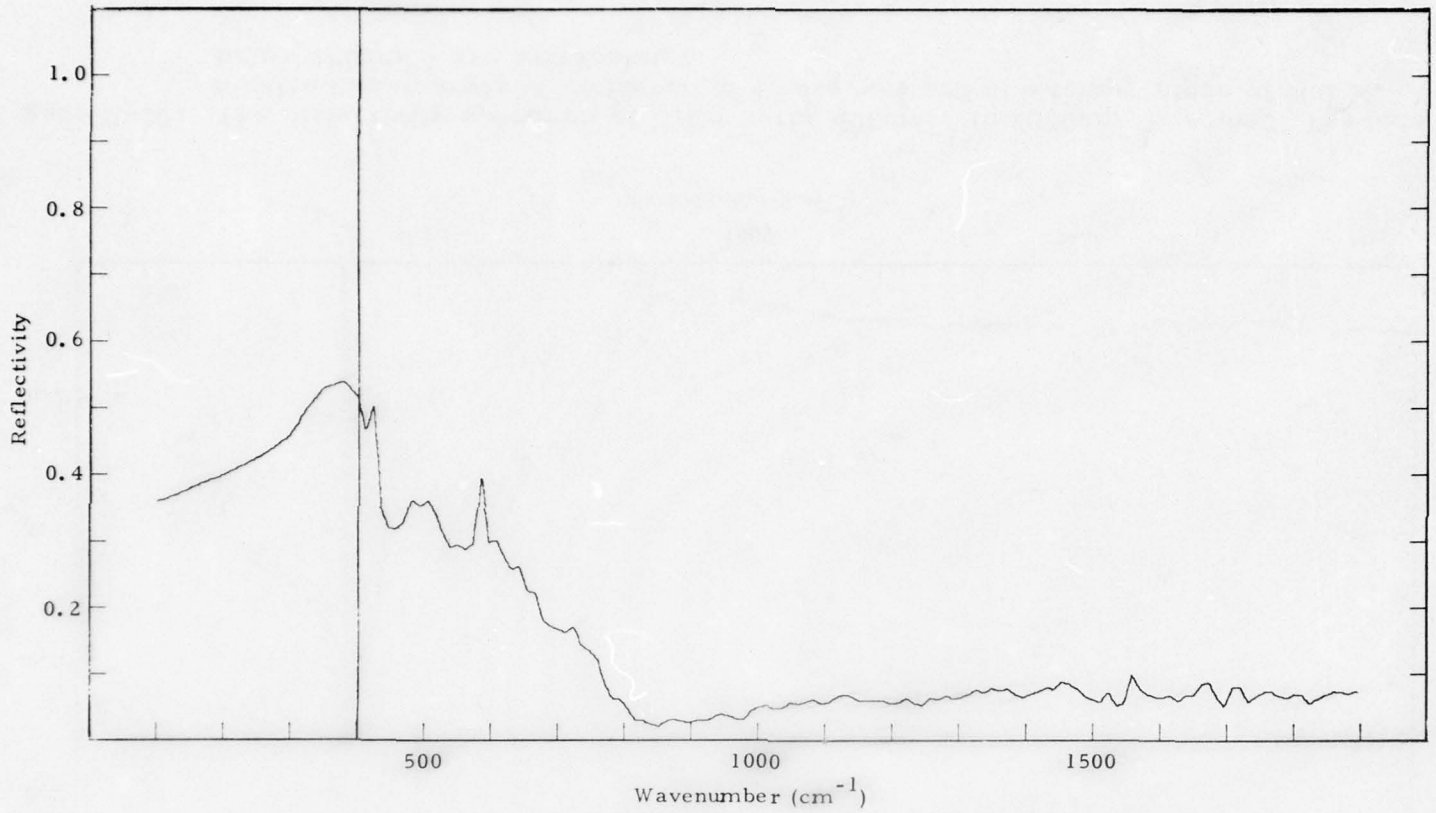

Figure II-21. The reflectivity spectrum of ZrO_2 in the 400cm^{-1} to 2000cm^{-1} region. The data were obtained at an angle of incidence of 45 degrees and at a temperature of 573°K. Values below 400cm^{-1} are extrapolated.

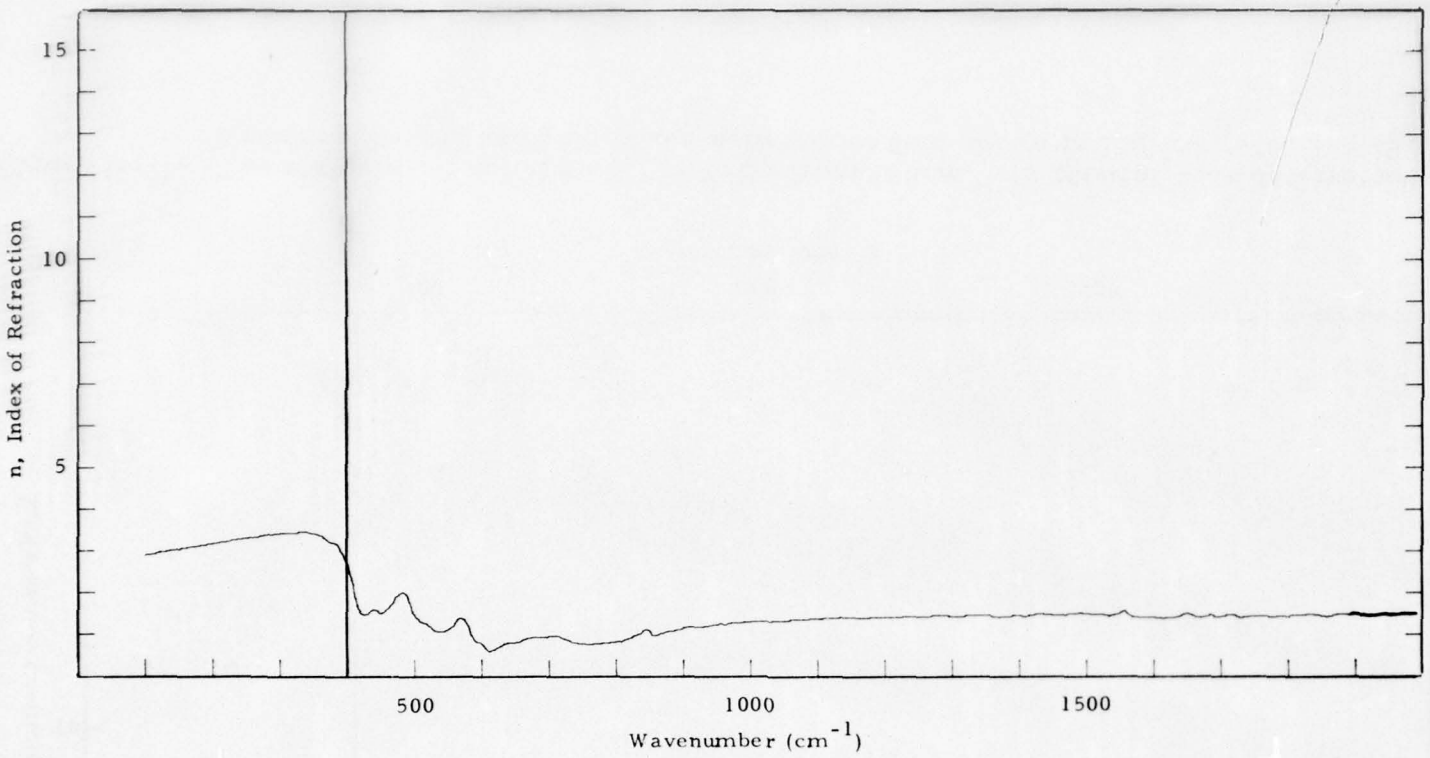

Figure II-22. The refractive index (n) of ZrO_2 from 400cm^{-1} to 2000cm^{-1} as determined from a Kramers-Kronig analysis of the reflectivity data shown in Figure II-20 (T = 300°K).

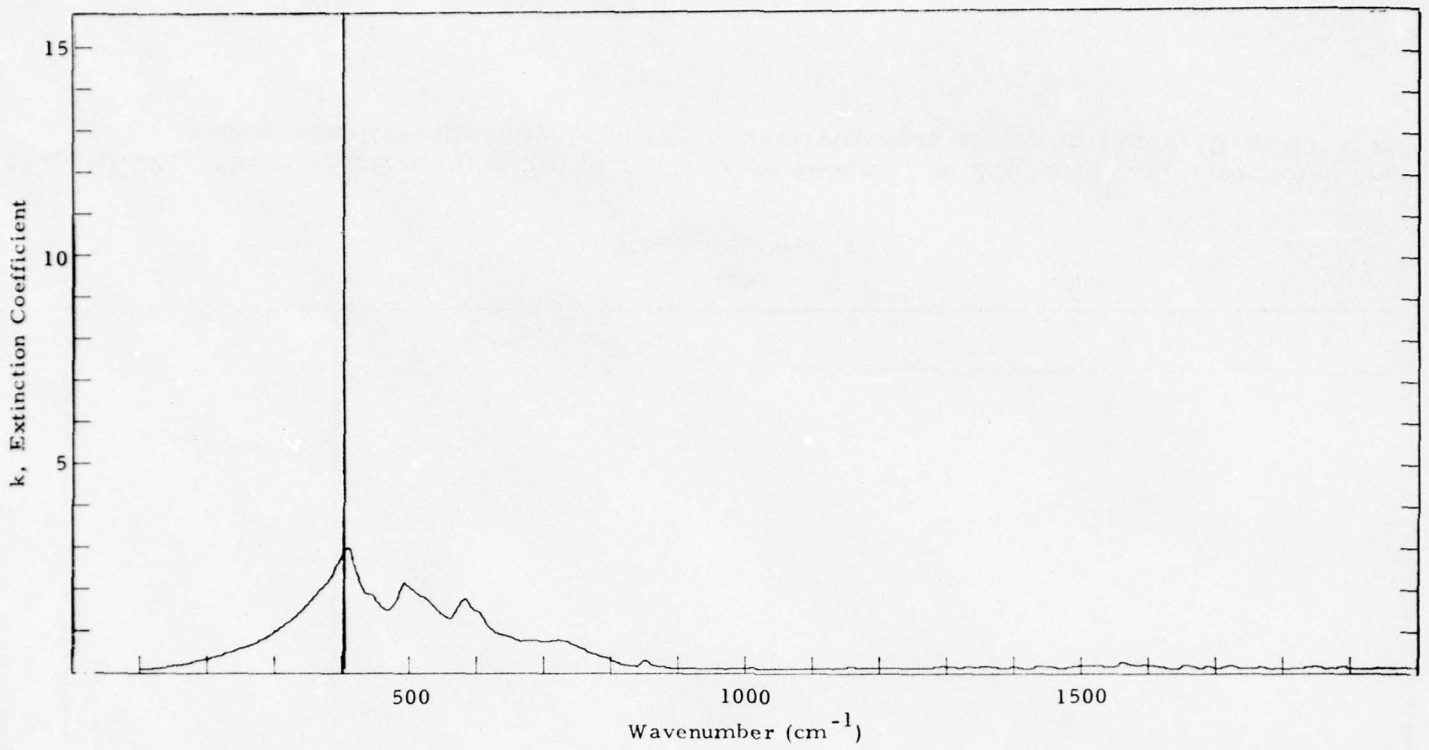

Figure II-23. The extinction coefficient (k) of ZrO_2 from 400cm^{-1} to 2000cm^{-1} as determined from a Kramers-Kronig analysis of the reflectivity data shown in Figure II-20 (T = 300 °K).

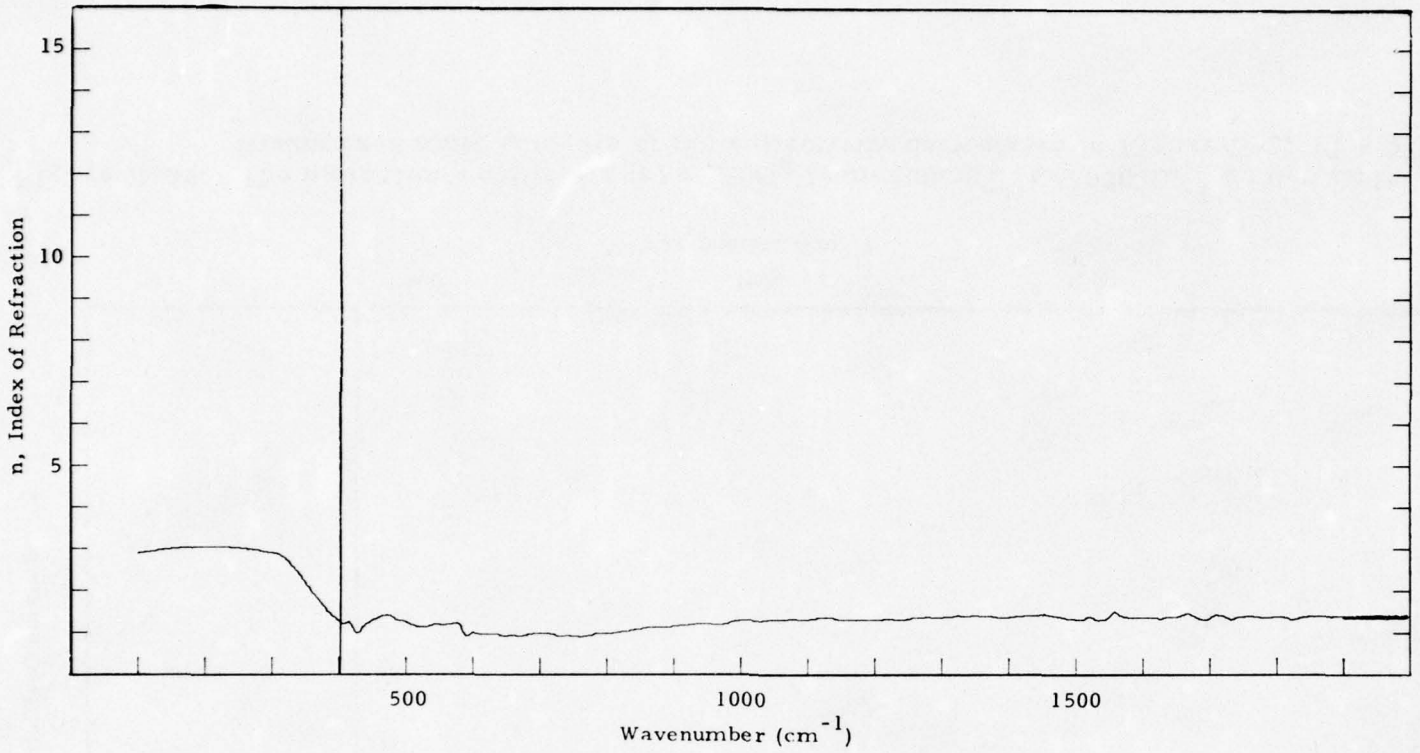

Figure II-24. The refractive index (n) of ZrO_2 from 400cm^{-1} to 2000cm^{-1} as determined from a Kramers-Kronig analysis of the reflectivity data shown in Figure II-21 (T = 573°K).

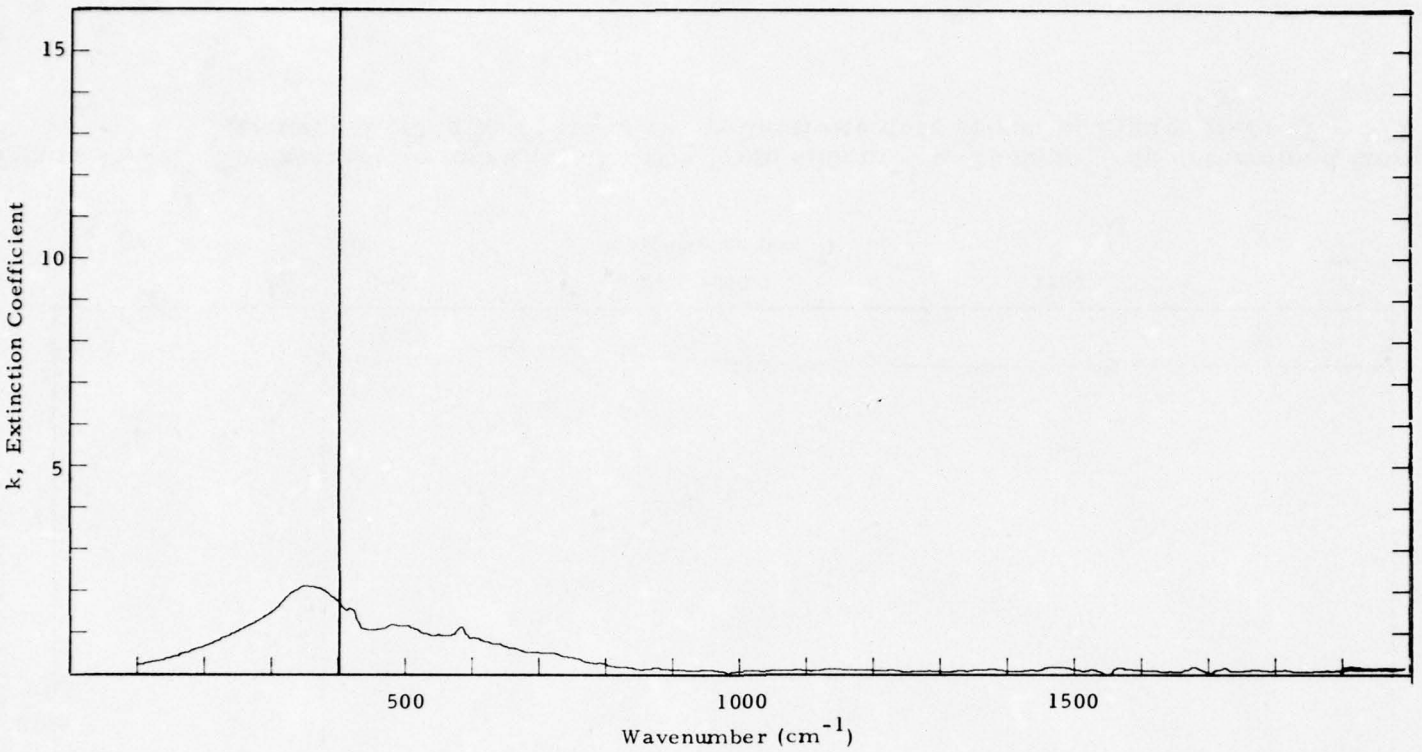

Figure II-25. The extinction coefficient (k) of ZrO_2 from 400cm^{-1} to 2000cm^{-1} as determined from a Kramers-Kronig analysis of the reflectivity data shown in Figure II-21 (T = 573°K).

A tabulation of n and k for ZrO_2 for the temperatures T = 300°K and 573°K is given in Table II-5 over the wavenumber interval from $400cm^{-1}$ to $2200cm^{-1}$ in $15cm^{-1}$ increments.

4. Al_2O_3

The reflectivity spectrum of a single crystal sample of Al_2O_3 was measured in the wavenumber region $400cm^{-1}$ to $2200cm^{-1}$ with the electric vector polarized perpendicular to the C axis of the crystal (E⊥C) at temperatures of 300°K and 678°K. Data were obtained also for E parallel to C, but appeared to be overly noisy and were not analyzed. The reflectivity spectra for T = 300°K and T = 678°K are shown in Figures II-26 and II-27, respectively, The spectra are very similar, but in general the higher temperature sample shows lower reflectivity than the cooler sample. Also for the higher temperature sample the structure in the reflectivity spectra appear broader and shifted slightly to lower wavenumber in comparison to the cooler reflectivity spectrum.

A Kramers-Kronig analysis was performed on each reflectivity spectrum and the derived values of the refractive index and the extinction coefficient for Al_2O_3 for the two temperatures are shown in Figures II-28 through II-31. Table II-6 lists the values of n and k as determined in this investigation of Al_2O_3 for the two temperatures in the wavenumber interval from $400cm^{-1}$ to $2200cm^{-1}$ in $15cm^{-1}$ increments.

The reflectivity and transmissivity of Al_2O_3 have been the subject of many investigations, usually with the object of determining n and k for the material. Whitson[Ref. II-17] has examined the literature and made a critical selection of values for n and k (for nominally 300°K temperature). These are shown in Figures II-32 and II-33, and are to be compared with Figures II-28 and II-29 (note scale difference), which are the present results. These values of n and k were then used to calculate a reflectance spectrum for Al_2O_3 at an incidence angle

Table II-5. The Refractive Index (n) and Extinction Coefficient (k) for ZrO_2 between $\nu = 400cm^{-1}$ and $2200cm^{-1}$ for T = 300°K and 573°K.

	T = 300°K		T = 573°K	
ν (cm^{-1})	n	k	n	k
400	2.72	2.79	1.28	1.76
15	1.67	2.77	1.26	1.57
30	1.48	2.07	1.01	1.26
45	1.58	1.88	1.25	1.08
60	1.62	1.58	1.38	1.08
75	1.94	1.59	1.42	1.16
90	1.91	2.08	1.29	1.18
505	1.39	2.01	1.22	1.17
20	1.24	1.84	1.14	1.06
35	1.08	1.64	1.16	0.97
50	1.11	1.41	1.20	0.96
65	1.38	1.37	1.21	0.95
80	1.22	1.74	1.21	1.10
95	0.83	1.55	0.95	0.90
610	0.61	1.34	0.97	0.86
25	0.69	1.02	0.96	0.78
40	0.78	0.95	0.96	0.75
55	0.83	0.83	0.94	0.66
70	0.92	0.78	0.92	0.61
85	0.96	0.79	0.97	0.55
700	0.96	0.77	0.98	0.54
15	0.96	0.79	0.98	0.53
30	0.86	0.79	0.93	0.48
45	0.79	0.69	0.94	0.44
60	0.77	0.58	0.91	0.38

Table II-5. (Continued)

ν (cm^{-1})	T = 300 °K		T = 573 °K	
	n	k	n	k
775	0.79	0.48	0.95	0.30
90	0.82	0.39	0.99	0.28
805	0.84	0.31	0.99	0.24
20	0.93	0.22	1.04	0.19
35	1.03	0.19	1.06	0.18
50	1.10	0.31	1.10	0.14
65	1.03	0.18	1.15	0.16
80	1.08	0.16	1.15	0.16
95	1.13	0.13	1.16	0.14
910	1.20	0.15	1.18	0.13
25	1.19	0.15	1.20	0.11
40	1.22	0.12	1.23	0.12
55	1.26	0.13	1.22	0.13
70	1.27	0.12	1.21	0.10
85	1.30	0.13	1.26	0.06
1000	1.32	0.13	1.30	0.08
15	1.32	0.14	1.31	0.11
30	1.33	0.13	1.30	0.10
45	1.34	0.14	1.33	0.09
60	1.36	0.13	1.32	0.11
75	1.36	0.14	1.34	0.11
90	1.38	0.12	1.33	0.13
1105	1.39	0.13	1.34	0.10
20	1.41	0.14	1.37	0.12
35	1.42	0.14	1.36	0.15

Table II-5. (Continued)

	T = 300°K		T = 573°K	
ν (cm^{-1})	n	k	n	k
1150	1.43	0.16	1.33	0.15
65	1.41	0.16	1.34	0.13
80	1.42	0.15	1.34	0.13
95	1.43	0.15	1.32	0.13
1210	1.43	0.15	1.34	0.10
25	1.43	0.14	1.35	0.12
40	1.44	0.15	1.32	0.10
55	1.45	0.14	1.37	0.07
70	1.46	0.14	1.37	0.08
85	1.47	0.17	1.38	0.10
1300	1.45	0.18	1.38	0.08
15	1.45	0.16	1.40	0.07
30	1.47	0.16	1.42	0.11
45	1.47	0.17	1.42	0.10
60	1.45	0.19	1.41	0.13
75	1.44	0.16	1.40	0.15
90	1.47	0.14	1.37	0.13
1405	1.45	0.16	1.39	0.09
20	1.48	0.13	1.41	0.09
35	1.50	0.18	1.43	0.12
50	1.48	0.18	1.45	0.13
65	1.46	0.15	1.43	0.18
80	1.51	0.16	1.37	0.20
95	1.52	0.19	1.34	0.15
1510	1.48	0.21	1.33	0.11

Table II-5. (Continued)

ν (cm^{-1})	T = 300°K n	T = 300°K k	T = 573°K n	T = 573°K k
1525	1.48	0.22	1.38	0.15
40	1.47	0.17	1.33	0.07
55	1.56	0.21	1.48	0.03
70	1.43	0.25	1.40	0.16
85	1.43	0.21	1.37	0.14
1600	1.42	0.22	1.36	0.12
15	1.40	0.19	1.38	0.11
30	1.42	0.14	1.36	0.08
45	1.49	0.13	1.39	0.08
60	1.45	0.21	1.45	0.08
75	1.42	0.15	1.43	0.19
90	1.44	0.19	1.33	0.14
1705	1.45	0.15	1.41	0.05
20	1.47	0.20	1.42	0.16
35	1.42	0.16	1.35	0.10
50	1.44	0.15	1.39	0.09
65	1.45	0.16	1.40	0.12
80	1.43	0.14	1.37	0.12
95	1.45	0.14	1.38	0.10
1810	1.47	0.14	1.38	0.12
25	1.48	0.15	1.34	0.08
40	1.48	0.18	1.38	0.06
55	1.44	0.17	1.41	0.08
70	1.47	0.14	1.41	0.10
85	1.49	0.17	1.40	0.09

Table II-5. (Concluded)

	T = 300 °K		T = 573 °K	
ν (cm^{-1})	n	k	n	k
1900	1.46	0.19	1.39	0.11
15	1.45	0.17	1.38	0.10
30	1.46	0.18	1.38	0.11
45	1.43	0.19	1.36	0.10
60	1.42	0.16	1.37	0.07
75	1.45	0.16	1.38	0.05
90	1.43	0.13	1.39	0.10
2005	1.47	0.12	1.37	0.05
20	1.48	0.16	1.45	0.04
35	1.45	0.20	1.44	0.11
50	1.42	0.15	1.39	0.11
65	1.45	0.14	1.40	0.09
80	1.43	0.13	1.39	0.09
95	1.46	0.14	1.39	0.09
2110	1.46	0.15	1.37	0.09
25	1.45	0.16	1.38	0.07
40	1.44	0.15	1.39	0.06
55	1.44	0.15	1.39	0.07
70	1.42	0.14	1.41	0.07
85	1.45	0.11	1.38	0.06
2200	1.44	0.12	1.37	0.04

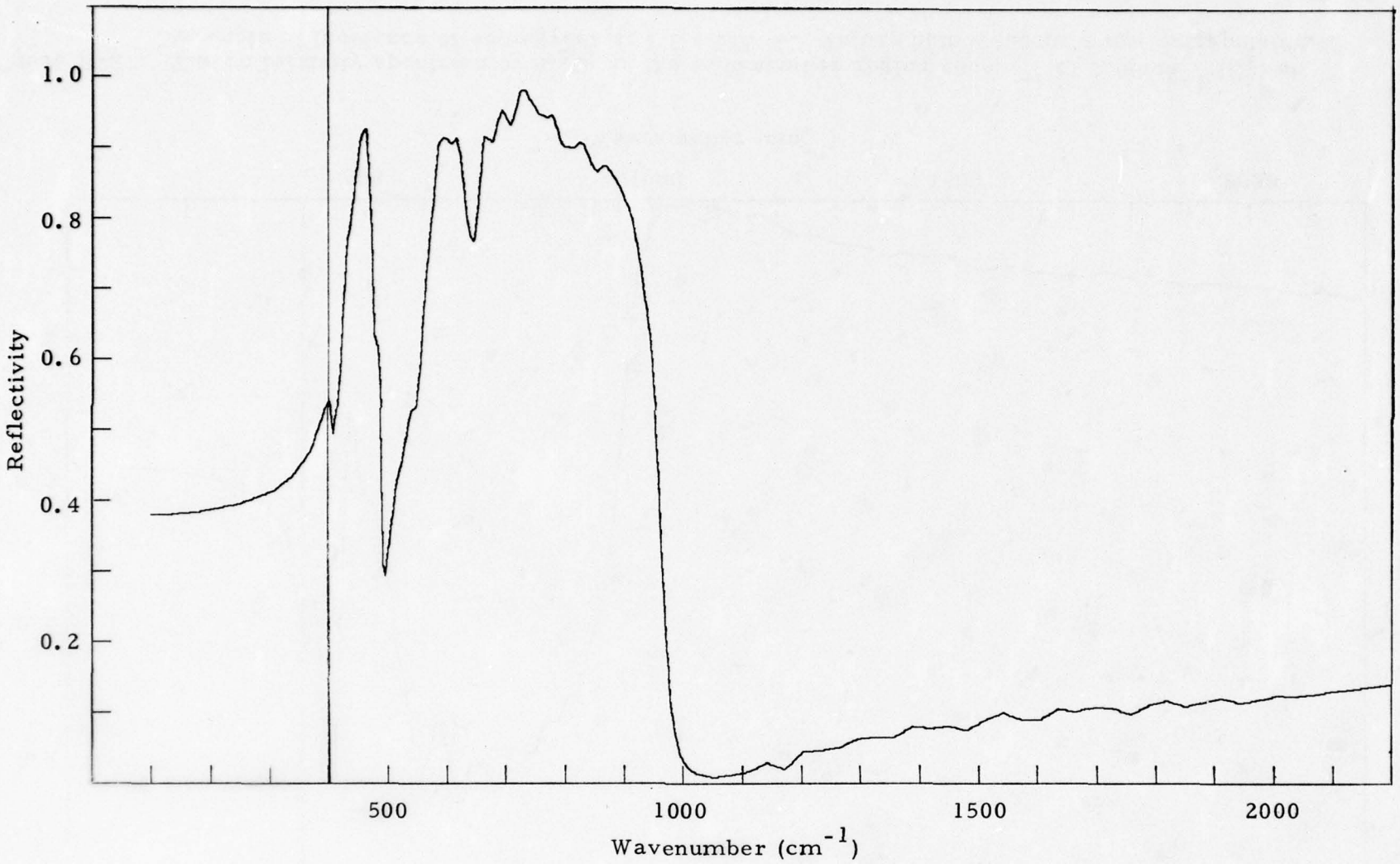

Figure II-26. The reflectivity spectrum of Al_2O_3 in the wavenumber region 400cm^{-1} to 2200cm^{-1} ($E_\perp$) at an angle of incidence of 45 degrees and T = 300°K. Values below 400cm^{-1} are extrapolated.

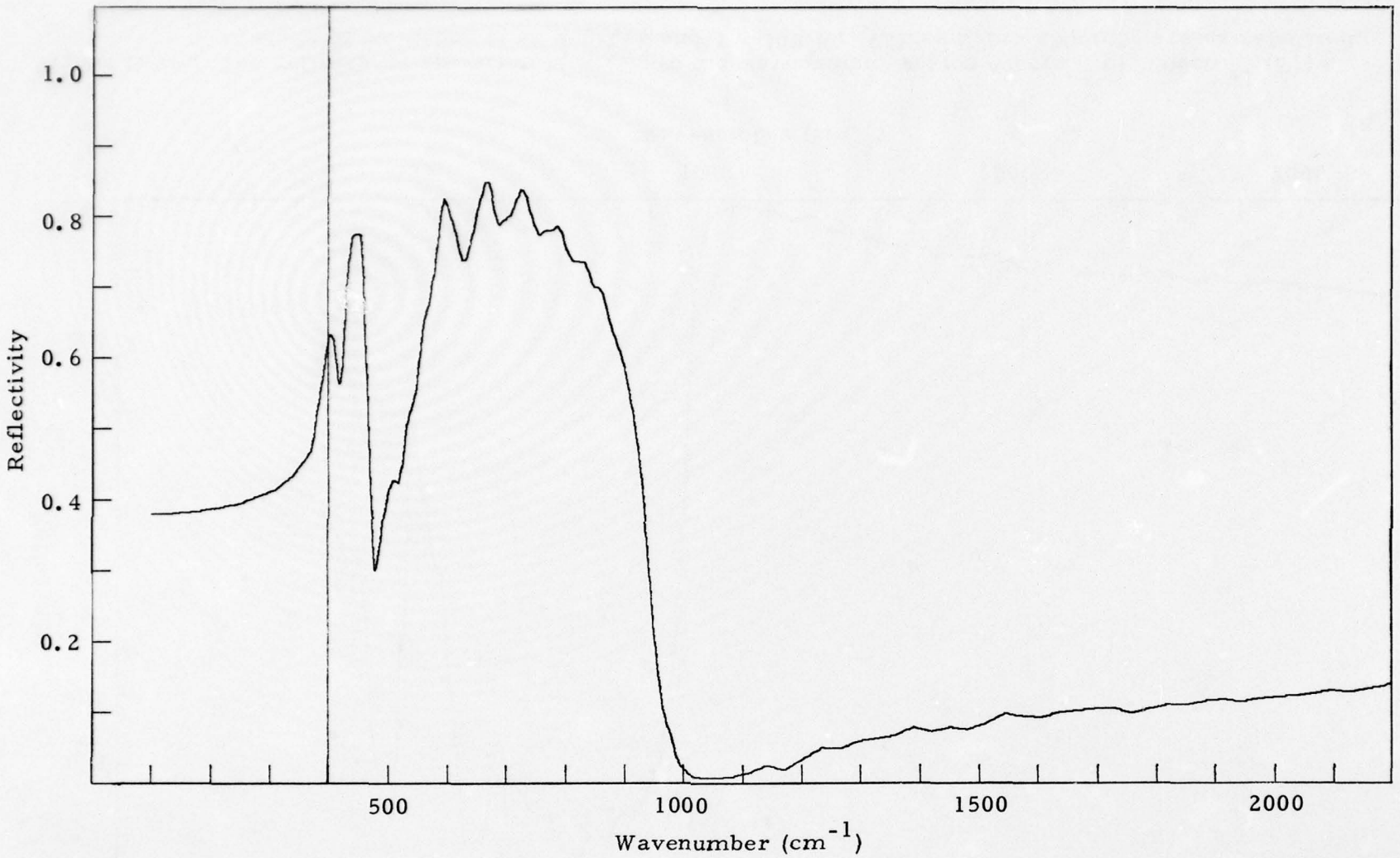

Figure II-27. The reflectivity spectrum of Al_2O_3 in the wavenumber region 400cm^{-1} to 2200cm^{-1} ($E_\perp$) at an angle of incidence of 45 degrees and T = 678°K. Values below 400cm^{-1} are extrapolated.

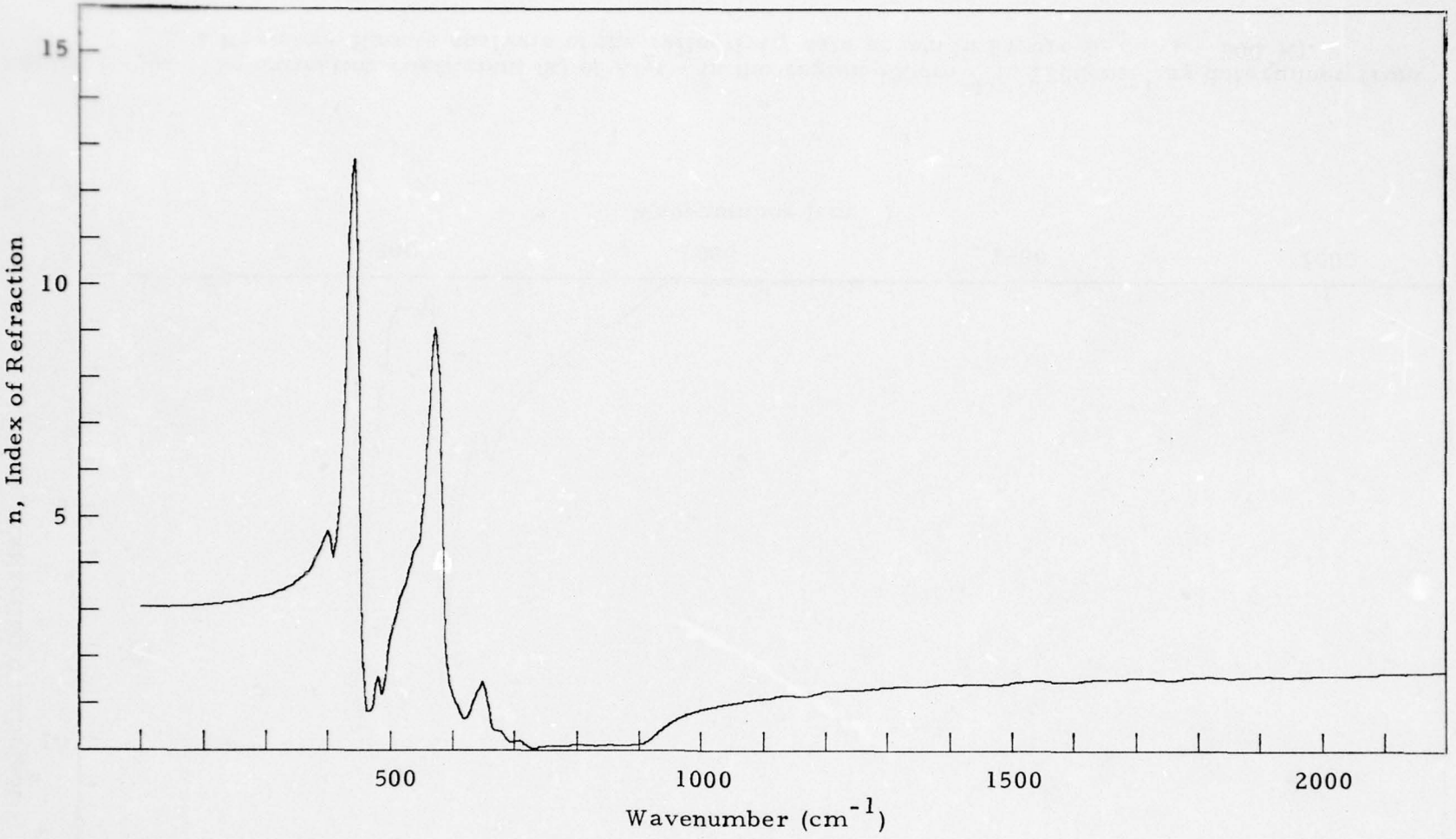

Figure II-28. The refractive index (n) of Al_2O_3 in the region 400cm^{-1} to 2200cm^{-1} as determined from a Kramers-Kronig analysis of the reflectivity data shown in Figure II-26 (T = 300 °K).

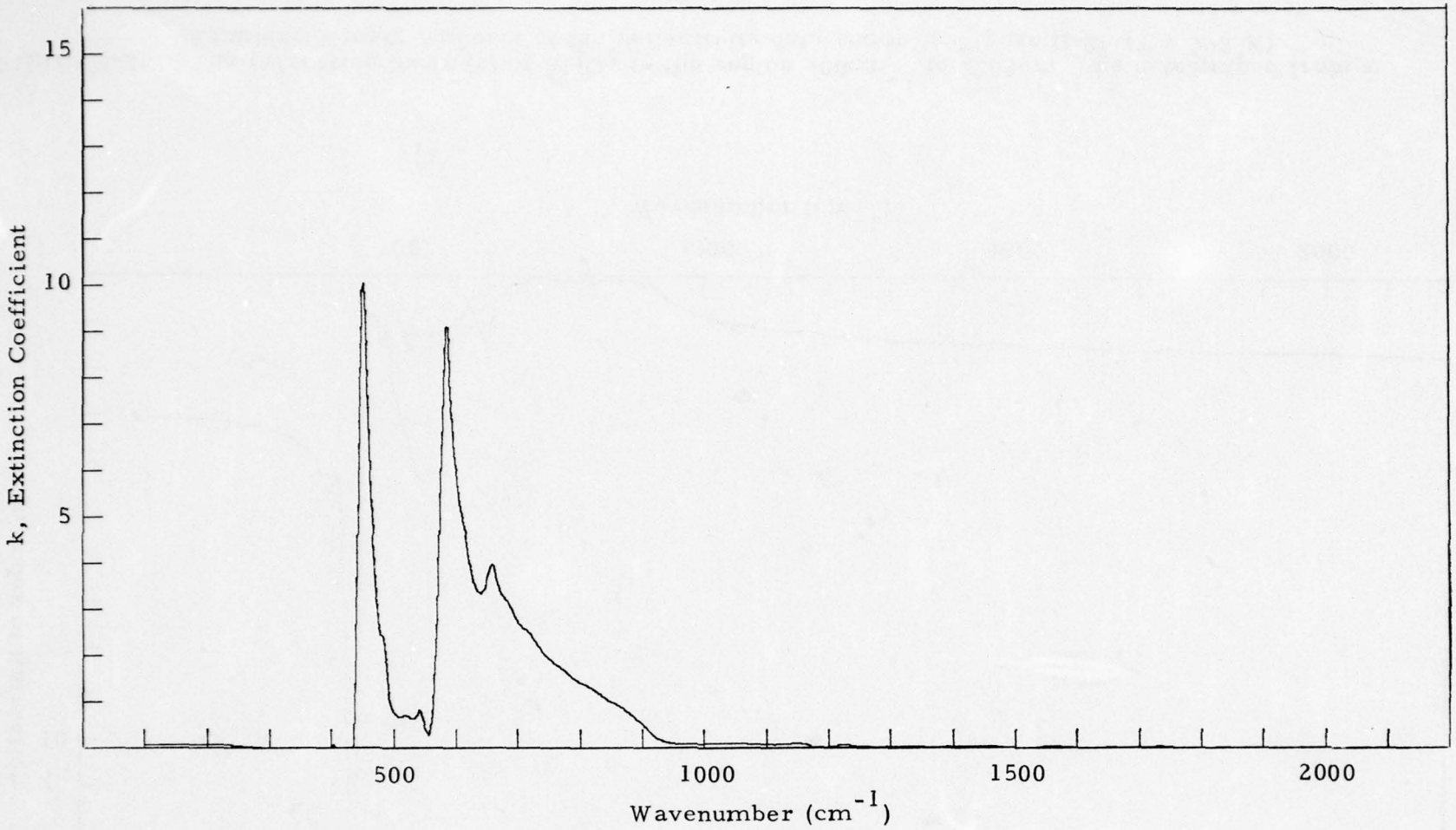

Figure II-29. The extinction coefficient (k) of Al_2O_3 in the region 400cm^{-1} to 2200cm^{-1} as determined from a Kramers-Kronig analysis of the reflectivity data shown in Figure II-26 (T = 300°K).

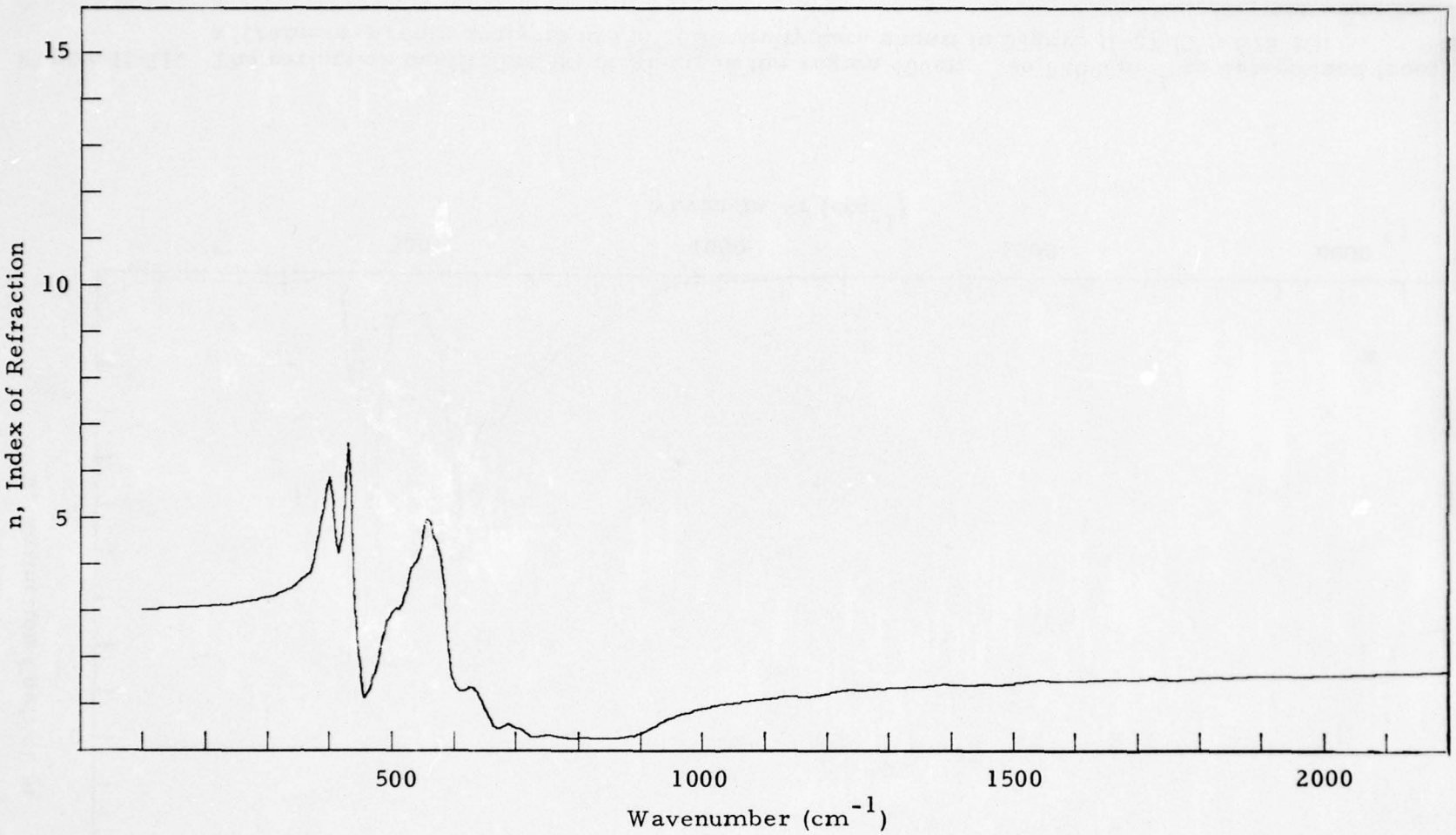

Figure II-30. The refractive index (n) of Al_2O_3 in the region 400cm^{-1} to 2200cm^{-1} as determined from a Kramers-Kronig analysis of the reflectivity data shown in Figure II-27 (T = 678°K).

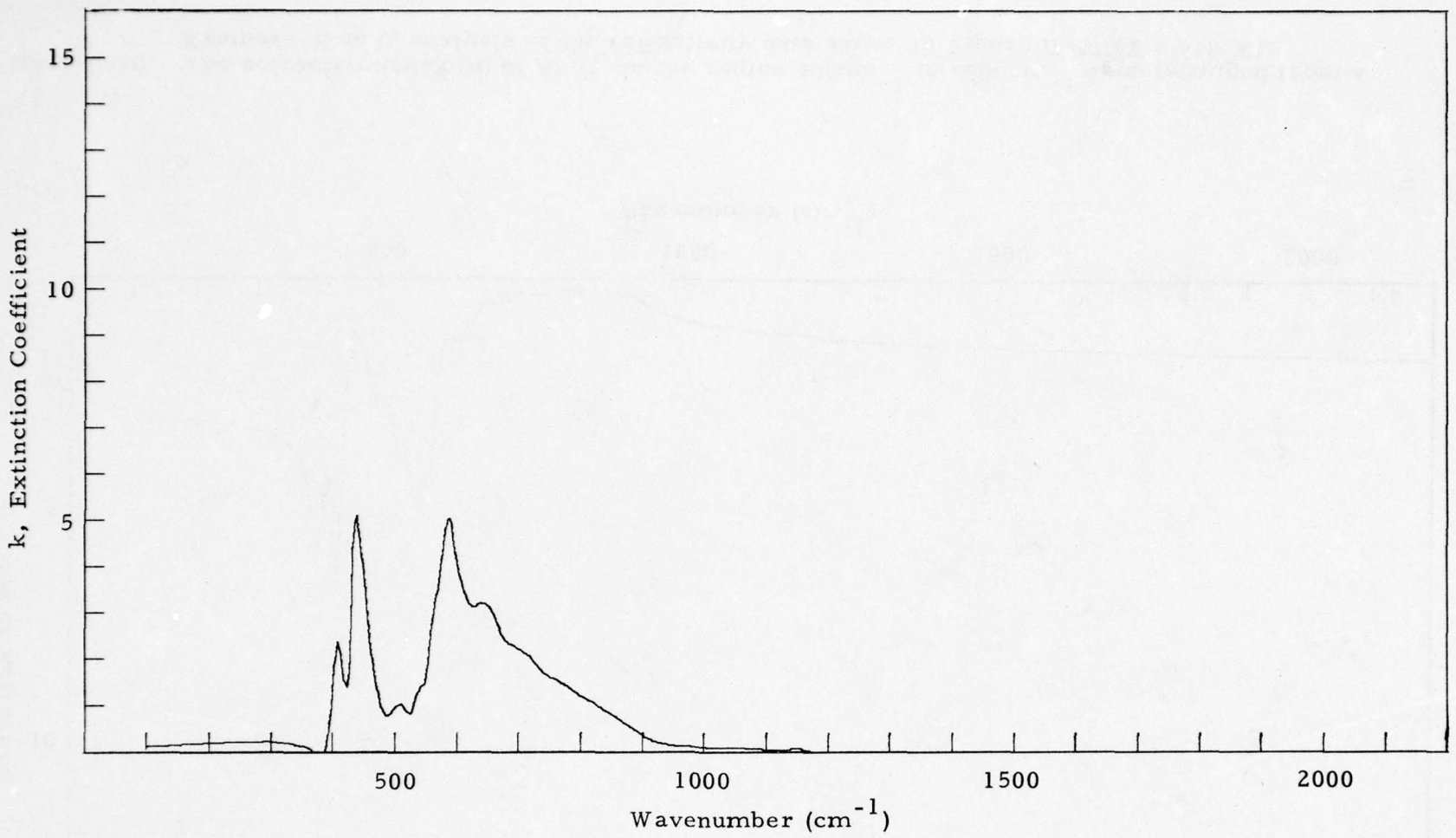

Figure II-31. The extinction coefficient (k) of Al_2O_3 in the region 400cm^{-1} to 2200cm^{-1} as determined from a Kramers-Kronig analysis of the reflectivity data shown in Figure II-27 (T = 678°K).

Table II-6. The refractive index (n) and extinction coefficient (k) for Al_2O_3 in the region 400cm^{-1} to 2200cm^{-1} at T = 300°K and 678°K.

	T = 300°K		T = 678°K	
ν (cm^{-1})	n	k	n	k
400	4.70	0.00	5.86	1.32
15	4.64	0.00	4.26	1.88
30	9.47	0.00	6.62	2.83
45	11.59	7.77	2.46	4.50
60	1.25	6.44	1.20	2.41
75	1.15	2.76	1.72	1.18
90	1.34	1.48	2.63	0.78
505	2.66	0.70	3.02	1.01
20	3.40	0.71	3.27	0.87
35	4.09	0.67	3.99	1.20
50	4.78	0.44	4.59	1.53
65	8.02	1.39	4.72	3.22
80	7.79	7.94	4.04	4.50
95	1.49	6.61	1.73	4.63
610	0.93	4.95	1.31	3.58
25	0.70	3.79	1.37	3.15
40	1.24	3.35	1.22	3.22
55	1.19	3.91	0.78	3.09
70	0.43	3.43	0.49	2.65
85	0.28	3.13	0.57	2.33
700	0.18	2.71	0.52	2.23
15	0.15	2.53	0.41	2.10
30	0.04	2.24	0.31	1.86
45	0.07	2.00	0.34	1.66
60	0.09	1.83	0.34	1.57

Table II-6. (Continued)

ν (cm^{-1})	T = 300 °K n	T = 300 °K k	T = 678 °K n	T = 678 °K k
775	0.08	1.67	0.30	1.45
90	0.11	1.50	0.27	1.30
805	0.12	1.39	0.28	1.17
20	0.11	1.28	0.28	1.07
35	0.10	1.13	0.26	0.94
50	0.12	1.01	0.27	0.82
65	0.11	0.89	0.27	0.68
80	0.11	0.74	0.31	0.55
95	0.13	0.58	0.36	0.42
910	0.17	0.40	0.45	0.29
25	0.31	0.21	0.55	0.21
40	0.48	0.13	0.66	0.16
55	0.62	0.10	0.75	0.14
70	0.73	0.09	0.81	0.13
85	0.81	0.09	0.86	0.10
1000	0.88	0.10	0.92	0.10
15	0.93	0.10	0.97	0.09
30	0.96	0.11	1.00	0.09
45	1.00	0.10	1.03	0.09
60	1.04	0.10	1.05	0.08
75	1.07	0.10	1.08	0.07
90	1.10	0.09	1.10	0.06
1105	1.12	0.08	1.13	0.05
20	1.16	0.08	1.16	0.05
35	1.19	0.09	1.19	0.05

Table II-6. (Continued)

ν (cm^{-1})	T = 300 °K		T = 678 °K	
	n	k	n	k
1150	1.18	0.11	1.18	0.06
65	1.17	0.08	1.17	0.04
80	1.21	0.02	1.19	0.00
95	1.27	0.02	1.23	0.00
1210	1.29	0.05	1.27	0.00
25	1.30	0.06	1.30	0.00
40	1.30	0.06	1.32	0.00
55	1.31	0.05	1.32	0.01
70	1.33	0.04	1.32	0.00
85	1.36	0.03	1.34	0.00
1300	1.37	0.05	1.36	0.00
15	1.38	0.05	1.37	0.00
30	1.38	0.06	1.38	0.00
45	1.38	0.05	1.39	0.00
60	1.39	0.03	1.40	0.00
75	1.42	0.02	1.42	0.00
90	1.45	0.04	1.44	0.00
1405	1.44	0.05	1.43	0.01
20	1.44	0.05	1.42	0.00
35	1.44	0.05	1.43	0.00
50	1.45	0.05	1.44	0.00
65	1.44	0.05	1.44	0.00
80	1.43	0.03	1.43	0.00
95	1.46	0.00	1.45	0.00
1510	1.49	0.00	1.47	0.00

Table II-6. (Continued)

ν (cm^{-1})	T = 300 °K		T = 678 °K	
	n	k	n	k
1525	1.51	0.05	1.49	0.00
40	1.53	0.02	1.52	0.00
55	1.51	0.05	1.52	0.00
70	1.49	0.05	1.51	0.00
85	1.49	0.03	1.51	0.00
1600	1.49	0.01	1.51	0.00
15	1.51	0.00	1.51	0.00
30	1.54	0.00	1.53	0.00
45	1.55	0.02	1.54	0.00
60	1.54	0.02	1.54	0.00
75	1.55	0.01	1.55	0.00
90	1.56	0.01	1.55	0.00
1705	1.57	0.03	1.56	0.00
20	1.56	0.03	1.56	0.00
35	1.55	0.04	1.55	0.00
50	1.54	0.03	1.54	0.00
65	1.54	0.00	1.53	0.00
80	1.56	0.00	1.55	0.00
95	1.59	0.00	1.56	0.00
1810	1.60	0.00	1.57	0.00
25	1.60	0.02	1.58	0.00
40	1.58	0.02	1.58	0.00
55	1.58	0.00	1.58	0.00
70	1.59	0.00	1.59	0.00
85	1.60	0.00	1.61	0.00

Table II-6. (Concluded)

ν (cm^{-1})	T = 300 °K		T = 678 °K	
	n	k	n	k
1900	1.61	0.00	1.61	0.00
15	1.62	0.01	1.61	0.00
30	1.61	0.02	1.60	0.00
45	1.59	0.00	1.60	0.00
60	1.60	0.00	1.61	0.00
75	1.61	0.00	1.62	0.00
90	1.62	0.00	1.62	0.00
2005	1.64	0.00	1.63	0.00
20	1.63	0.00	1.63	0.00
35	1.63	0.00	1.63	0.00
50	1.64	0.00	1.62	0.00
65	1.64	0.00	1.65	0.00
80	1.65	0.00	1.66	0.00
95	1.66	0.00	1.66	0.00
2110	1.67	0.00	1.66	0.00
2125	1.67	0.00	1.66	0.00
40	1.68	0.00	1.67	0.00
55	1.69	0.00	1.68	0.00
70	1.69	0.00	1.69	0.00
85	1.70	0.00	1.69	0.00
2200	1.71	0.01	1.71	0.00

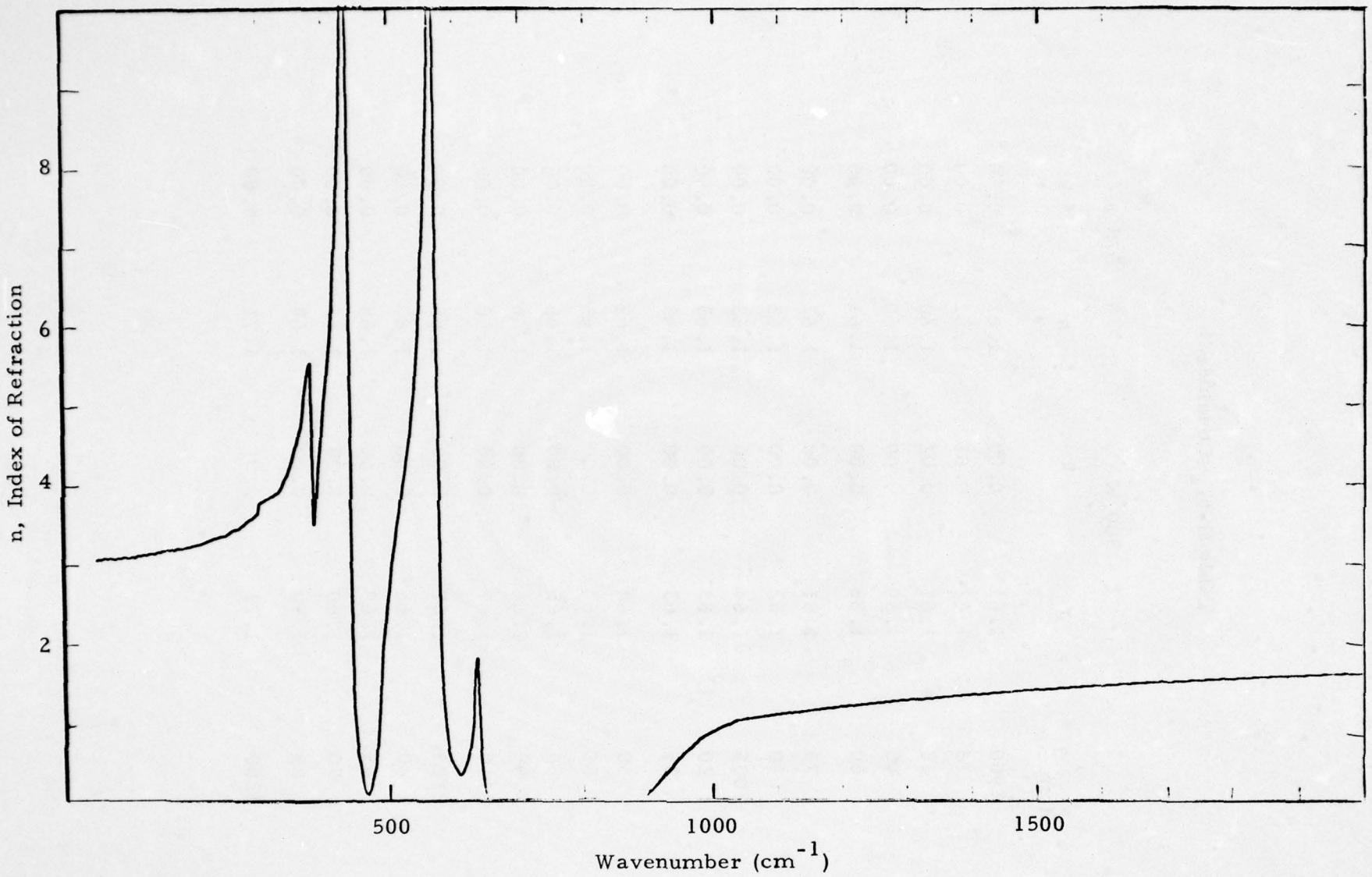

Figure II-32. Representative values of refractive index (n) in the region 100cm^{-1} to 2000cm^{-1} as compiled by Whitson (Ref. II-17) from the literature.

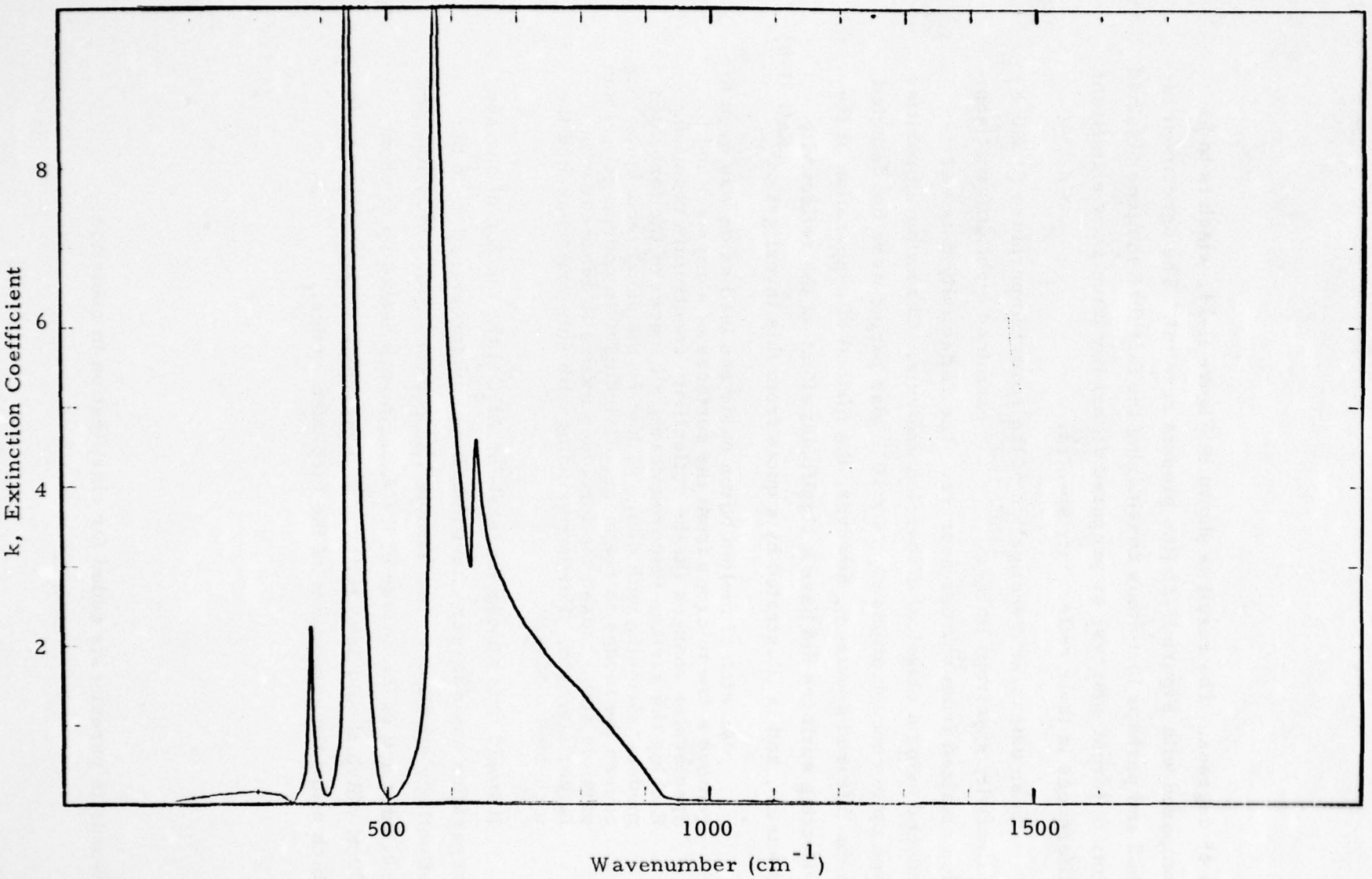

Figure II-33. Representative values of extinction coefficient (k) in the region 100cm^{-1} to 2000cm^{-1} as compiled by Whitson (Ref. II-17) from the literature.

of 45 degrees. The result is shown in Figure II-34, which is to be compared with Figure II-26 (the present results). The agreement is good and perhaps fortuitous considering the fact that samples obtained from different sources, or prepared differently often show significant differences in their reflectivity spectra.

In an extensive investigation of the room temperature ($\simeq 300^{\circ}K$) reflectivity spectrum Barker[Ref. II-8] examined eight different samples obtained from various sources. The reflectivity data were reduced using a classical dispersion analysis. Chromium impurities even up to concentrations of 2.4×10^{20} ions per cc were not detected in the infrared spectrum, however, the method of preparation of the reflecting surfaces did have a significant effect on the reflectivity spectrum, and is illustrated by a quote from this investigation[Ref. II-8]

> "An etch of molten boron oxide and lead oxide was used to remove a few microns from the surfaces of samples 3 and 5. Spectacular changes (in the reflectivity spectrum)* resulted. Etching the surface removes nearly all traces of the forbidden modes. Grinding with diamond dust by the usual techniques then caused the modes to reappear. Grinding with course grit, 15μm particle size, caused the forbidden modes to reappear with larger strength. Further grinding with 6μm grit weakened the forbidden modes."

It would thus appear (at least for Al_2O_3) the method of surface preparation has a larger effect than impurity concentration on the reflectivity spectrum. Our sample was polished with a very fine grit ($\sim 0.3\mu m$) and in the course of the experiments heated up to about $700^{\circ}K$ which should have relieved to a large degree any of the strain which allow the appearance of the forbidden modes.

*Words in parenthesis added for clarification in quotation.

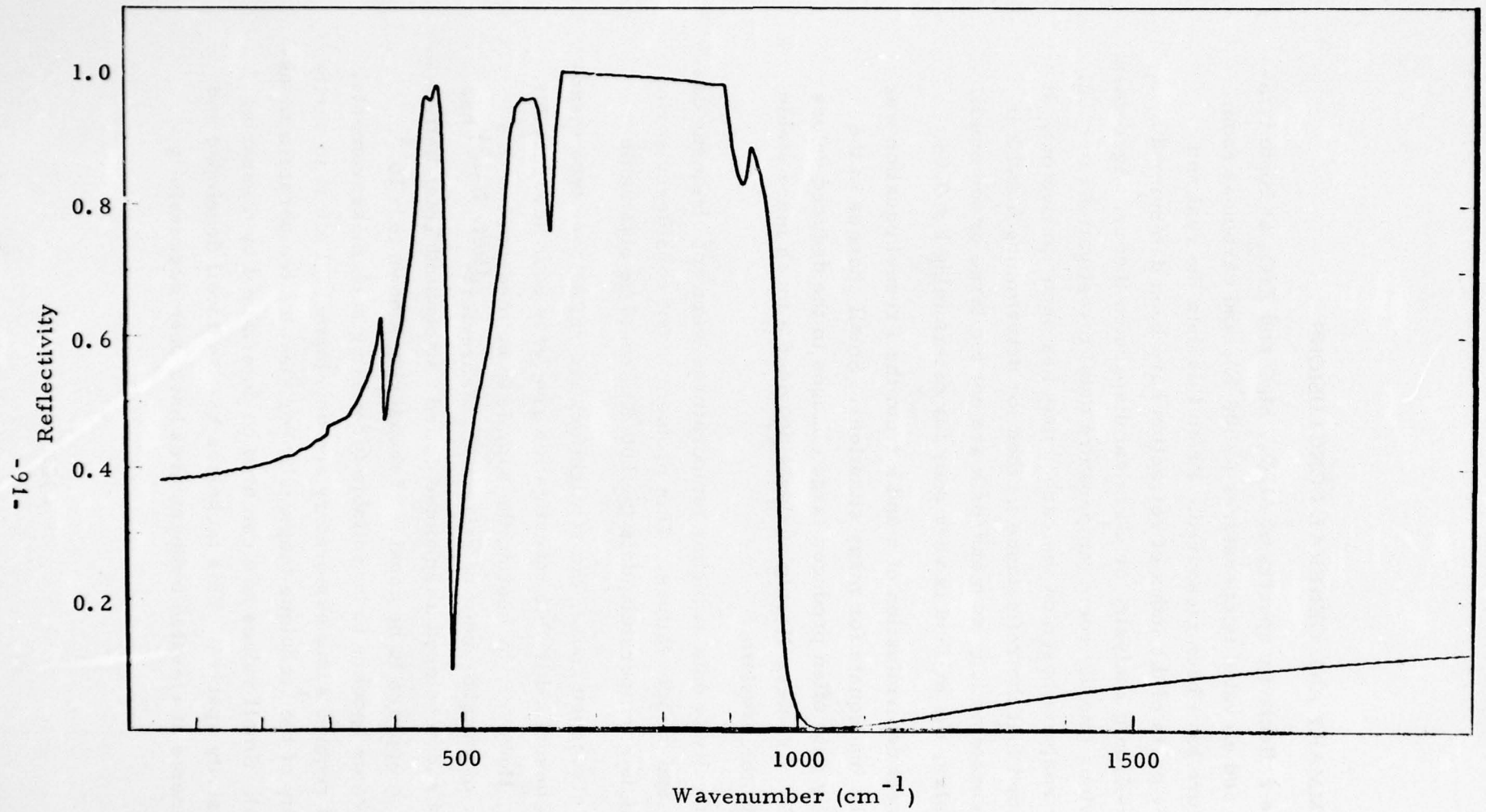

Figure II-34. Calculated reflectivity at 45 degrees incidence for Al_2O_3 ($T \simeq 300^{\circ}K$) in the region $100cm^{-1}$ to $2000cm^{-1}$. The n and k values used are the representative values from the compilation by Whitson (Ref. II-17).

D. SUMMARY AND GENERAL CONCLUSIONS

The reflectivity spectra of Al_2O_3, MgO and ZrO_2 at room temperature and elevated temperatures ($\sim 600^\circ K$), and carbon at room temperature have been measured. From this data the real and imaginary parts of the index of refraction have been determined by a Kramers-Kronig analysis, or classical dispersion theory. Agreement with previous (mostly room temperature data) investigations is good. An error analysis based on the carbon data has been carried out. It is concluded that the reflectance method for determining n and k is fairly accurate as long as n and/or k are not too large or too small. In particular, the method is very poor for determining $k \lesssim 0.05$.

Direct determination of n and k from the Fresnel equation was found to be inadequate for many situations. Small changes in the reflectivity data often produced large changes in the deduced values of n and k. Kramers-Kronig analysis provided a much more stable solution to the problem.

Reflectivity data at higher temperatures were not obtained, due to heater and sample failure. This problem is not considered serious and the higher temperature data ($\gtrsim 1000^\circ K$) should be obtainable.

As discussed above, the straightforward reflectance type measurements described in this investigation give very poor accuracy for $k \lesssim 0.05$. However, by coating the sample to be measured with a dielectric of suitable index of refraction, Fahrenfort[Ref. II-23] has described and developed a technique called "Attenuated Total Reflection" which appears to be capable of measuring k down to $\sim 10^{-4}$. Our apparatus appears to be suitable for making such measurements, but would require some exploratory and developmental effort to verify the validity of the technique (especially for elevated temperature measurements). Small values of k can also be determined by measuring transmissivity spectra. This technique has been well developed and measurements at elevated temperatures have been successfully

AD-A042 144 AEROSPACE CORP EL SEGUNDO CALIF CHEMISTRY AND PHYSICS LAB F/G 20/8
INFRARED EMISSIVITIES OF MICRON-SIZED PARTICLES OF C, MGO, AL S--ETC(U)
APR 77 J M DOWLING , C M RANDALL F04701-76-C-0077
UNCLASSIFIED TR-0077(2641)-1 AFRPL-TR-77-14 NL

2 OF 3
AD A042144

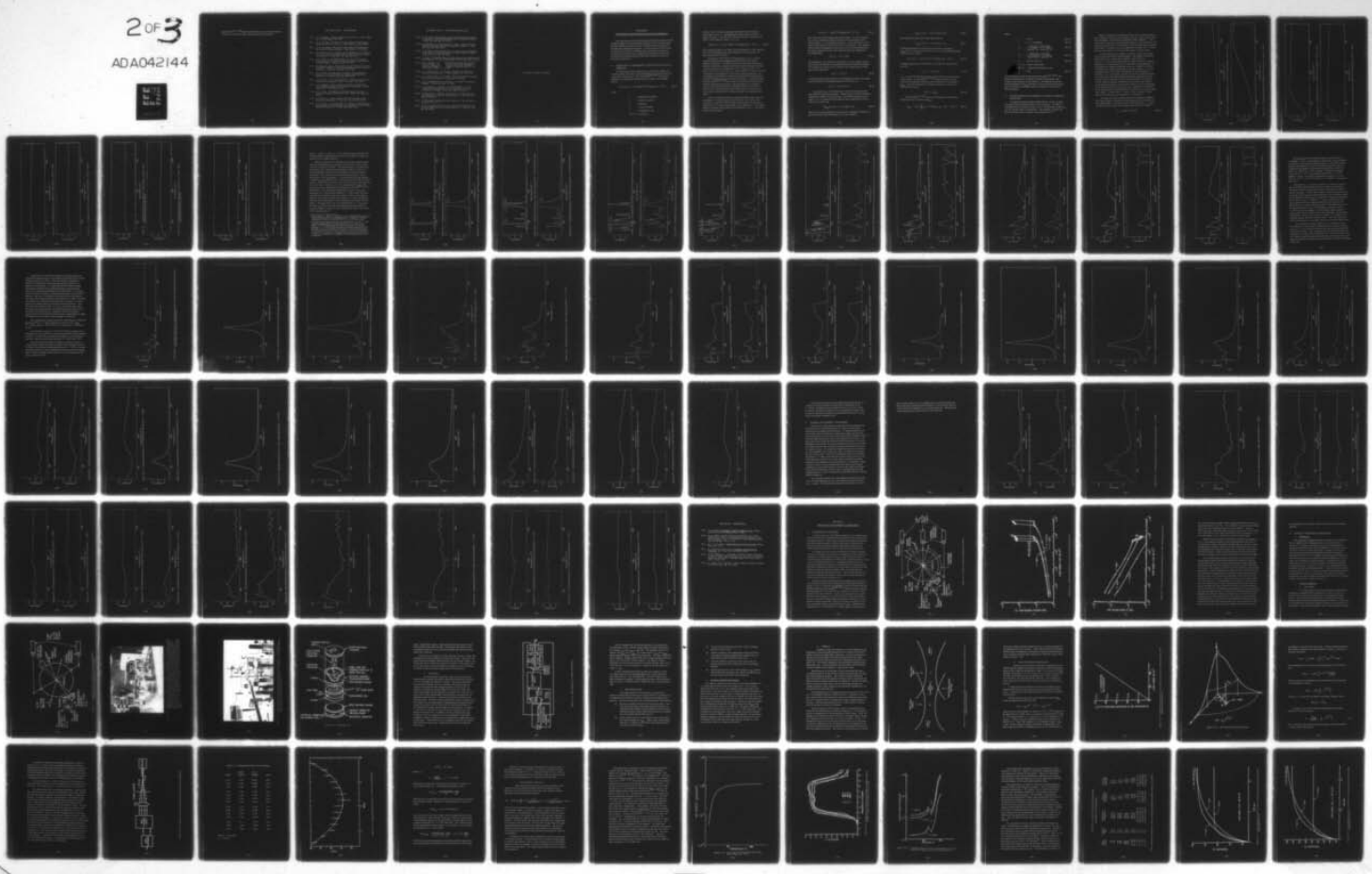

performed.[Ref. II-24] Major modifications of our present apparatus would be required to perform transmissivity measurements.

SECTION I AND II. REFERENCES

II-1. T. S. Robinson, "Optical Constants by Reflection," Proc. Phys. Soc. (London) B65, 910 (1952).

II-2. D. M. Roessler, "Kramers-Kronig Analysis of Non-Normal Incidence Reflection," Brit. J. Appl. Phys. 16, 1359 (1965).

II-3. D. W. Berreman, "Kramers-Kronig Analysis of Reflectance Measured at Oblique Incidence," Appl. Opt. 6, 1519 (1967).

II-4. M. R. Querry, R. C. Waring, W. E. Holland, G. M. Hale and W. Nijm, "Optical Constants in the Infrared for Aqueous Solutions of NaCl," J. Opt. Soc. Am. 62, 849 (1972).

II-5. G. M. Hale, W. E. Holland and M. R. Querry, "Kramers-Kronig Analysis of Relative Reflectance Spectra Measured at an Oblique Angle," Appl. Opt. 12, 48 (1973).

II-6. Che-Kuang Wu and G. Andermann, "Improved Kramers-Kronig Dispersion Analysis of Infrared Reflectance Data for Lithium Fluoride," J. Opt. Soc. Am. 58, 519 (1968).

II-7. P. N. Schatz, S. Maeda and K. Kozima, "Determination of Optical Constants from Reflection Bands using Dispersion Relations," J. Chem. Phys. 38, 2658 (1963).

II-8. A. S. Barker, Jr., "Infrared Lattice Vibrations and Dielectric Dispersion in Corundum," Phys. Rev. 132, 1474 (1963).

II-9. C. M. Randall, "User's Guide to Computer Programs for Fourier Spectroscopy," The Aerospace Corporation, TR-0073 (9260-01)-8, 30 November 1972.

II-10. D. G. Avery, "An Improved Method for Measurement of Optical Constants by Reflection," Proc. Phys. Soc. B65, 425 (1952).

II-11. M. R. Querry, "Direct Solution of the Generalized Fresnel Reflectance Equations," J. Opt. Soc. Am. 59, 876 (1969).

II-12. R. F. Miller, L. S. Julien and A. J. Taylor, "A New Computational Method of Obtaining Optical Constants from Reflectance Ratio Measurements," J. Phys. D5, 2288 (1972).

II-13. D. M. Kolb, "Determination of the Optical Constants of Solids by Reflectance-Ratio Measurements at Non-Normal Incidence," J. Opt. Soc. Am. 62, 599 (1972).

II-14. G. Andermann, A. Caron and D. A. Dows, "Kramers-Kronig Dispersion Analysis of Infrared Reflectance Bands," J. Opt. Soc. Am. 55, 1210 (1965).

II-15. R. S. Bauer, W. E. Spicer and J. J. White, III, "Investigation of the Kramers-Kronig Analysis: Revised Constants of AgCl," J. Opt. Soc. Am. 64, 830 (1974).

II-16. F. Stern, "Elementary Theory of Optical Properties of Solids," Solid State Physics, Vol. 15, 338 (Academic Press, New York, 1963).

II-17. M. E. Whitson, Jr., "[illegible]dbook of the Infrared Optical Properties of Al_2O_3, Car[illegible]gO and ZrO_2," The Aerospace Corporation Report T[illegible]5(5548)-2, (SAMSO Report TR-75-131), Vols. I and II, [illegible]e 1975.

II-18. J. T. Twitty and J. A. Weinman, "Radiative Properties of Carbonaceous Aerosols," J. Appl. Meteor. 10, 725 (1971).

II-19. P. J. Foster and C. R. Howarth, "Optical Constants of Carbons and Coals in the Infrared," Carbon 6, 719 (1968).

II-20. A. P. Lenham and D. M. Treherne, "The Optical Constants of Graphite," Observatory 86, 36 (1966).

II-21. J. R. Jasperse, A. Kahan, J. N. Plendl and S. S. Mitra, "Temperature Dependence of Infrared Dispersion in Ionic Crystals Lif and MgO," Phys. Rev. 146, 526 (1966).

II-22. B. Piriou and J. Tsakiris, "Reflection et Transmission dans l'infra Rouge de la Zircone Monoclinique," C. R. Acad. Sci. 261, 3079 (1965).

II-23. J. Fahrenfort, "Attenuated Total Reflection," Spectrochemica Acta 17, 698 (1961).

II-24. D. A. Gryvnak and D. E. Burch, "Optical and Infrared Properties of Al_2O_3 at Elevated Temperatures," J. Opt. Soc. Am. 55, 625 (1965).

This page left blank on purpose.

SECTION III

THEORETICAL COMPUTATION OF PARTICLE EMISSIVITY

One requirement of the Particle Optical Properties Measurements (POPM) Program is to calculate the emissivity in the infrared region of small spherical particles from the complex index of refraction of the material composing the particle. It is the purpose of this section to outline the derivation of mathematical expressions necessary to make these calculations and to apply them to predict the emissivity for particles of the materials for which bulk refractive indices are presented in Section II.

A. DERIVATION OF THEORETICAL FORMULAS FOR PARTICLE EMISSIVITY

At temperatures above absolute zero, all matter radiates and absorbs energy in the form of electromagnetic waves distributed over a spectrum of frequencies. The well known[Ref. III-1] theoretical expression for the power radiated from the surface of a radiating body is:

$$R(\nu, T)\, d\nu = \epsilon(\nu, T)\, (2\pi h\nu^3/c^2)\, [\exp(h\nu/kT) - 1]^{-1}\, d\nu \qquad \text{(III-1)}$$

where

k = Boltzmann's constant,

h = Planck's constant,

ν = frequency,

c = velocity of light,

T = temperature, and

$\epsilon(\nu, T)$ = emissivity.

and $R(\nu, T)\, d\nu$ is the power per unit area emitted in the frequency range from ν to $\nu + d\nu$. Multiplying this by the surface area of a sphere of radius r, we obtain the total radiated power emitted by the sphere in the frequency range ν to $\nu + d\nu$,

$$P(\nu, T)\, d\nu = \epsilon(\nu, T)\, \pi r^2 (8\pi h\nu^3/c^2)\, [\exp(h\nu/kT) - 1]^{-1}\, d\nu. \qquad \text{(III-2)}$$

The emissivity appears as a factor in this expression. Thus, equation III-2 can be regarded as the basic definition of the emissivity of a spherical particle of radius r.

The spectral distribution of radiated power, $P(\nu, T)$, can be computed theoretically by applying Kirchhoff's law and solving Maxwell's equations. Kirchhoff's law states that under conditions of thermal equilibrium, the power emitted in any small frequency range is equal to the power absorbed in the same frequency range. The power absorbed is then computed by solving Maxwell's equations for the scattering of electromagnetic waves from a spherical particle. By comparing the expression we obtain by this method with equation III-2 we obtain a theoretical formula for the emissivity. A recent detailed study by Baltes[Ref. III-2] has shown the emissivity obtained by these thermal equilibrium arguments is also appropriate for conditions when the radiating object and the radiation field are not in thermal equilibrium. In the remaining part of this section we will carry out the procedure outlined above to obtain formulae for computing emissivity.

Imagine a spherical particle suspended inside a hollow enclosure (hohlraum). The entire system which consists of the walls of the enclosure, the particle and the radiation field inside the enclosure is assumed to be in thermal equilibrium at a temperature T. The volume density of radiant energy between the frequencies ν and $\nu + d\nu$ is given by the Planck formula,

$$U(\nu, T)\, d\nu = (8\pi h\nu^3/c^3)\,[\exp(h\nu/kT) - 1]^{-1}\, d\nu. \qquad \text{(III-3)}$$

This radiation field is homogeneous and isotropic. It can be analyzed into a sum of individual unpolarized plane waves traveling with the speed of light, c, in all possible directions. Let us establish a coordinate system with its origin at the center of the particle. The intensity of the radiation traveling in the direction of a unit vector specified by the polar coordinates θ and φ and contained within the infinitesimal solid angle $d\Omega$ is,

$$dI(\nu, T) = K(\nu, T)\, d\Omega. \qquad \text{(III-4)}$$

The quantity $K(\nu, T)$, defined by equation III-4, has no angular dependence and can be related to the energy density by the following analysis. The intensity of a plane wave is related to the energy density in that wave by the expression,

$$I(\nu, T) = cU(\nu, T). \qquad \text{(III-5)}$$

Combining equations III-4 and III-5 and integrating over all solid angles gives the desired relationship between $K(\nu, T)$ and $U(\nu, T)$,

$$K(\nu, T) = (c/4\pi)\, U(\nu, T). \qquad \text{(III-6)}$$

Each plane wave of intensity $dI(\nu, T)$ is scattered and partially absorbed by the spherical particle. This process is most conveniently expressed in terms of a cross section. The amount of power in the range ν to $\nu \pm d\nu$ absorbed by the particle from a plane wave of intensity $dI(\nu, T)$ is given by,

$$dP_{abs}(\nu, T)\, d\nu = \sigma(\nu, T)\, dI(\nu, T)\, d\nu, \qquad \text{(III-7)}$$

where $\sigma(\nu, T)$ is the absorption cross section. Substitute equation III-4 into equation III-7 and integrating over all solid angles,

$$P_{abs}(\nu, T)\, d\nu = 4\pi\sigma(\nu, T)\, K(\nu, T)\, d\nu. \qquad \text{(III-8)}$$

Then substitute equation III-6 into equation III-8,

$$P_{abs}(\nu, T)\, d\nu = c\sigma(\nu, T)\, U(\nu, T)\, d\nu. \qquad \text{(III-9)}$$

Utilizing Kirchhoff's law which equates the power absorbed, $P_{abs}(\nu, T)\, d\nu$, to the power emitted, $P(\nu, T)\, d\nu$, and substituting from equation III-3 we obtain,

$$P(\nu, T)\, d\nu = \sigma(\nu, T)\, (8\pi h\nu^3/c^2)\, [\exp(h\nu/kT) - 1]^{-1}\, d\nu. \qquad \text{(III-10)}$$

Comparing equations III-10 and III-2 we see that the emissivity is given by,

$$\epsilon(\nu, T) = \sigma(\nu, T)/\pi r^2, \qquad \text{(III-11)}$$

i.e., it is just the absorption cross section divided by the geometric cross section. Van de Hulst[Ref. III-3] calls this ratio of cross sections the absorption efficiency and has denoted it by the symbol Q_{abs}. Thus, the emissivity of a spherical particle is equal to its absorption efficiency,

$$\epsilon(\nu, T) = Q_{abs}. \qquad \text{(III-12)}$$

Van de Hulst[Ref. III-3] gives the following set of Mie theory formulas for the calculation of Q_{abs}.

$$Q_{abs} = (2/x^2) \sum_{n=1}^{\infty} (2n + 1)\, [\mathrm{Re}(a_n + b_n) - |a_n|^2 - |b_n|^2], \qquad \text{(III-13)}$$

where

$$x = 2\pi r/\lambda, \tag{III-14}$$

$$\lambda = c/\nu = \text{wavelength}, \tag{III-15}$$

$$a_n = \frac{j_n'(y)\, j_n(x) - m j_n(y)\, j_n'(x)}{j_n'(y)\, h_n^{(2)'}(x) - m j_n(y)\, h_n^{(2)'}(x)}, \tag{III-16}$$

$$b_n = \frac{m j_n'(y)\, j_n(x) - j_n(y)\, j_n'(x)}{m j_n'(y)\, h_n^{(2)}(x) - j_n(y)\, h_n^{(2)'}(x)}, \tag{III-17}$$

$$m = n(\nu, T) - ik(\nu, T), \tag{III-18}$$

$n(\nu, T)$ = index of refraction,

$k(\nu, T)$ = coefficient of extinction, and

$$y = mx. \tag{III-19}$$

$j_n(x)$ and $h_n^{(2)}(x)$ are the Ricatti-Bessel functions.[Ref. III-4] The primes in equations III-16 and III-17 denote differentiation with respect to the argument of the function. The temperature and frequency dependence of Q_{abs} [and thus of $\epsilon(\nu, T)$] is due to the dependence of the index of refraction and the coefficient of extinction on these quantities.

B. CALCULATIONS OF THE EMISSIVITY OF SMALL SPHERICAL PARTICLES

A computer program entitled "SPECTRUM", which calculates the emissivity by the method above has been written. The input to the program is the refractive index, $n(\nu, T)$, the extinction coefficient, $k(\nu, T)$, and the radius of the particle. The program computes and plots the emissivity as a function of wavenumber (cm^{-1}).

Shown in Figures III-1 through III-10 are the calculated emissivities of spherical carbon particles whose radii vary from 0.5μm to 50μm. The wavenumber range of the calculations is 300 to 1800cm^{-1}. The n and k values used are from the smoothed data for carbon (Section II-C.1) except for Figure III-8, which used the n and k derived from the experimental data. This figure is to be compared with Figure III-7. The differences between the two curves are noticeable, but quite small.

As was expected, the variation of emissivity with wavenumber is very smooth and rather slowly varying. The change in emissivity with particle size is much more dramatic, and in fact, for $1.0\mu m \leq r \leq 10\mu m$ sized particles the calculated emissivity is greater than one over a large portion of the wavenumber interval plotted. At first glance this appears surprising, however, it should be remembered that these sized particles are in the "Mie" region, i.e., their circumference is of the order of magnitude of the wavelength of radiation. As is well known, particles in this size region frequently have scattering cross sections larger than their geometrical cross sections, due to resonance between vibration modes of the particle and the radiation and thus, absorption or emission cross sections larger than the geometric cross section should not be too surprising. As the particle size becomes larger (i.g., Figures III-9 and III-10), the calculated emissivity falls below one and is more or less constant above 500cm^{-1} (shorter than $\lambda = 20\mu m$). Thus, the larger carbon particles act like classical greybodies, as they should.

For particles large compared with the wavelength of radiation, the computed particle emissivity should approach the emissivity of a plane bulk sample. The emissivity at normal incidence, ϵ_n, is particularly easy to compute for an opaque material such as carbon.

$$\epsilon_n = 4n/[(n+1)^2 + k^2] \qquad \text{(III-20)}$$

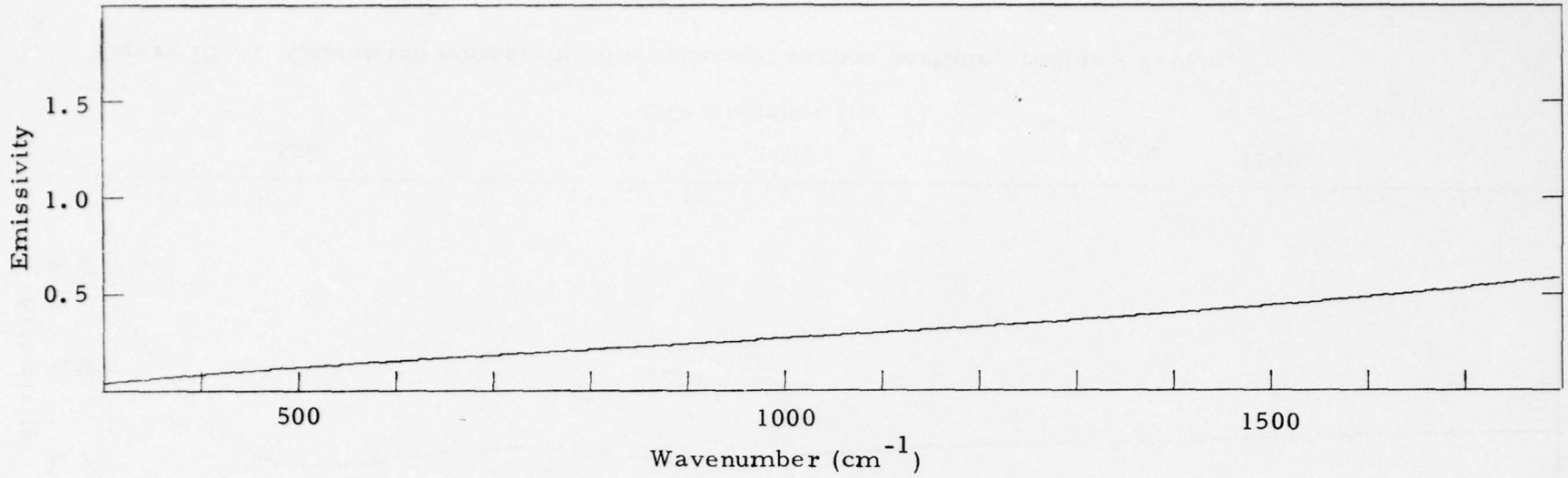

Figure III-1. Calculated emissivity of a spherical carbon particle, radius = 0.5μm.

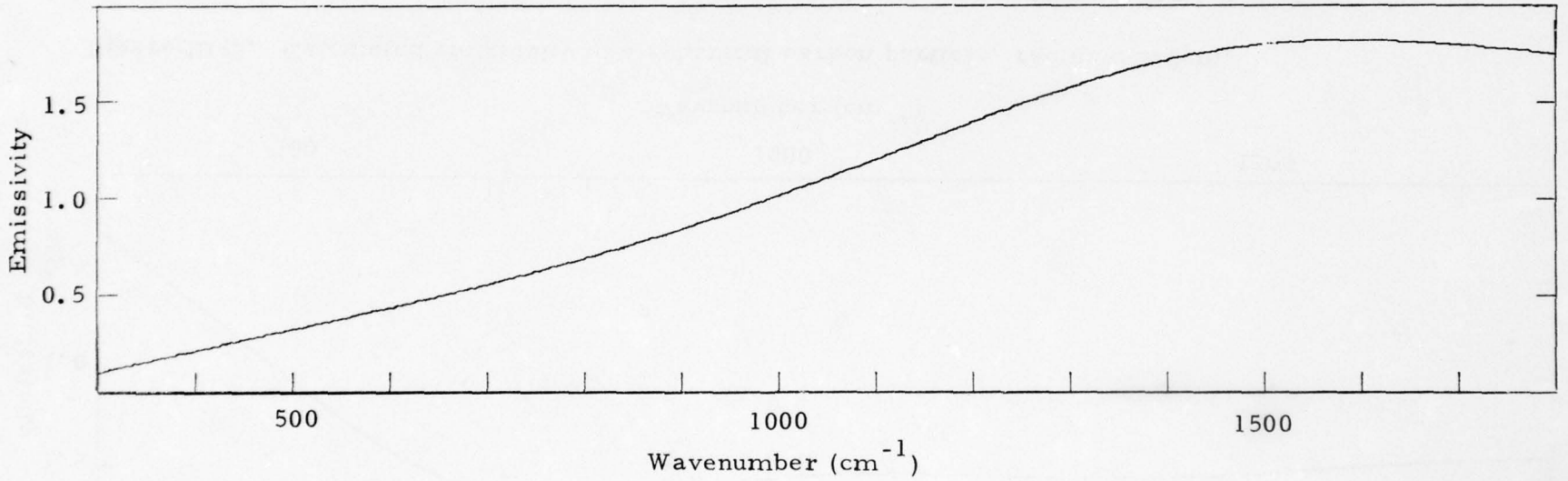

Figure III-2. Calculated emissivity of a spherical carbon particle, radius = 1.0μm.

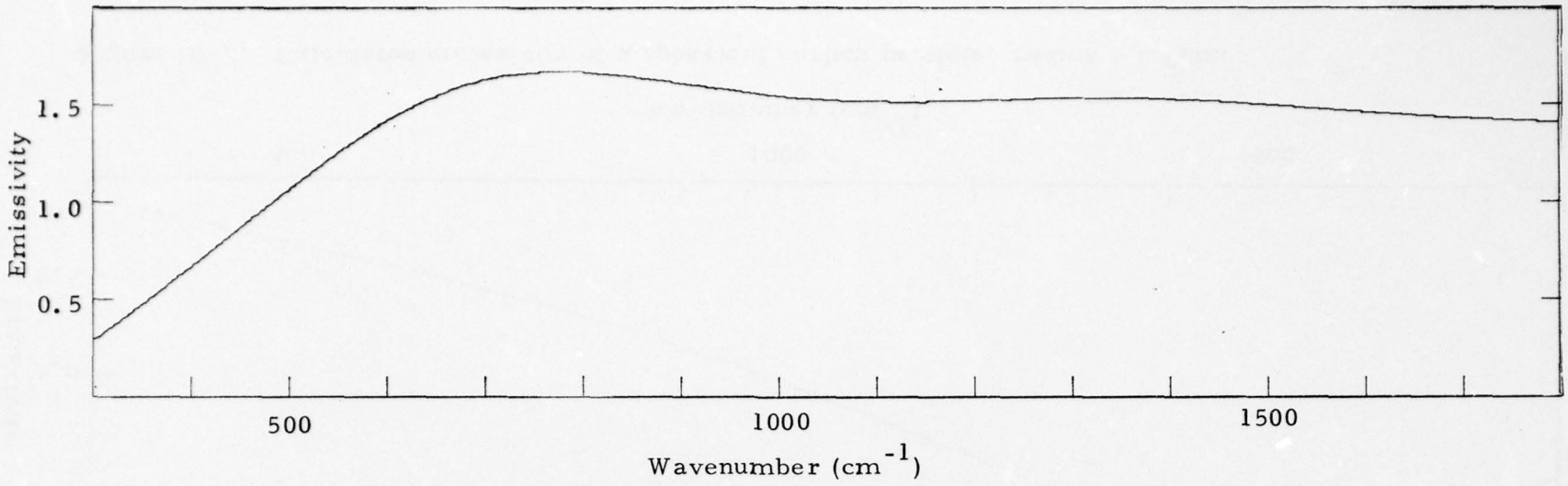

Figure III-3. Calculated emissivity of a spherical carbon particle, radius = 2.0μm.

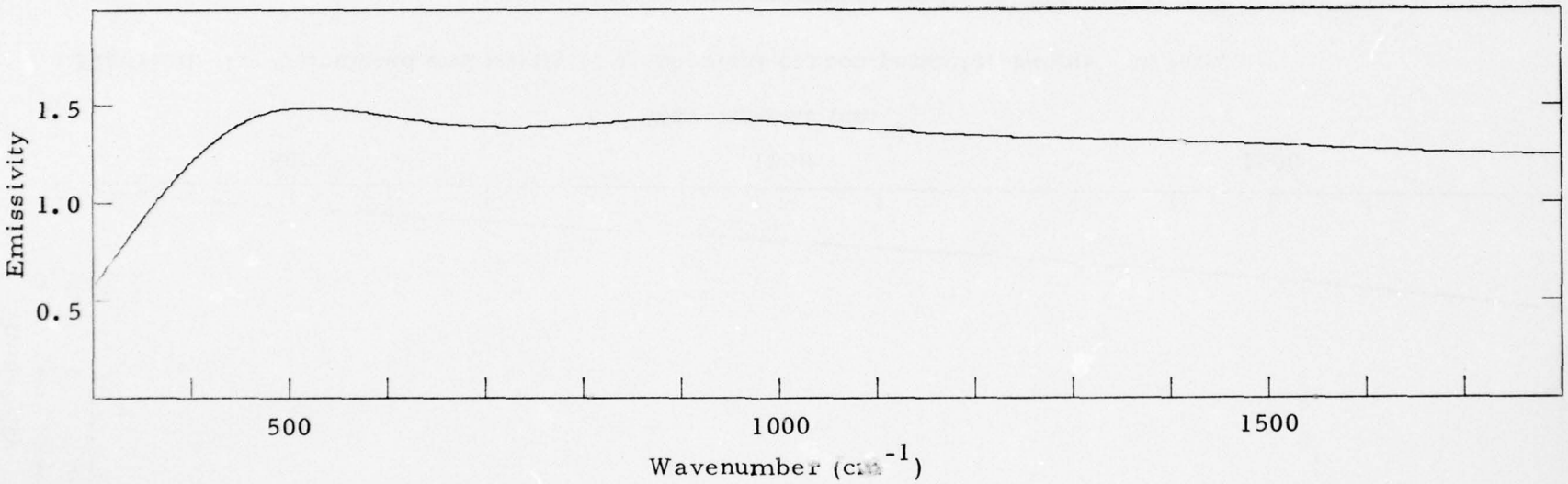

Figure III-4. Calculated emissivity of a spherical carbon particle, radius = 3.0μm.

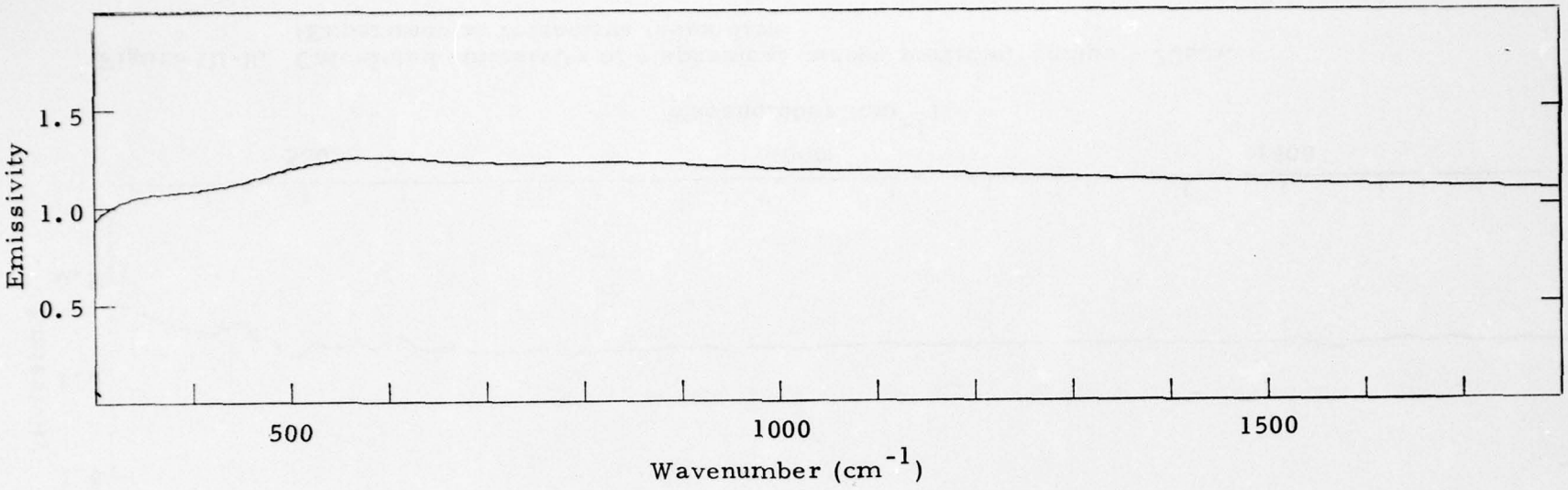

Figure III-5. Calculated emissivity of a spherical carbon particle, radius = 5.0μm.

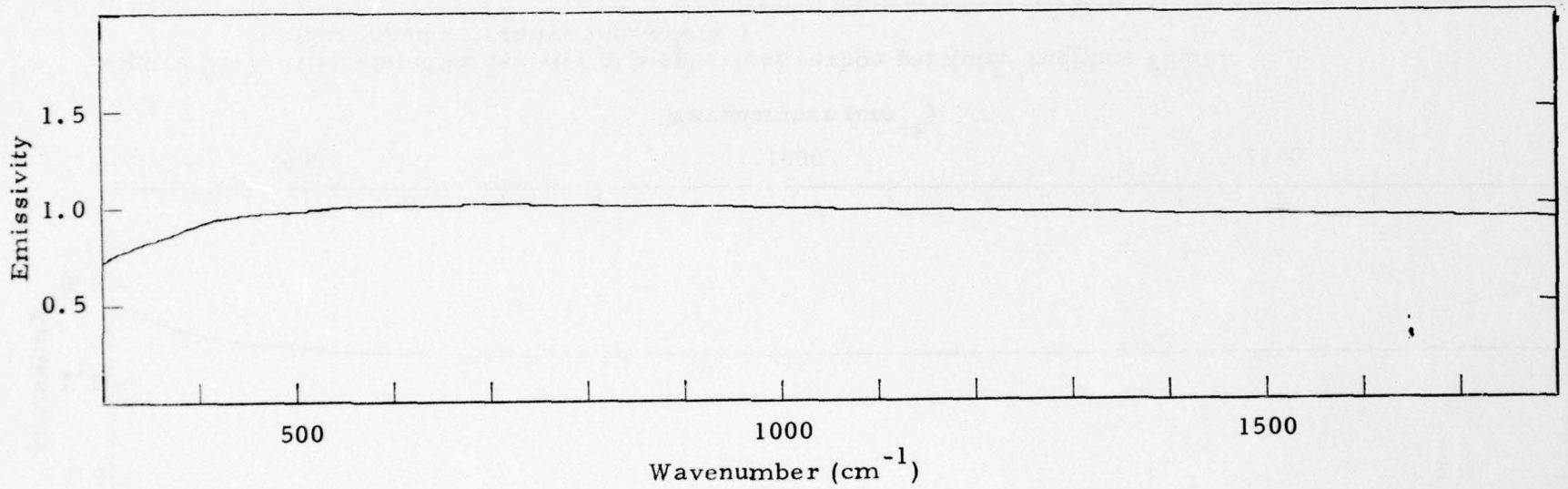

Figure III-6. Calculated emissivity of a spherical carbon particle, radius = 10.0μm.

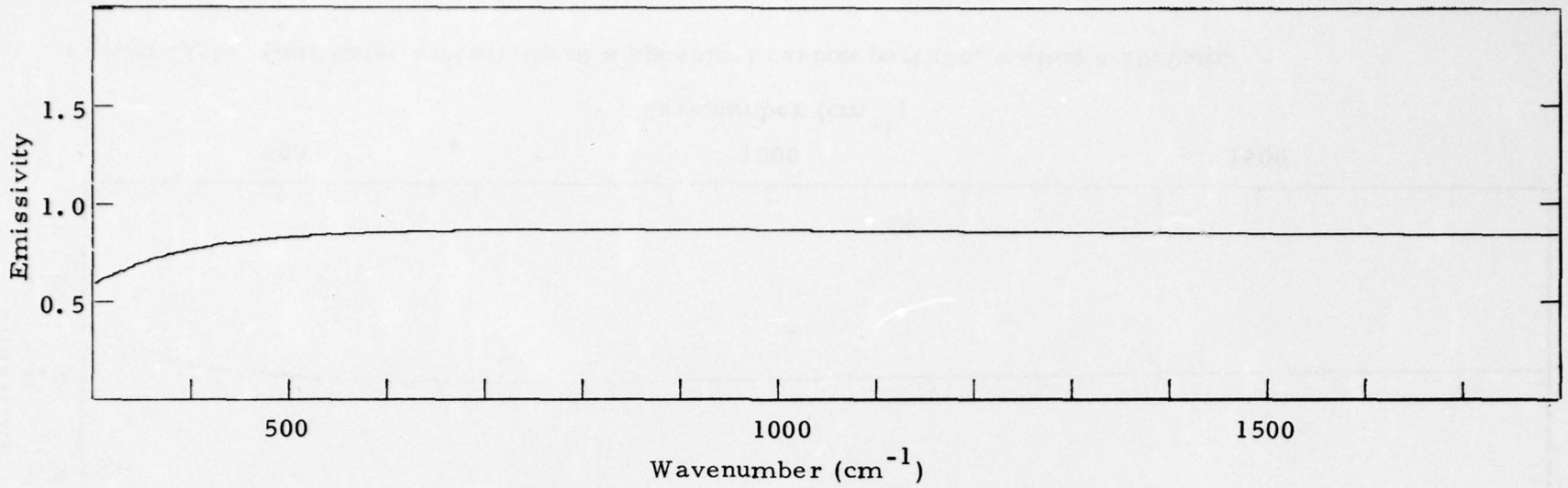

Figure III-7. Calculated emissivity of a spherical carbon particle, radius = 20μm. (Smoothed refractive index data.)

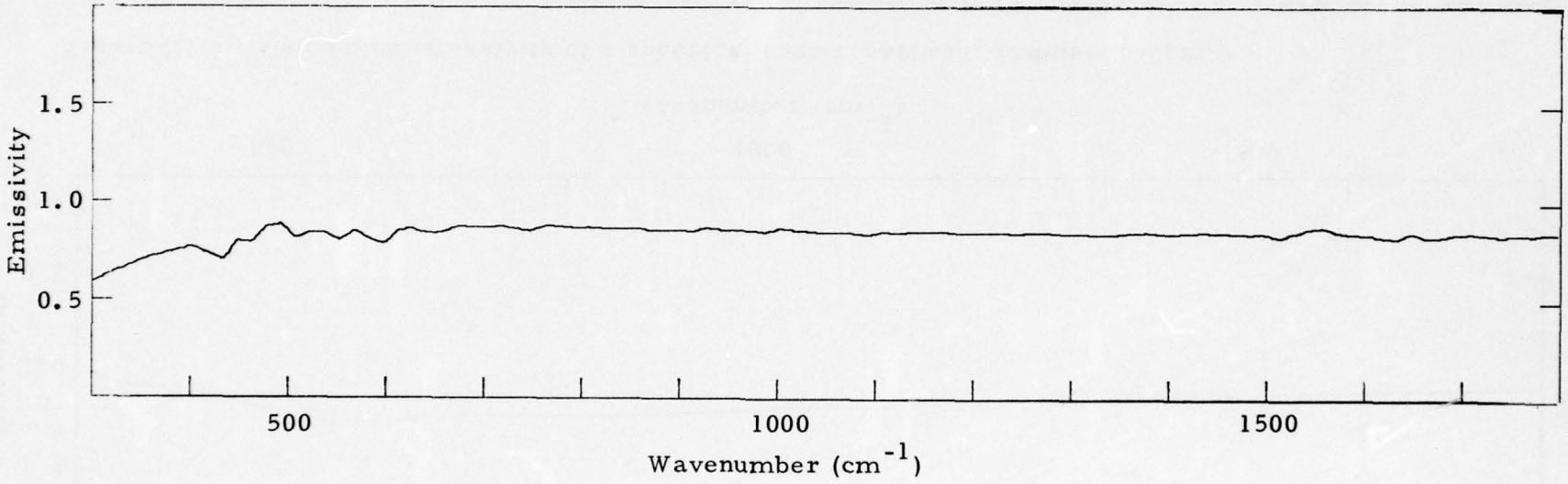

Figure III-8. Calculated emissivity of a spherical carbon particle, radius = 20μm. (Experimental refractive index data.)

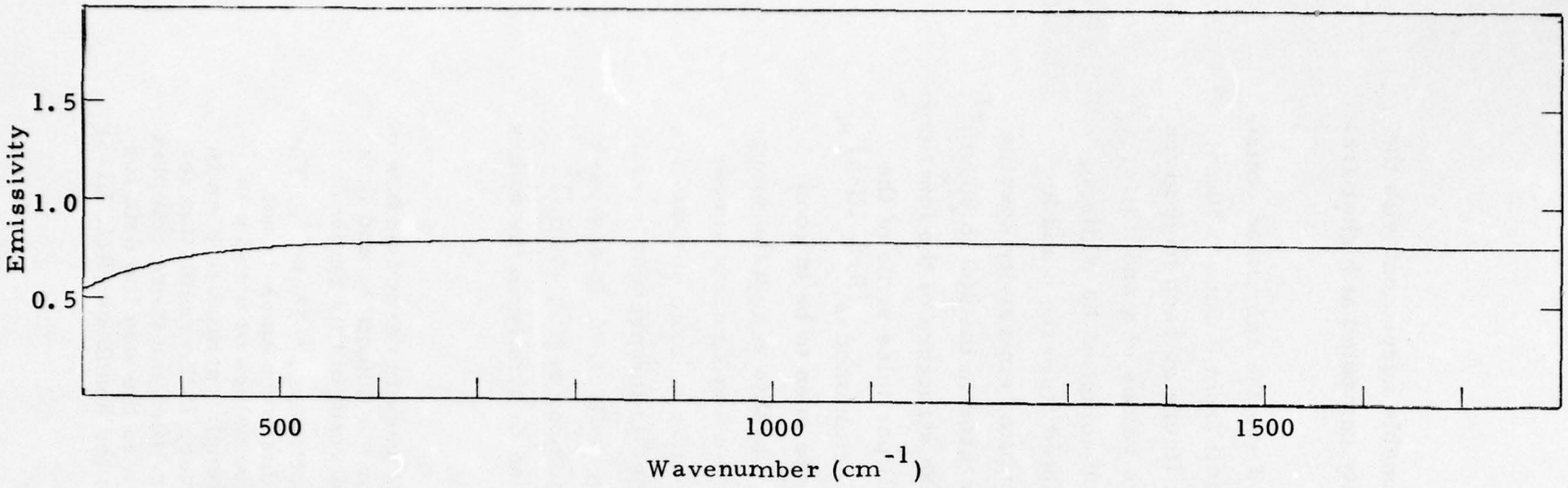

Figure III-9. Calculated emissivity of a spherical carbon particle, radius = 30μm.

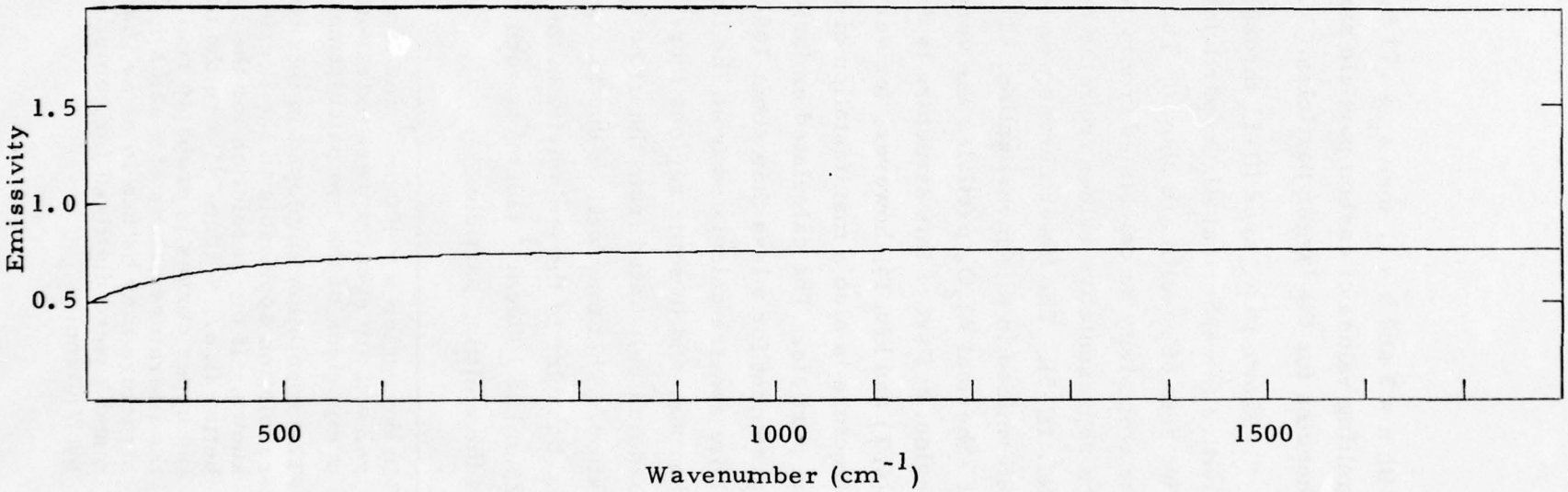

Figure III-10. Calculated emissivity of a spherical carbon particle, radius = 50μm.

With n = 3 and k = 1, then $\epsilon_n = .71$ in reasonable agreement with the limiting values of carbon particle emissivity computed at higher frequencies for the larger particles.

Shown in Figures III-11 through III-28 are the calculated emissivities for spherical Al_2O_3 particles of radii from 0.5μm to 50μm. Two sets of results are shown. The upper figure on each page gives the emissivity as calculated from literature values of n and k (i.e., the representative values from the handbook compiled by Whitson, Ref. III-5). The lower curves were calculated from the n and k determined in this investigation. The calculated emissivity spectra of spherical Al_2O_3 particles are very structured in the 400 to 900cm^{-1} region.* Part of this structure is due to the structure of the functions $n(\nu, T)$ and $k(\nu, T)$, however, for very small particles some of the structure is also a manifestation of the polariton modes[Ref. III-6] of the particle. The calculated emissivities are seen to be in good agreement for ν less than about 1000cm^{-1}. In this region the emissivity spectra calculated from the literature n and k values appear sharper, and in some regions more intense (i.e., large emissivity) than that calculated from the n and k obtained in the present investigation. This may well be due to a resolution effect.** In any case the behavior of the emissivity in the wavenumber region 400cm^{-1} (25μm) to 1000cm^{-1} (10μm) is seen to depend critically on the radius of the emitting particle.

---

*In the region ν = 400cm^{-1} and lower, our results depend on how our reflectivity spectra were extrapolated for $\nu \leq 400cm^{-1}$, and thus comparison of the two calculations is not valid in this region.

**The resolution employed in this investigation was ~ 15cm^{-1}. The resolution applicable to the literature values of n and k is not known. If the resolution for the literature values of n and k is better (i.e., < 15cm^{-1}) then the more complex structure seen in the upper curves is probably real, however, if the resolution for the literature values of n and k is poorer, then the more complex structure may be due to an artifact, such as the way the data for n and k were digitized for compilation in the handbook (Ref. III-5) by Whitson.

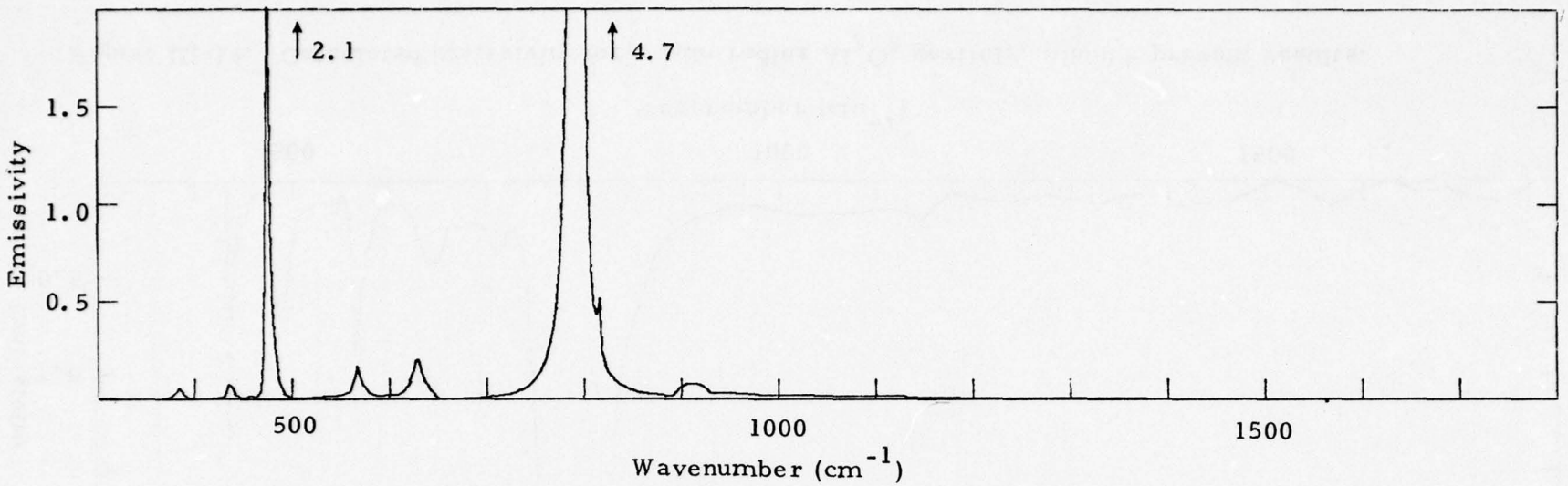

Figure III-11. Calculated emissivity for a 0.5μm radius Al_2O_3, n and k literature values.

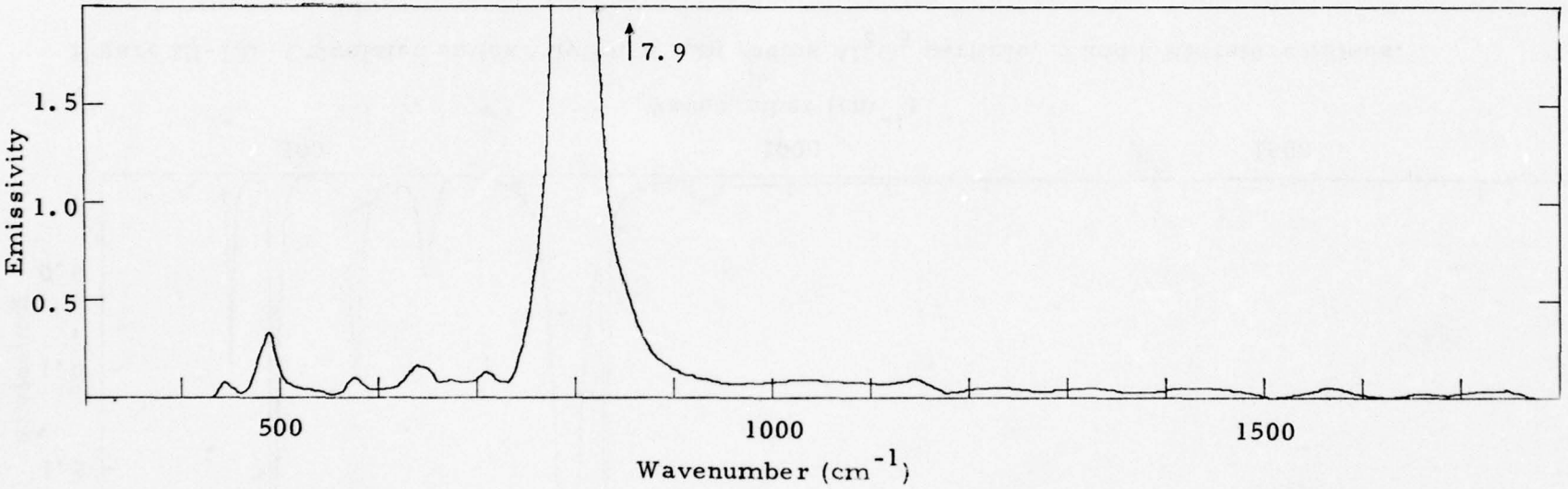

Figure III-12. Calculated emissivity for a 0.5μm radius Al_2O_3 particle, n and k present results.

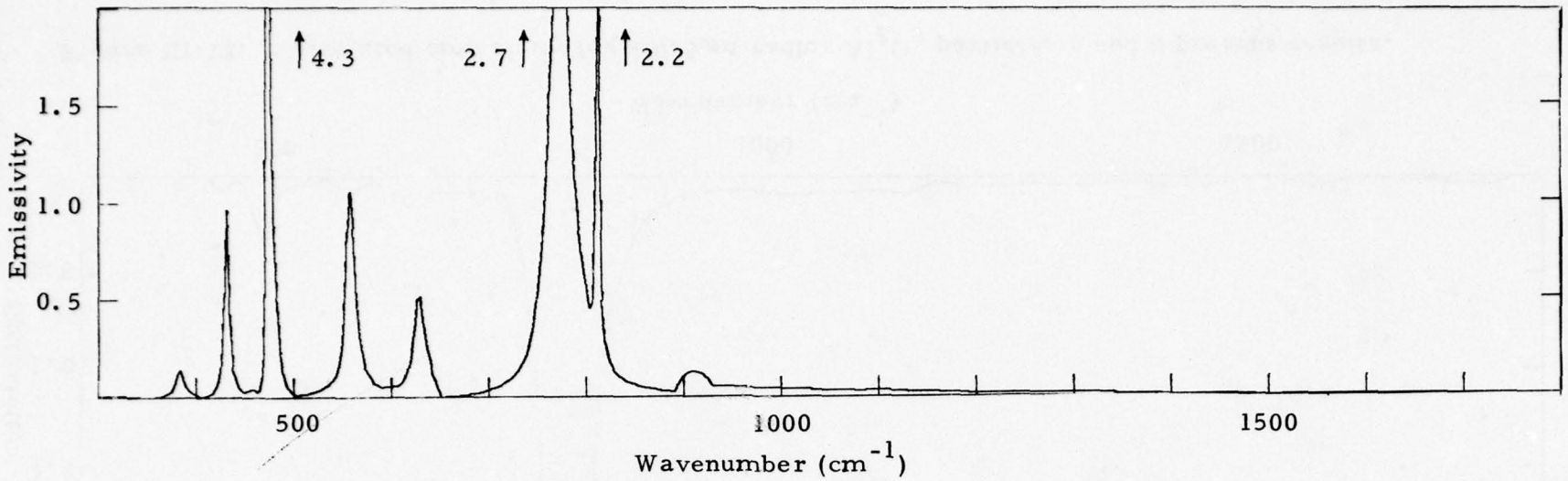

Figure III-13. Calculated emissivity for a 1μm radius Al_2O_3 particle, n and k literature values.

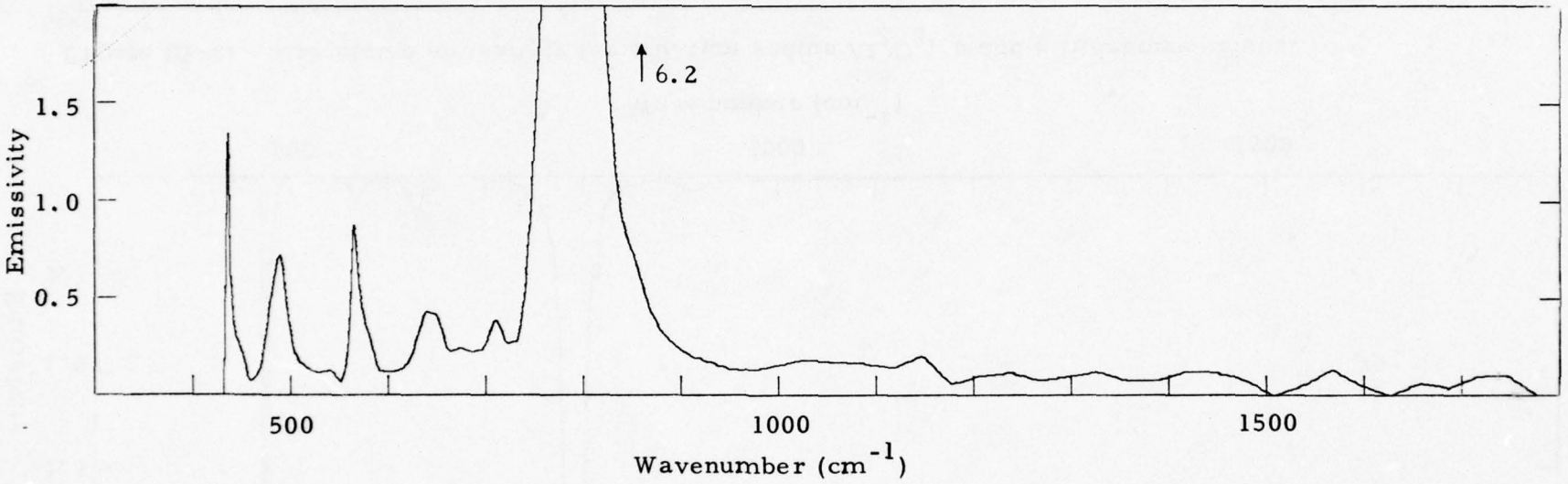

Figure III-14. Calculated emissivity for a 1μm radius Al_2O_3 particle, n and k present results.

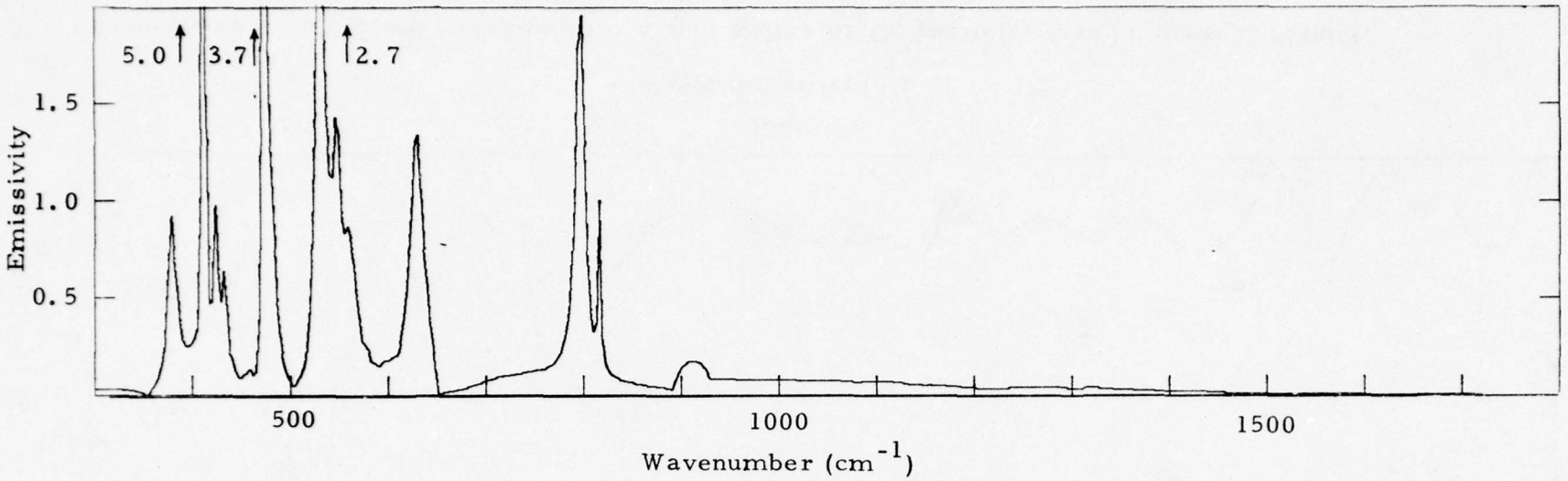

Figure III-15. Calculated emissivity for a 2μm radius Al_2O_3 particle, n and k literature values.

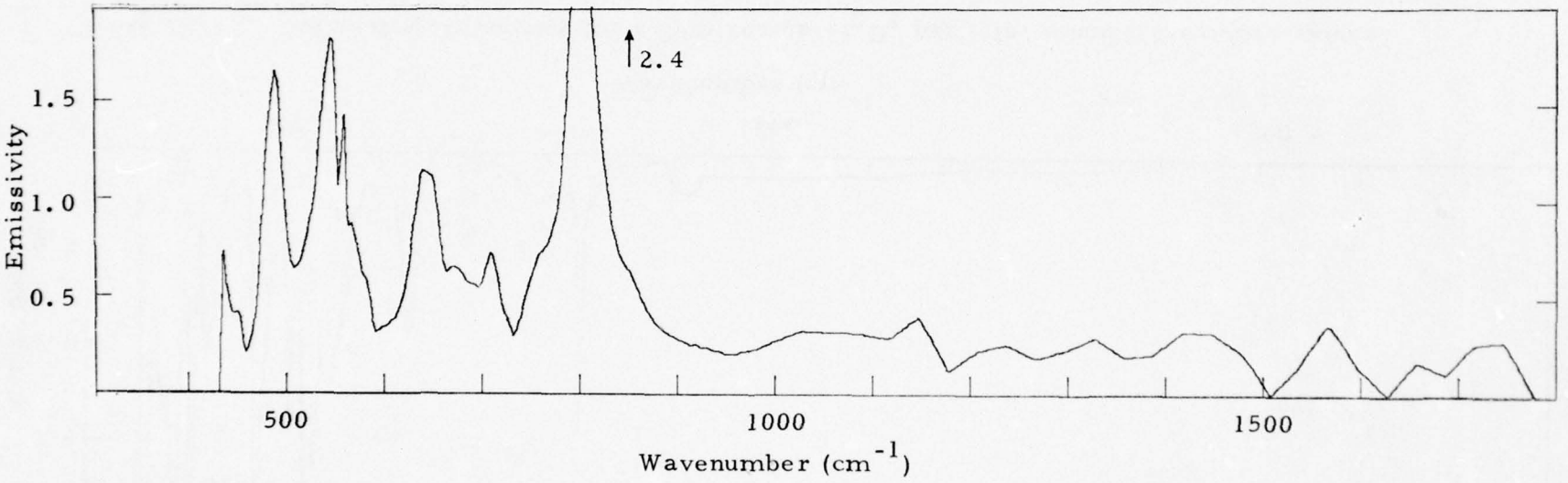

Figure III-16. Calculated emissivity for a 2μm radius Al_2O_3 particle, n and k present results.

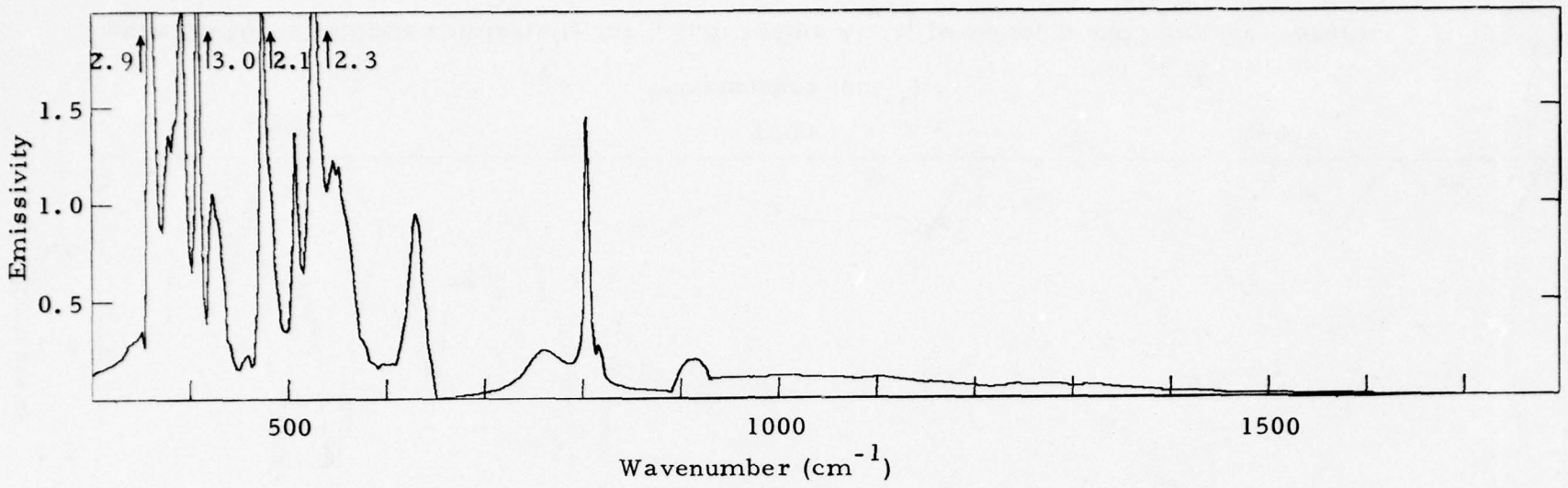

Figure III-17. Calculated emissivity for a 3μm radius Al_2O_3 particle, n and k literature values.

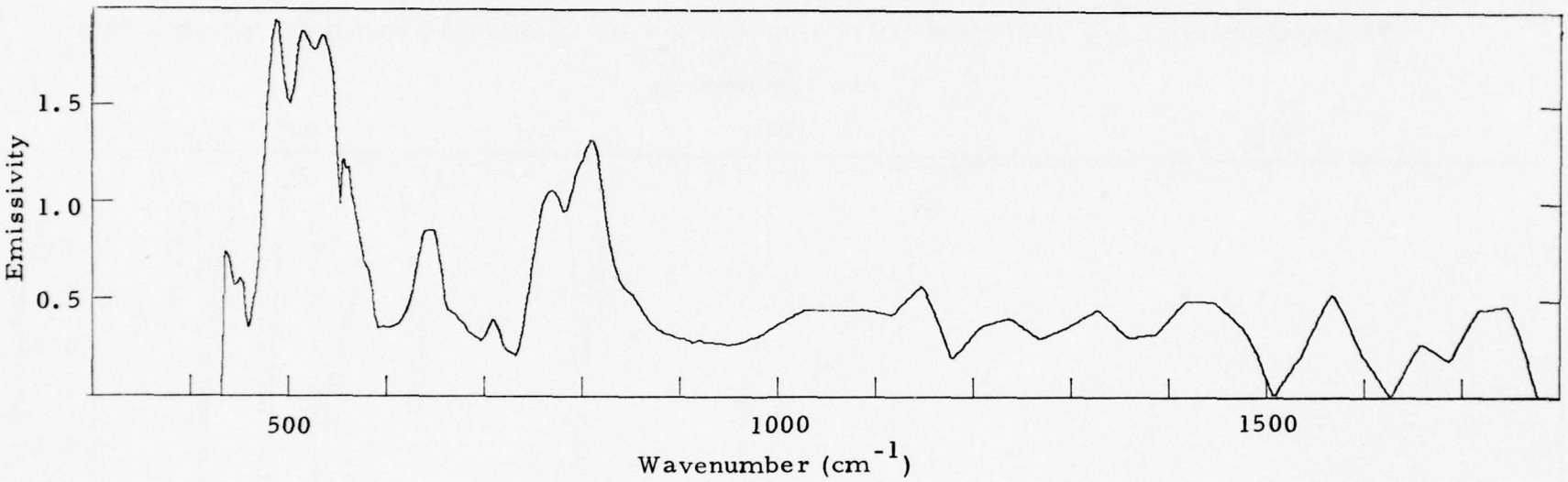

Figure III-18. Calculated emissivity for a 3μm radius Al_2O_3 particle, n and k present results.

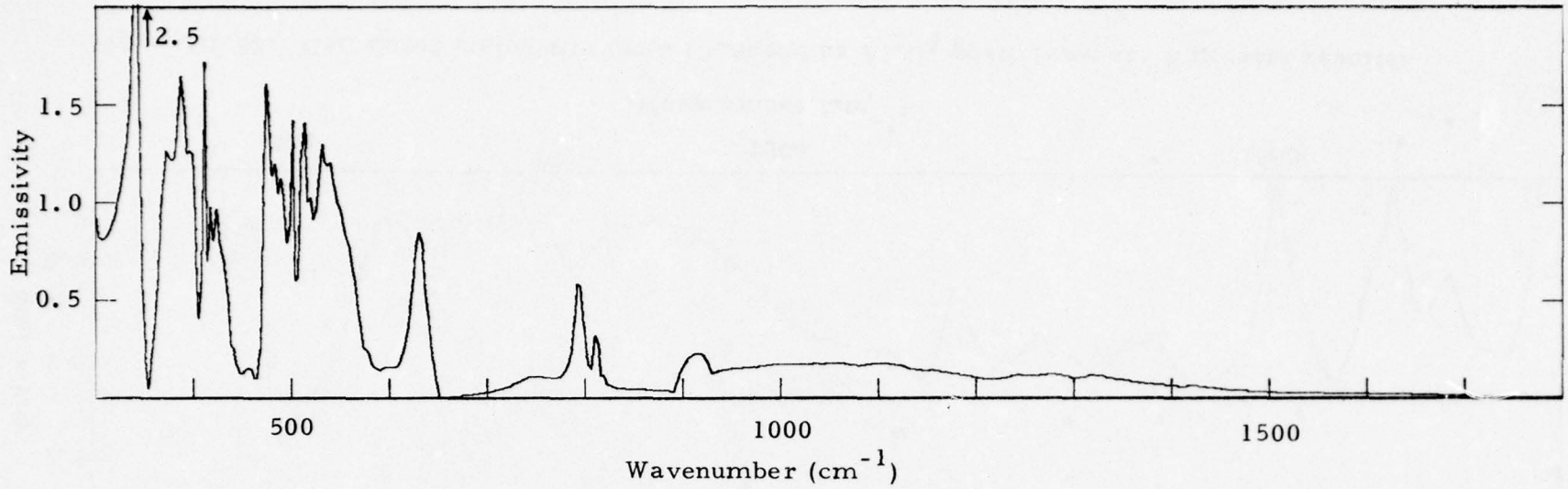

Figure III-19. Calculated emissivity for a 5μm radius Al_2O_3 particle, n and k literature values.

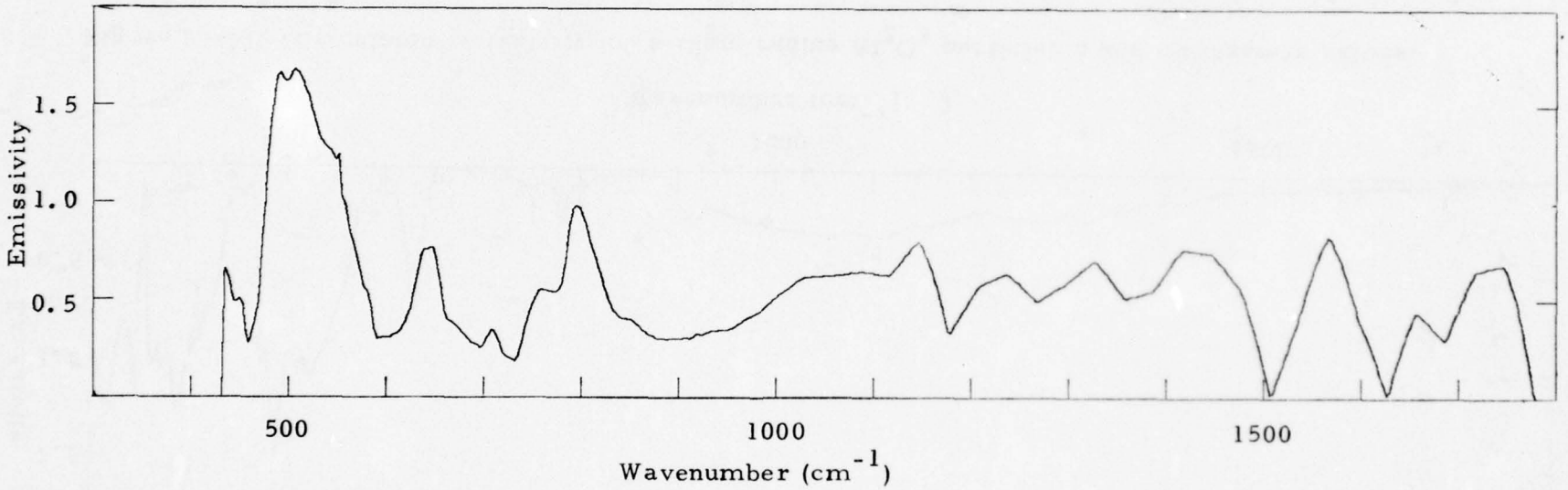

Figure III-20. Calculated emissivity for a 5μm radius Al_2O_3 particle, n and k present results.

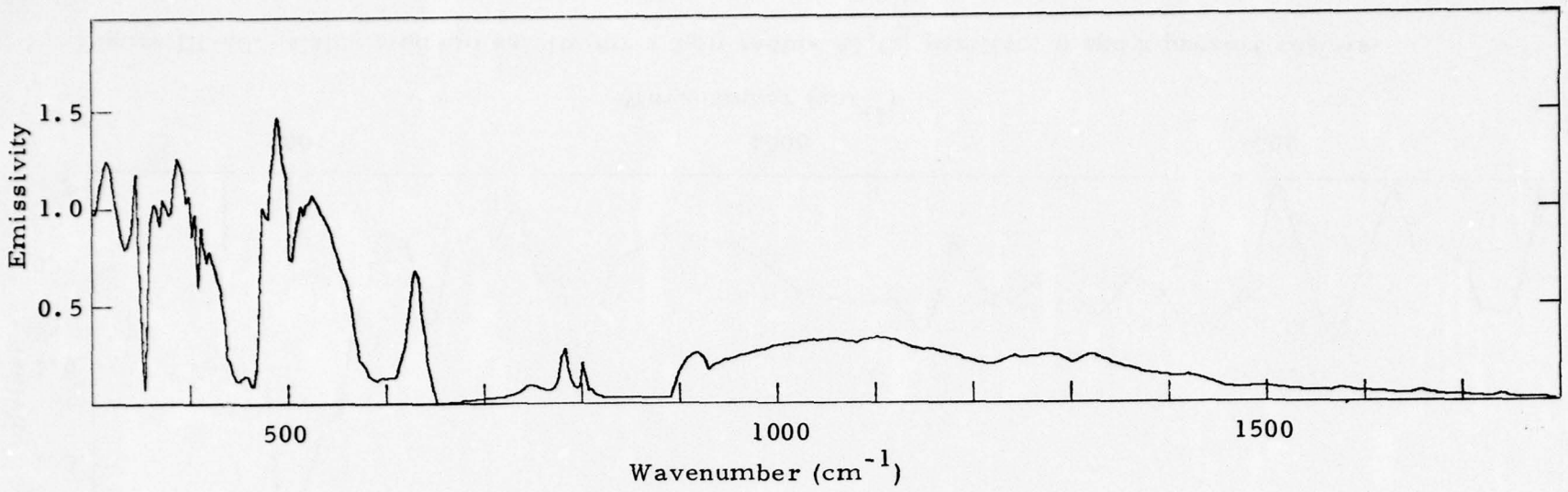

Figure III-21. Calculated emissivity for a 10μm radius Al_2O_3 particle, n and k literature values.

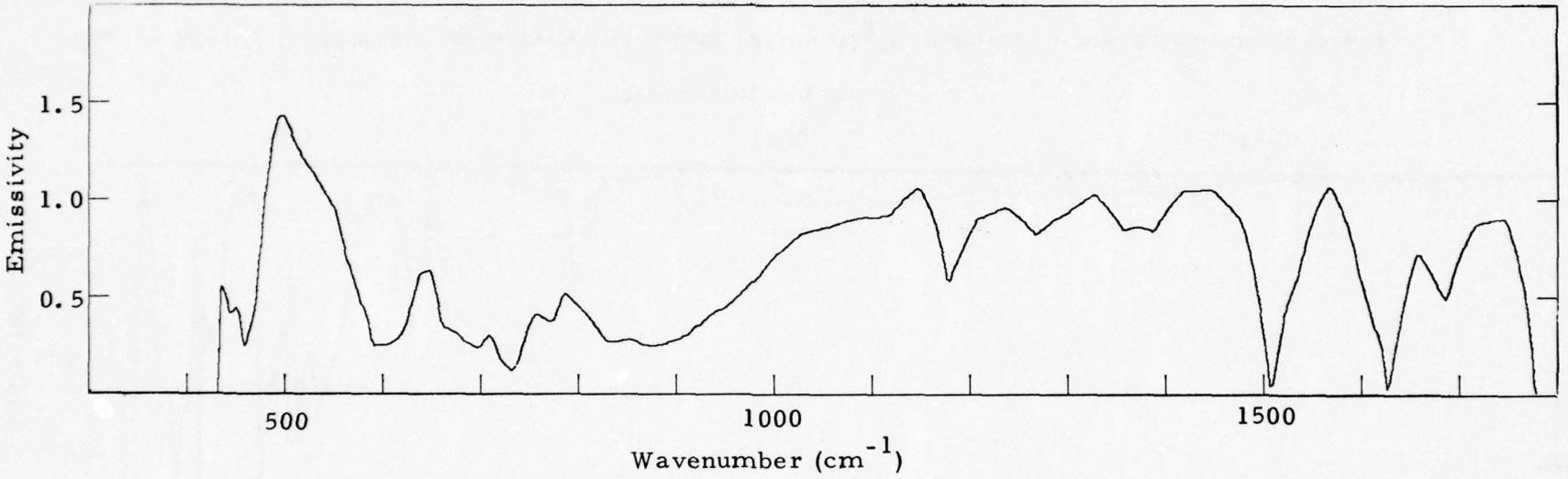

Figure III-22. Calculated emissivity for a 10μm radius Al_2O_3 particle, n and k present results.

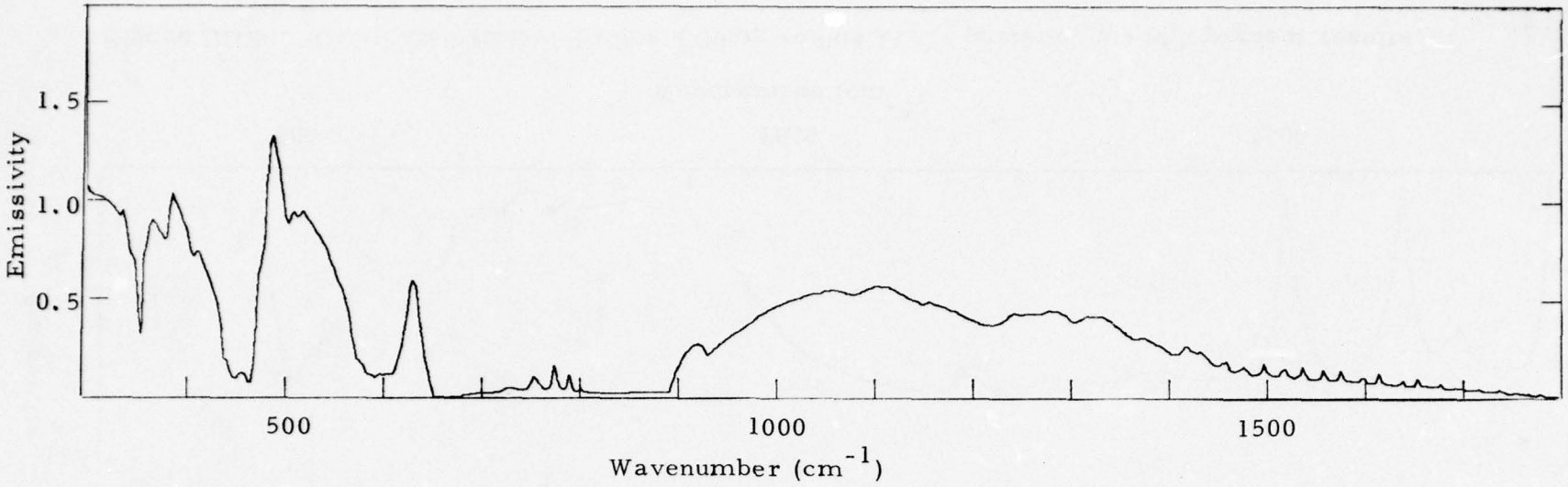

Figure III-23. Calculated emissivity for a 20μm radius Al_2O_3 particle, n and k literature values.

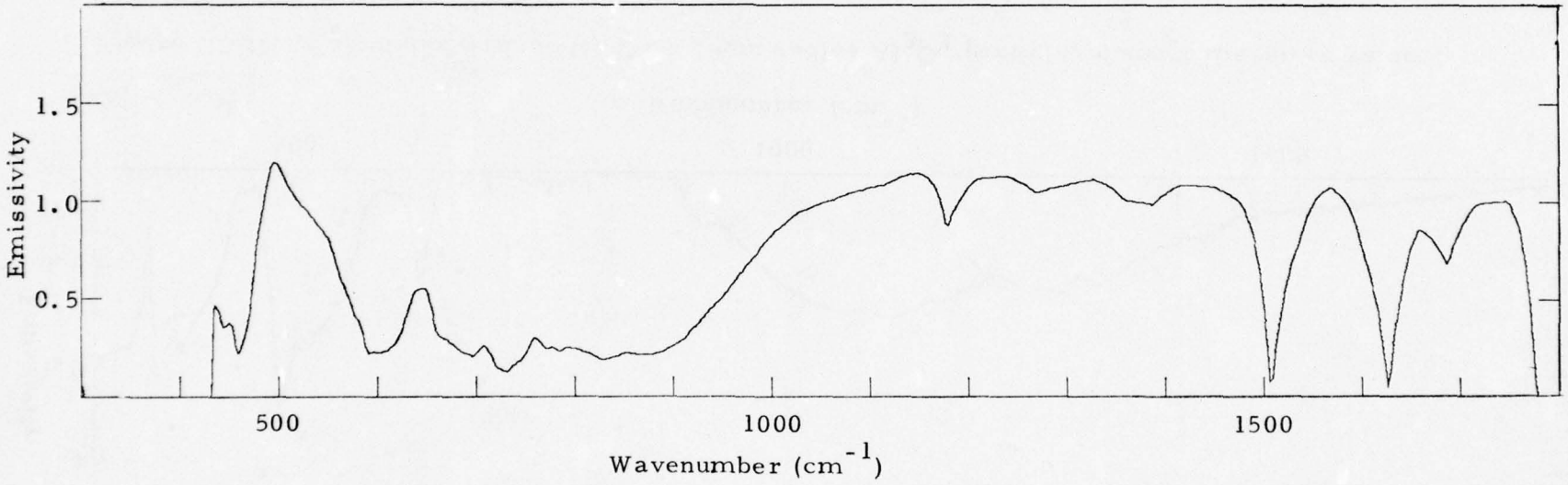

Figure III-24. Calculated emissivity for a 20μm radius Al_2O_3 particle, n and k present results.

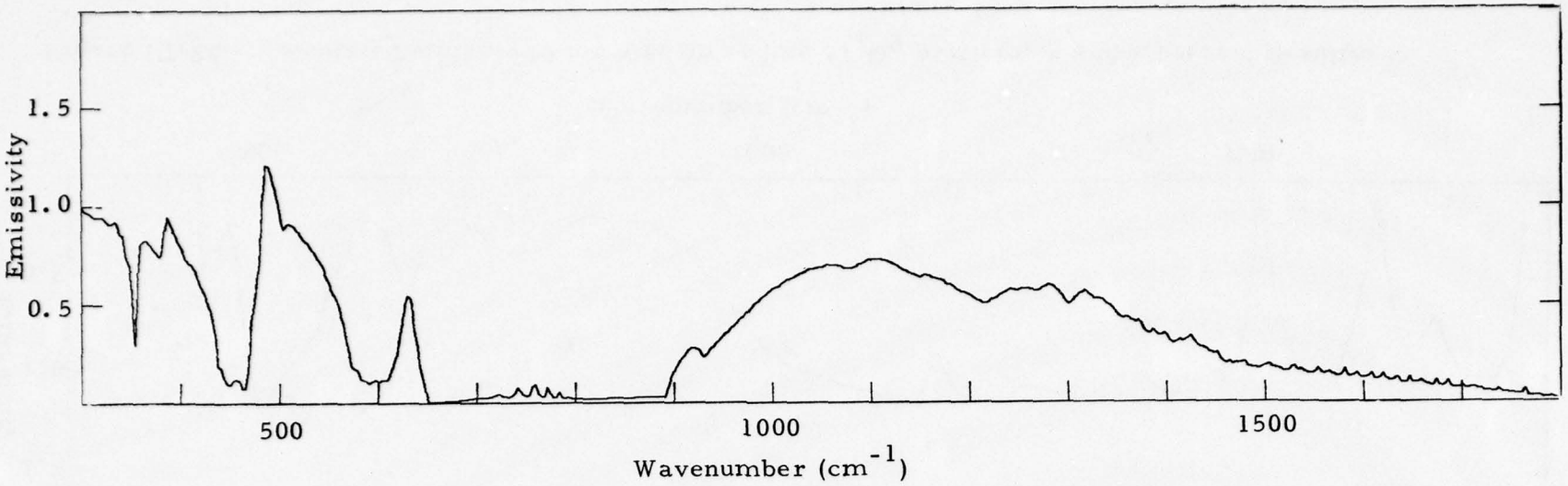

Figure III-25. Calculated emissivity for a 30μm radius Al_2O_3 particle, n and k literature values.

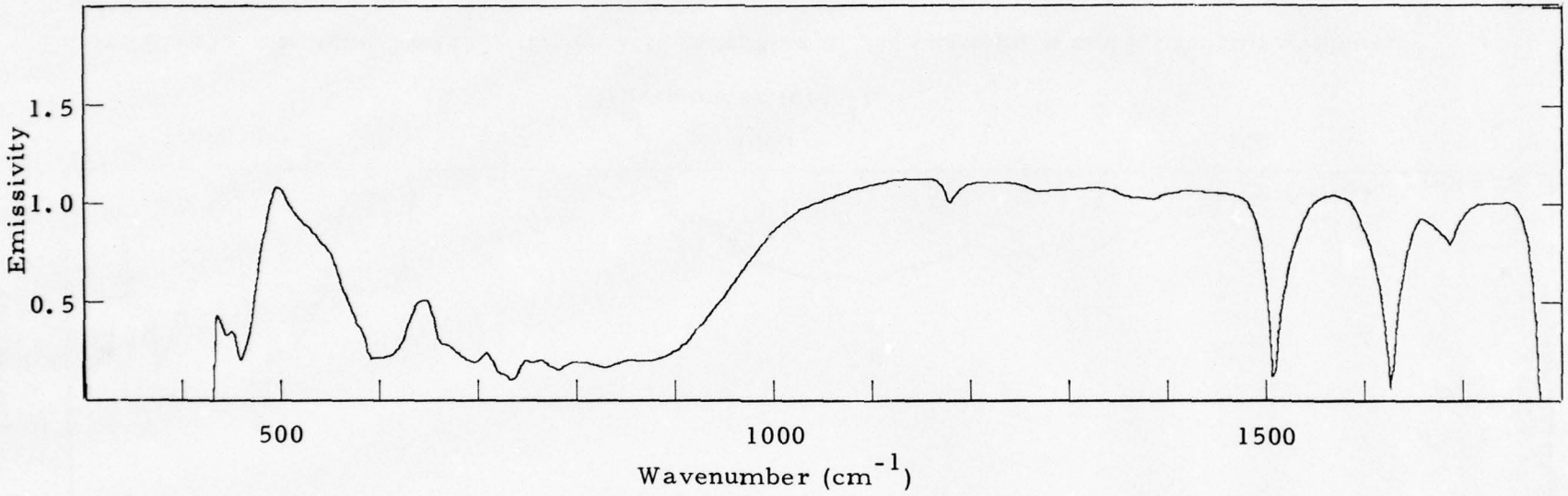

Figure III-26. Calculated emissivity for a 30μm radius Al_2O_3 particle, n and k present results.

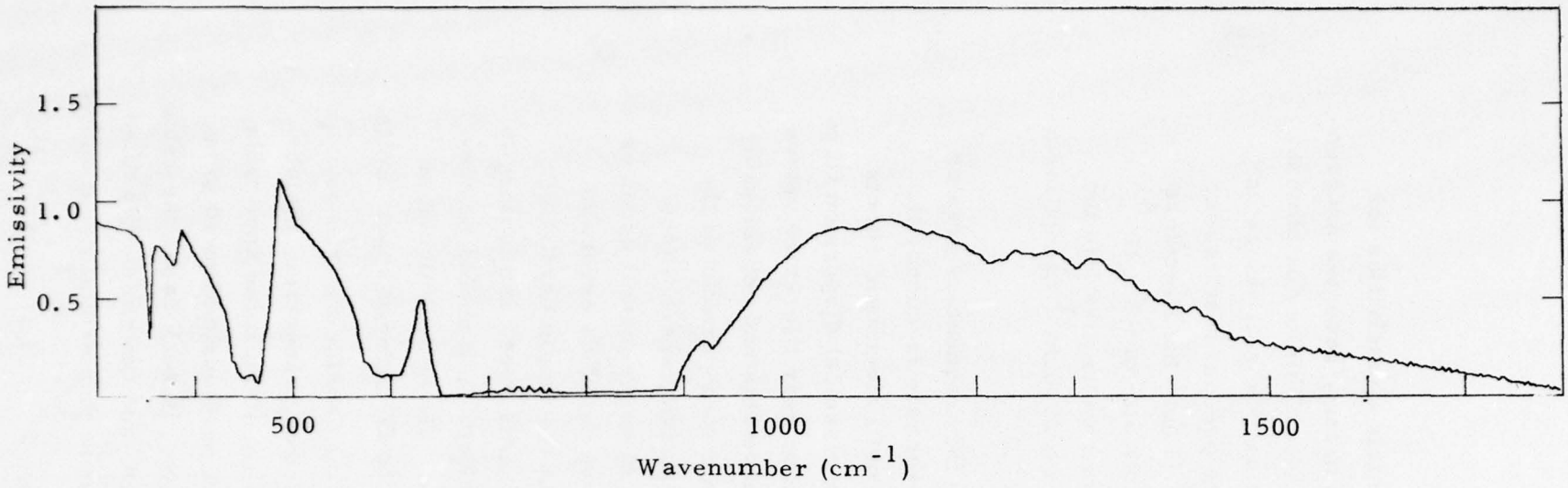

Figure III-27. Calculated emissivity for a 50μm radius Al_2O_3 particle, n and k literature values.

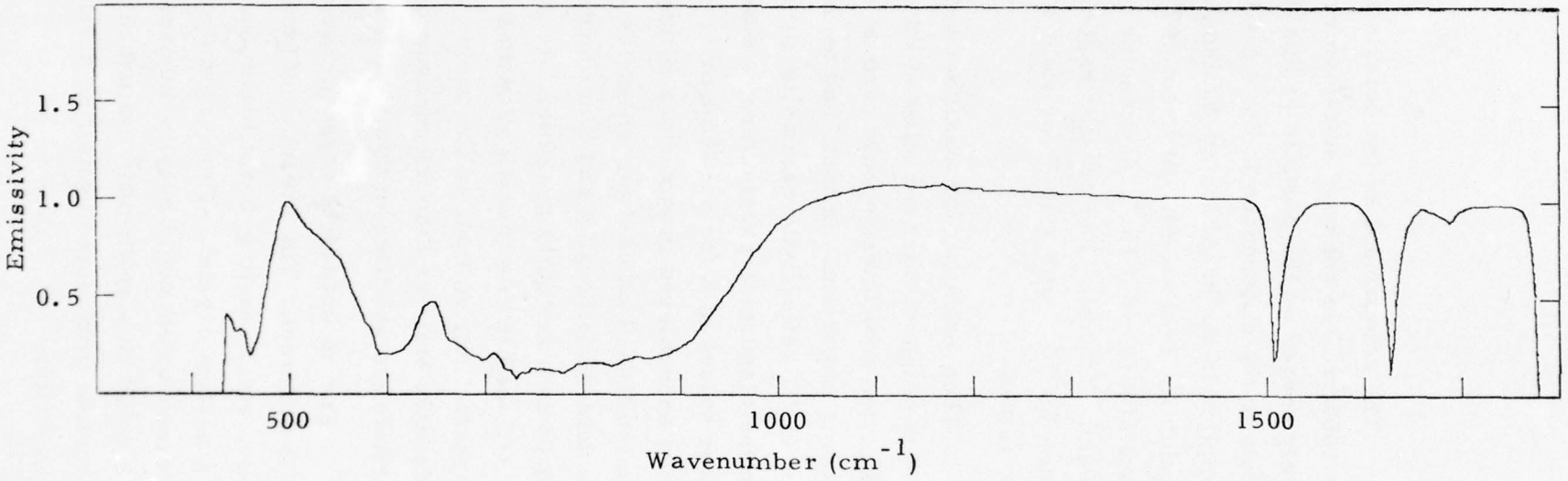

Figure III-28. Calculated emissivity for a 50μm radius Al_2O_3 particle, n and k present results.

The comparison of the calculated particle emissivities for $\nu > 1000\text{cm}^{-1}$ is not very satisfactory, and in fact, becomes progressively poorer as the particle radius increases. This is due almost solely to the differences in the k (extinction coefficient) values as compiled in the handbook by Whitson and the present results (see Section II, Table II-6). At about 1000cm^{-1} (10μm) the literature value of k is $\sim 3 \times 10^{-2}$, decreasing monotonically to $\sim 3 \times 10^{-6}$ 2000cm^{-1} (5μm). The present experimental results give k in the range 1×10^{-2} to 5×10^{-2} for $1000\text{cm}^{-1} \leq \nu \leq 2000\text{cm}^{-1}$ except for a few values.

Theoretically, for a perfect crystal, for frequencies greater than the highest infrared allowed lattice resonance frequency the extinction coefficient should become small until electronic effects become important. In fact, had we made a classical dispersion fit to our Al_2O_3 reflectivity data using literature or near literature values for the dispersion parameters, we would have obtained considerably lower values of k for $\nu > 1000\text{cm}^{-1}$. From a consideration of the noise encountered in our experimental reflectivity spectra (see Section II-C.1 on carbon, where the effect of experimental error on the determination of n and k is discussed) we conclude errors of ~ 0.05 in k are quite possible. We feel that the single crystal of Al_2O_3 used in this investigation was sufficiently pure, and lacking in imperfection, so that, in the region $\nu > 1000\text{cm}^{-1}$, k should be considerably smaller than the measured value. Thus, the calculated particle emissivities in this region should be considered upper limits.

For an imperfect crystal, however, the conclusions can be quite different. The presence of impurity sites, vacancies, dislocations, etc., can in general break down the selection rules applicable to a perfect crystal. Thus, resonances not previously allowed to be infrared active could become infrared active. In such cases the value of k could be significantly perturbed upward, and the emissivity of an spherical imperfect crystalline particle would then exhibit much higher emissivity.

Figure III-29 is a plot of the emissivity of Al_2O_3 which was calculated using the simple formula shown in equation III-20, and the literature values for n and k. This plot should be compared to Figure III-27 which was calculated using exact Mie theory for a particle of radius 50μm. It is apparent that this simple limiting formula has reproduced the complicated shape of the emissivity quite well in the region of frequency less than $1000cm^{-1}$. The only feature it failed to reproduce is the sharp minimum at about $350cm^{-1}$, however, this is at a wavelength of the same order as the particle size and so the simple formula is not expected to be valid. Mie theory will predict zero emissivity if the extinction coefficient, k, is zero whereas the simple formula can predict a finite emissivity. This will only cause difficulty when k is zero or extremely small and is the reason the emissivity falls off at high frequency in Figure III-27 and does not in Figure III-29. Keeping in mind its limitations, equation III-20 is an extremely useful formula, adding physical insight and enabling one to do "back of the envelope" calculations.

For completeness, particle emissivity calculations for spherical particles ($0.5\mu m \leq r \leq 50\mu m$ range) were carried out for Al_2O_3 ($T = 678^\circ K$), MgO ($T = 300^\circ K$ and $573^\circ K$), and ZrO_2 ($T = 300^\circ K$ and $573^\circ K$).

The results for Al_2O_3 ($T = 678^\circ K$) are shown in Figures III-30 through III-38. The results are seen to be quite different than obtained from the $T = 300^\circ K$ data, and reflect the changes in n and k deduced from the reflectivity spectrum measured at $T = 300^\circ K$ and $678^\circ K$.

The calculated emissivities for spherical particles ($0.5\mu m \leq r \leq 50\mu m$ range) of MgO are shown in Figures III-39 through III-47 for $T = 300^\circ K$, and Figures III-48 through III-56 for $T = 573^\circ K$. The MgO emissivity spectra are much simpler than those calculated for Al_2O_3. This is because the MgO crystal structure is much simpler than the Al_2O_3 crystal structure.

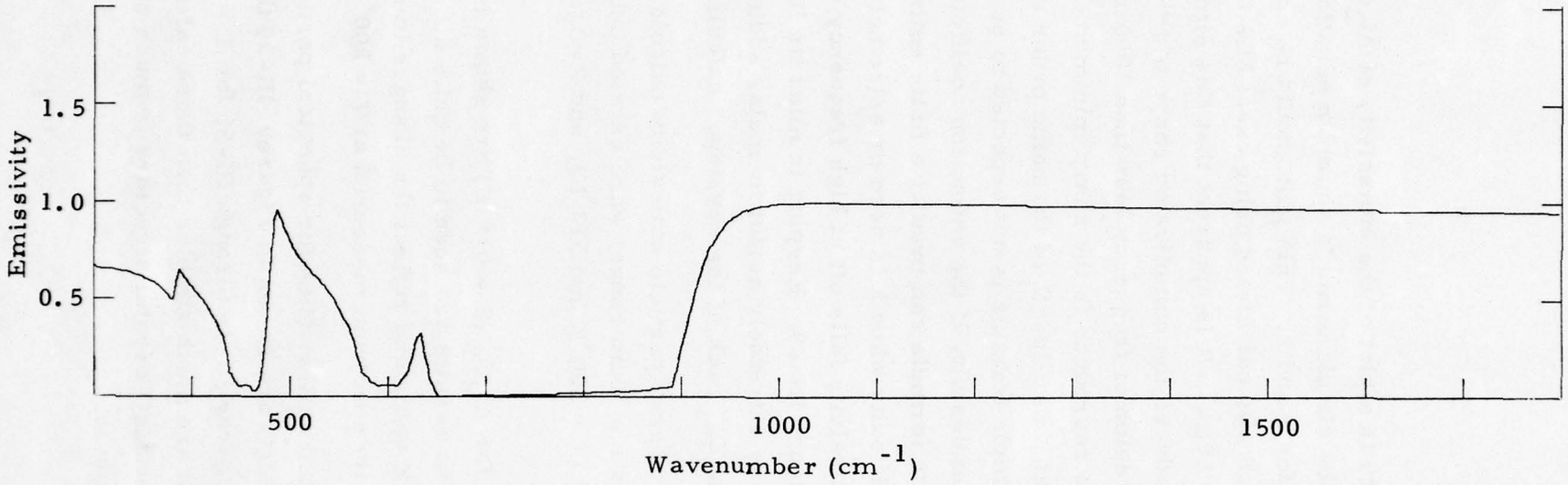

Figure III-29. Calculated emissivity of an infinitely thick sample of Al_2O_3 using the data from Ref. III-5 and formula represented by equation III-20.

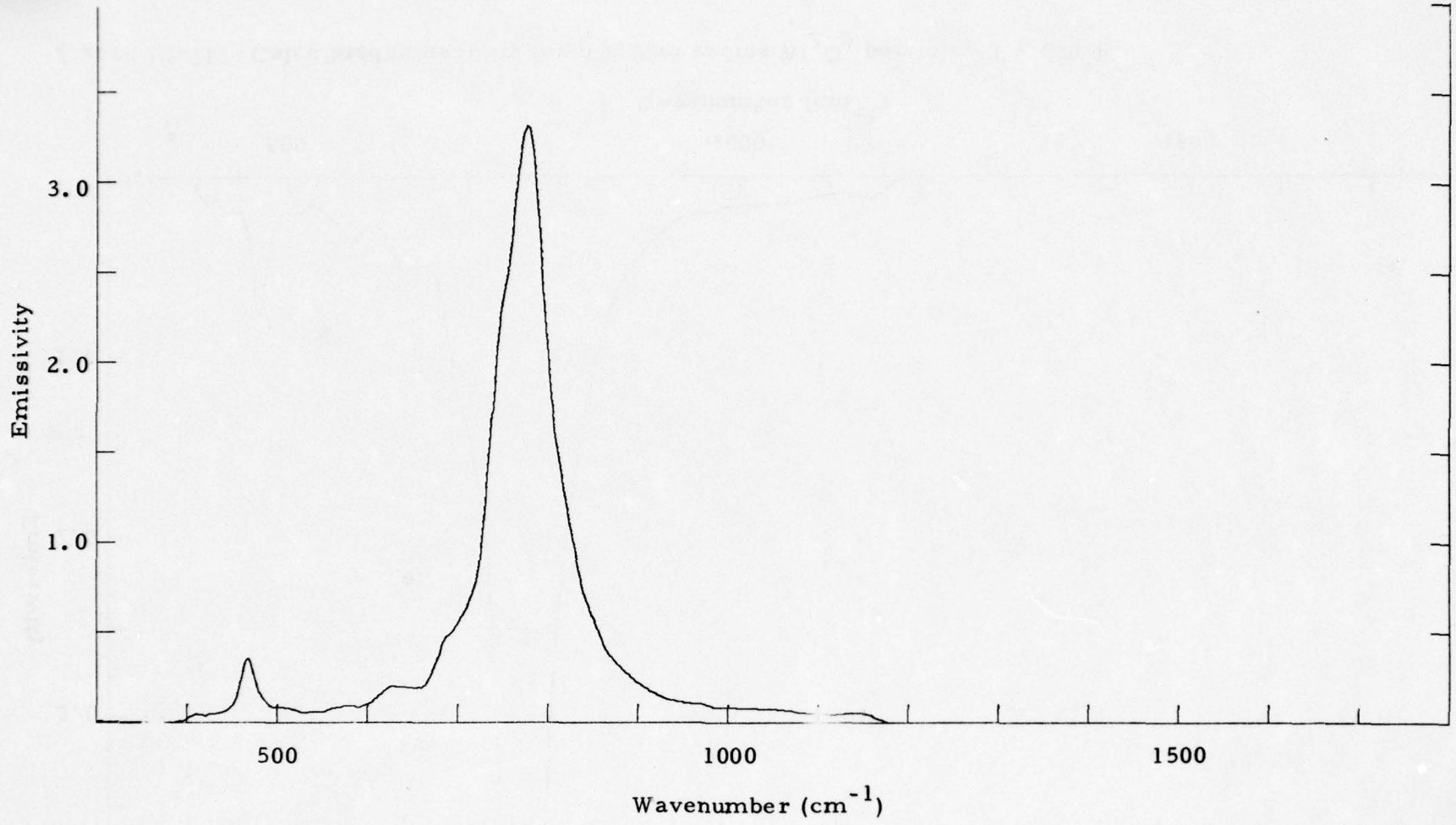

Figure III-30. Calculated emissivity for a 0.5μm radius Al_2O_3 particle, T = 678°K.

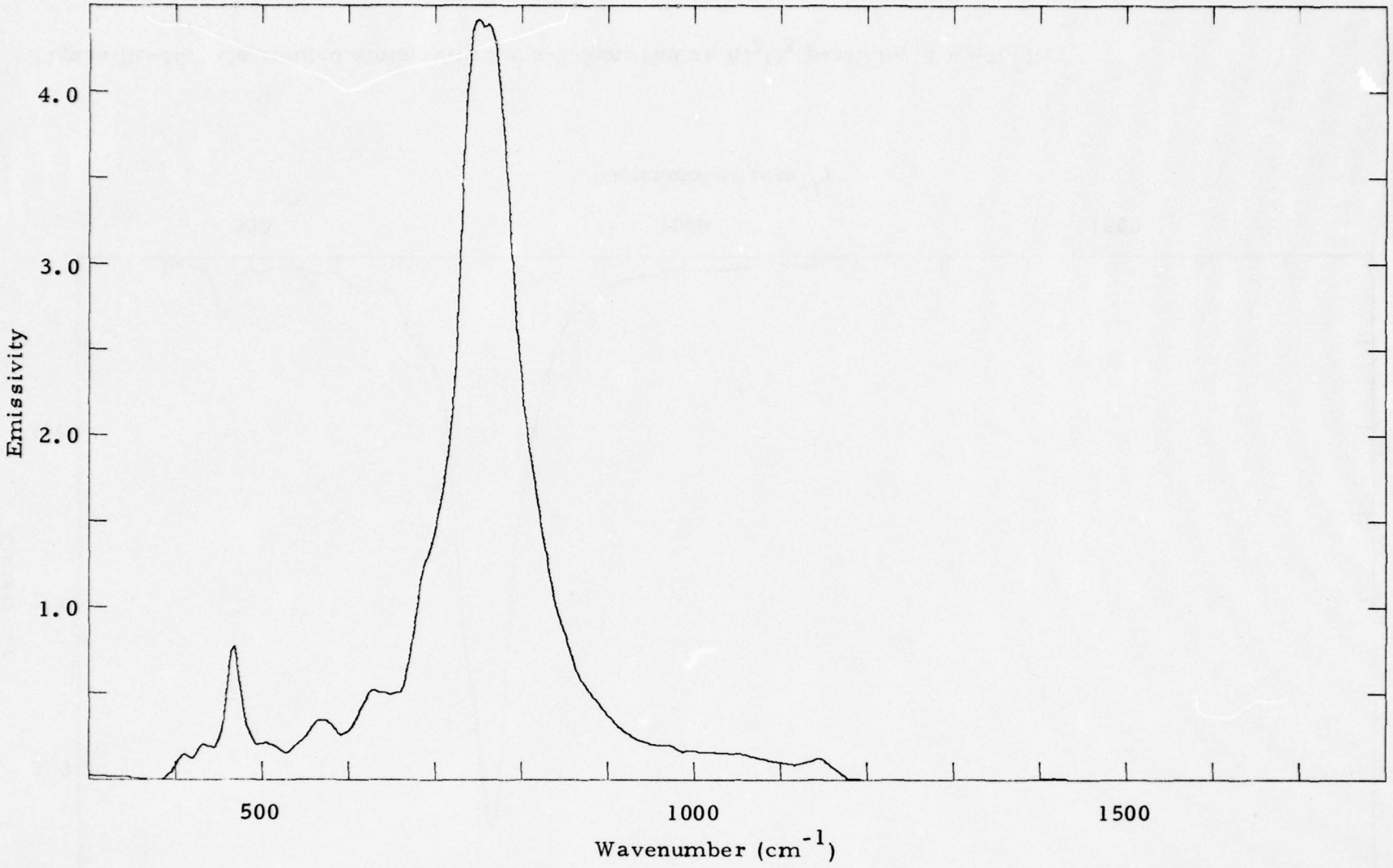

Figure III-31. Calculated emissivity for a 1.0μm radius Al_2O_3 particle, T = 678°K.

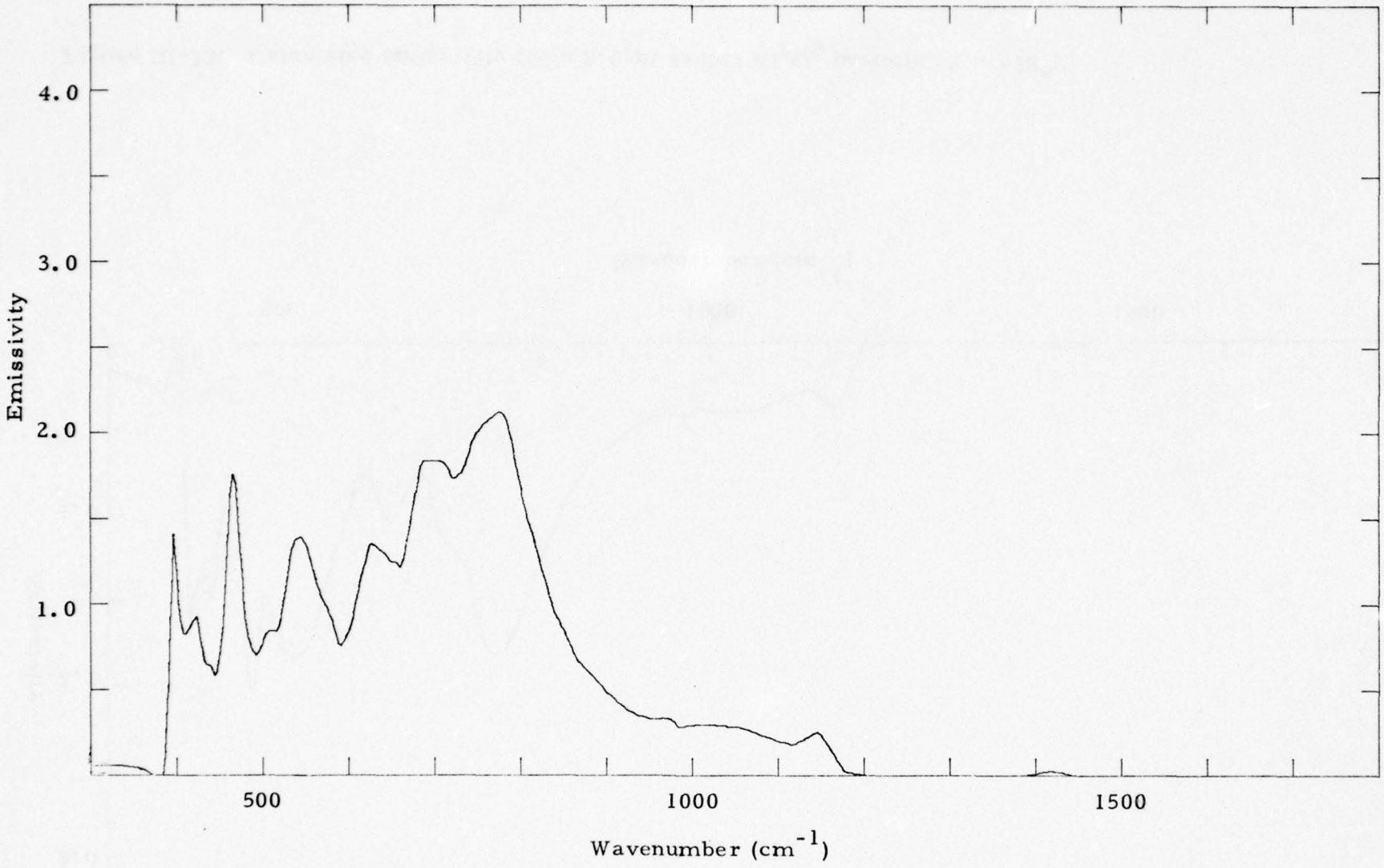

Figure III-32. Calculated emissivity for a 2.0μm radius Al_2O_3 particle, T = 678 °K.

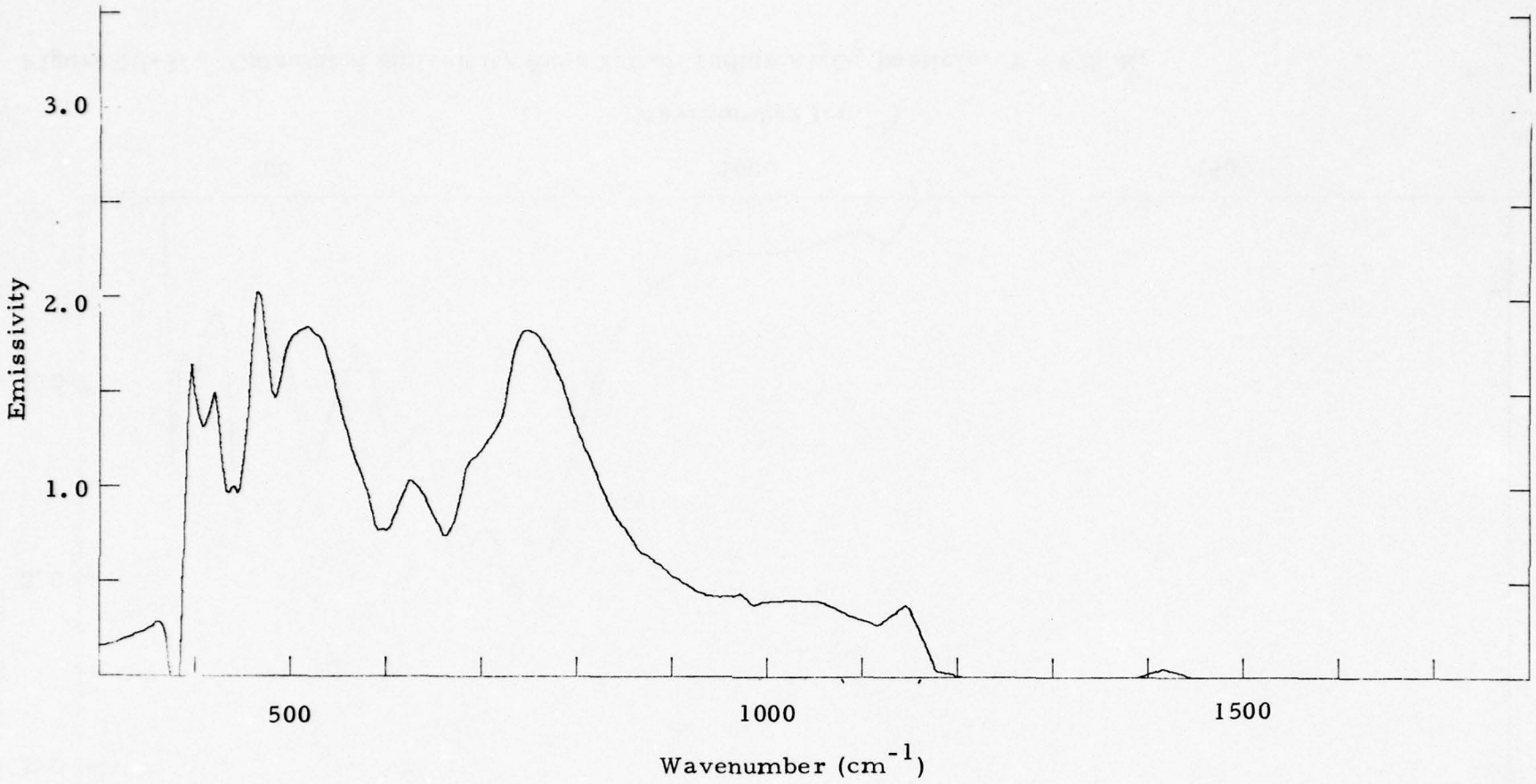

Figure III-33. Calculated emissivity for a 3.0μm radius Al_2O_3 particle, T = 678°K.

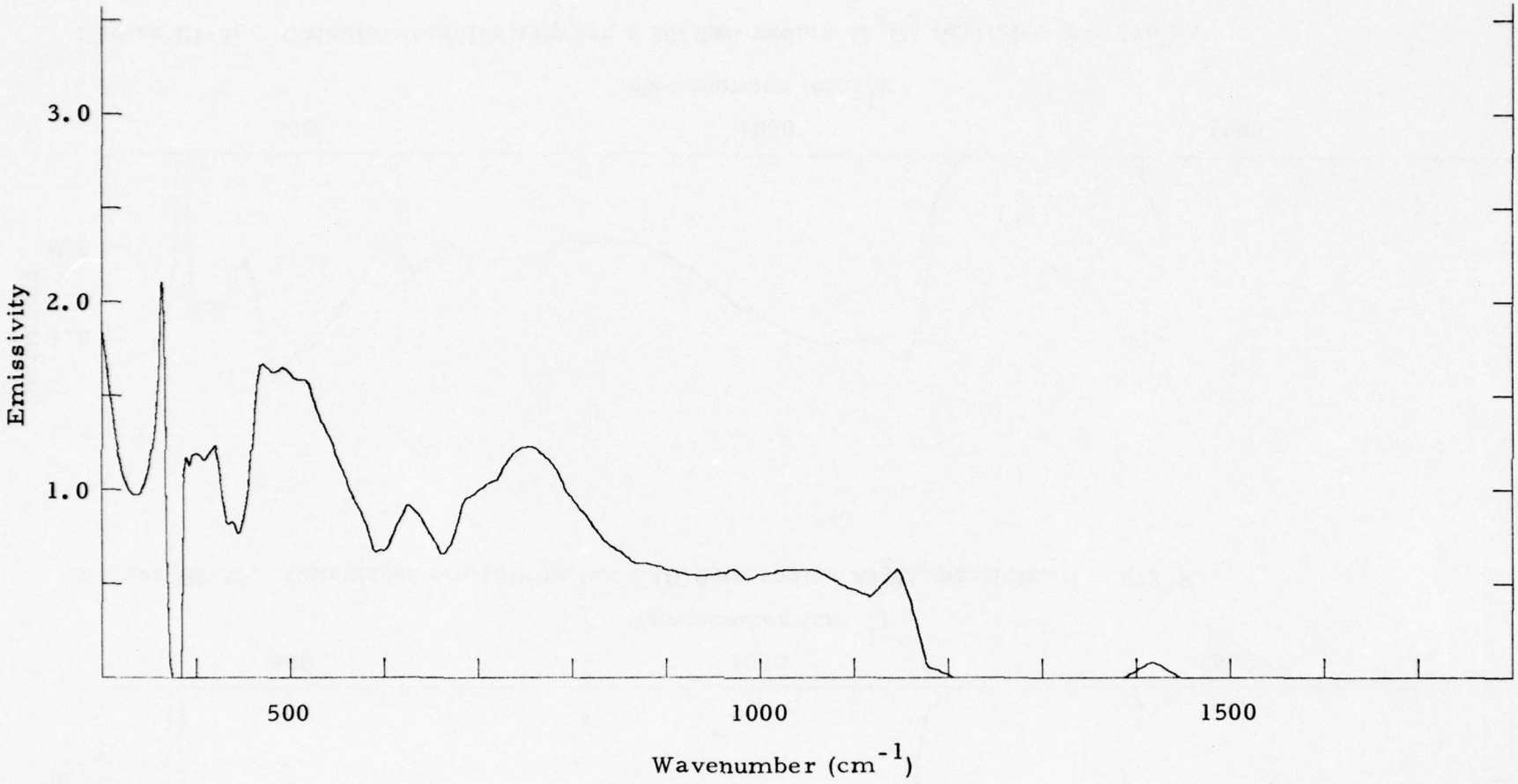

Figure III-34. Calculated emissivity for a 5.0μm radius Al_2O_3 particle, T = 678 °K.

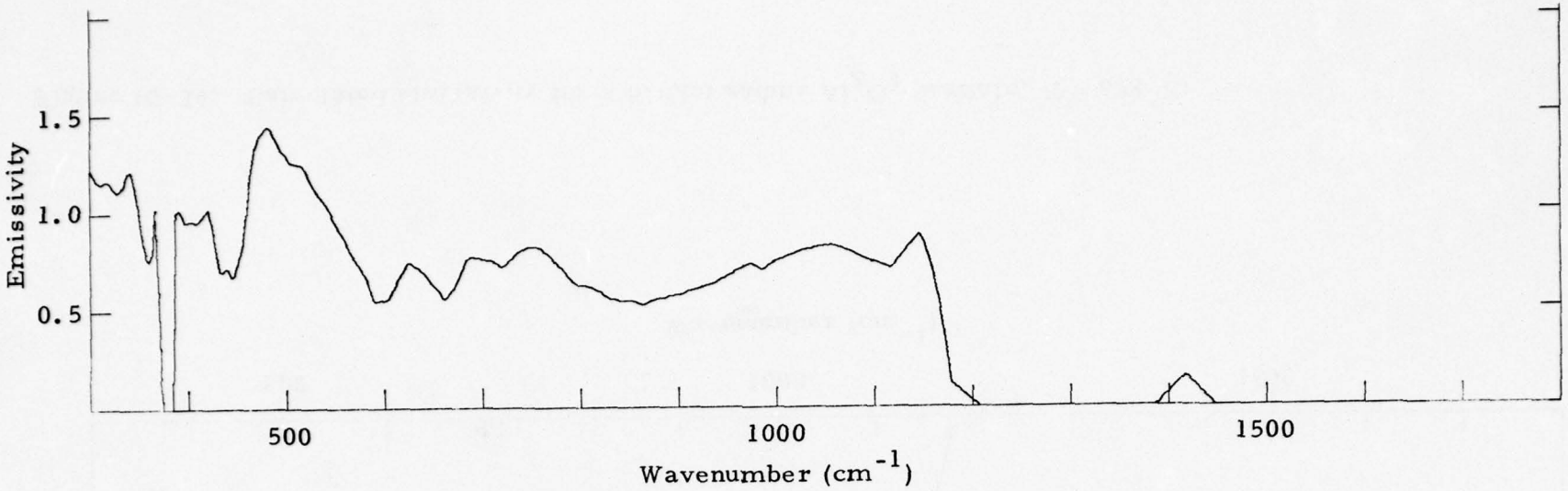

Figure III-35. Calculated emissivity for a 10.0μm radius Al_2O_3 particle, T = 678°K.

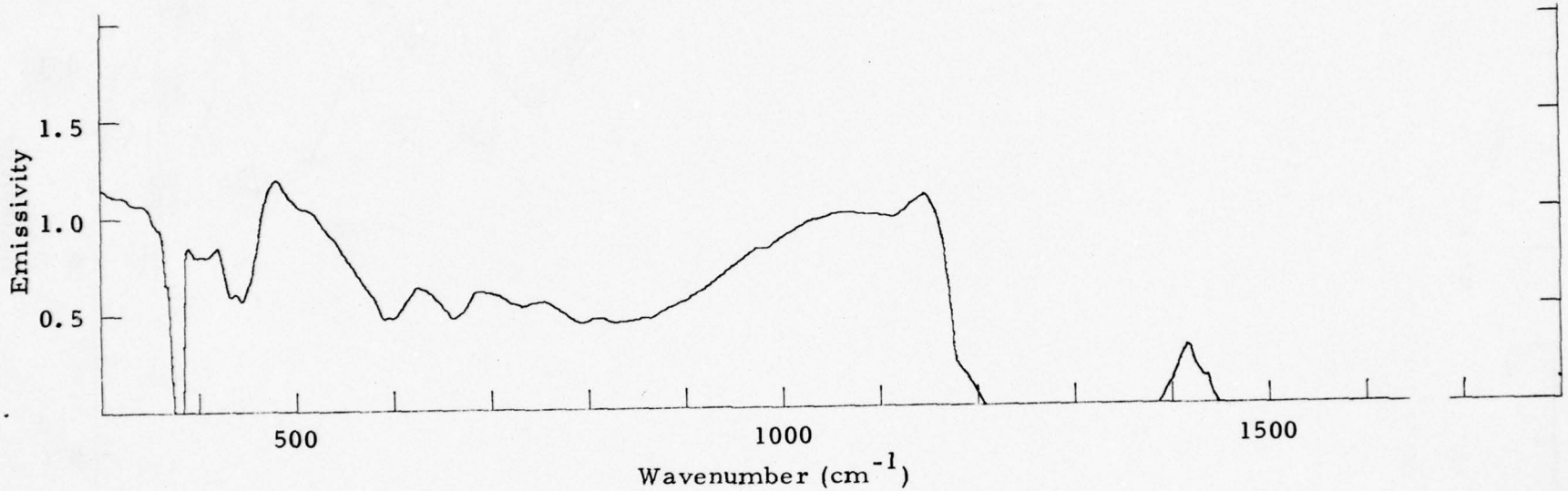

Figure III-36. Calculated emissivity for a 20.0μm radius Al_2O_3 particle, T = 678°K.

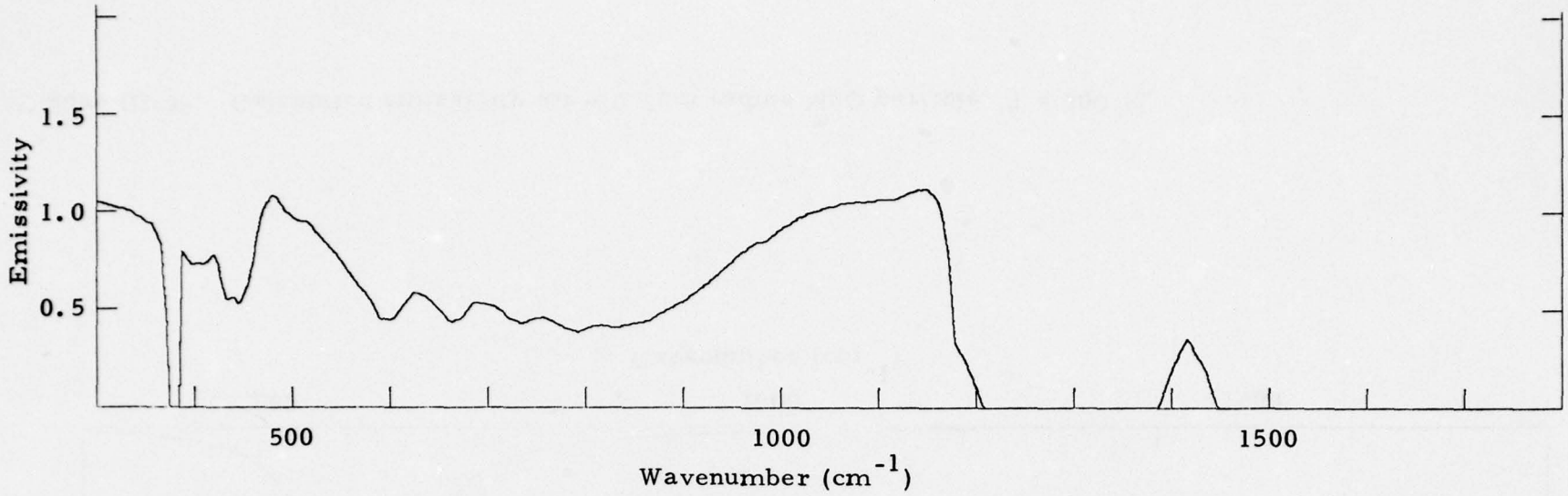

Figure III-37. Calculated emissivity for a 30.0μm radius Al_2O_3 particle, T = 678 °K.

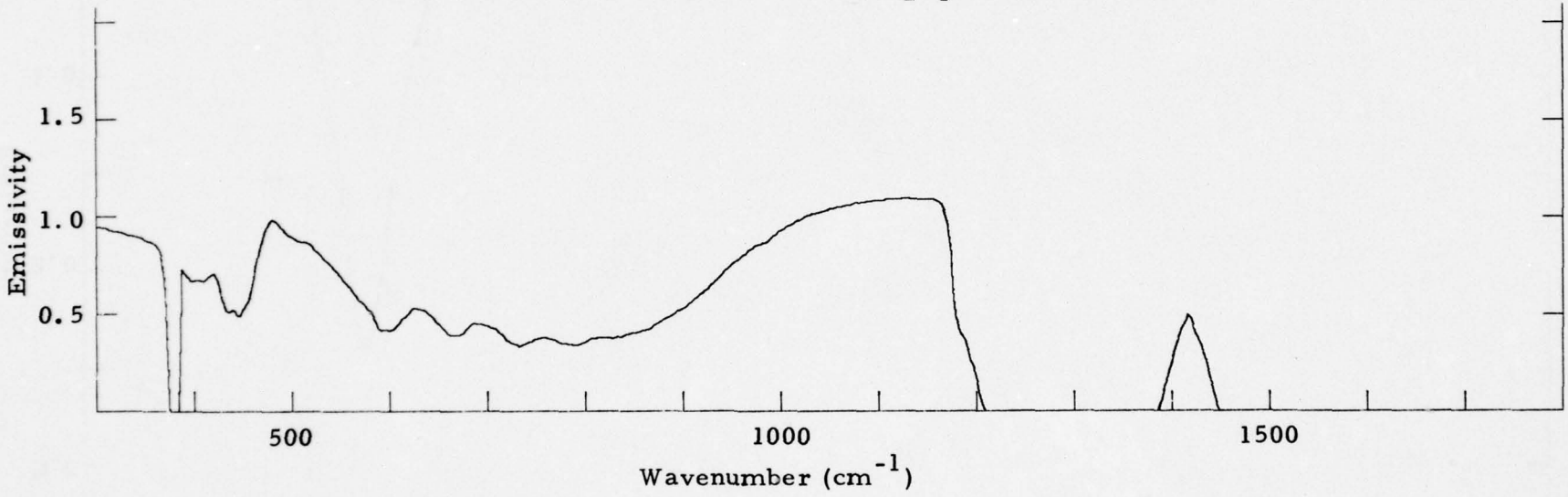

Figure III-38. Calculated emissivity for a 50.0μm radius Al_2O_3 particle, T = 678 °K.

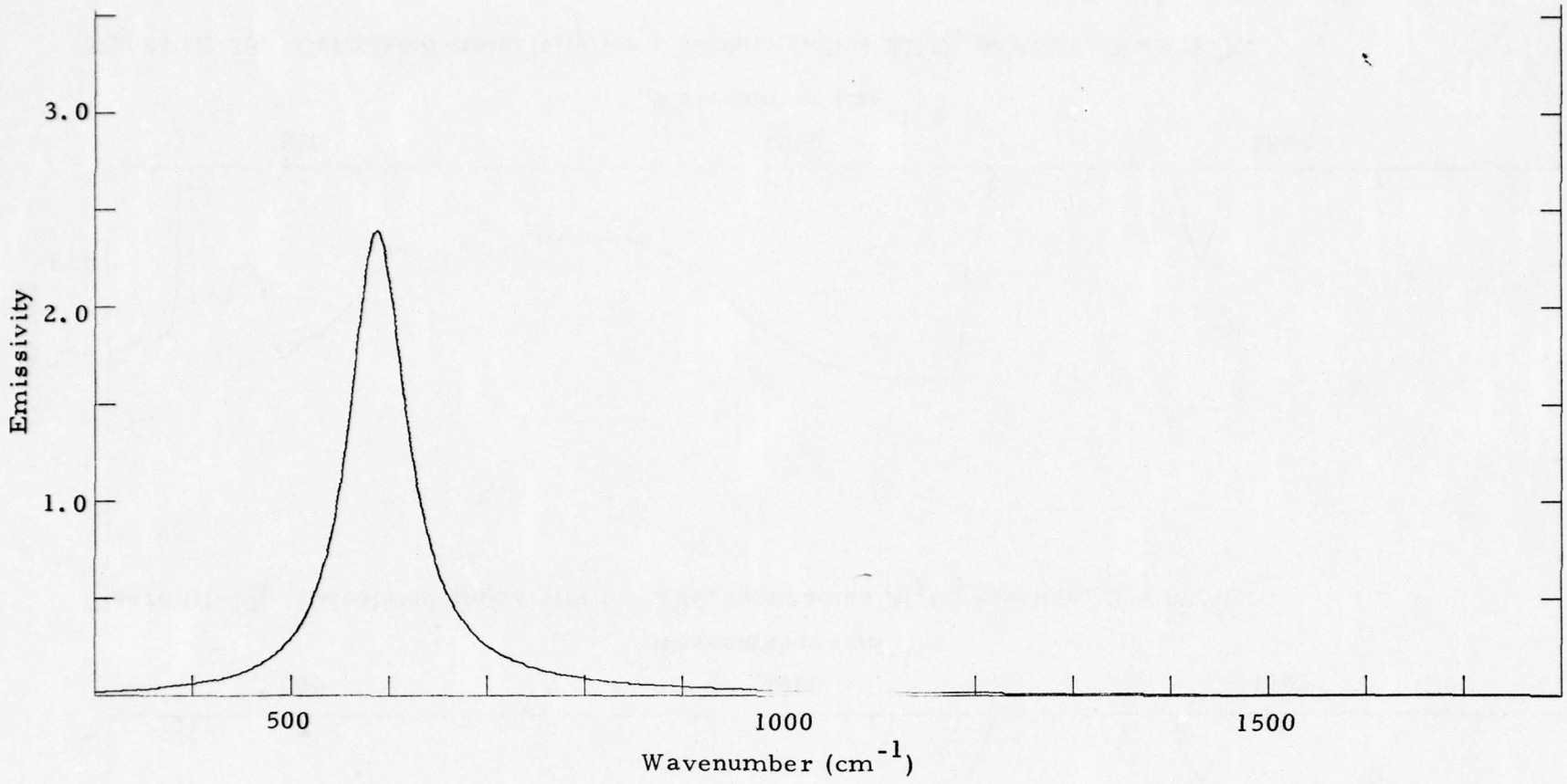

Figure III-39. Calculated emissivity for a 0.5μm radius MgO particle, T = 300°K.

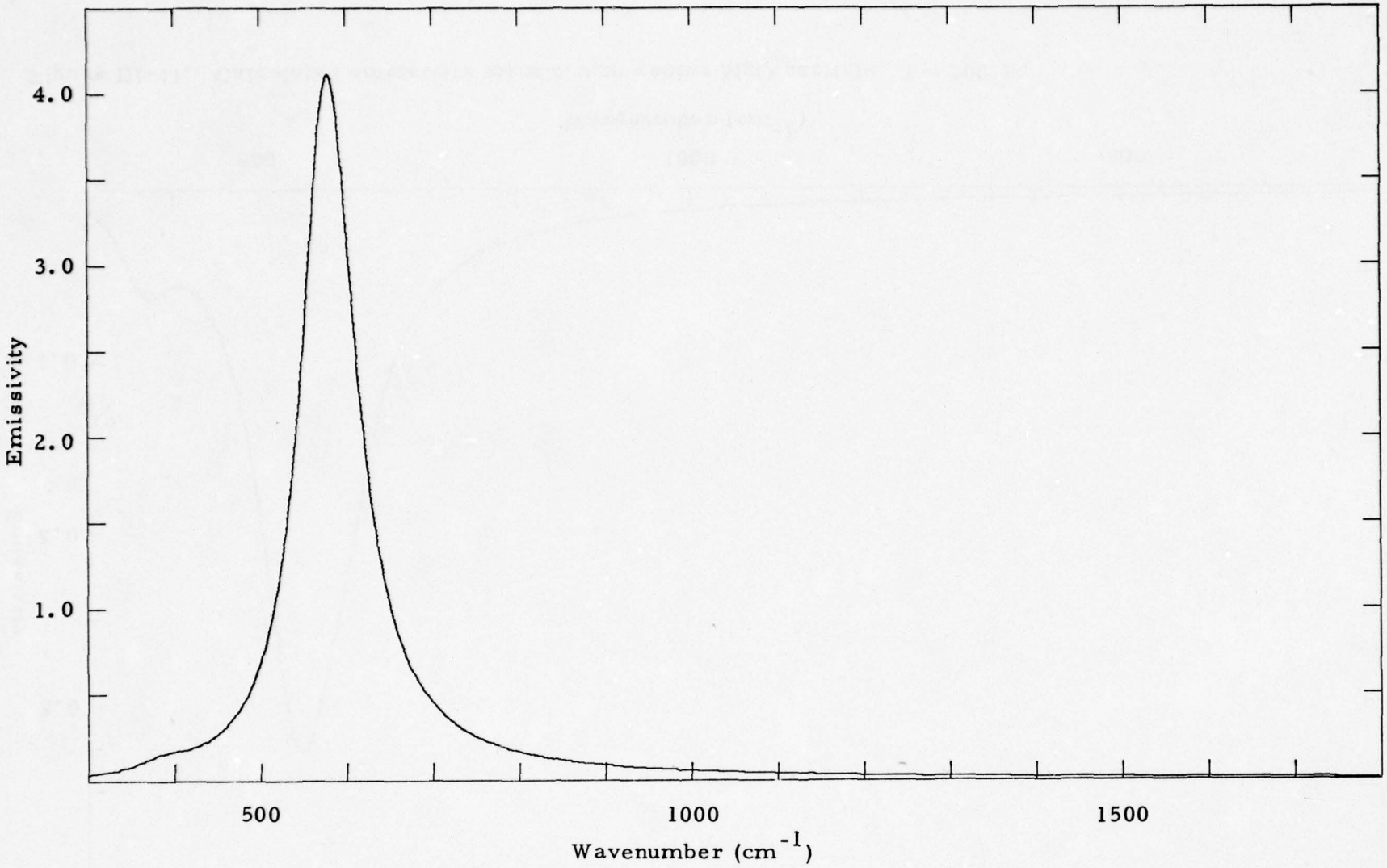

Figure III-40. Calculated emissivity for a 1.0μm radius MgO particle, T = 300°K.

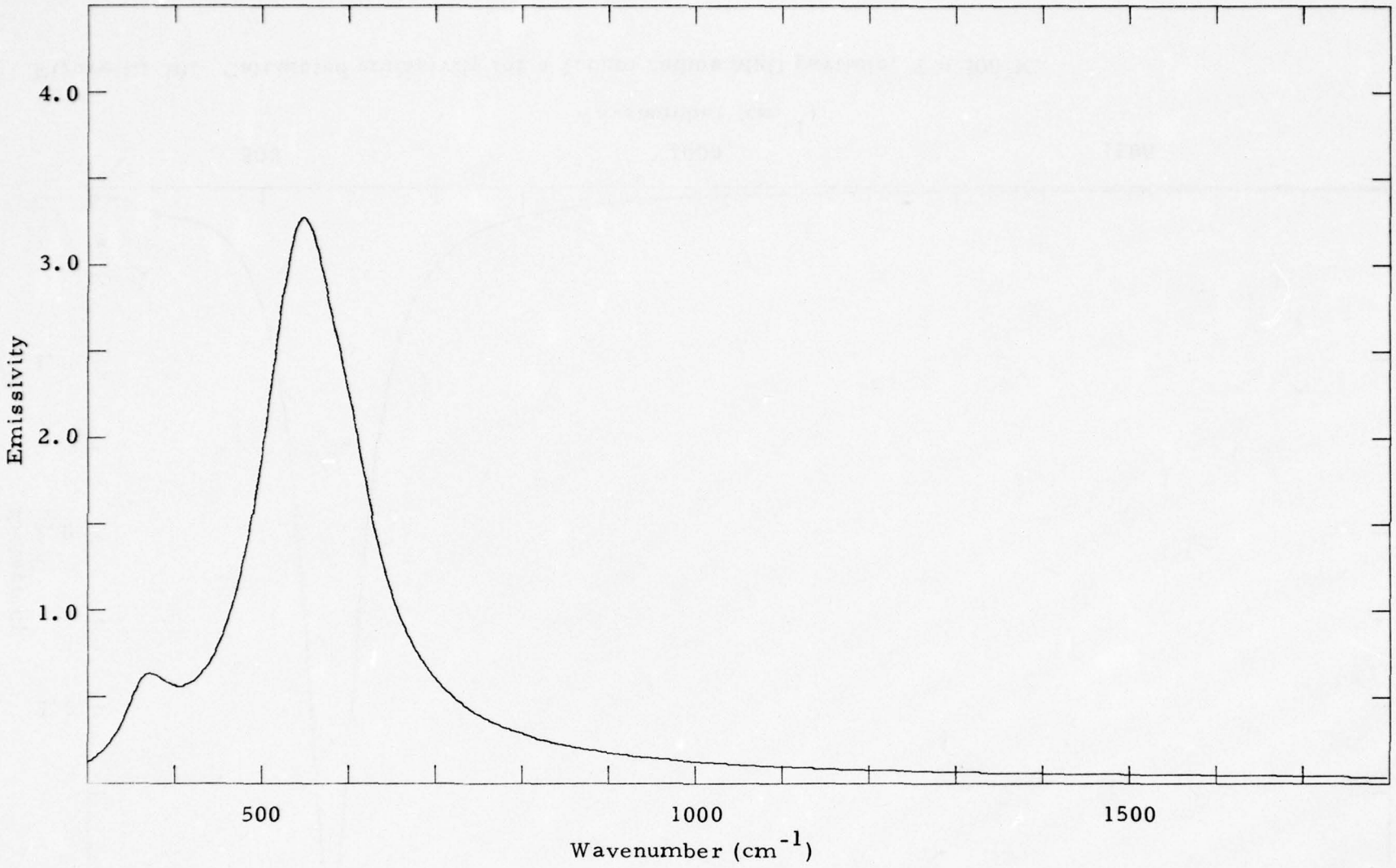

Figure III-41. Calculated emissivity for a 2.0μm radius MgO particle, T = 300°K.

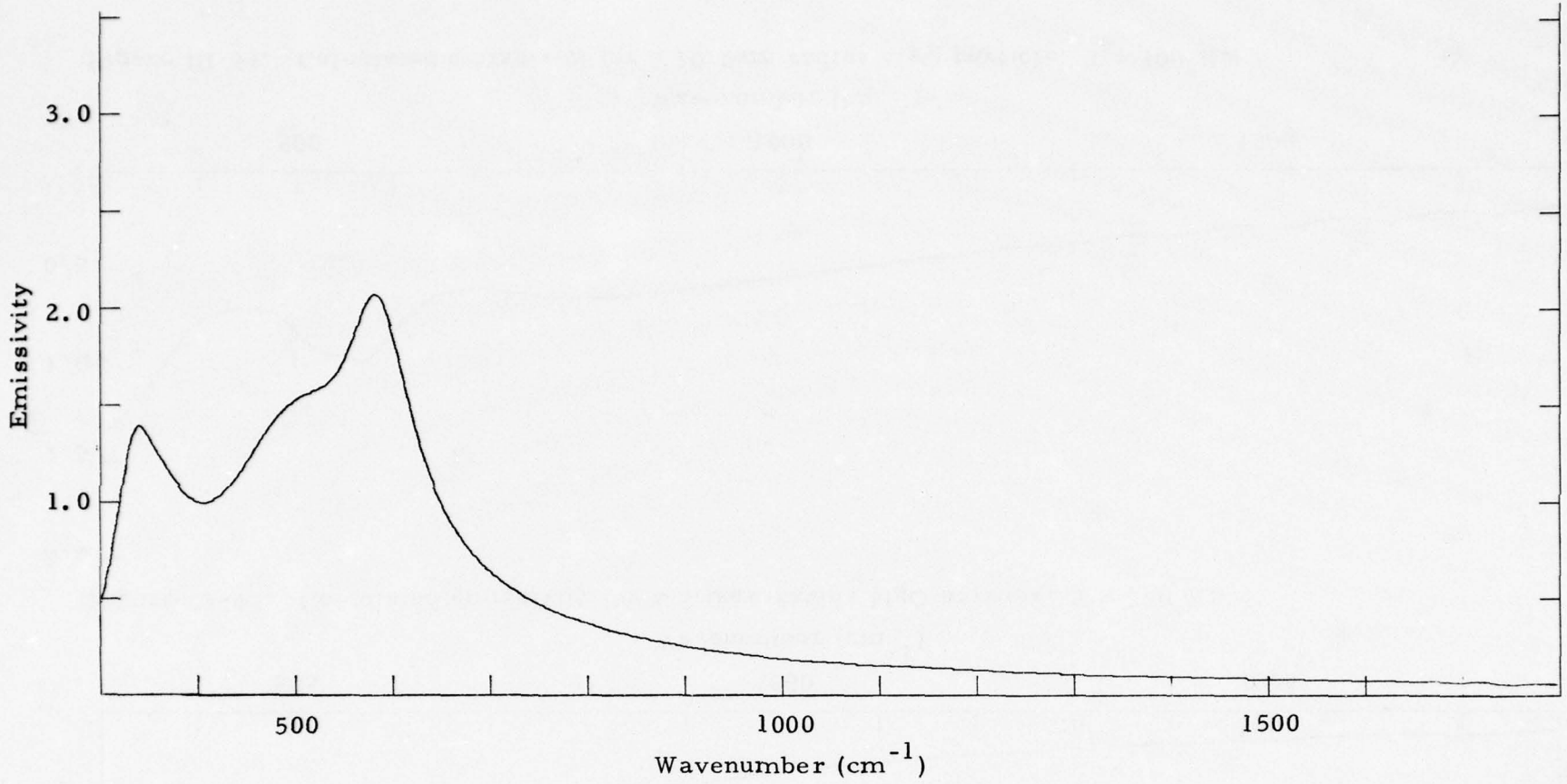

Figure III-42. Calculated emissivity for a 3.0μm radius MgO particle, T = 300°K.

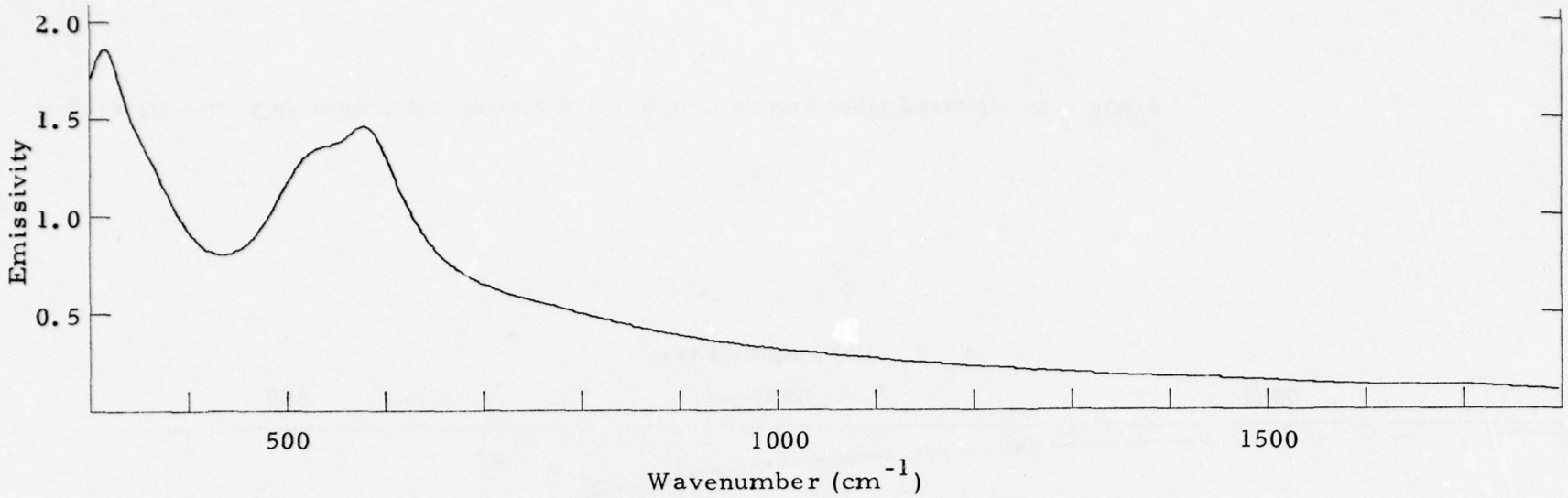

Figure III-43. Calculated emissivity for a 5.0μm radius MgO particle, T = 300°K.

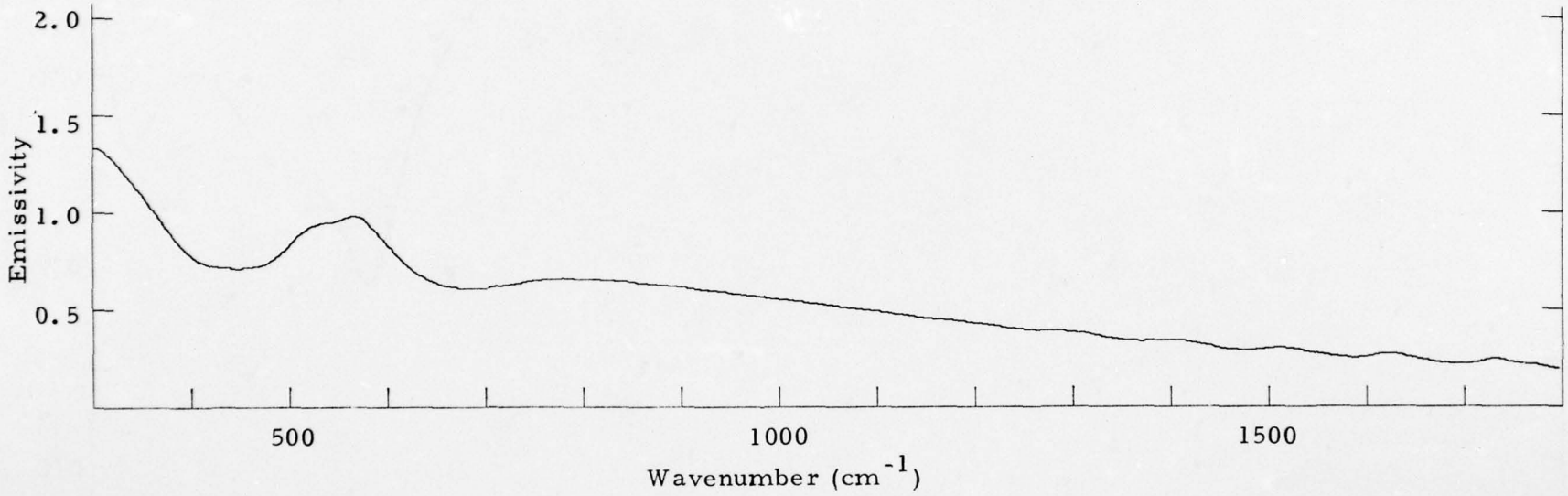

Figure III-44. Calculated emissivity for a 10.0μm radius MgO particle, T = 300°K.

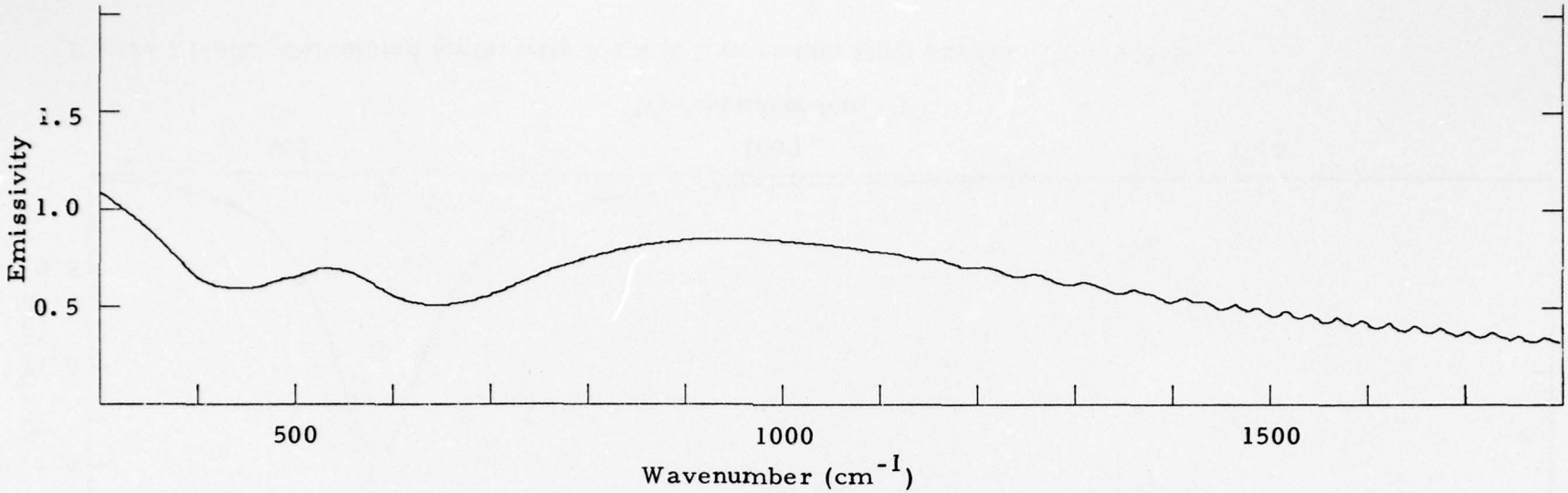

Figure III-45. Calculated emissivity for a 20.0μm radius MgO particle, T = 300°K.

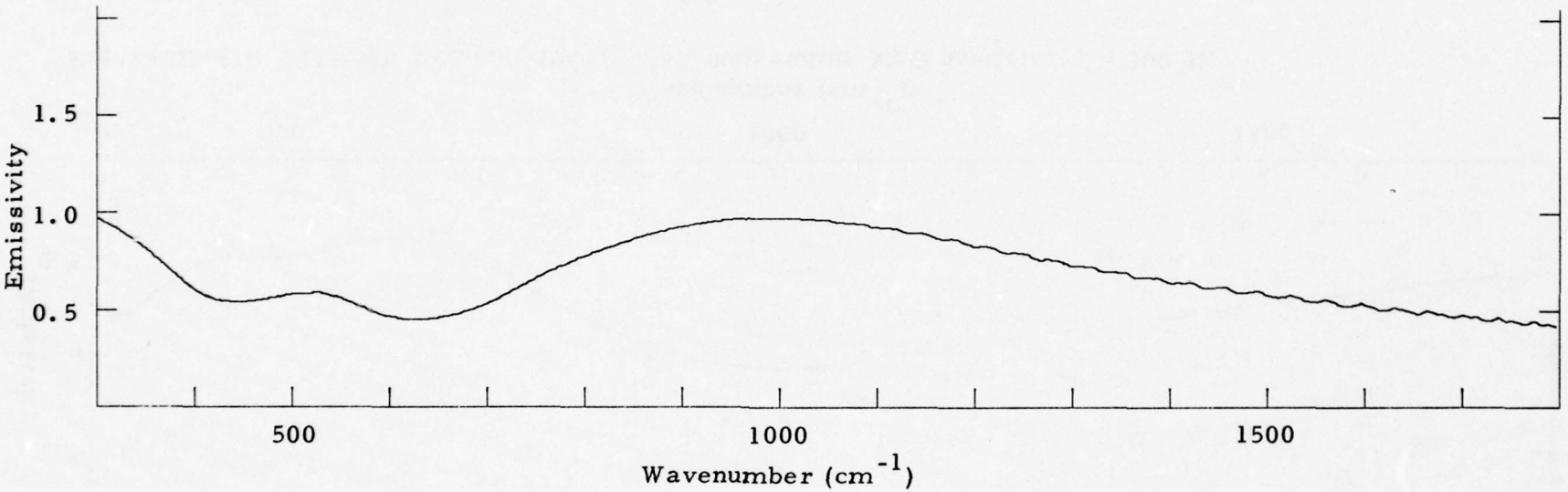

Figure III-46. Calculated emissivity for a 30.0μm radius MgO particle, T = 300°K.

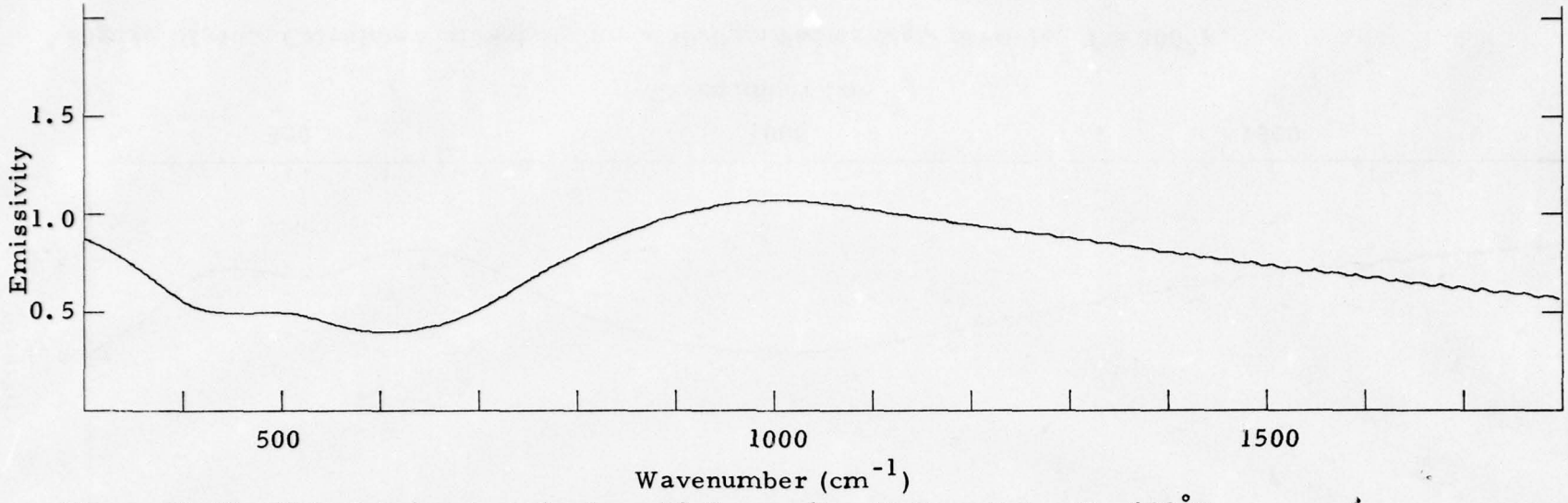

Figure III-47. Calculated emissivity for a 50.0μm radius MgO particle, T = 300°K.

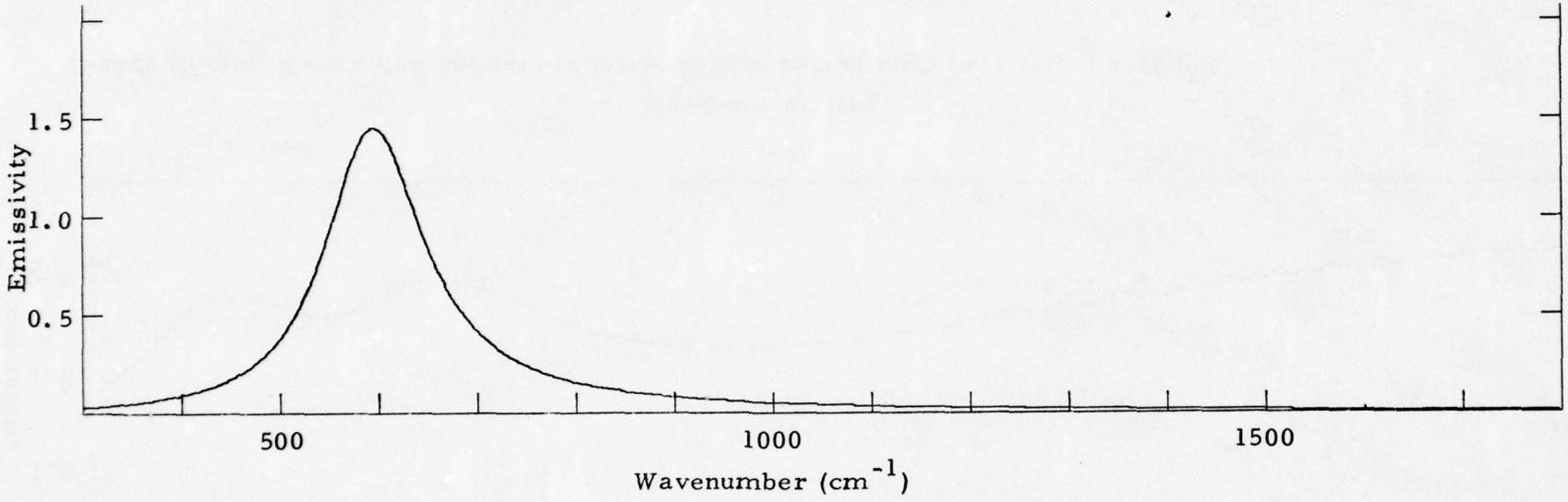

Figure III-48. Calculated emissivity for a 0.5μm radius MgO particle, T = 573°K.

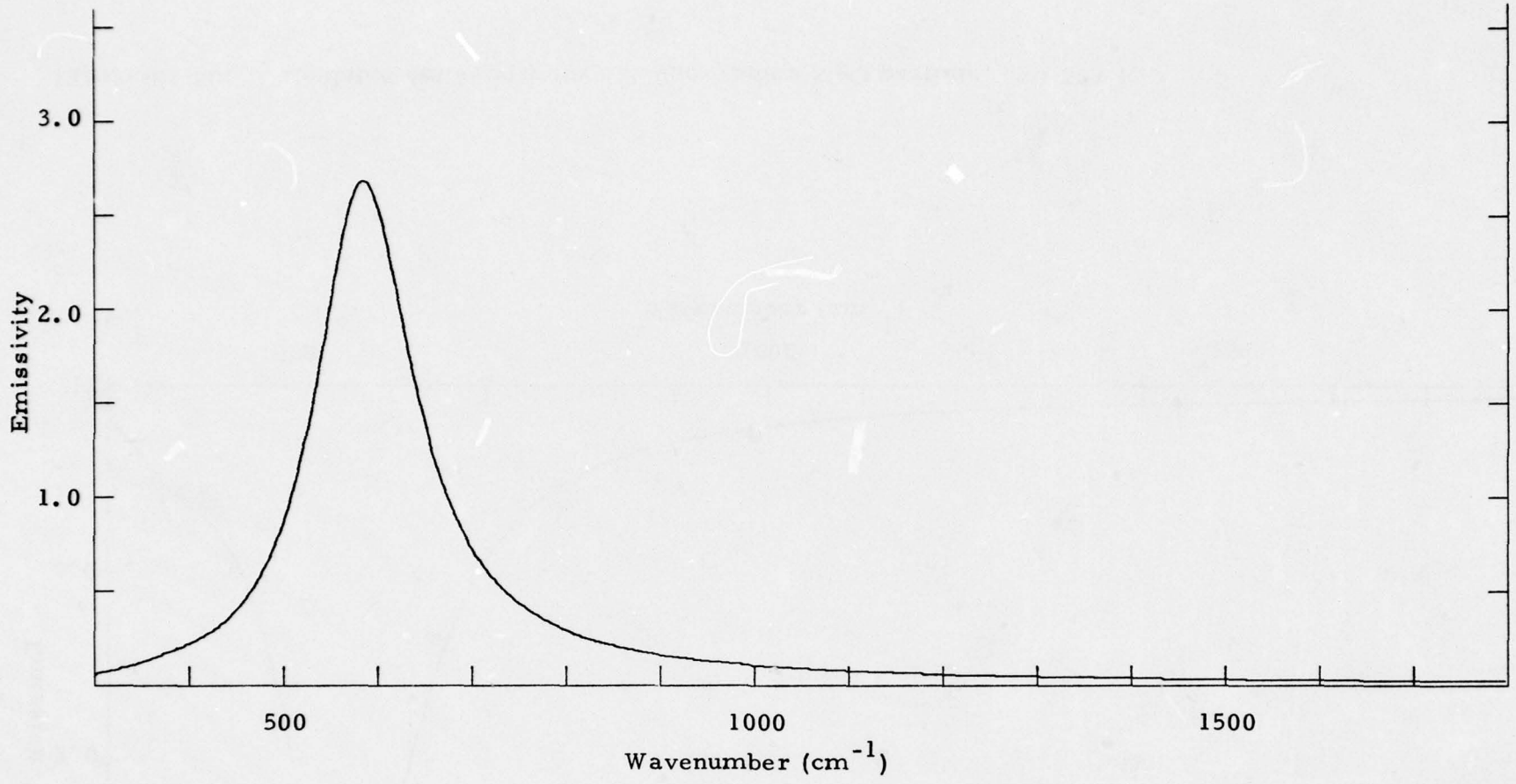

Figure III-49. Calculated emissivity for a 1.0μm radius MgO particle, T = 573°K.

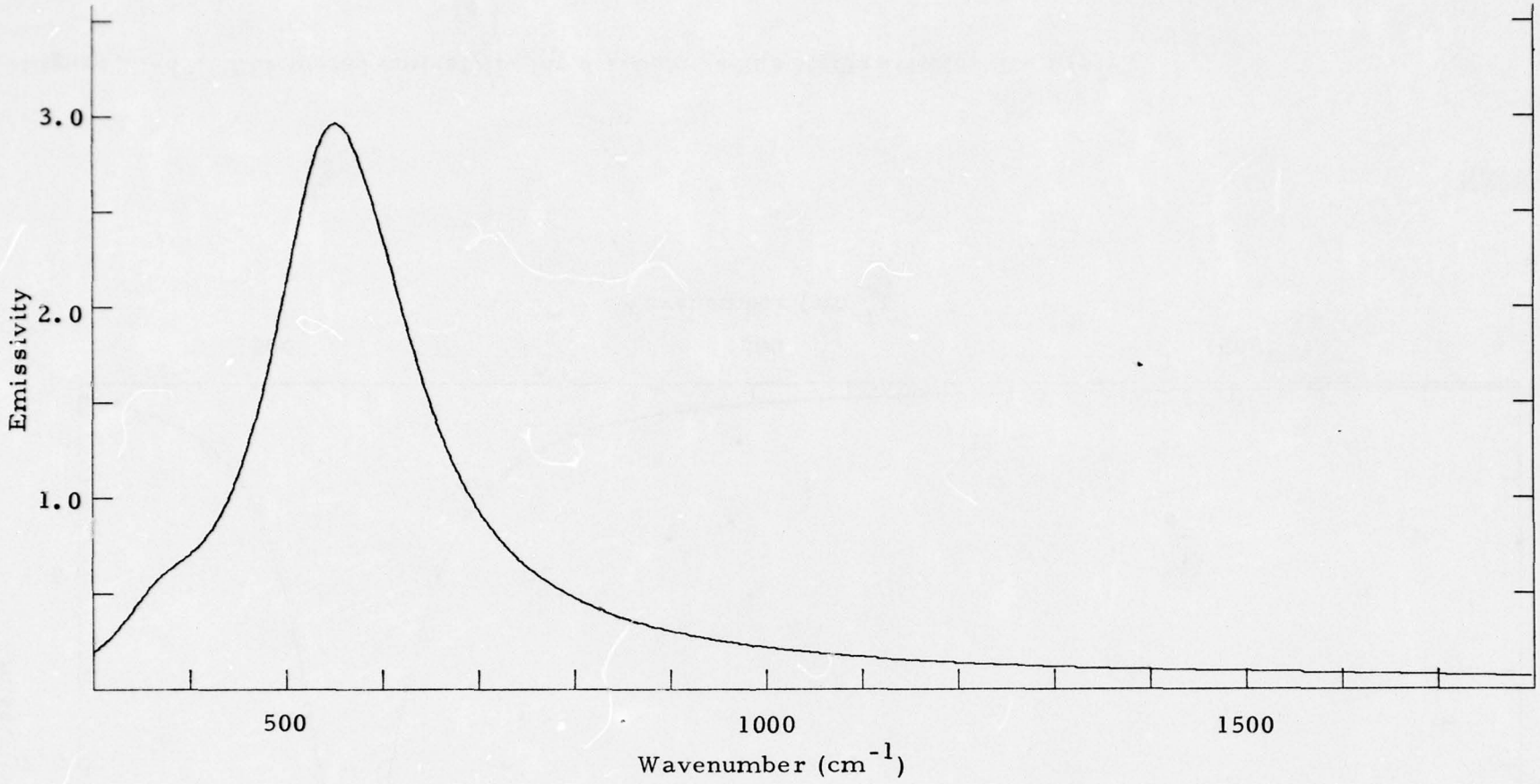

Figure III-50. Calculated emissivity for a 2.0μm radius MgO particle, T = 573°K.

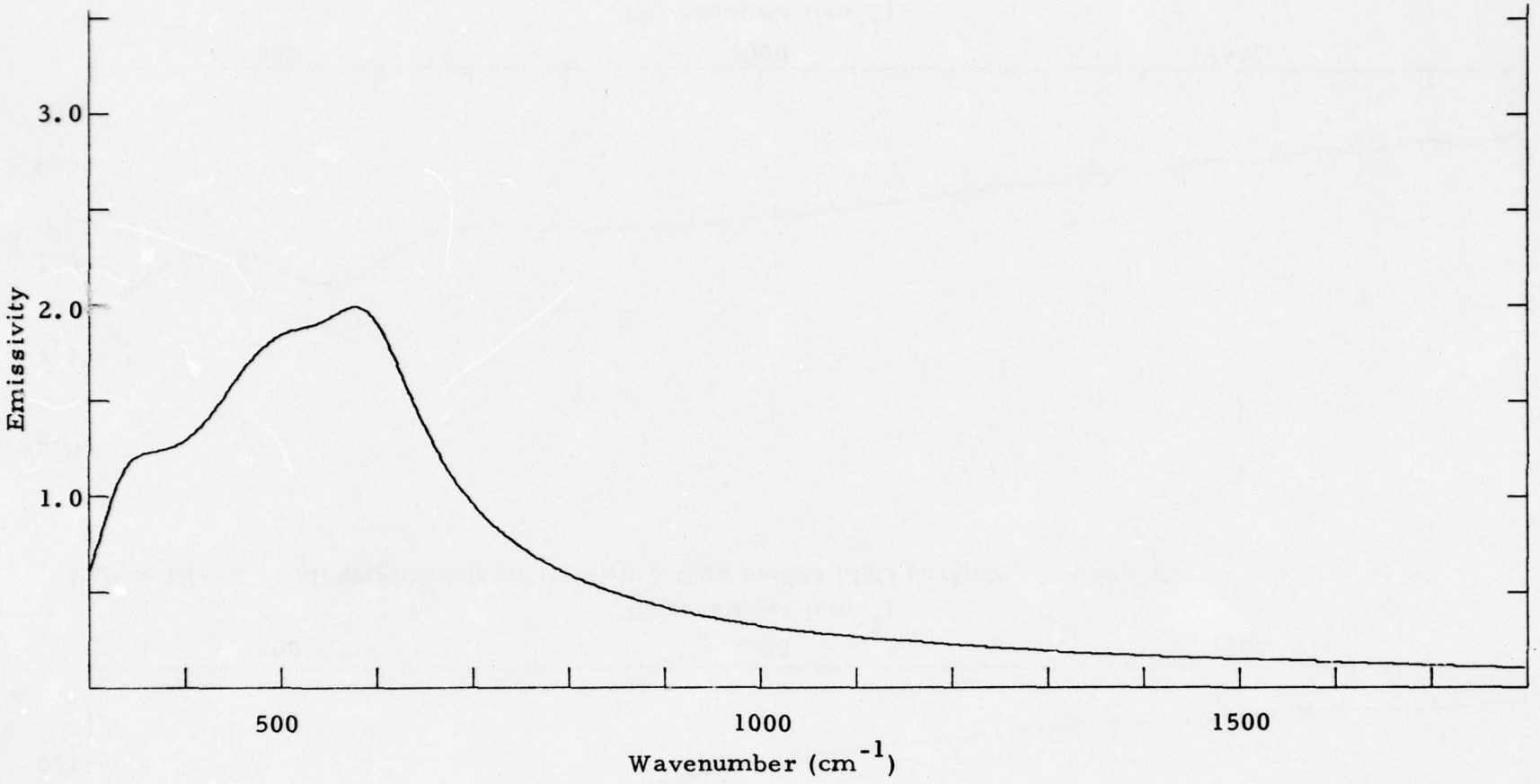

Figure III-51. Calculated emissivity for a 3.0μm radius MgO particle, T = 573 °K.

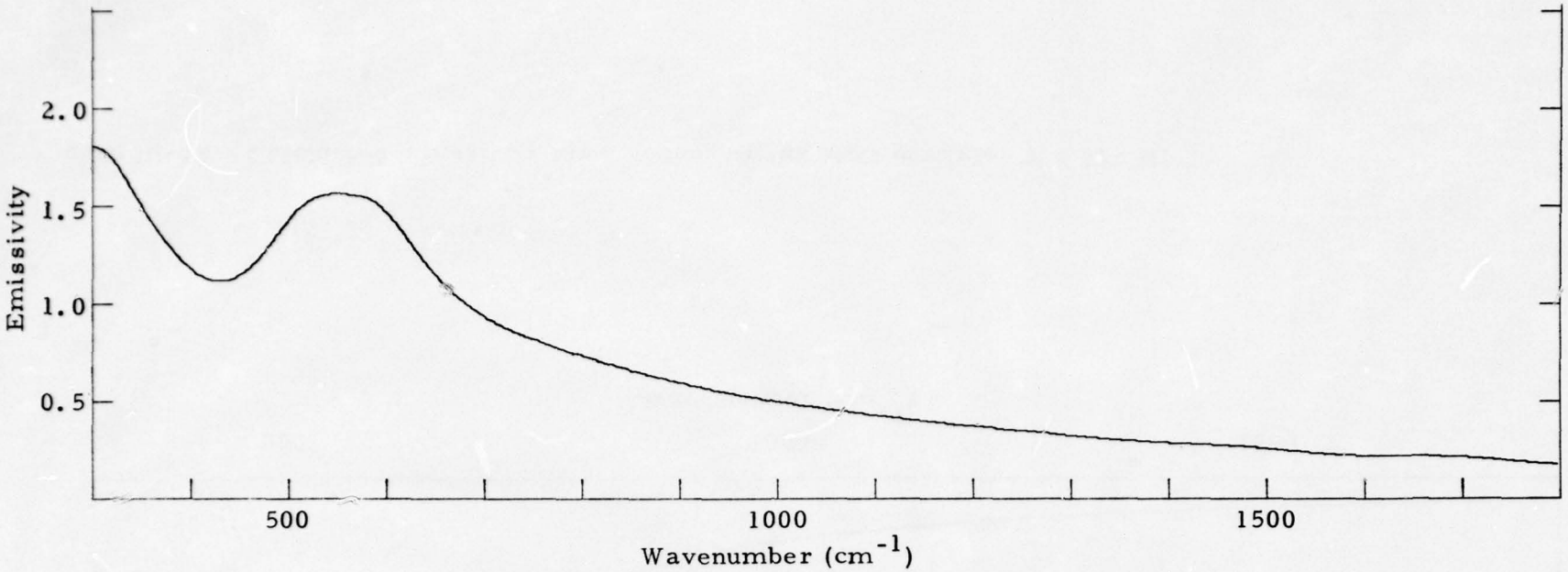

Figure III-52. Calculated emissivity for a 5.0μm radius MgO particle, T = 573°K.

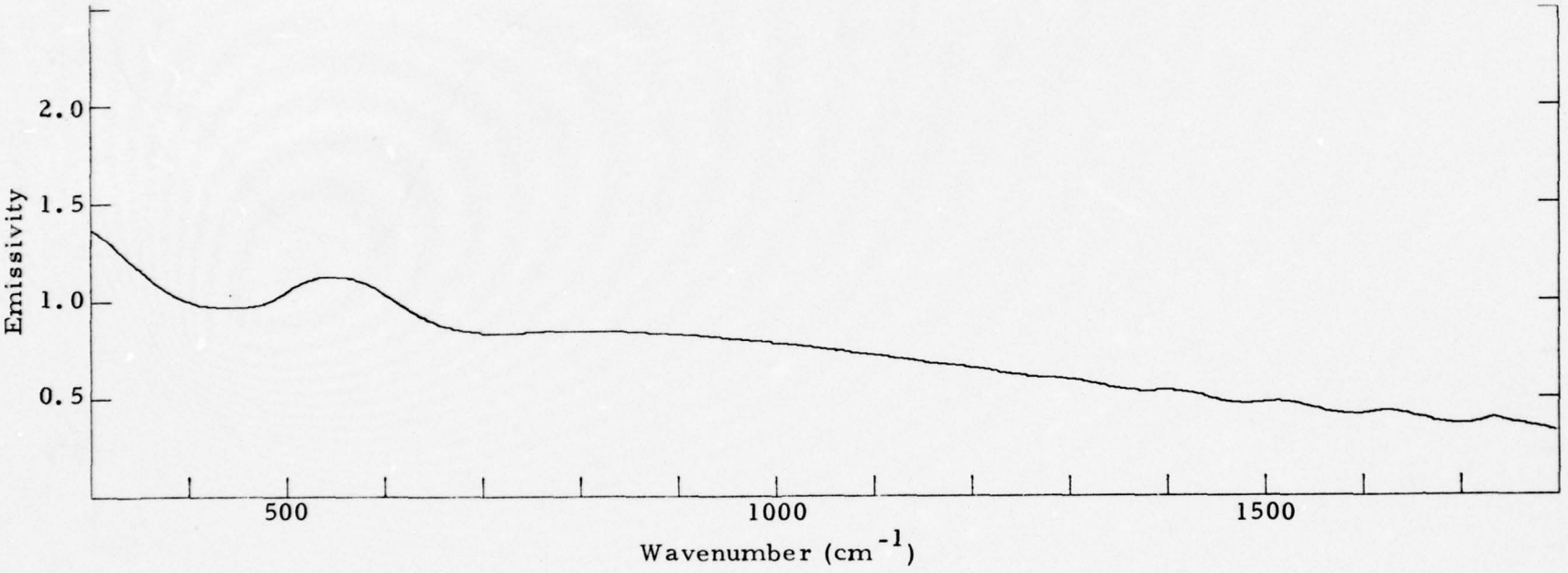

Figure III-53. Calculated emissivity for a 10.0μm radius MgO particle, T = 573°K.

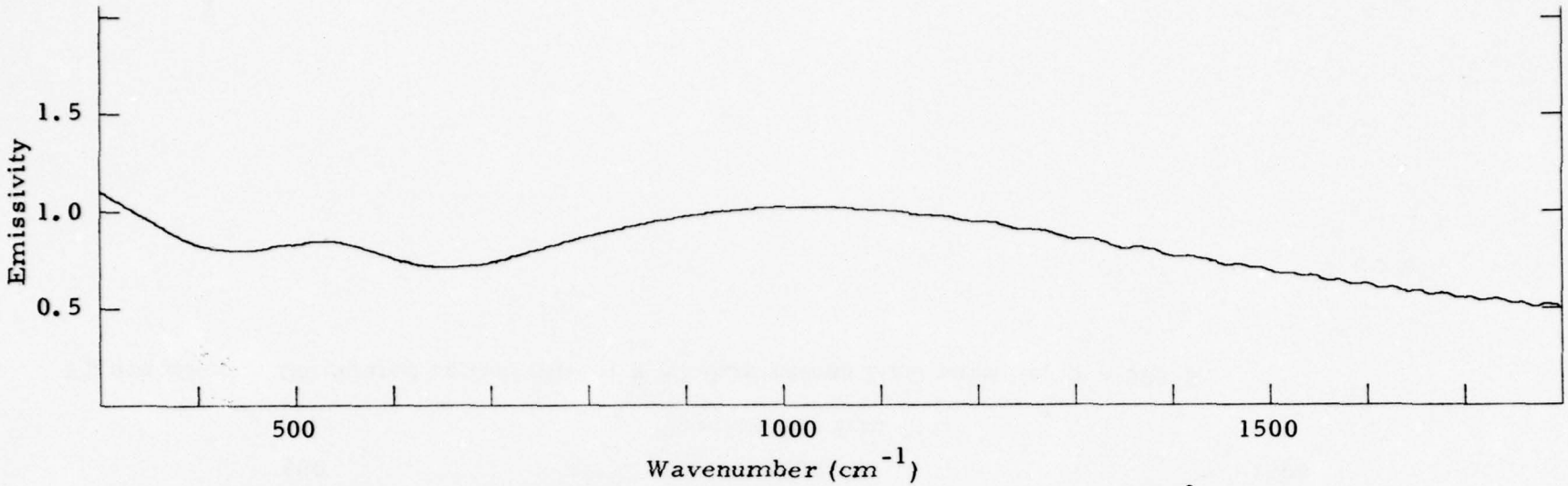

Figure III-54. Calculated emissivity for a 20.0μm radius MgO particle, T = 573°K.

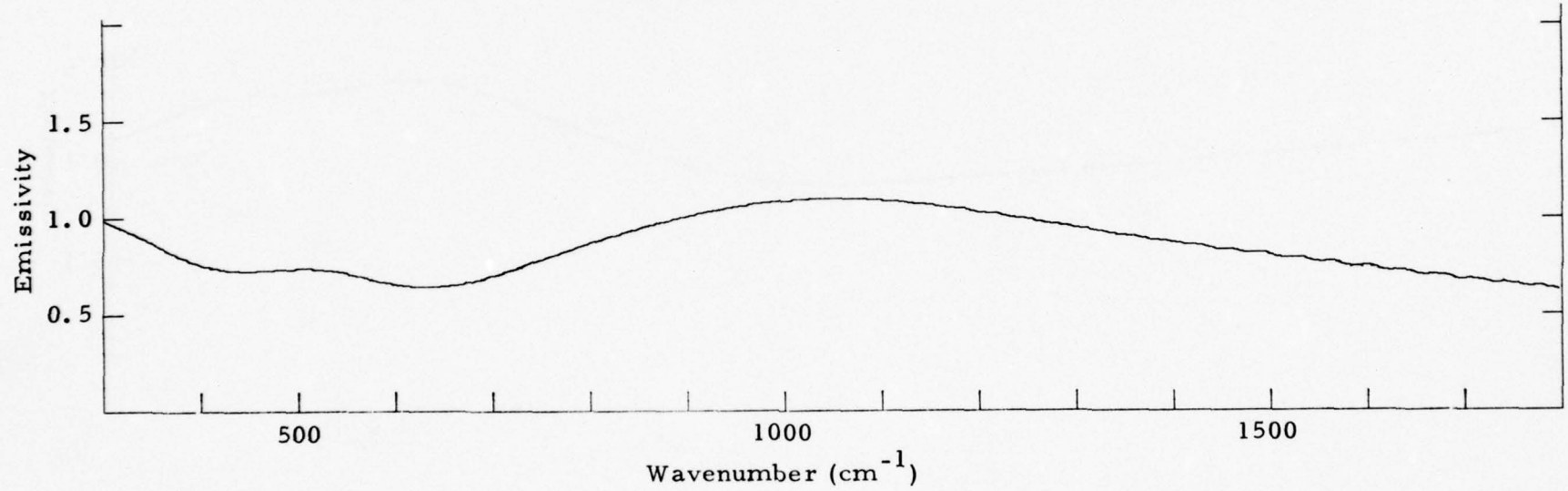

Figure III-55. Calculated emissivity for a 30.0μm radius MgO particle, T = 573°K.

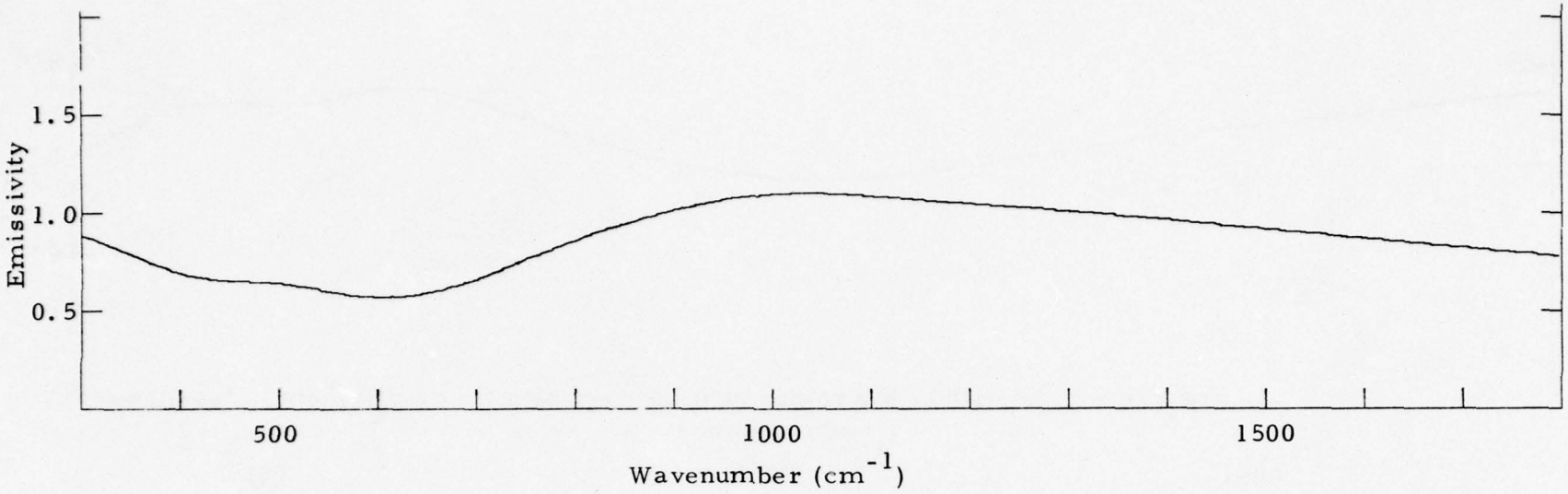

Figure III-56. Calculated emissivity for a 50.0μm radius MgO particle, T = 573 °K.

The calculated emissivities for spherical particles ($0.5\mu m \leq r \leq 50\mu m$) for ZrO_2 are shown in Figures III-57 through III-65 for $T = 300^\circ K$, and Figures III-66 through III-74 for $T = 573^\circ K$. Since the reflectivity data were obtained for a polycrystalline sample, the results are applicable to spherical polycrystalline particles of ZrO_2 and not the single crystalline form.

C. SUMMARY AND GENERAL CONCLUSIONS

The theory of small particle emissivity has been summarized. The emissivity of a spherical particle is equal to its absorption efficiency as calculated from Mie theory. A computer program has been written which calculates the emissivity of spherical particles. Using the data given in Section II, spherical particle emissivities have been calculated for particle sizes in the range $0.5\mu m$ to $50\mu m$. For small particles ($\lesssim 10\mu m$) the emissivity often exceeds one, since the absorption cross section is larger than the geometrical cross section. For larger particles the calculated emissivity does indeed reduce to its classical value. The emissivity of spherical particles is found to be very dependent on the values of n and k, as well as the size (diameter) of the particle. Also, the calculated emissivity of intermediate ($10\mu m \leq r \leq 50\mu m$) sized particles becomes quite large ($\simeq 1$) for relatively small values of k (~ 0.02), which in general are poorly determined by reflectance type measurements. Furthermore, these values of k which can lead to high emissivity values under proper conditions are much more likely to occur for the impure and imperfect crystals in particular than for large, carefully prepared bulk samples where $k < 0.001$ at frequencies greater than the last infrared allowed frequency.

The calculated emissivity of small spherical particles is seen to be critically dependent on size, and complex index of refraction (i.e., n and k). We therefore conclude that real particles, even if

they are quasi-spherical, will probably have an emissivity quite different from that calculated from Mie theory, since the bulk values of n and k may not be applicable to very small particles. Measurement of individual particle emissivities are still required.

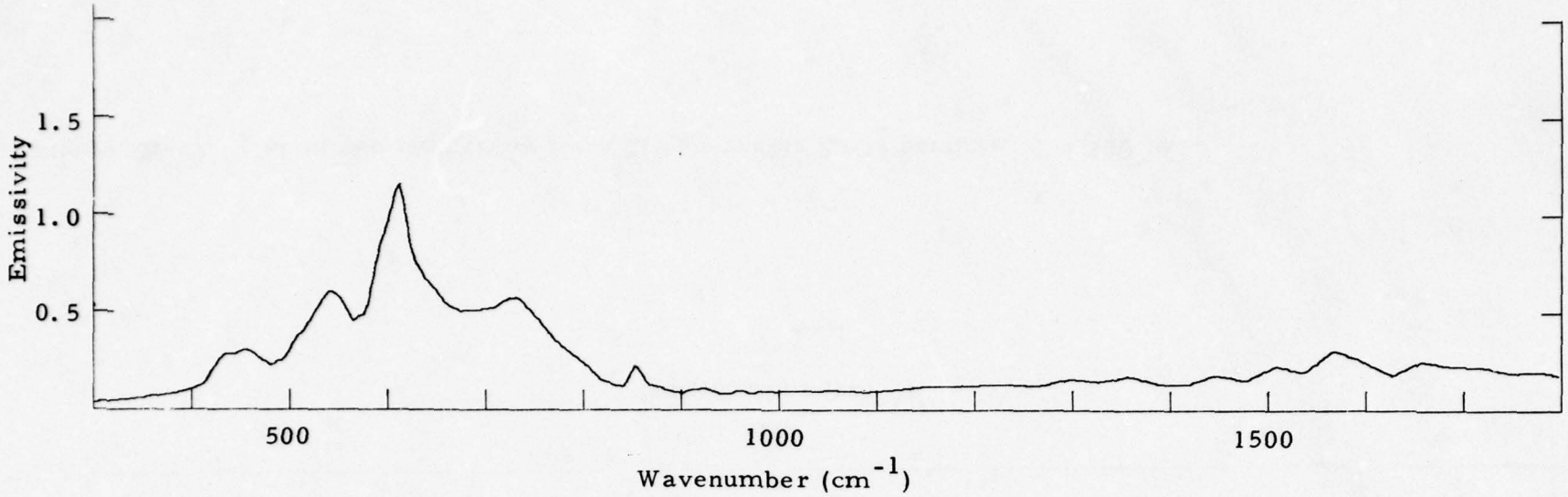

Figure III-57. Calculated emissivity for a 0.5μm radius ZrO_2 particle, T = 300°K.

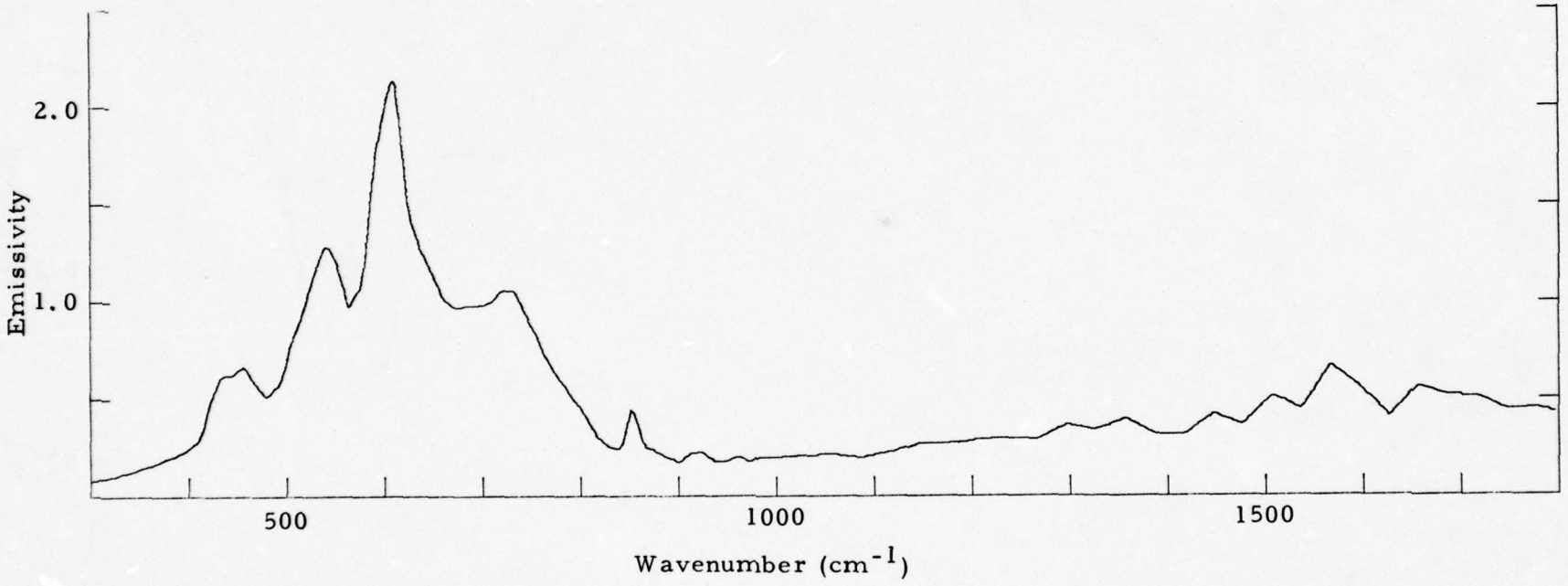

Figure III-58. Calculated emissivity for a 1.0μm radius ZrO_2 particle, T = 300°K.

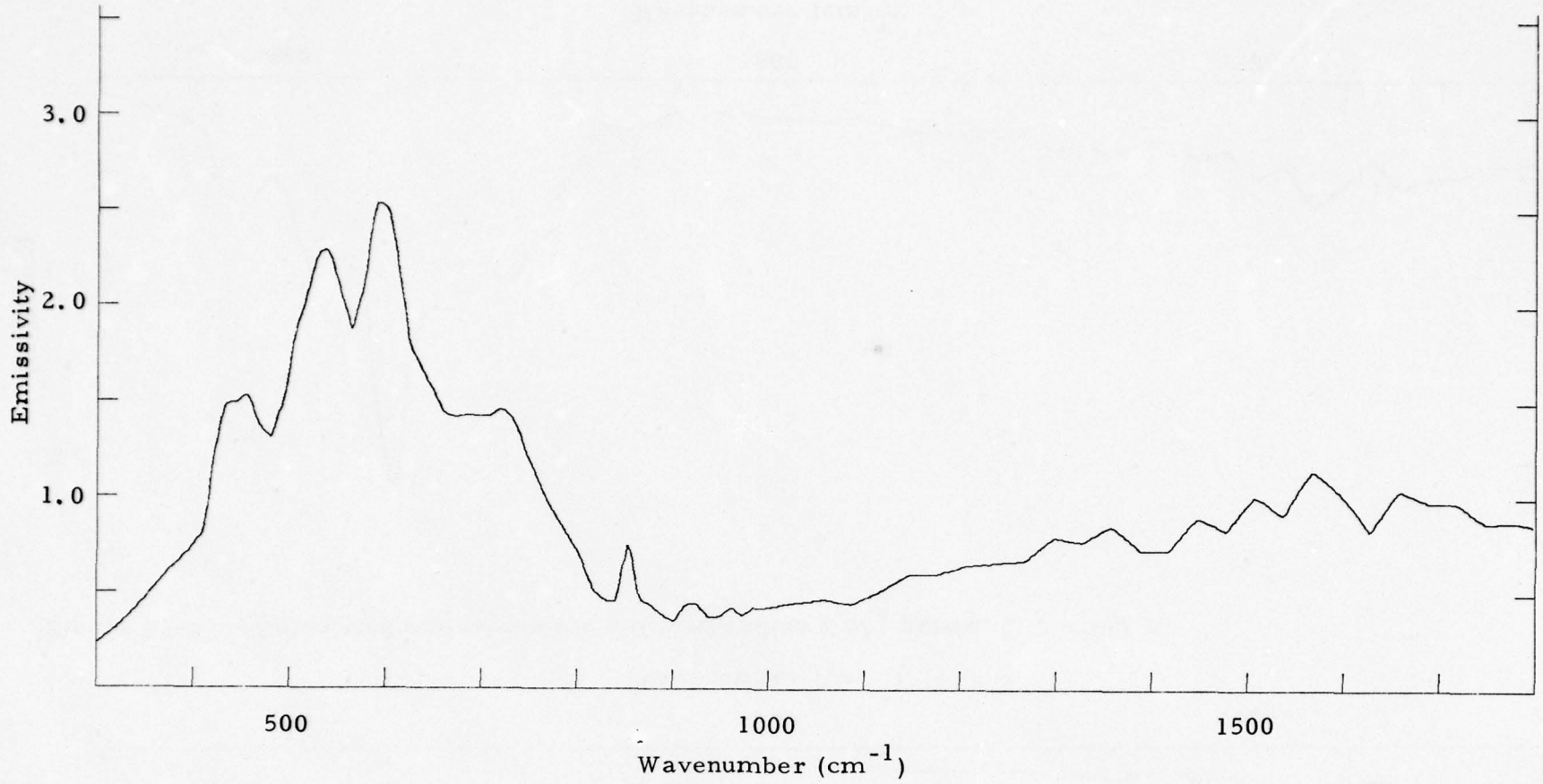

Figure III-59. Calculated emissivity for a 2.0μm radius ZrO_2 particle, T = 300°K.

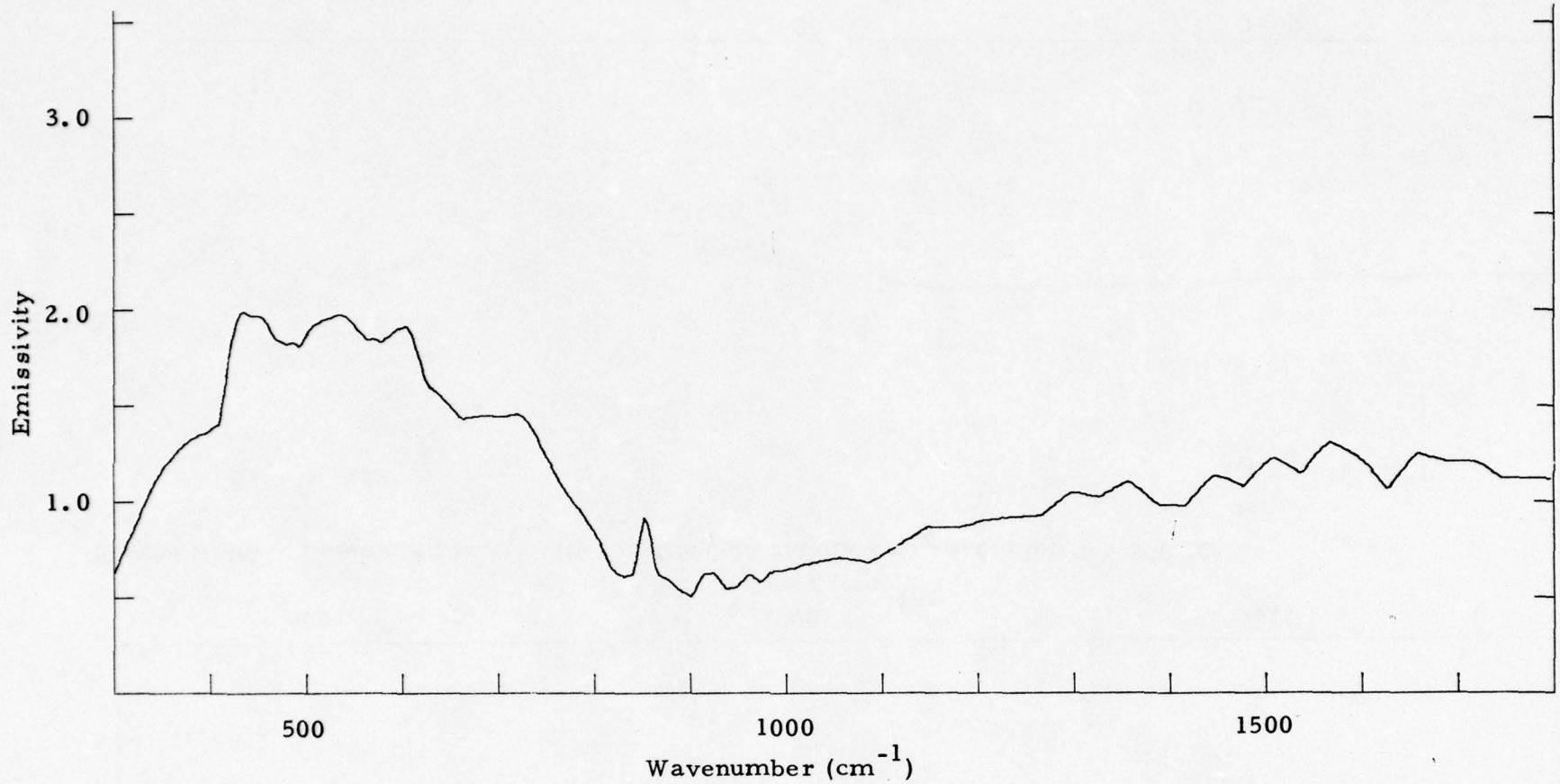

Figure III-60. Calculated emissivity for a 3.0μm radius ZrO particle, T = 300°K.

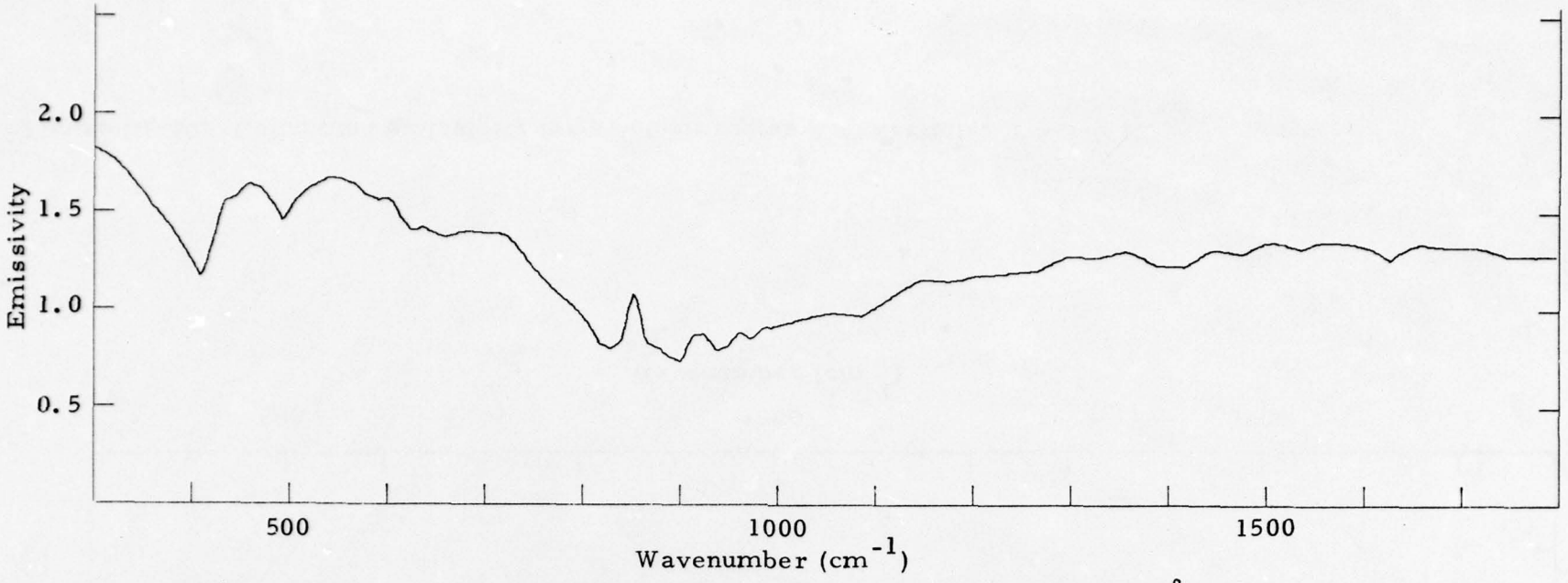

Figure III-61. Calculated emissivity for a 5.0μm radius ZrO_2 particle, T = 300°K.

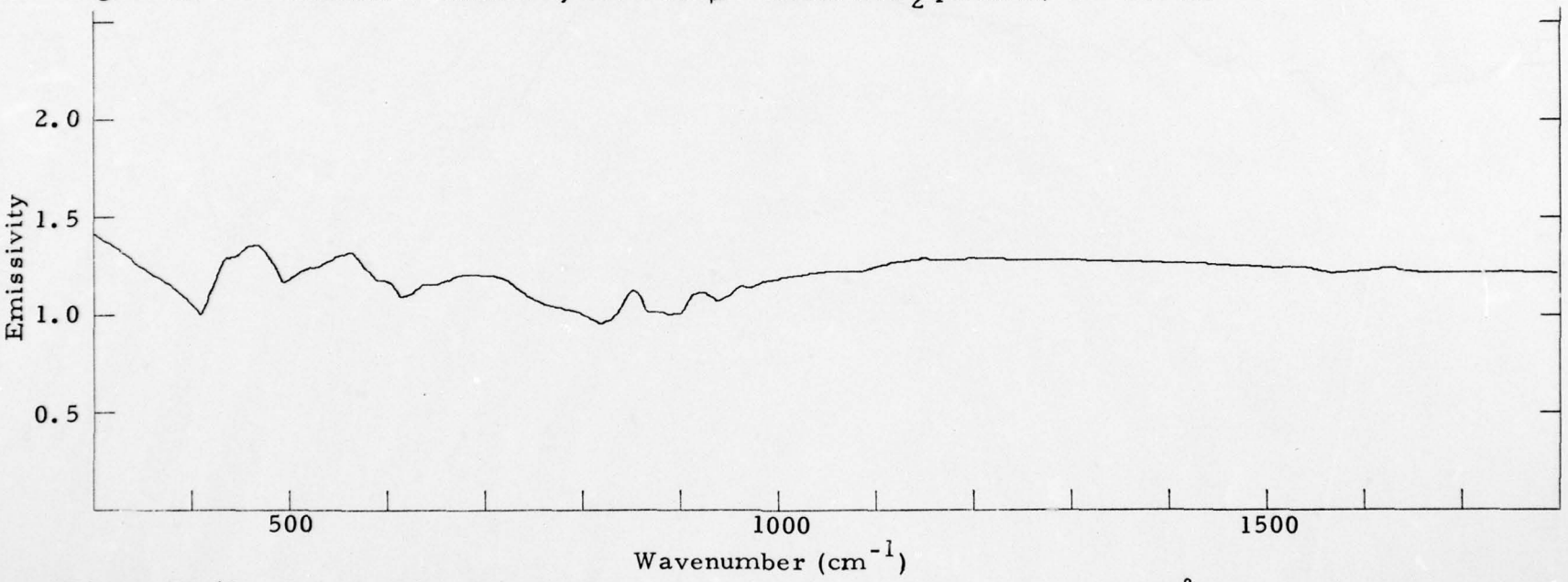

Figure III-62. Calculated emissivity for a 10.0μm radius ZrO_2 particle, T = 300°K.

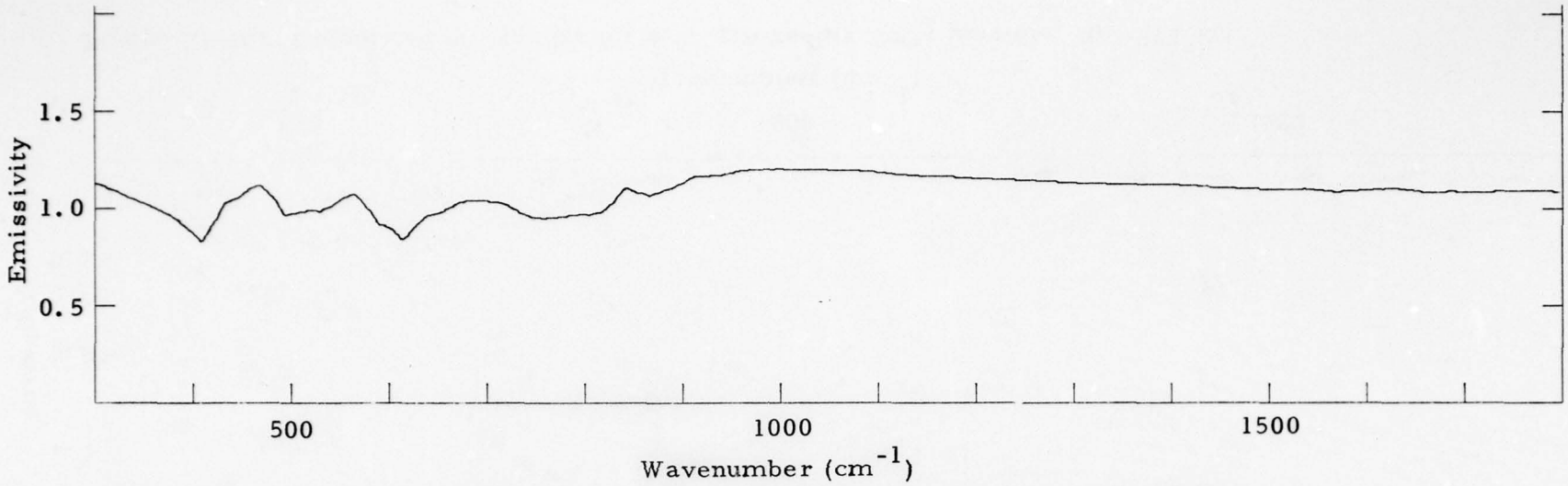

Figure III-63. Calculated emissivity for a 20.0μm radius ZrO_2 particle, T = 300°K.

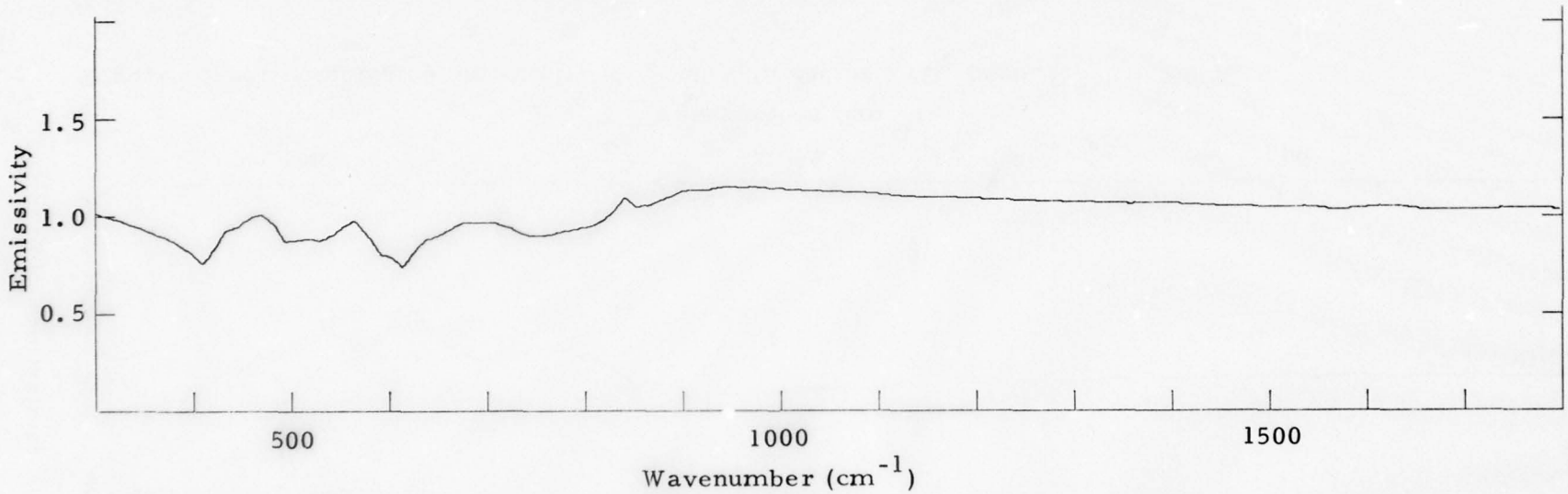

Figure III-64. Calculated emissivity for a 30.0μ radius ZrO_2 particle, T = 300°K.

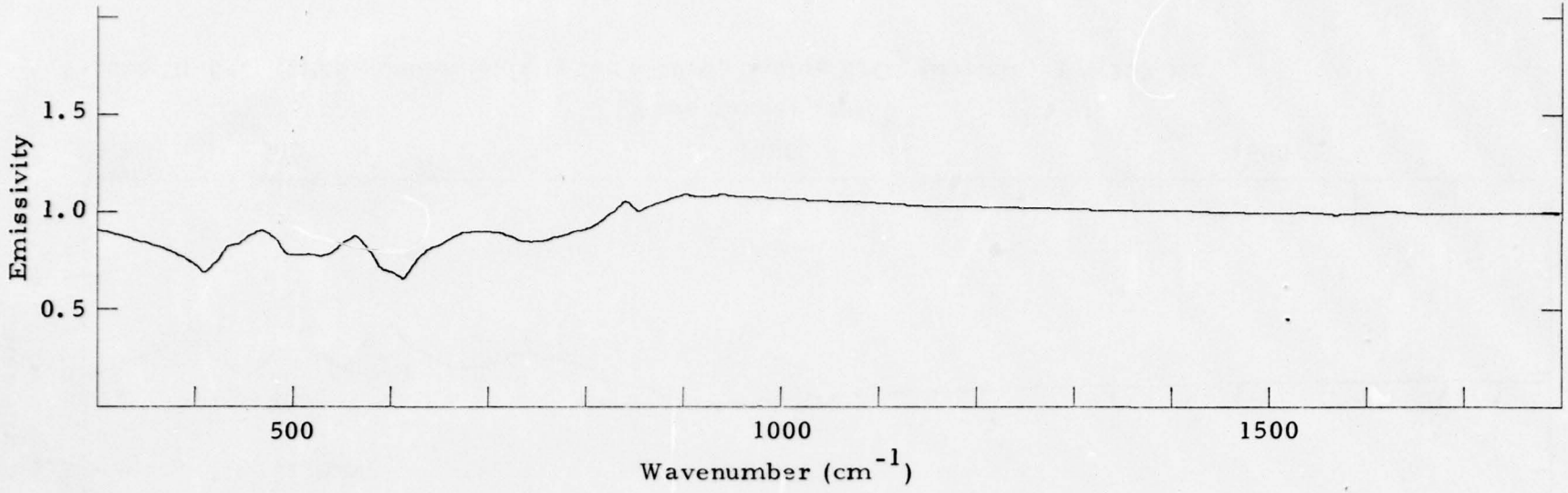

Figure III-65. Calculated emissivity for a 50.0μm radius ZrO_2 particle, T = 300°K.

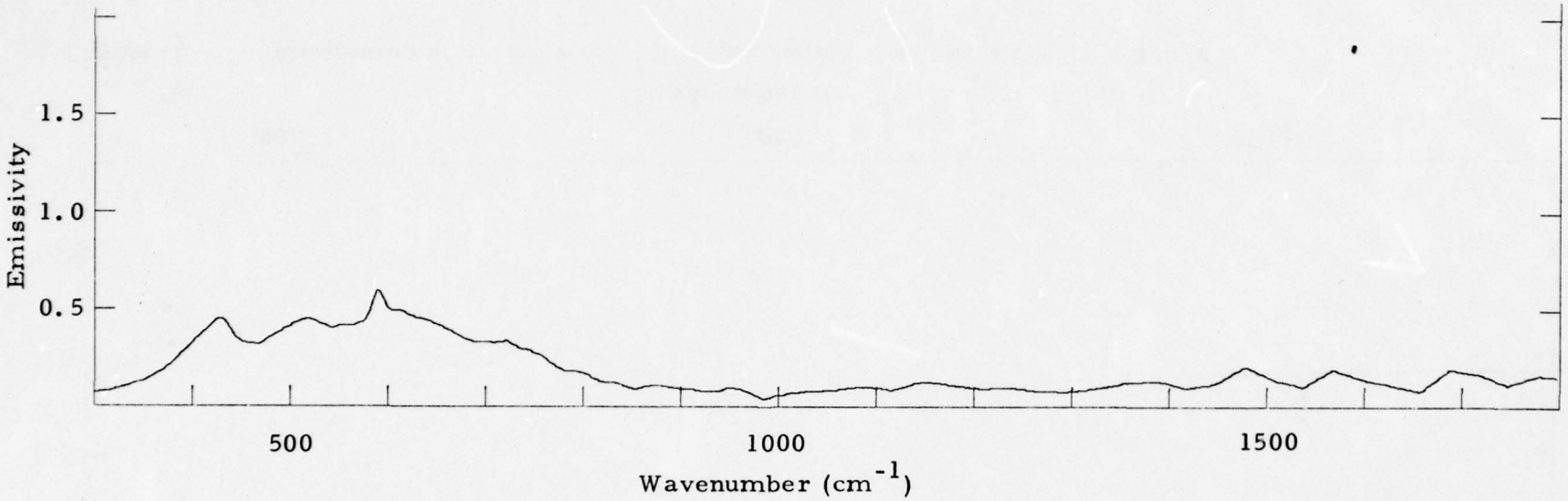

Figure III-66. Calculated emissivity for a 0.5μm radius ZrO_2 particle, T = 573°K.

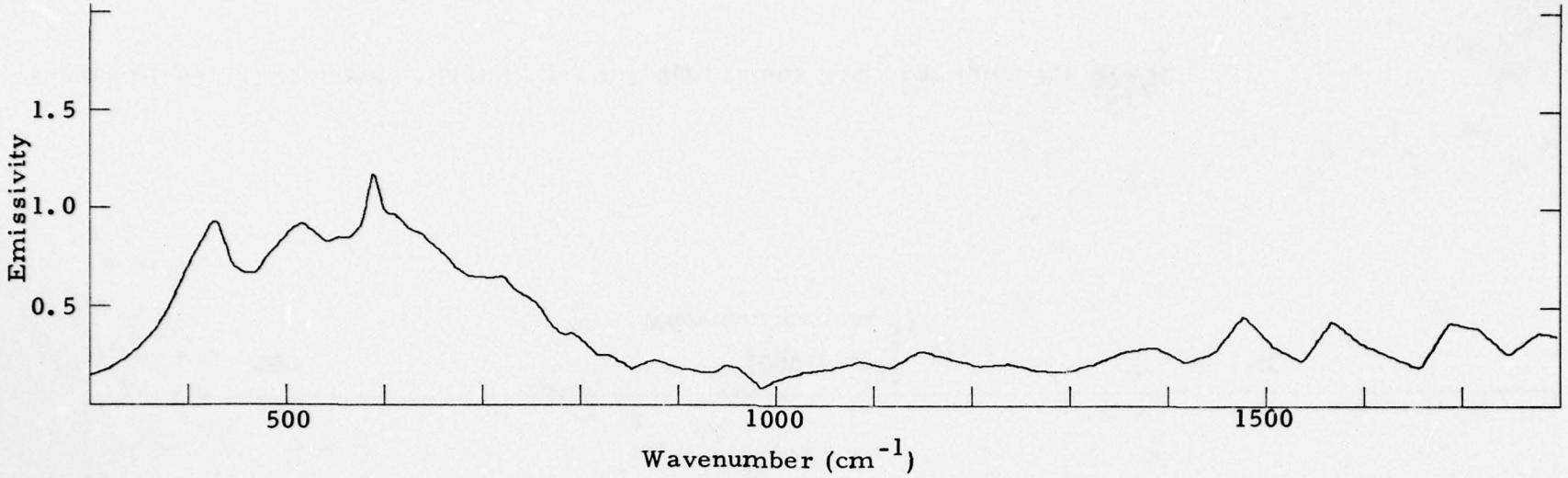

Figure III-67. Calculated emissivity for a 1.0μm radius ZrO_2 particle, T = 573°K.

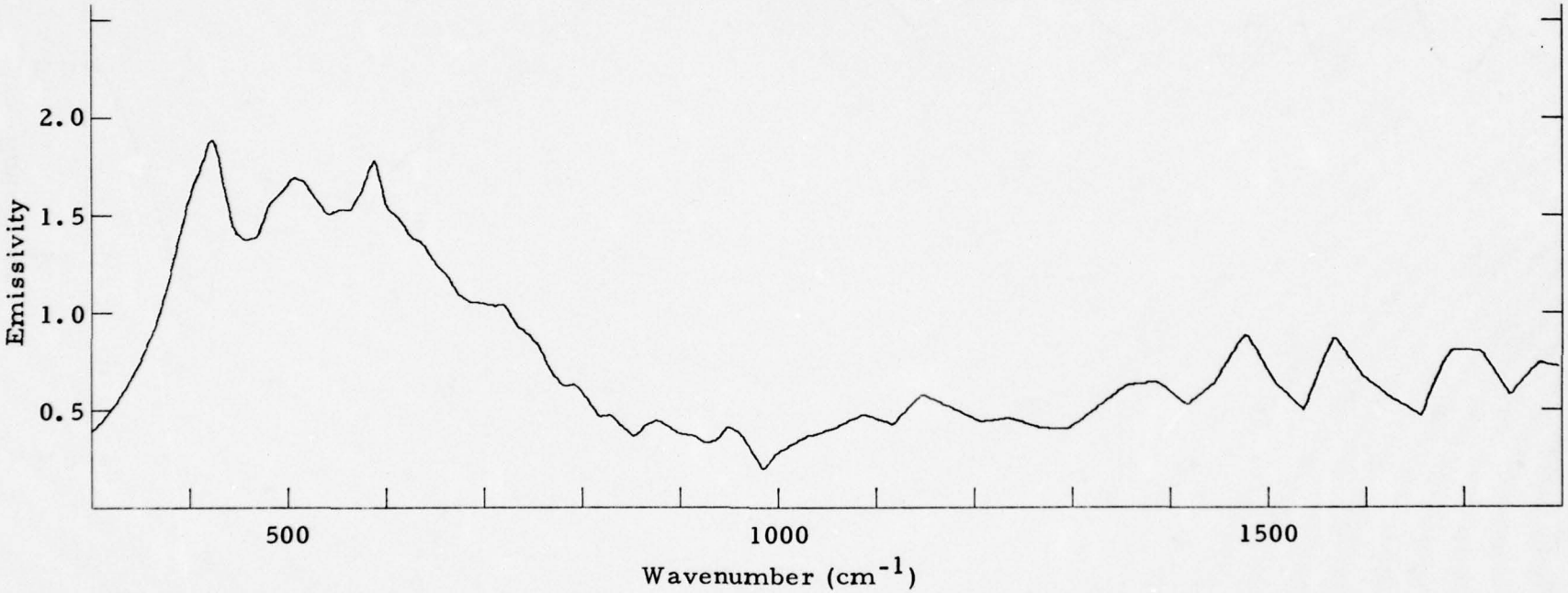

Figure III-68. Calculated emissivity for a 2.0μm radius ZrO particle, T = 573°K.

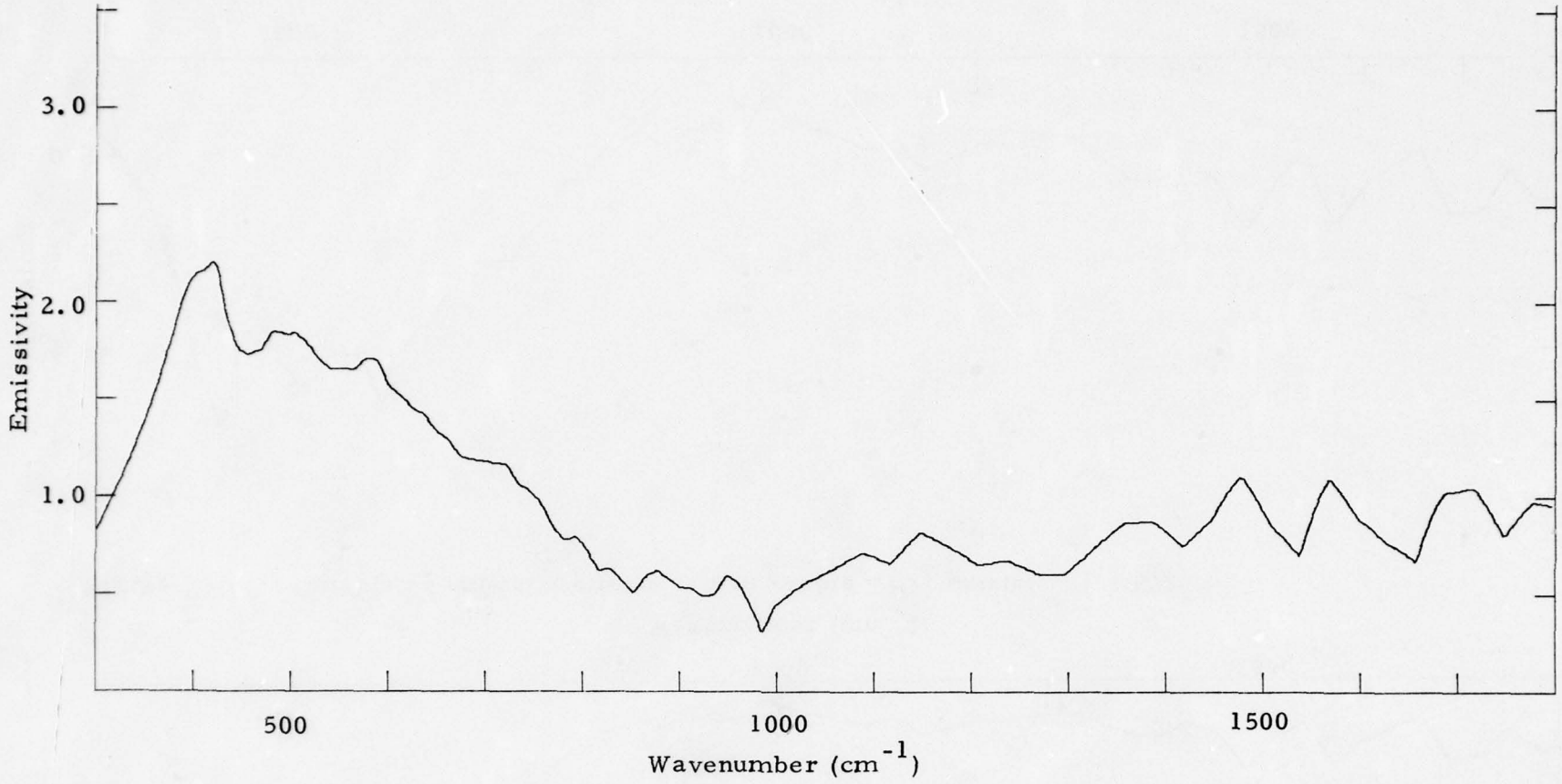

Figure III-69. Calculated emissivity for a 3.0μm radius ZrO_2 particle, T = 573°K.

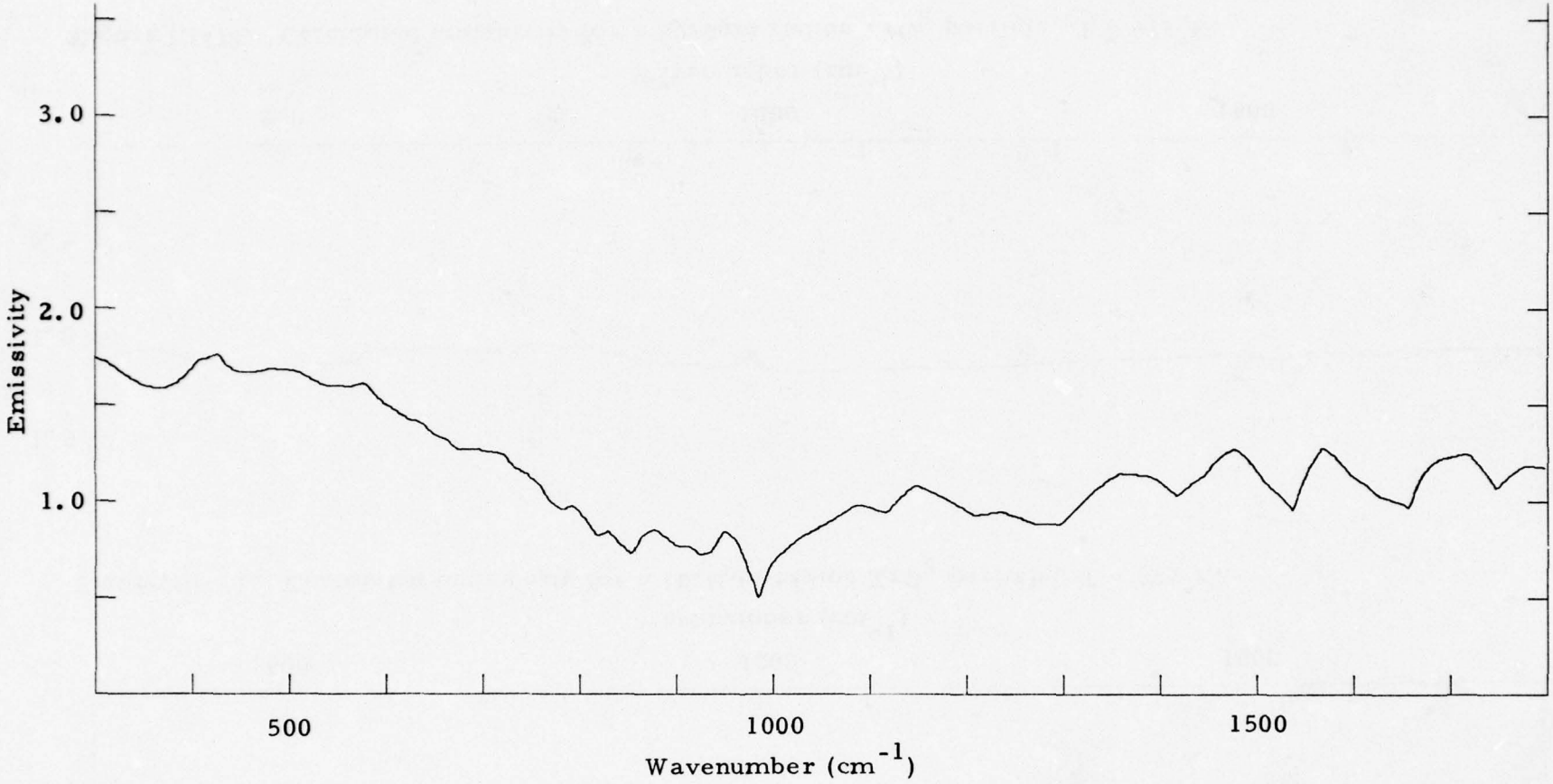

Figure III-70. Calculated emissivity for a 5.0μm radius ZrO_2 particle, T = 573°K.

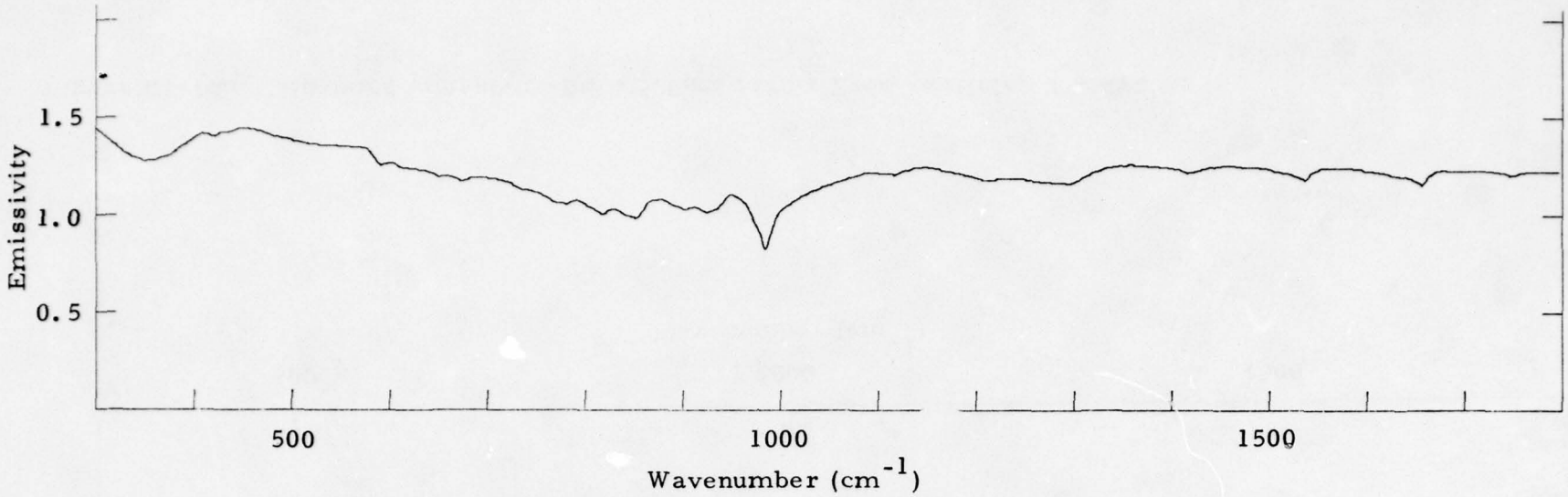

Figure III-71. Calculated emissivity for a 10.0μm radius ZrO_2 particle, T = 573°K.

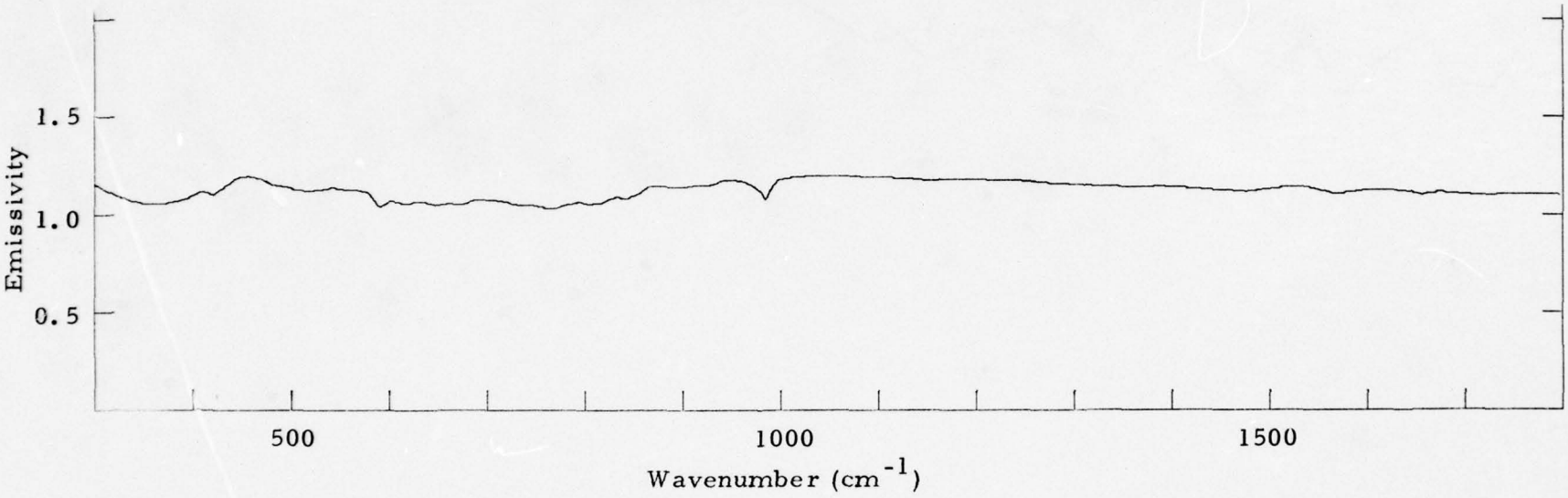

Figure III-72. Calculated emissivity for a 20.0μm radius ZrO_2 particle, T = 573°K.

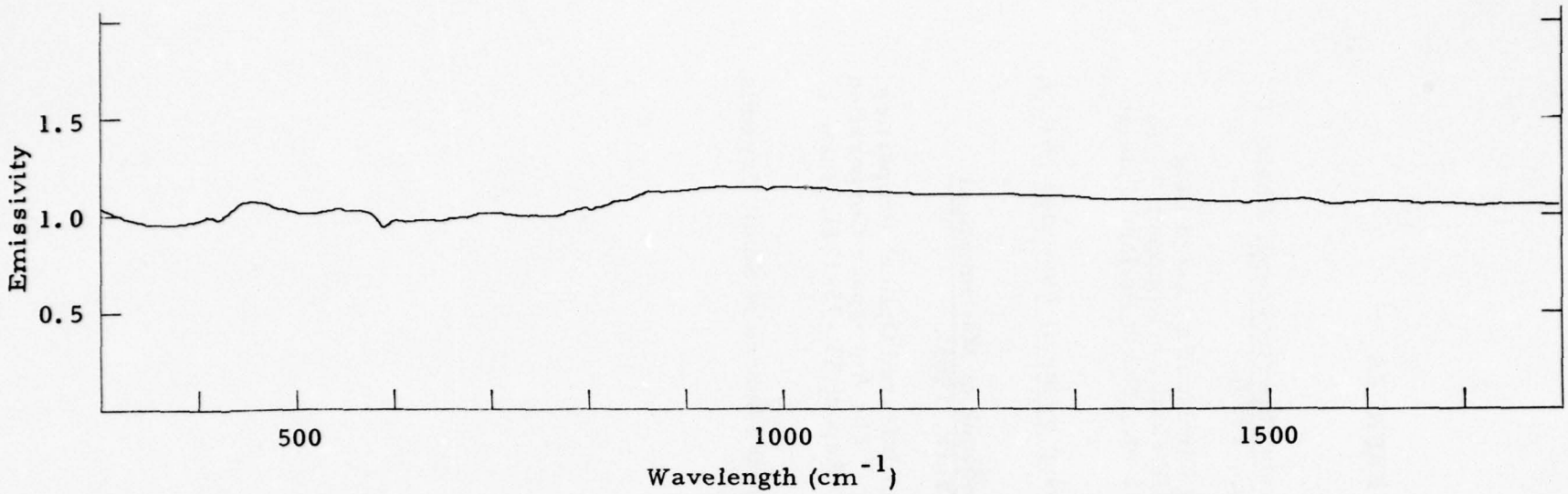

Figure III-73. Calculated emissivity for a 30.0μm radius ZrO_2 particle, T = 573 °K.

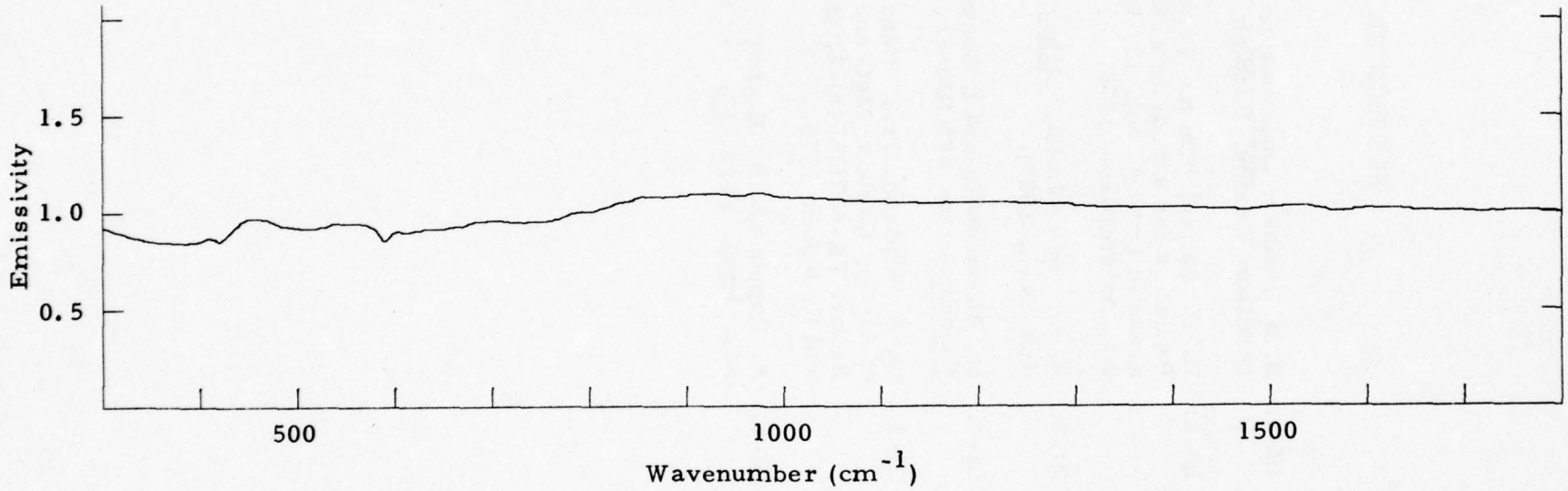

Figure III-74. Calculated emissivity for 50.0μm radius ZrO_2 particle, T = 573 °K.

SECTION III. REFERENCES

III-1. S. S. Penner, Quantitative Molecular Spectroscopy, Chapt. 1 (Addison-Wesley, Reading, Mass., 1959).

III-2. H. P. Baltes, "On the Validity of Kirchhoff's Law of Heat Radiation for a Body in a Nonequilibrium Environment," Progress in Optics, Vol. 13, E. Wolf ed., North Holland Publishing, Amsterdam, 1976, p 1-25.

III-3. H. C. van de Hulst, Light Scattering by Small Particles (Wiley, New York, 1957).

III-4. M. Abramowitz and I. Segun, Handbook of Mathematical Functions, pp. 445 (Dover, New York, 1965).

III-5. M. E. Whitson, Jr., "Handbook of Infrared Optical Properties of Al_2O_3, Carbon, MgO and ZrO_2," The Aerospace Corporation Report TR-0075(5548)-2, (SAMSO Report TR-75-131), Vols. I and II, 4 June 1975.

III-6. A. Ruppin and R. Englman, "Optical Phonons of Small Crystals," Rep. Prog. Phys. 33, 149 (1970).

SECTION IV

SINGLE PARTICLE EMISSIVITY EXPERIMENT

A. EXPERIMENTAL APPROACH

The basic objective of the POPM program is the comparison of particle emissivities computed from bulk data with values measured for single particles. This section describes the progress which has been made experimentally in holding and heating a single particle, then observing the infrared radiation from the hot particle, and finally analyzing the infrared data to obtain particle emissivities.

The single particle emissivity experiment is based on simple scientific principles which require a combination of state-of-the-art techniques. A single particle of Al_2O_3, MgO, ZrO_2 or carbon is electrostatically suspended at the focal point of a Nd:YAG laser, which is used for heating the particle. Conventional optics are used to collect and spectrally analyze the radiation from the heated particle. Blackbody calibration techniques are used to allow conversion of this radiative signal into spectral radiance data, which may then be analyzed to provide spectral emissivity. The original operative concept of the apparatus necessary to make these spectral emissivity measurements is shown in Figure IV-1.

Calculations performed to predict the temperature achieved by laser heating of micron-size Al_2O_3 particles (discussed in detail in Section IV-B.3.c) using the representative values of n and k from the POPM literature survey report[Ref. IV-1] indicate that laser energy density fluxes near 10^4 watts/cm^2 are required to heat 4μm to 8μm diameter particles to 1000°K. Figure IV-2 presents this computed equilibrium temperature as a function of laser energy flux density. The time required to attain equilibrium is given in Figure IV-3 as a function of laser energy flux, and is seen to be on the order of a few tens of seconds for 4μm to 8μm particles of Al_2O_3. Maximum flux densities of 1.6×10^5 watts/cm^2 in a 48μm spot size diameter have

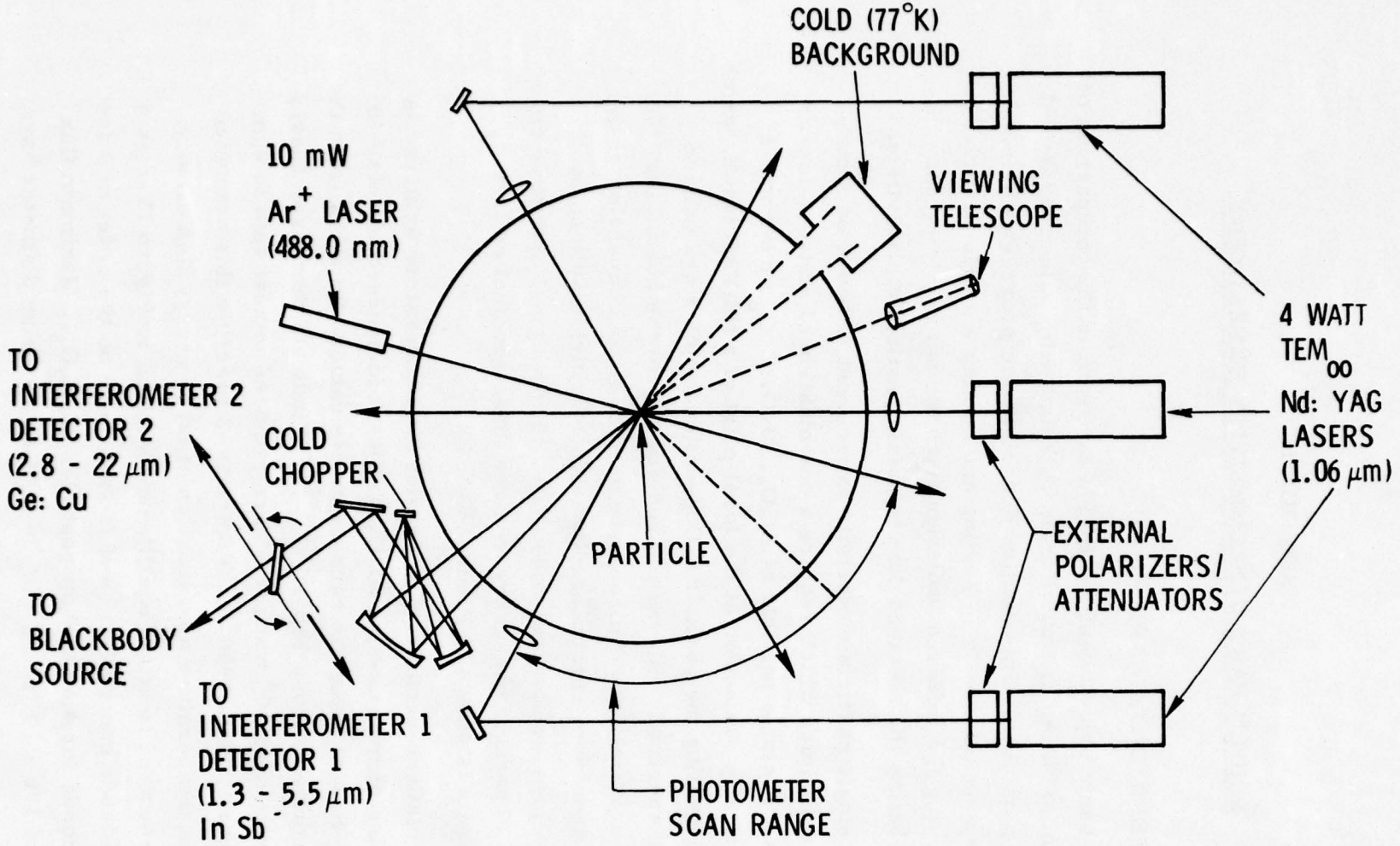

Figure IV-1. Particle emissivity experimental setup.

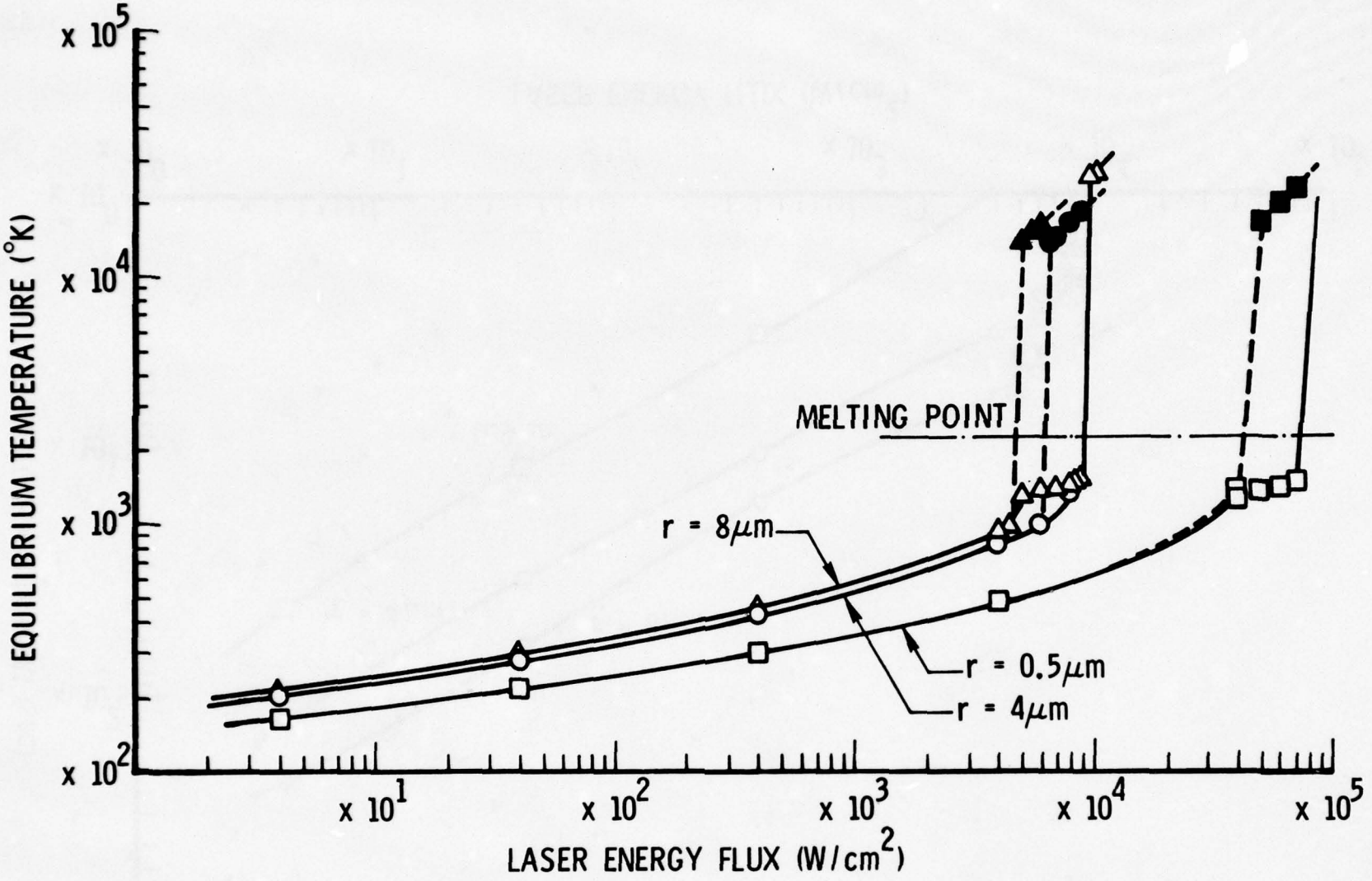

Figure IV-2. Equilibrium temperature of laser-heated Al_2O_3 particles.

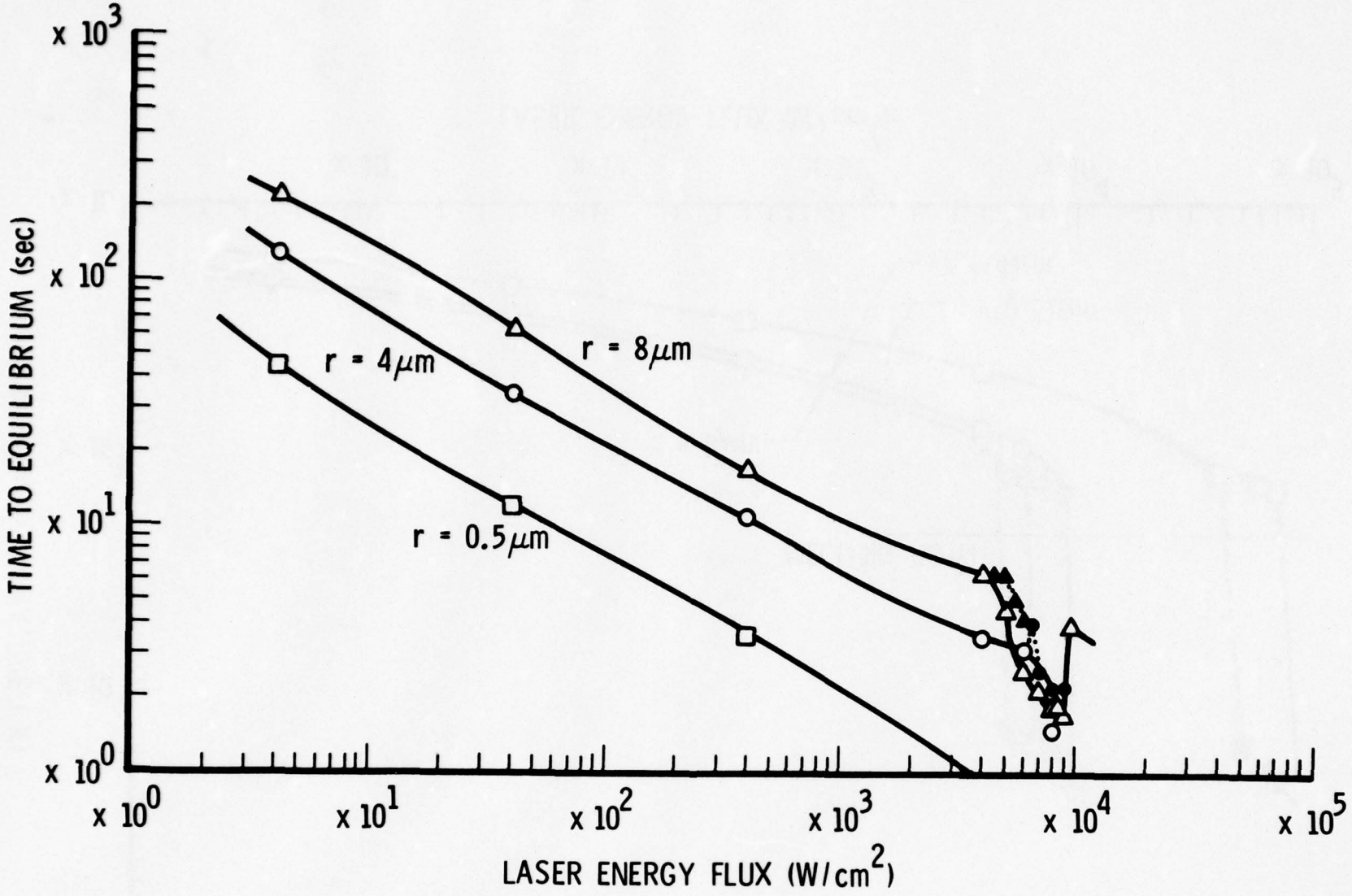

Figure IV-3. Time to attain equilibrium temperature for laser-heated Al_2O_3 particles.

been observed using a single 4-watt TEM_{00} Nd:YAG lasers and focusing optics (Section IV-B.3.b). This indicates the feasibility of heating Al_2O_3 particles to temperatures in excess of 1000°K. Based on these results we expect that MgO, ZrO_2 and carbon can also be heated to at least 1000°K, since these materials are less transparent, i.e., more absorbing, to the 1.06μm laser radiation than is Al_2O_3.

Signal to noise calculations assuming a collection solid angle of $\pi/9$, a .5μm diameter particle, and an interferometer efficiency of 0.4 (Section IV-B.4), along with reasonable detector electronics and background assumptions, predict for a 2sec observation time that 17 interferograms are required to obtain a S/N = 100 from observations of a 900°K particle. Thus we conclude that the actual detection and analysis of radiation from a small 1000°K particle should be possible.

The levitation of particles in the presence of forces produced by the intense radiation from the heating laser beams has required considerable effort. The commercially purchased Science Spectrum particle levitator which we expected to use proved to have unreliable electronics, and a sample cell which had to be modified for the present experiments. With the modified cell and electronics, particles of all four materials of interest were successfully levitated when introduced into the sample cell by means of an aspirator through the electrical discharge from a Tesla coil. We found, however, that a laser energy flux of 50 watts/cm^2, corresponding to the unfocused, polarized output of one Nd:YAG laser exerted sufficiently strong forces (radiation and/or photophoresis) upon the particle to drive it from the potential well of the levitator. The geometrical arrangement of three symmetrically placed beams proved to be ineffective in preventing particle loss, although with modified levitation electronics we were able to achieve retention times on the order of 10sec at full power. Retention of the irradiated particle at the levitation cell equilibrium position has only recently been achieved by replacing the three symmetrically oriented laser beams system with a two-laser opposed beam system in which

the focal points of the beams, and the laser powers, are carefully adjusted.

B. EMISSIVITY EXPERIMENT DESCRIPTION

1. Introduction

The experimental apparatus shown in Figure IV-1 modified to the two opposing laser configuration is shown schematically in Figure IV-4. Up to the conclusion of the work reported here no spectral measurements have been completed, so the external infrared optics consist of a collection mirror, chopper, and detector rather than the combination of blackbodies and interferometers planned in Figure IV-4. Two opposed 4-watt TEM_{00} Nd:YAG lasers are focused to a point at the particle equilibrium position in the levitator, for the purpose of particle heating. Through this point also passes the beam of an Ar^+ laser, used for illuminating the particle for position sensing. Figures IV-5 and IV-6 are photographs of the levitation cell and surrounding apparatus. Not shown are the Nd:YAG lasers and the Ar^+ laser. The rest of this section contains details of the subsystems which are critical parts of the particle emissivity experiment, as well as analysis methods for the reduction of infrared emission observations to obtain emissivity.

2. Levitation Apparatus

a. Cell Design

The configuration of the Science Spectrum Differential II levitation cell supplied by the manufacturer, shown in Figure IV-7, has been used except for modifications to the transparent window section. This portion of the cell has been modified to accept thin quartz windows to pass the Nd:YAG heating laser beams. An IR transparent window for viewing the thermal radiation from the particle was also added. It was found necessary to use 5-15cm long 6mm diameter

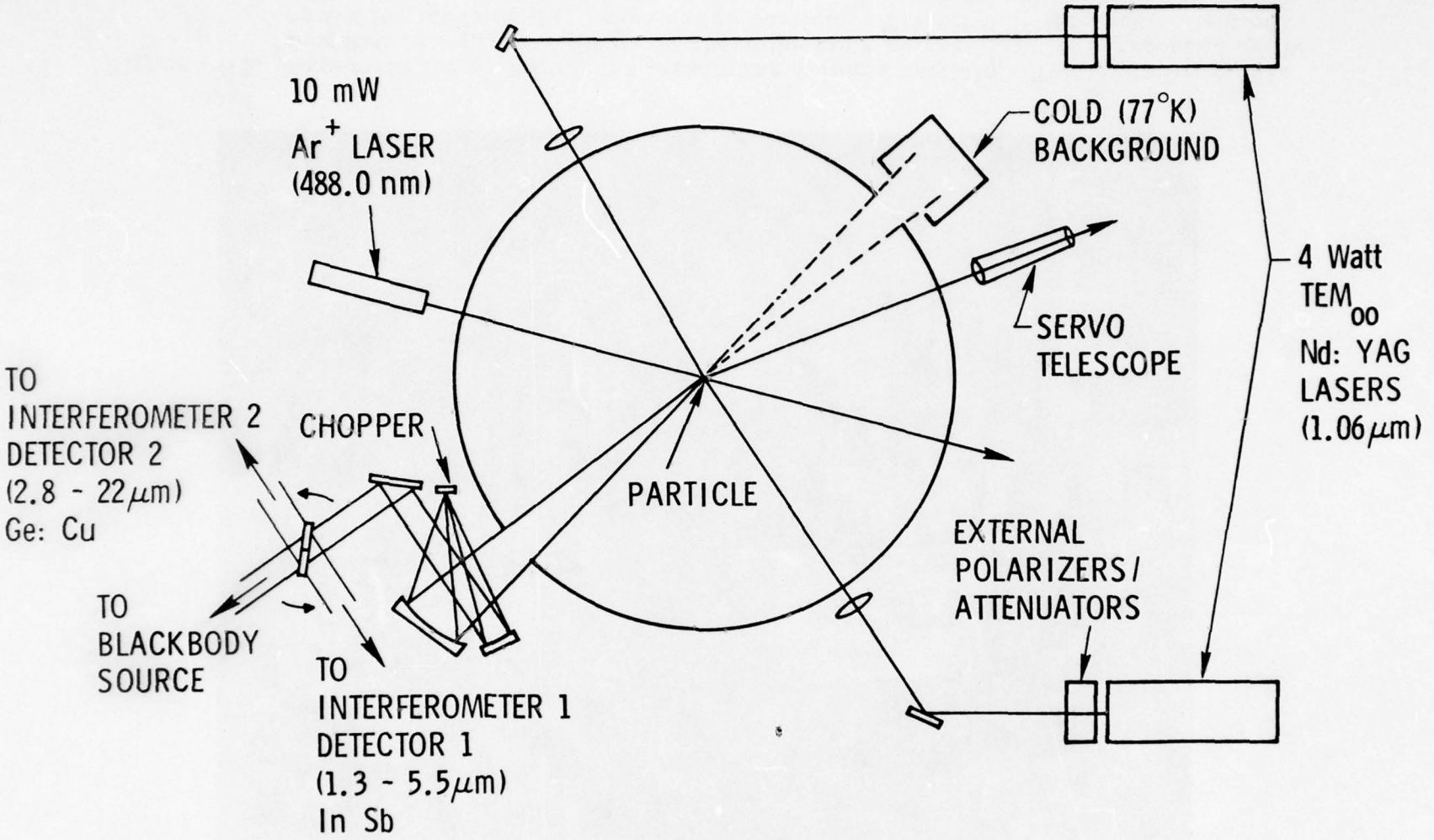

Figure IV-4. Schematic diagram of the particle emission experiment as modified for two opposing lasers for heating.

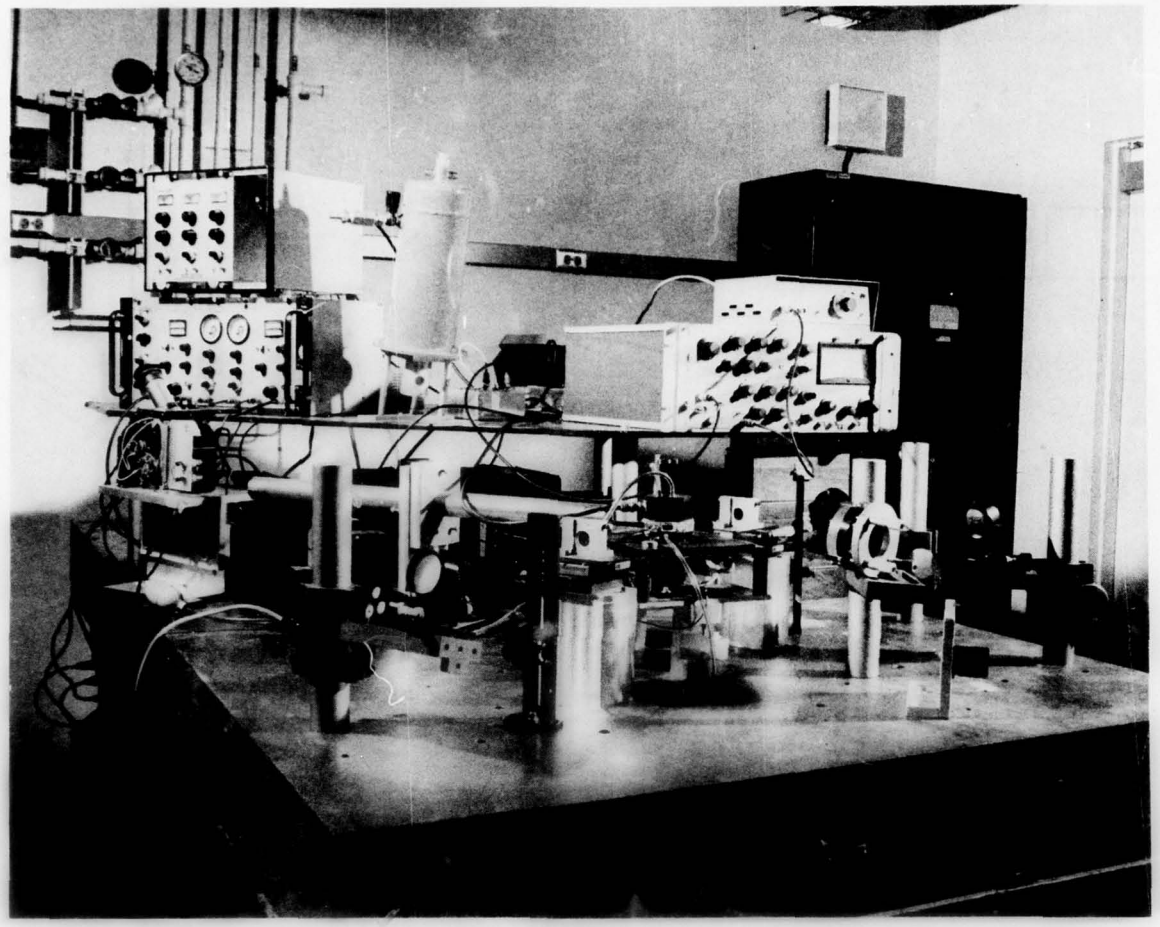

Figure IV-5. Apparatus for levitating and irradiating a single particle. The levitation cell is mounted on a platform elevated above the table surface, and is surrounded by the optics for focusing the lasers on the particle. The off-axis infrared collection mirror is near the right front of the table. The tube extending to the left from the cell is the telescope that brings the image of the particle to the electro-optical servo box. Under the shelf mounted on the table are the Nd:YAG lasers. On the shelf, starting from the left, are the levitation electronics, helium-cooled detector, and lock-in amplifier. Not visible is the Ar^+ laser mounted under the table.

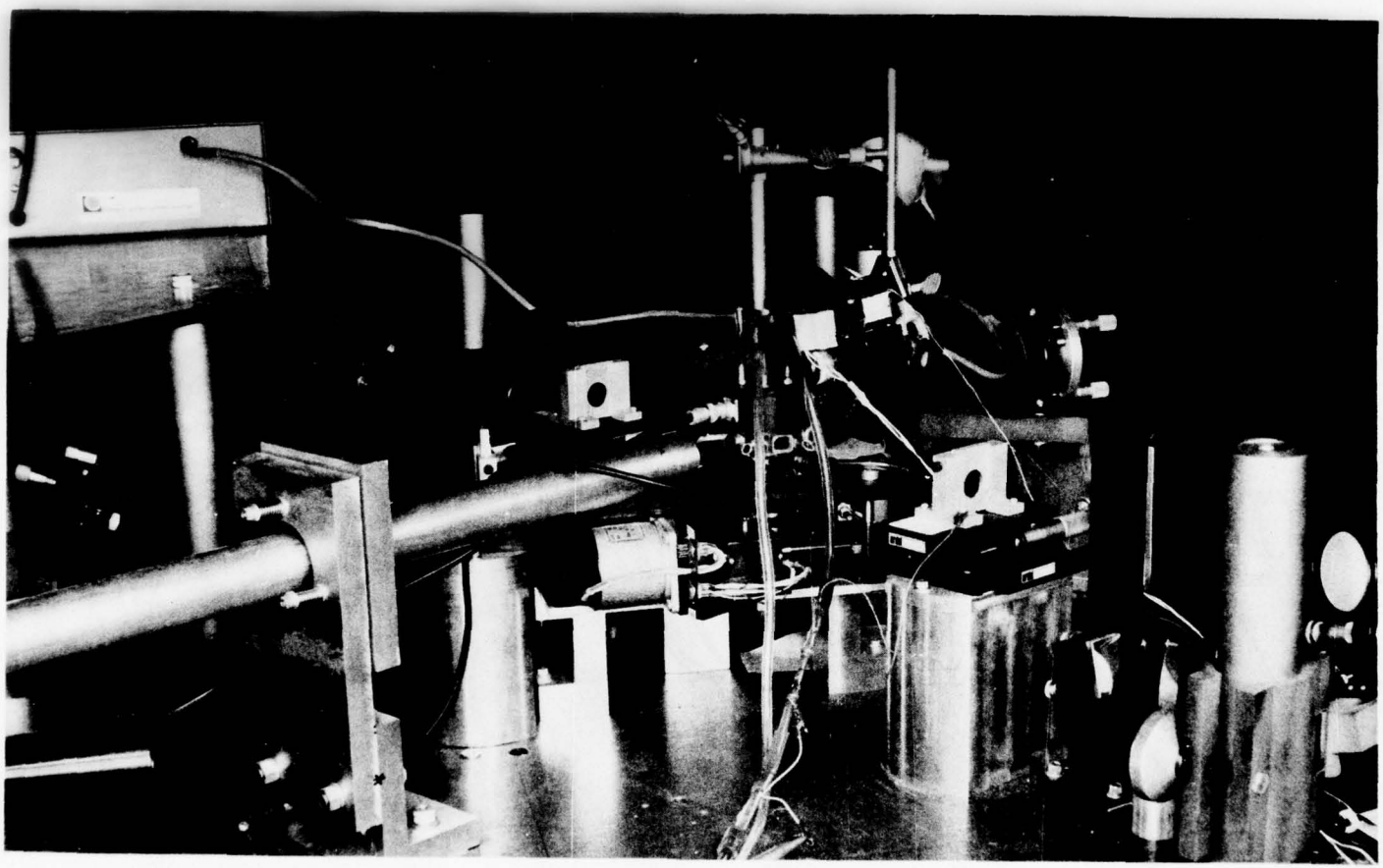

Figure IV-6. Close-up of the levitation cell, focusing lenses and telescope. The chopper and collection mirror are on the right far side of the levitation cell. The beam expanders for the Nd:YAG lasers are shown on the left.

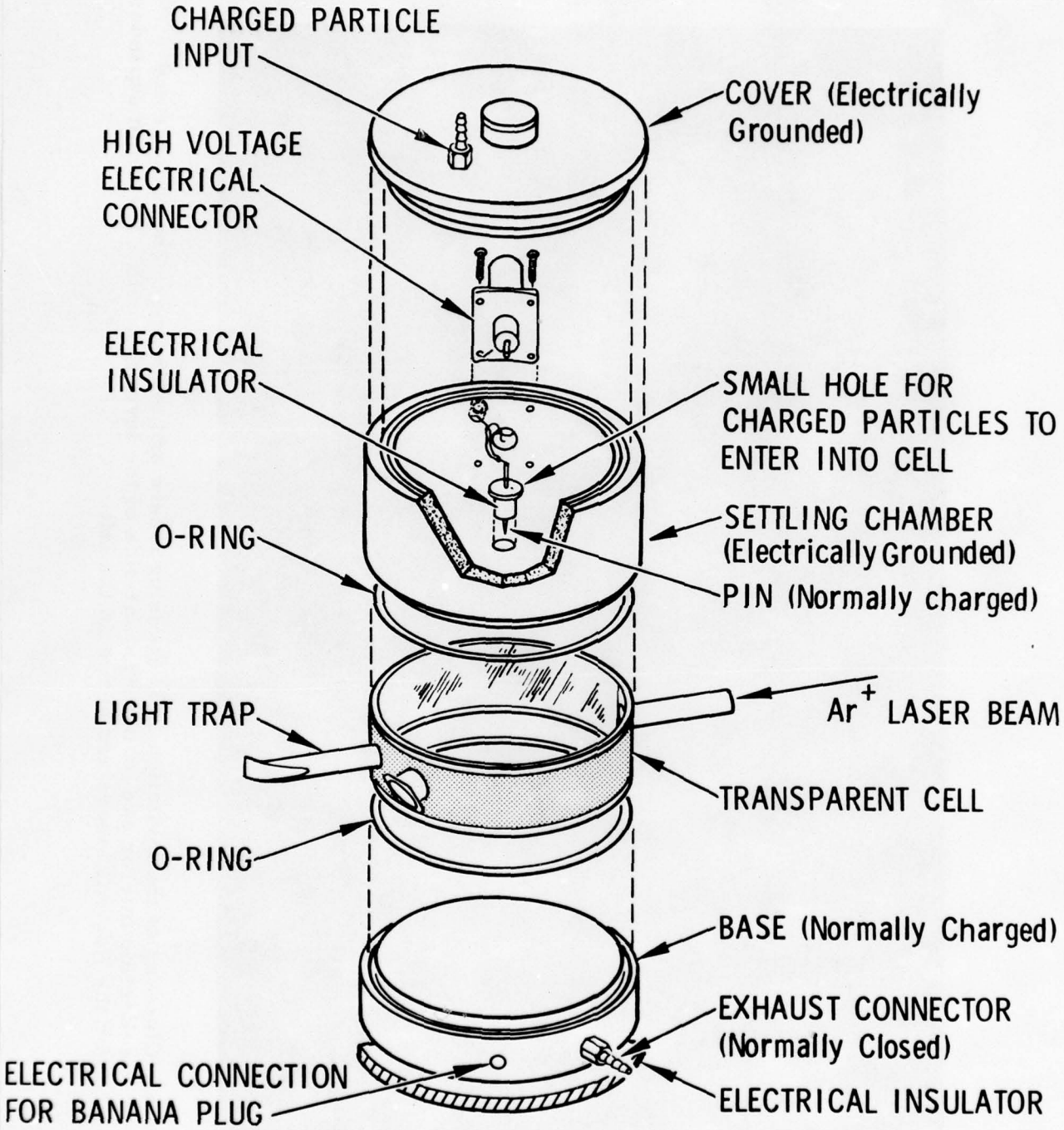

Figure IV-7. Scattering cell.

tubes, painted black inside, to space the Nd:YAG and argon ion laser beam windows away from the cell. This greatly reduced the levels of scattered light in the cell, and thus increased the sensitivity of the optical servo system.

Particles were charged in an RF discharge located in a glass tube through which sample particles were blown by a bulb. These particles passed through a length of rubber tubing, into the setting chamber, and on into the cell with sufficient charge for levitation. The exhaust connector was sealed closed after particle injection to prevent variations in outside air pressure from displacing a levitated particle.

b. Electronics

Several months of operation using the Science Spectrum Differential II levitation electronics demonstrated that these electronics were unreliable and difficult to repair. Interference problems from the RF discharge unit were insoluble, and required that the levitator be turned off while charged particles were injected. In addition, the maximum voltage output for the unit was $\leq$ 300 volts, which was not high enough to generate a potential well within the levitation cell of sufficient strength to hold particles in the presence of radiation produced forces. A new set of levitation electronics was therefore built. The block diagram of this unit is given in Figure IV-8. The image of the levitated particle illuminated by the argon ion laser is split horizontally and projected onto two 4818 photomultipliers. We retained the original optics designed for this purpose, but added a 61cm long 1:1 telescope to space the electro-optical servo box from the levitation cell. In addition, the two photomultiplier high voltage circuits were separated, so fine adjustments in the photomultiplier voltages could be made to compensate for slight differences in tube gains. Type 4818 tubes were employed instead of the original 1P21 tubes since these have a high gain with very low background noise level.

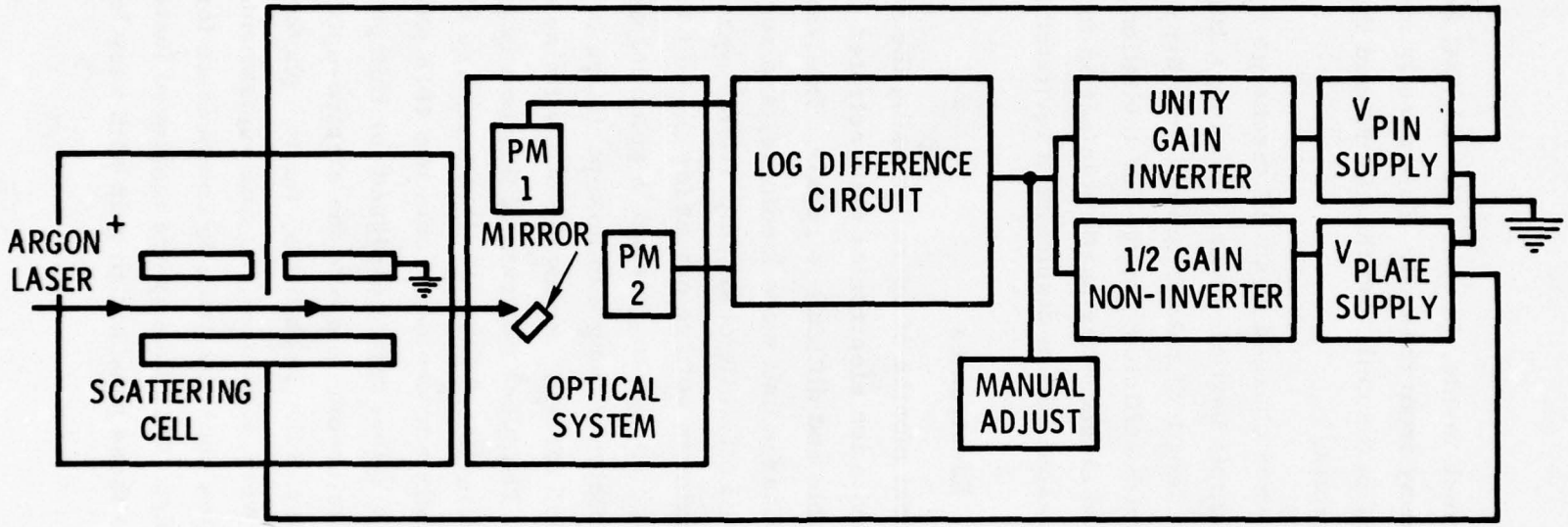

Figure IV-8. Block diagram of levitation electronics.

The two signals from the photomultipliers are processed by a log-difference circuit, and this output signal ultimately determines the voltages V_{pin} and V_{plate} in the cell. The top plate of the cell is ground, and V_{pin} is 2 x V_{plate}; the actual signs of V_{pin} and V_{plate} depend upon the charge of the levitated particle. Two Ortec Model 456 power supplies, slightly modified for msec voltage tracking characteristics, are used as high voltage supplies. The highest voltages attainable are on the order of 3kV but such high voltages cause arcing within the cell, so actual operation is usually in the 600 to 800 volt range for V_{pin}.

A future planned modification for this servo system involves the replacement of the two photomultipliers by a single split field solid state detector, UDT PIN SPOT/8D. This will eliminate two high voltage power supplies, a bulky optical system, and an expensive argon ion laser. The laser will be replaced by a low-cost 5mW HeNe unit.

c. Operational Details

Successful operation of the levitator is a skill which requires several hours of practice to acquire; however, particles can be captured and levitated in a matter of minutes by an experienced operator. The general procedure for levitating particles is as follows:

(1) Place the levitator electronics in the manual mode. This disconnects the optical servo and allows the operator to manually adjust voltages to hold a particle in the levitator during the period of time when other particles are settling out of the optical system field of view.

(2) Set the system gain to a level which results in only 100 to 200 volts maximum for V_{pin}. Higher gains make manual operation very difficult and result in the capture of particles with a smaller charge.

(3) Turn on the RF discharge and blow a cloud of charged particles into the cell.

(4) Capture a particle of the appropriate charge and hold it in position by manually adjusting the voltages until all other particles have settled out of the cell.

(5) Turn the levitator electronics to the servo mode; the particle should be held automatically at the equilibrium position.

(6) Increase the gain to a value which results in V_{pin} between 600 and 800 volts maximum; this should strongly hold the particle and greatly reduce any oscillations.

3. Particle Irradiation and Heating

The optical configuration required for successful irradiation of a levitated particle has been given in Figure IV-4. Two focused, opposed Nd:YAG lasers are used, together with coaxial HeNe alignment lasers. The laser output is first expanded using a Holobeam type 1006190 upcollimator, then focused to a point approximately 48μm in diameter by a 2.5cm diameter, 20cm focal length lens made from fused silica and antireflection coated for use at 1.06μm. This focusing lens has a depth of field on the order of 5mm. The lasers used for heating are two Holobeam 255 Nd:YAG CW lasers used in the TEM_{00} mode. Typical single mode output is ~4 watts CW. The laser energy flux measured at the focal point in the cell is $\sim 1.6 \times 10^5$ watts/cm^2. This is sufficient to heat particles in the size range of interest to temperatures in excess of 1000°K, as will be shown shortly. For convenient alignment purposes a Spectra-Physics Model 156 1mwatt HeNe laser is mounted with the Nd:YAG lasers and aligned to produce a .63μm beam colinear with the 1.06μm Nd:YAG beam.

a. Alignment

Alignment of the laser beams is a critical problem in this experiment because the Nd:YAG and levitator beams must intersect within a volume less than 20μm in diameter. We have demonstrated that the use of Oriel Model 1460 high precision mounts for beam adjustment mirrors allows micron-scale adjustments within the levitation cell. Initial beam adjustments are performed using the HeNe alignment laser. Final adjustments are then made with the Nd:YAG scattered signal from the particle, using an IR viewer.

Experiments have shown that a single focused Nd:YAG laser irradiating a particle in the levitator rapidly moves the particle away from the equilibrium position. The original concept of balancing laser-induced forces on the particle by means of three symmetrically placed beams has proven impossible to implement. Particle residence times in excess of 10sec in the cell were achieved with high cell voltages and some minor changes in cell electrode configuration, but the particle was ultimately lost.

The configuration of two opposed lasers has proven to be successful in irradiating the particle without moving it. Adjustment of the laser power levels to the point where the forces effectively cancel has proven to be quite difficult, and typically occupies approximately 30 minutes. With the irradiated particle in a stable position, observations on the order of hours are possible.

The focal points of the two lasers must be carefully placed to entrap the levitated particle, as shown in Figure IV-9. The radiative forces are proportional to the flux density in laser beams. Thus, for example, if the particle moves to the left F_2 increases and F_1 decreases, tending to return the particle to the neutral point. In fact, it is unimportant which direction the laser induced forces act on the particle since an adjustment of the focusing optics to interchange the positions of the focal points of the two lasers will compensate if the forces act in the opposite direction. This opposed laser balancing is required

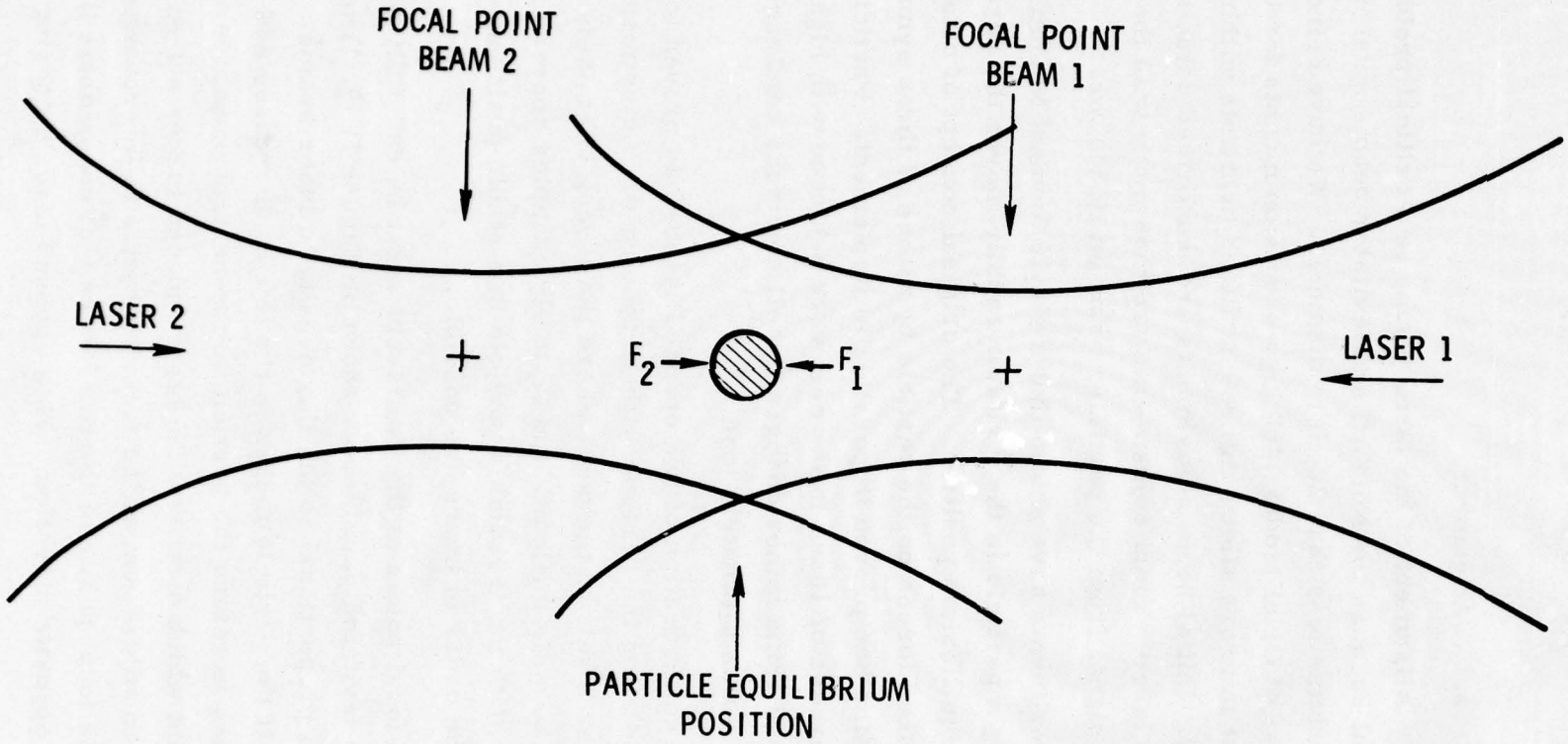

Figure IV-9. Schematic diagram of possible conditions for irradiated particle equilibrium in an opposed laser configuration.

because we observe that the radiation forces are strong compared to the potential well of the levitator. These observations are consistent with the order of magnitude calculations for photon momentum transfer to a particle through either absorption or reflection, and is illustrated in Figure IV-10.

b. Laser Flux Density Measurements

The success of the particle emissivity experiment in the POPM program depends critically on being able to heat the suspended particle with a high flux density laser beam. For micron-size Al_2O_3 particles flux densities of $\sim 10^5$ watts/cm^2 on the particle are needed to achieve temperatures near the melting point. Given a nominal five watt laser, this requires that the spot size, at the particle, be of the order of tens of microns in order to achieve the required flux density.

An experiment was performed to measure the maximum flux density obtainable from a nominal five watt, single mode, Nd:YAG laser. A description of this experiment and the results are contained in this section.

The flux density contour for a laser operated in the TEM_{00q} mode is Gaussian, and may be written

$$F(r) = F_0 e^{-(x^2 + y^2)/\sigma^2} = F_0 e^{-r^2/\sigma^2}$$

where F(r) is the flux density at a distance $r = (x^2 + y^2)^{1/2}$ away from the beam axis, $F_0 = F(0)$, and σ is a measure of how narrow the beam is. For instance, when $r = \sigma$, $F(\sigma)/F_0 = e^{-1}$, the so-called "one over e point". A plot of F(r) as a function of x and y (or r) is shown in Figure IV-11. This is the Gaussian or "bell shaped" surface, where x and y are the orthogonal spatial coordinates perpendicular to the laser beam axis and the z coordinate gives F(r), the flux density, at

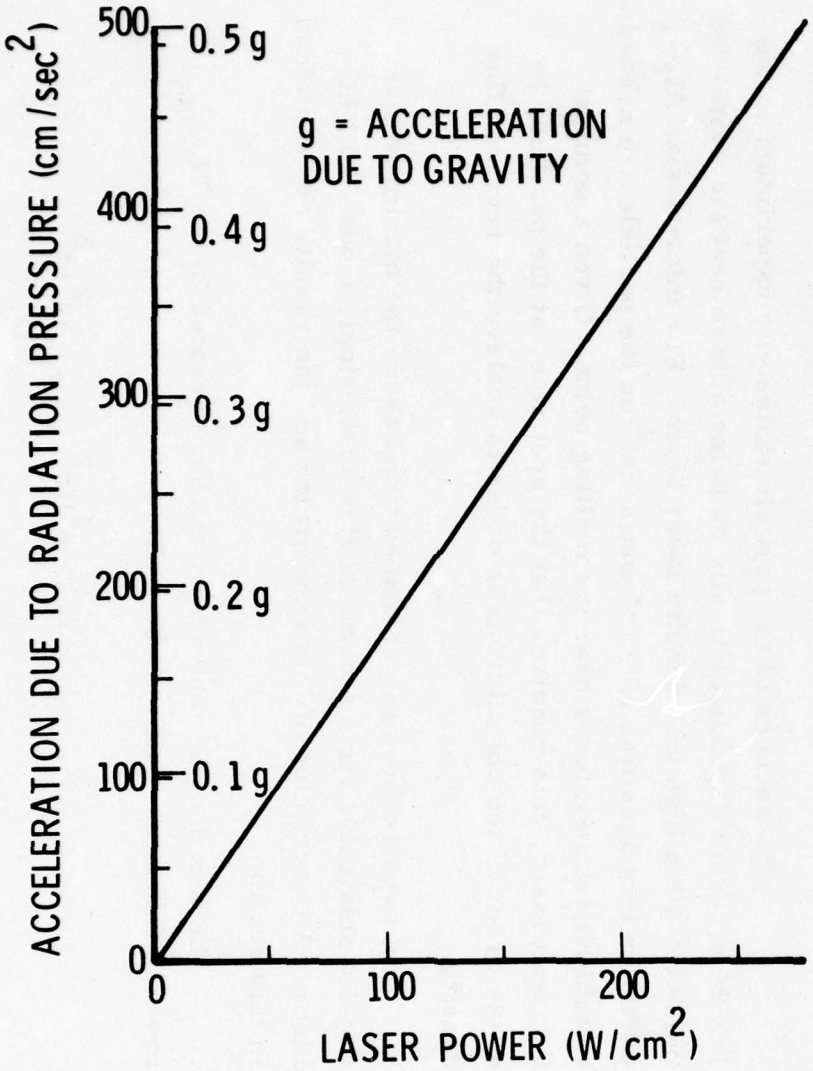

Figure IV-10. Computed acceleration of a 5μm carbon particle due to radiation pressure and neglecting all drag forces.

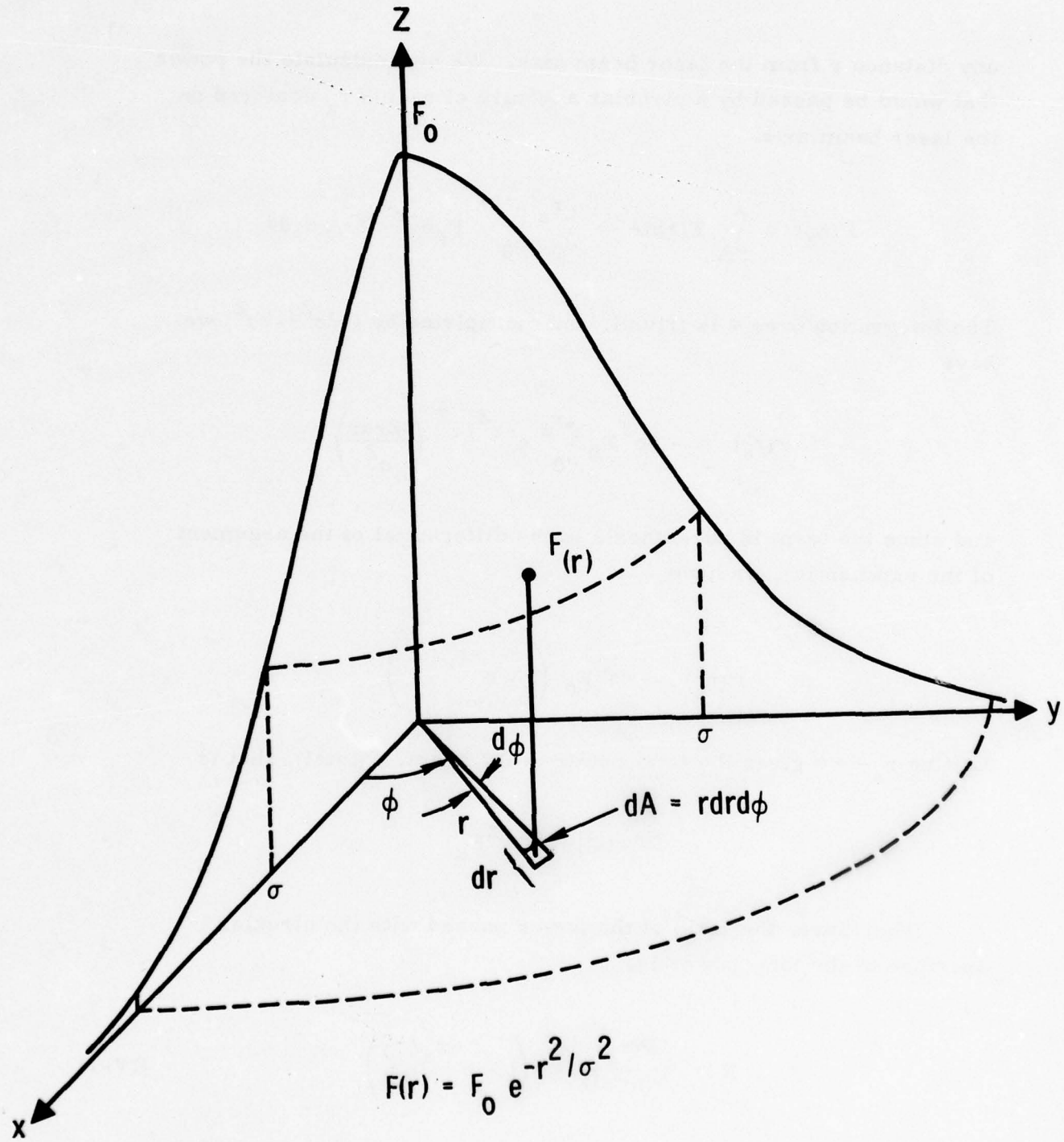

Figure IV-11. The Gaussian flux density surface

any distance r from the laser beam axis. We now calculate the power that would be passed by a circular aperture of radius r_a centered on the laser beam axis.

$$P(r_a) = \int_A F(r)dA = \int_0^{r_a} \int_0^{2\pi} F_0 e^{-r^2/\sigma^2} \, r dr d\varphi$$

The integration over φ is trivial, and multiplying by $(-2\sigma^2/-2\sigma^2)$ we have

$$P(r_a) = -\pi\sigma^2 F_0 \int_0^{r_a} e^{-r^2/\sigma^2} \left(\frac{-2rdr}{\sigma^2}\right)$$

and since the term in parenthesis is the differential of the argument of the exponential, we have

$$P(r_a) = \pi\sigma^2 F_0 \left(1 - e^{-r_a^2/\sigma^2}\right)$$

Letting $r_a \longrightarrow \infty$ gives the total power in the beam, P(total), that is

$$P(\text{total}) = \pi\sigma^2 F_0$$

Therefore, the ratio of the power passed with the circular aperture to the total power is,

$$R = \frac{P(r_a)}{P(\text{total})} = \left(1 - e^{-r_a^2/\sigma^2}\right) \qquad \text{(IV-1)}$$

Thus a measure of this ratio with a known pinhole radius determines σ, or how narrow the beam is.

A schematic of the laser flux density experiment is shown in Figure IV-12. The laser beam is expanded and goes into a beam alignment device which allows the beam to be translated in any direction perpendicular to the axis of the beam. The beam is focused by a lens and somewhat after the focus point is located a detector which intercepts the entire beam. The beam profile is probed by means of a pinhole aperture which can be moved along the axis of the beam.

The beam diameter, σ, will be a function of where along the beam the pinhole is located, and by definition has a minimum value at the focus. Flux density will be a maximum where σ is a minimum.

The experimental data were obtained as follows. With the pinhole aperture removed, the laser was adjusted to give three watts at the detector (detector element area large with respect to beam diameter). The pinhole aperture was mounted on a micrometer stage such that its 12mm travel was approximately centered on the focal point. Power passed by the pinhole aperture was measured as a function of distance (d in Figure IV-12) in steps of 0.25mm. The pinhole aperture center could not be made to center on the laser beam axis exactly (crude analysis indicates it moved about 20μ over a travel of 3.75mm). However, the beam alignment device provided the mechanism whereby the beam could be translated so that it could be centered on the pinhole. A typical set of data is given in Table IV-1. The first column gives the micrometer reading, and the second column the number of watts passed by the 99μm diameter pinhole aperture. The third column is the ratio $P(r_a)/P(\text{total})$, and the fourth column is the value of σ calculated from equation IV-1. The data are plotted in Figure IV-13. The error bars were determined assuming an error of $\pm$ 0.05 watts and are representative of the noise encountered in the measurements. A smooth curve was drawn, and although it is not a fit in the least squares sense, it is estimated from the minimum in the curve and the size of the error bars that,

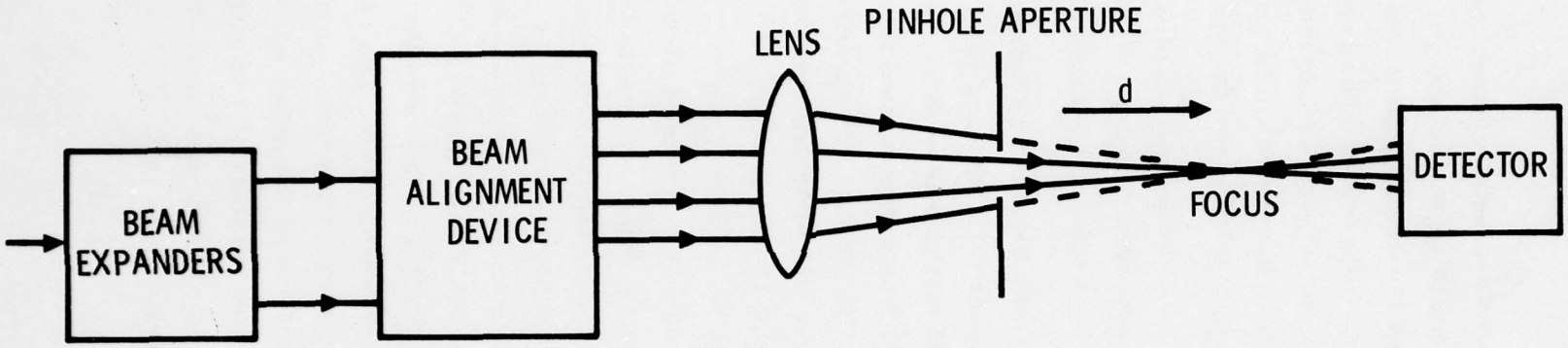

Figure IV-12. Schematic of focused heating laser flux measurement apparatus.

Table IV-1. Pinhole probe data of laser intensity.

d(mm)	Power (watts)	$P(r_1)$/ P(total)	$\sigma(\mu m)$
6.50	2.45	0.817	38.0
6.75	2.65	0.883	33.8
7.00	2.82	0.940	29.5
7.25	2.85	0.950	28.6
7.50	2.87	0.957	27.9
7.75	2.90	0.967	26.8
8.00	2.92	0.973	26.1
8.25	2.97	0.990	23.1
8.50	2.95	0.983	24.5
8.75	2.90	0.967	26.8
9.00	2.85	0.950	28.6
9.25	2.75	0.917	31.4
9.50	2.70	0.900	32.6
9.75	2.45	0.817	38.0

P(total = 3.00 watts

r_a = 49.5μm

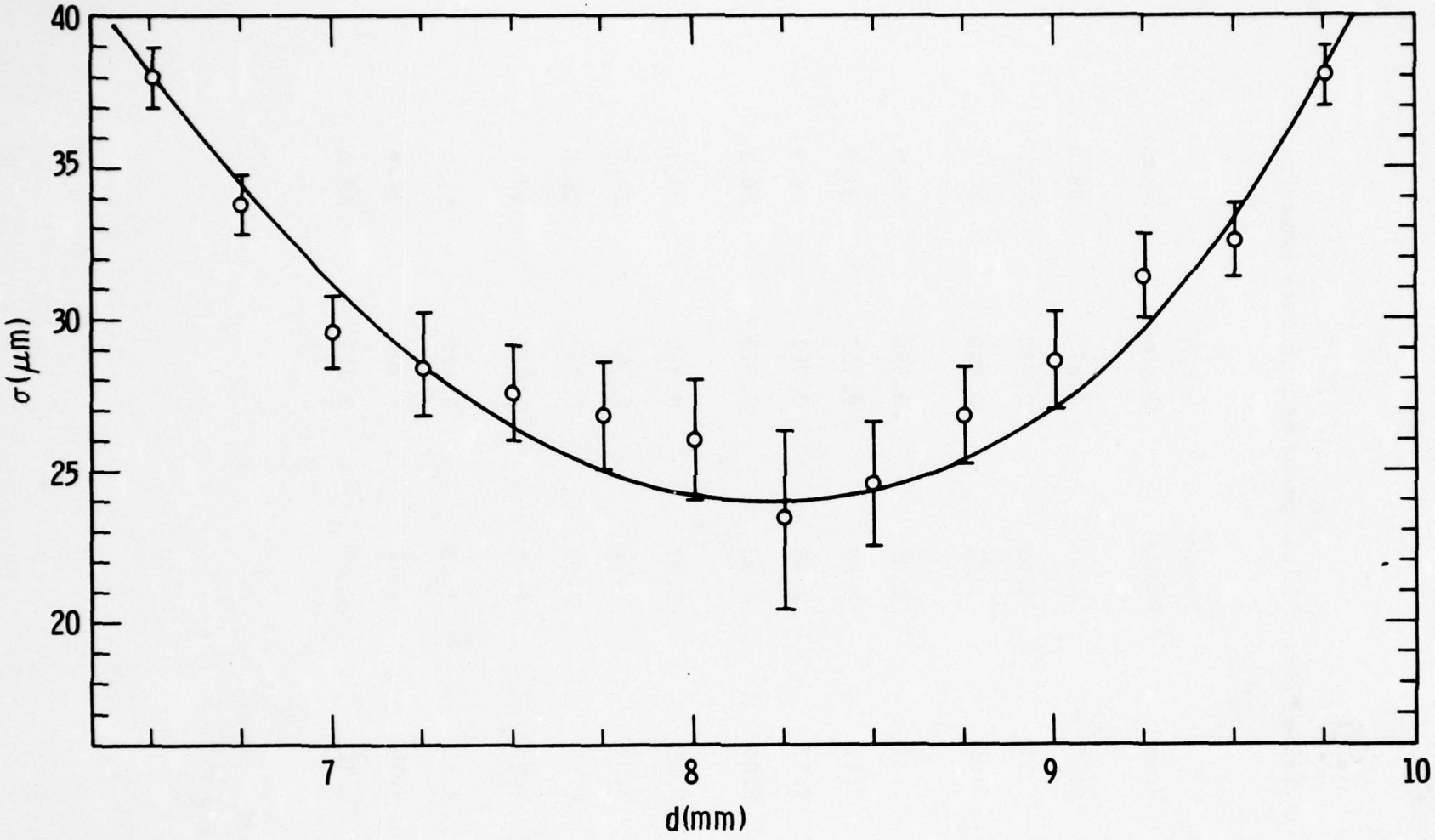

Figure IV-13. Heating laser beam diameter σ versus d from pinhole data.

$$\sigma(\text{min}) = 24 \pm 2\mu\text{m}.$$

When $r = \sigma$,

$$R = \frac{P(\sigma)}{P(\text{total})} = 1 - e^{-1} \simeq 0.6321,$$

which says 63.21 percent of the power in the beam is confined in a circle whose radius is σ. The average flux density is then,

$$F(\sigma)_{avg} = \frac{(0.6321)\ P(\text{total})}{\pi\sigma^2} \frac{\text{watts}}{\text{cm}^2}$$

When the laser is optimally tuned and the excitation lamp is operated near maximum output, P(total) $\simeq$ 4.5 watts and using $\sigma = 24\mu$m, we obtain

$$F(\sigma)_{avg} = 1.57 \times 10^5 \text{ watts/cm}^2$$

The choice of the "one over e point" as the limiting radius is somewhat arbitrary. What it means, however, is that if we could center a 48μm diameter particle in the laser beam, it would experience an average flux density of $\sim 1.6 \times 10^5$ watts/cm^2. For a smaller particle the average flux would be higher. For instance, for a 24μm diameter particle (i.e., $\sigma/2$) we have

$$F(\sigma/2)_{avg} = \frac{(0.2212)\ (4.5)}{\pi(1.2 \times 10^{-3})} \frac{\text{watts}}{\text{cm}^2} = 2.20 \times 10^5 \frac{\text{watts}}{\text{cm}^2}$$

It will be shown in the following section that it should be possible to melt Al_2O_3 micron-sized particles with flux densities in this range.

Figure IV-13 also provides an estimate of the depth of field we have at our disposal. If we allow σ to vary by $\sim$ 10 percent (2.5μm) the allowable variation in d is $\sim$ 1.3mm (see Figure IV-12). That is, if we locate the particle to within $\pm$ 0.65mm of the true σ(min) we will have a maximum degradation of $\sim$ 20 percent in flux density.

c. Laser Heating of Particles

This subsection describes the results of computer calculations of the laser particle heating scheme for aluminum oxide. Ignoring convection and conduction the basic heat transfer equation applicable to laser irradiation heating is:

$$H\sigma = \frac{4}{3}\pi r^3 \rho C_p \frac{dT}{dt} + 4\epsilon \int \frac{C_1 \lambda^{-5}}{\exp(C_2/\lambda T)-1} d\lambda - 4\epsilon \int \frac{C_1 \lambda^{-5}}{\exp(C_2/\lambda T_0)-1} d\lambda \quad \text{(IV-2)}$$

where H is the incident laser power, σ the absorption efficiency factor, r the particle radius, ρ the particle density, C_p the heat capacity of the particle, T the temperature, T_0 the temperature of the surroundings, t the time, ϵ the emissivity, C_1 the first radiation constant, C_2 the second radiation constant, and λ the wavelength of the radiation emitted. The term on the left describes the steady-state energy input to the particle from the laser. The first term on the right side of the equation describes the heat stored within the particle. The second term describes the energy emitted by the particle as a blackbody. The last term describes the energy absorbed by the particle from the surroundings.

A program was written which computed the particle temperature as a function of time. The calculations were carried out long enough in time for equilibrium to occur. Since equation IV-2 is a differential equation in time, the methods of numerical analysis had to be used to perform the integration. The Runge-Kutta method was used to perform the integration.

The parameters of equation IV-2 were evaluated from the best available data for aluminum oxide. Three values of the particle radius were used for the calculations – 0.5, 4.0 and 8.0μm. The density of Al_2O_3 [Ref. IV-2] was taken to be 3.965gms/cm^3. The heat capacity of aluminum oxide is a function of temperature as is shown in Figure IV-14.[Ref. IV-2] These data were tabulated at closely spaced temperature intervals and interpolated linearly by the computer. The emissivity of aluminum oxide was taken to be 0.85 in the wavelength interval of 4.5 to 11.5μm and 0.0 outside this range. This is a reasonable approximation of the data of Mergerian[Ref. IV-3] which is shown in Figure IV-15. The blackbody integrals were evaluated over the corresponding wavelength interval – 4.5 to 11.5μm. The efficiency factor for absorption, σ, was calculated from Mie theory for λ = 1.06μm and the three particle radii given above from absorption coefficient data. The absorption coefficient of aluminum oxide is also a function of temperature. Unfortunately, there does not exist data by the same experimenter and apparatus over the whole temperature range of interest. Mergerian[Ref. IV-3] covers the range from 373 to 1273°K. Gryvnak and Burch[Ref. IV-4] cover the range from 1473 to 1973°K. Unfortunately, the two sets of data do not join smoothly. The calculated efficiency factors for absorption are shown in Figure IV-16. The discontinuity around 1400°K is obvious. The data were linearly interpolated by the computer. For some high temperature calculations an artificial value of σ at 1473°K was inserted. This artificial value is a simple interpolation of the data at 1273 and 1773°K and are shown as solid symbols on Figure IV-16. The laser power was varied between 40 and 4×10^5 watts/cm^2. The laser intensity measurements described in the previous subsection show that the Nd:YAG lasers used in the particle experiment are capable of fluxes as high as 2×10^5 watts/cm^2.

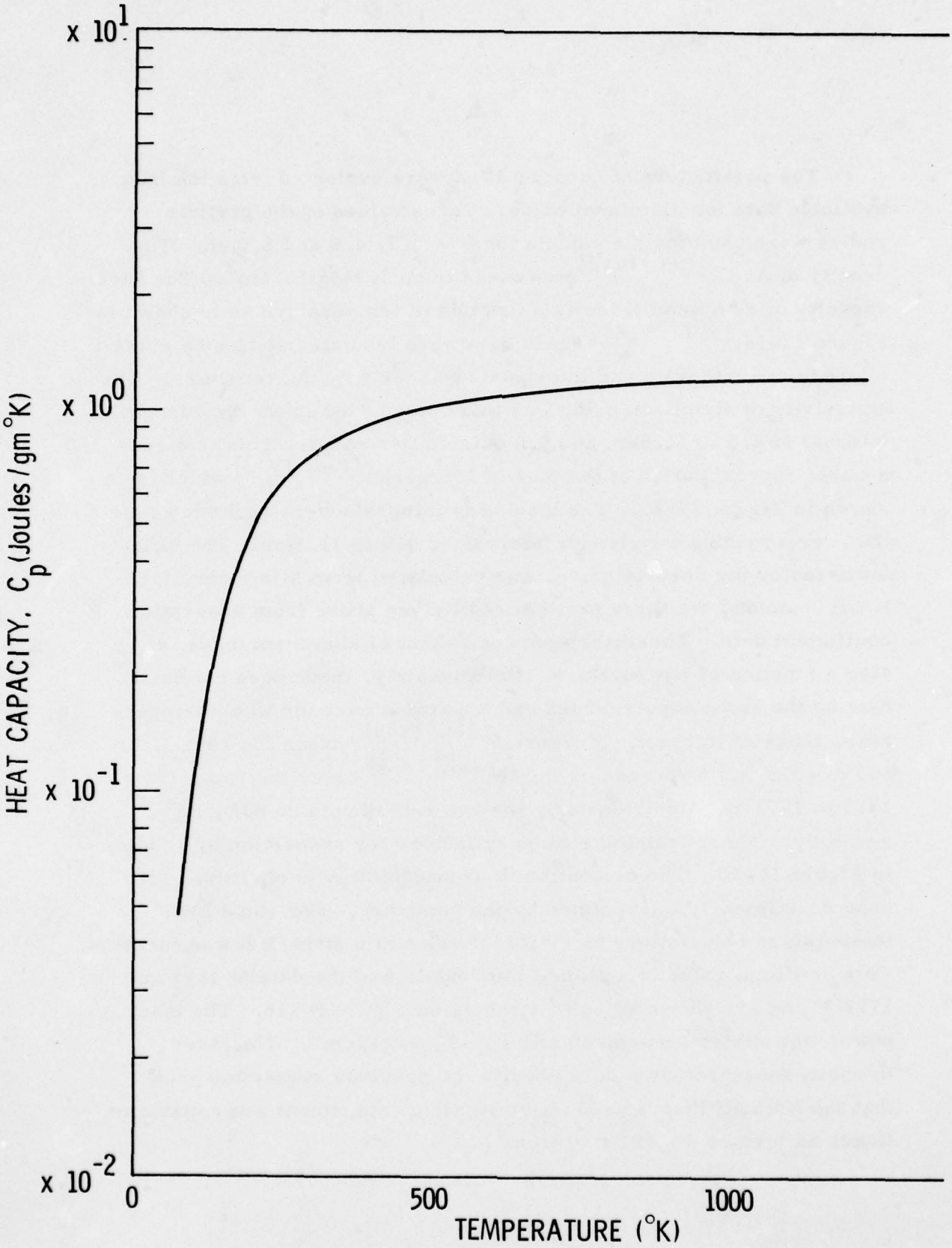

Figure IV-14. Heat capacity of aluminum oxide, Al_2O_3 (from Lange, Ref. IV-2).

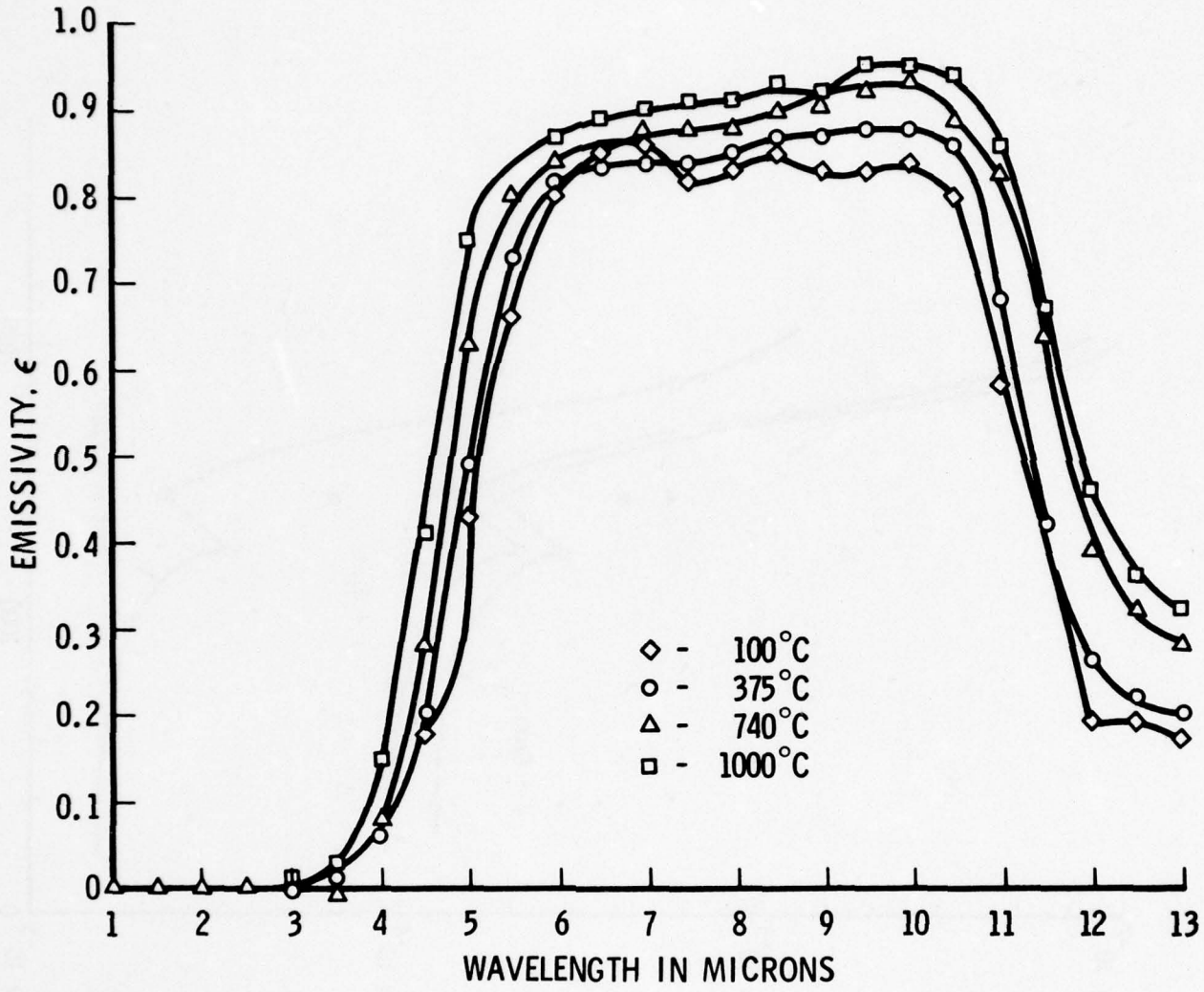

Figure IV-15. Emissivity as a function of wavelength for sapphire (Al_2O_3) of 5mm thickness (from Mergerian, Ref. IV-3).

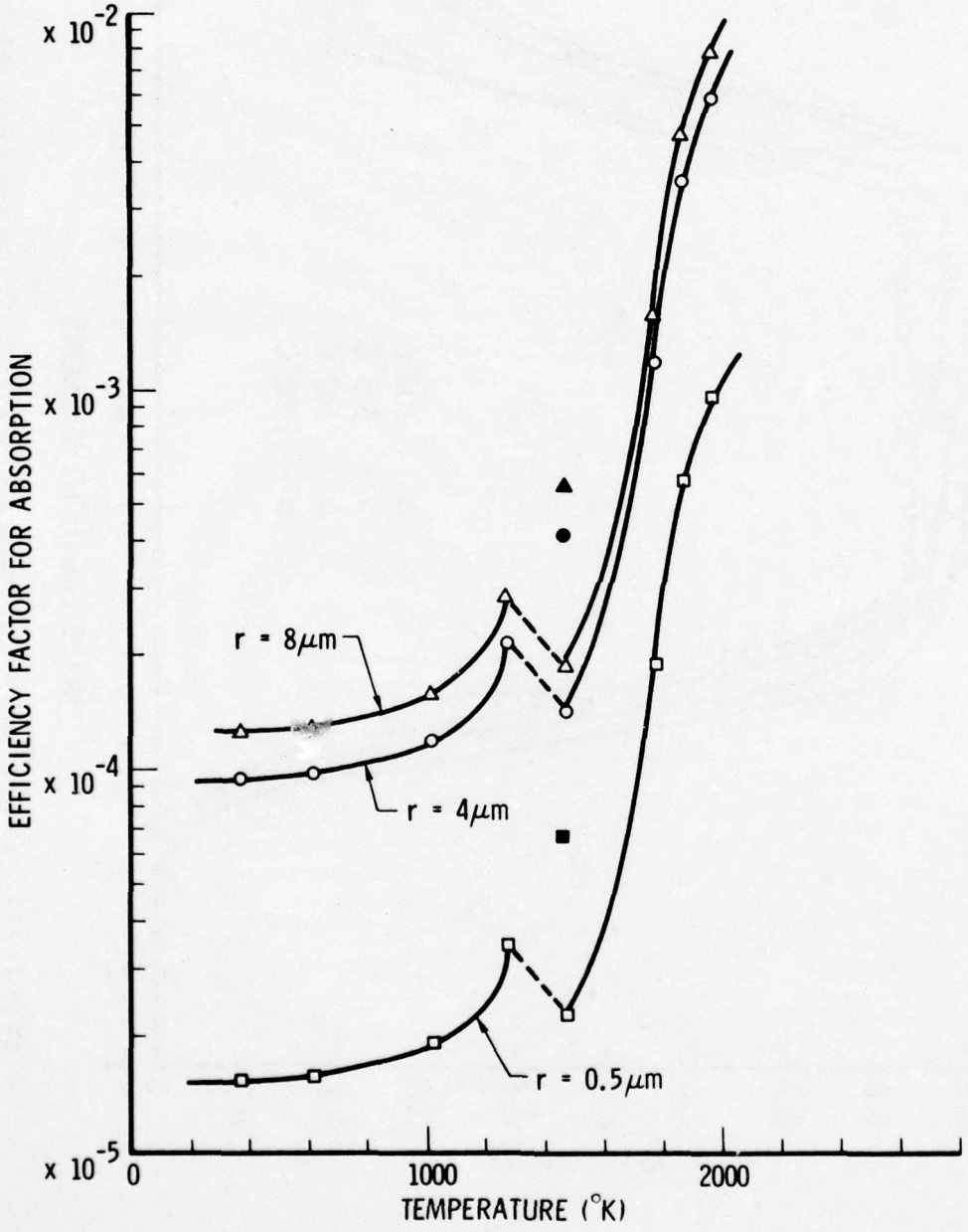

Figure IV-16. Computed efficiency factor for absorption of 1.06μm radiation by Al_2O_3 as a function of temperature.

The results of the calculation are given in Table IV-2 and in Figures IV-2 and IV-3. Figure IV-2 shows the equilibrium temperature attained as a function of laser power. Figure IV-3 shows the time required to achieve this equilibrium temperature as a function of laser power. The open symbols are for the unsmoothed σ data and the solid symbols for the artificially smoothed σ data.

The results shown in Table IV-2 show an interesting feature of the time history of the heating of a particle. That is the asymptotic approach to equilibrium. The length of time to achieve the last one percent of the equilibrium temperature, particularly at low laser power levels, can be significant. For example, 16μm diameter particles with 40 watts/cm^2 incident laser power attain 99 percent of the equilibrium temperature in less than one minute but require almost three more minutes to achieve the last one percent. Great care must be exercised when conducting the particle emissivity experiments to allow sufficient time for equilibrium to be attained. Figures IV-17 and IV-18 show the time history of the heating of various diameter particles for two different laser power levels. In general, the small particles equilibrate much more rapidly than the larger particles. Also, the higher the laser power, the faster equilibrium is attained.

The calculations indicate a potential problem with aluminum oxide. This problem is graphically illustrated in Figure IV-2 with the step function behavior of the equilibrium temperature. The problem is thermal runaway caused by the precipitous increase in the efficiency factor for absorption of energy above 1500°K. Figure IV-19 is an additional illustration of this problem. This figure shows the time history of the heating of a 16μm diameter particle with an incident laser power level of 6×10^4 watts/cm^2. The calculations were made with the smoothed data for the efficiency factor for absorption. The temperature of the particle is well behaved up to 1600-1700°K at which point thermal runaway occurs. If the absorption coefficient of

Table IV-2. Results of laser heating calculations.

(Assuming a 77°K background)

Laser Power W/cm^2	Particle Radius μm	Equilibrium Temperature °K	Time to Equilibrium (seconds)	Time to (T_{eq}-1%) (seconds)
40	0.5	161.65	45.7	12.5
40	4.0	200.73	130.7	33.5
40	8.0	208.41	221.3	56.7
400	0.5	213.82	12.3	3.2
400	4.0	280.28	35.0	8.9
400	8.0	293.91	64.4	15.0
4000	0.5	303.64	3.54	0.85
4000	4.0	431.80	11.04	2.49
4000	8.0	460.41	17.24	4.27
4×10^4	0.5	481.35	0.899	0.242
4×10^4	4.0	831.02	3.58	0.920
4×10^4	8.0	937.59	6.60	1.69
5×10^4	8.0	1304.11 [14183.4]	4.61 [6.41]	3.24 [4.21]
8×10^4	4.0	1356.83 [16775.9]	1.49 [2.20]	0.700 [1.08]
4×10^5	0.5	1294.90 [13827.9]	0.496 [0.615]	0.400 [0.467]
5×10^5	0.5	1359.26 [16990.5]	0.167 [0.266]	0.086 [0.134]

Note: Figures in brackets are from calculations using the smoothed value of σ at 1473°K.

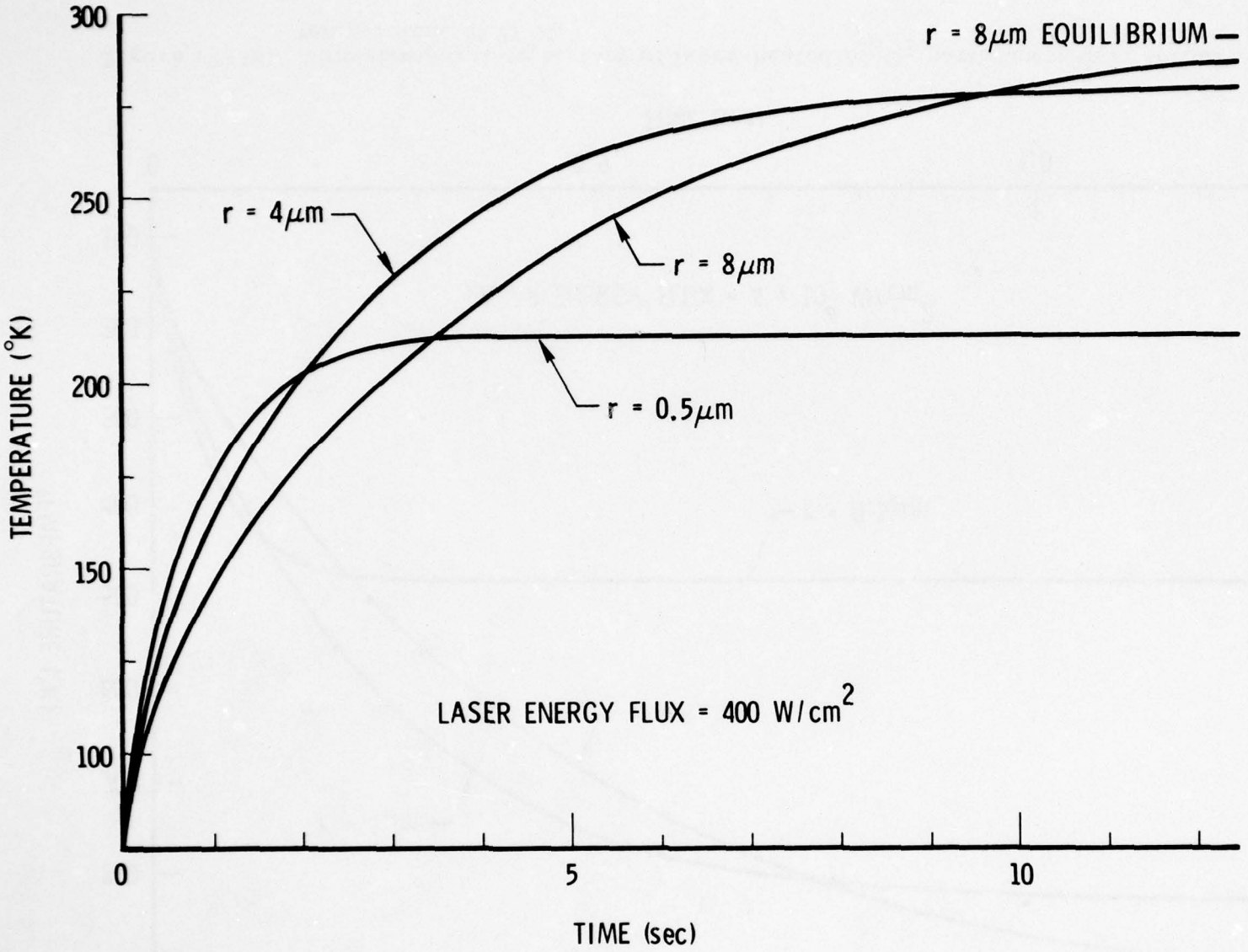

Figure IV-17. Time-temperature history of laser-heated Al_2O_3 particles with an initial temperature of 77°K.

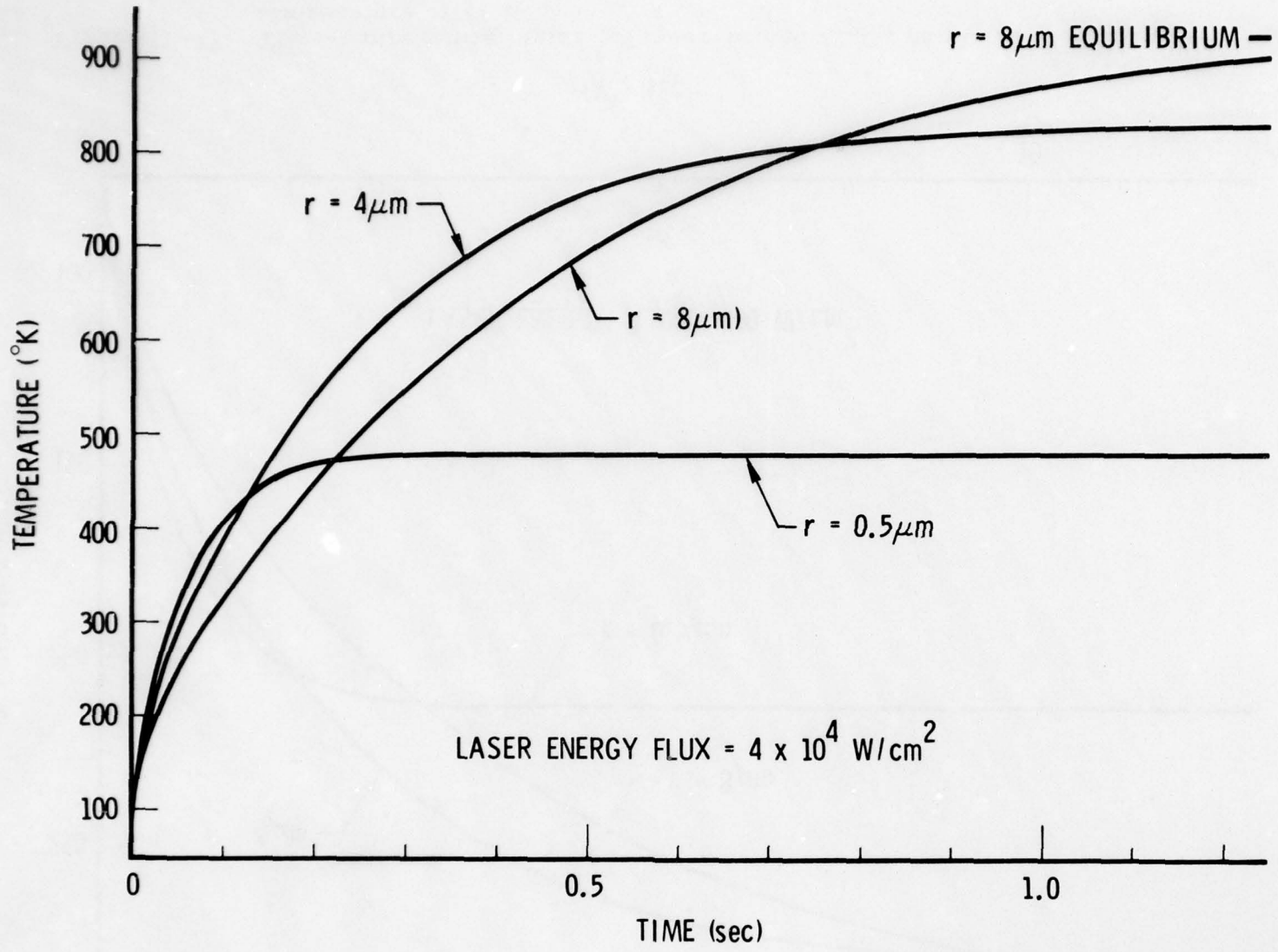

Figure IV-18. Time-temperature history of laser-heated Al_2O_3 particles with an initial temperature of 77 °K.

AD-A042 144 AEROSPACE CORP EL SEGUNDO CALIF CHEMISTRY AND PHYSICS LAB F/G 20/8
INFRARED EMISSIVITIES OF MICRON-SIZED PARTICLES OF C, MGO, AL S--ETC(U)
APR 77 J M DOWLING , C M RANDALL F04701-76-C-0077
UNCLASSIFIED TR-0077(2641)-1 AFRPL-TR-77-14 NL

3 OF 3
ADA042144

END

DATE FILMED
8-77

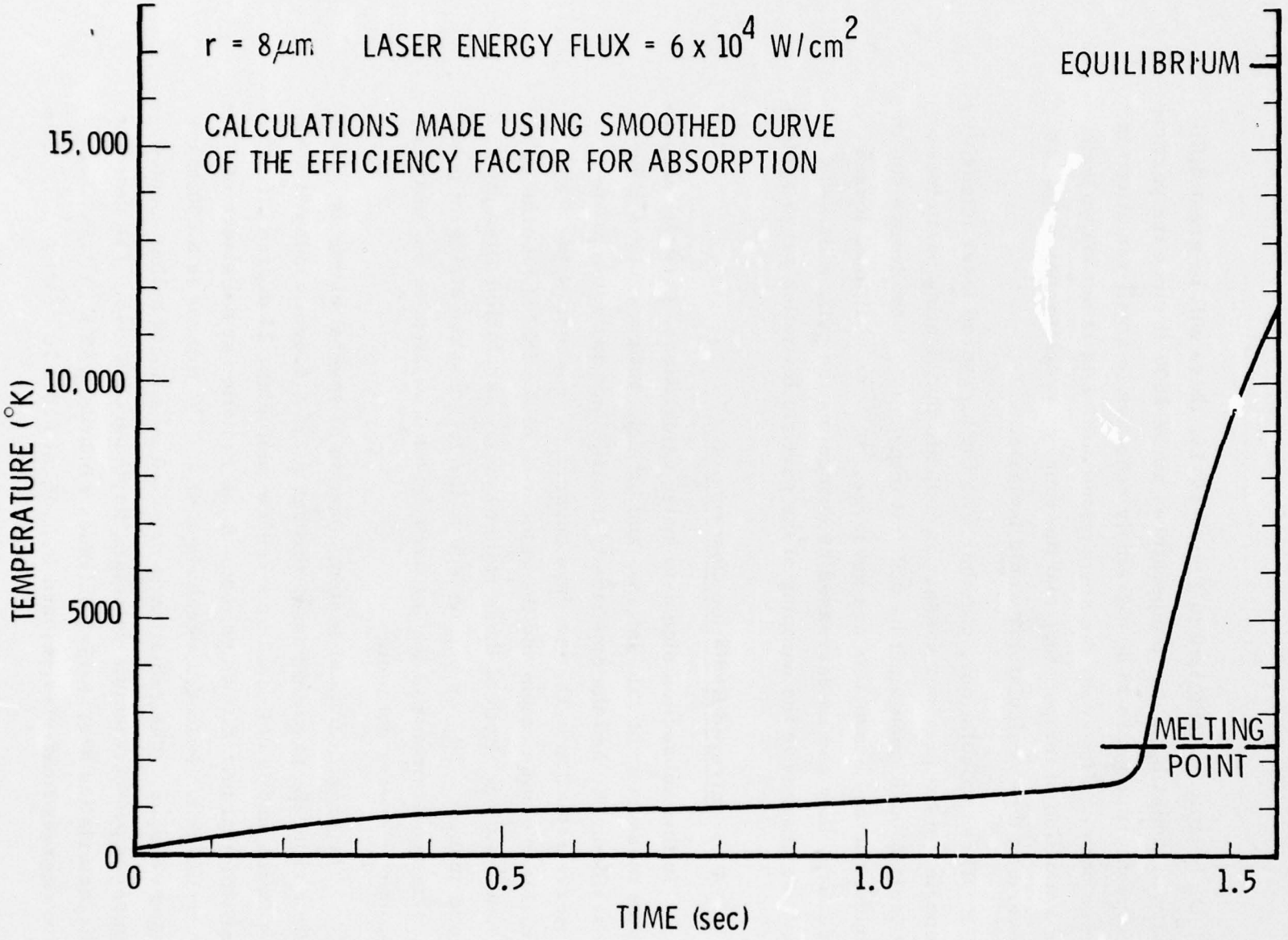

Figure IV-19. Time-temperature history of laser-heated Al_2O_3 particles with an initial temperature of 77°K. Calculation based on smoothed curve of absorption efficiency factor.

Al_2O_3 is truly as indicated in Figure IV-16, there will be great difficulty in achieving stable temperatures above 1600°K since the particle temperature appears to be extremely sensitive to small variations in laser power. However, the absorption coefficient is not known well as a function of temperature and the runaway problem may not be as severe as these calculations would indicate.

These calculations, together with the measured laser intensities reported in the previous subsection indicate that heating particles to at least 1000°K should not be difficult in principle if the losses due to convection and conduction are not large. If these additional losses are large they can be decreased by evacuating the cell, which will require changes in the damping of the particle levitation servo system.

4. Infrared Radiation Observation

In this subsection signal-to-noise calculations, particle temperature measurement calculations, and optical configurations will be described. We had the opportunity to make only two attempts to observe radiation in the few days between the success of the stable two-laser configuration and the relocation of the POPM laboratory to a new building. Both of these rather quickly assembled attempts were unsuccessful, we believe due to the fact that the stringent positioning requirements of the infrared detector relative to the image of the particle were not met.

The present optical system consists of several elements. Radiation from the particle passes through a .75 x 1.5cm window in the cell wall, and is collected by a 7.95cm diameter, 23 degree off-axis paraboloidal mirror, which focuses the radiation at a distance of ~1m from the cell. Placed between the cell and the mirror is a 790Hz circular chopper. The radiation is detected by a liquid helium-cooled copper doped germanium detector, Raytheon QKN1546. The detector characteristics are: KRS-5 entrance window, $7.85 \times 10^{-3} cm^2$ area, five degrees field-of-view, and N.E.P. of $6.8 \times 10^{-12} WHz^{-1/2}$. The

procedure for optical alignment will be to use the detector without a blocking filter to detect the scattered 1.06μm Nd:YAG laser radiation from the particle. When this is accomplished, a broadband filter will be placed in front of the detector, and the radiation from the heated particle will be examined.

The final optical system is shown in Figure IV-4. The same collection mirror will be employed, the converging particle radiation will pass through a Digilab fast scanning Michelson interferometer and be chopped at ~ 9kHz using a high speed rotating chopper, Laser Precision CTX 534. The detector to be used will be a Raytheon copper-doped germanium with an area of 5×10^{-4} cm^2 and 2.5 degree field of view. The subsequent signal processing will be similar to that already described for the bulk experiment.

a. Signal-to-Noise Calculations

The hot particles are small in size and therefore provide only a small infrared signal. In this subsection we show by calculation that adequate signal levels should be available to make spectral measurements of the particle radiance with the multiplex advantage of Fourier transform spectroscopy. To carry out this calculation we must begin by summarizing the performance characteristics of our interferometer.

The Aerospace Michelson interferometer can operate in the wavelength region ~ 2.8 to 25μm ($\nu \sim 3600$ to $400 cm^{-1}$). The stationary mirror of the interferometer has been displaced (~ 0.25cm) so that two sided interferograms (- 0.25cm ≤ x ≤ 0.25cm) can be obtained which can be transformed into spectra without the need for phase correction. The corresponding resolution is ~ $4cm^{-1}$. However, with little difficulty, the stationary mirror could be further displaced, so that a spectral resolution of ~ $1cm^{-1}$ could be achieved if desired.

The scan velocity of the moving mirror is ~ 0.5 optical cm/sec which for $\nu = 400\text{cm}^{-1}$ yields $f_L = 200\text{Hz}$. (That is a spectral "line" at $\nu = 400\text{cm}^{-1}$ would have as its interferogram a cosine wave of frequency 200Hz.) Likewise, for $\nu = 3600\text{cm}^{-1}$, $f_H = 1800\text{Hz}$ for a nominal bandwidth of $\sim 1600\text{Hz}(= \Delta f)$. This bandwidth will have to be increased slightly because of the practical limitations of the interferometer.

Sampling theory dictates that the interferogram must be sampled at least as frequently (in optical path difference) as

$$\Delta x = \frac{1}{2\nu_c}, \qquad \text{(IV-3)}$$

where ν_c is the largest wavenumber, with non-zero intensity, in the spectrum. In our case $\nu_c \approx 3600\text{cm}^{-1}$, due to optical components in the interferometer, so $\Delta x(\text{max}) \approx 1.3889\mu\text{m}$. However, Δx for our interferometer is measured in integral powers of two times half the wavelength of the HeNe laser line ($\lambda = 0.6328\mu\text{m}$), that is,

$$\Delta x = \frac{\lambda}{2}, \lambda, 2\lambda, 4\lambda, 8\lambda, \text{ etc. For our case,}$$

$$\frac{\Delta x(\text{optimum})}{\lambda/2} = \frac{1.3889\mu\text{m}}{0.3164\mu\text{m}} = 4.4.$$

Therefore, $\Delta x(\text{practical}) = 1.2656 \times 10^{-4}\text{cm}$. The number of points per interferogram n, is then,

$$n = \frac{\text{optical path traversed}}{\Delta x(\text{practical})} \simeq 4 \times 10^3 \text{pts.}$$

The fast Fourier transform program efficiently transforms interferograms with $n = 2^m$. For $m = 12$, $n = 4.096 \times 10^3$pts. Working backwards and remembering that two-sided interferograms are being measured,

$$L = \frac{n\Delta x}{2} = (2048)\,(1.2656 \times 10^{-4}) = 0.2592\text{cm},$$

which yields a resolution of $\sim 3.86\text{cm}^{-1}$. Also, Δx(practical) = 1.2656×10^{-4}cm, and so $\nu_c \simeq 3950\text{cm}^{-1}$, which for our moving mirror velocity of 0.5cm/sec yields $f_H = 1975$Hz and $\Delta f = 1775$Hz. The region from $\sim 3600\text{cm}^{-1}$ to 3950cm^{-1} will be "empty" (i.e., no spectra) because of the natural cut-off at $\nu \approx 3600\text{cm}^{-1}$. Although there will be no useful spectroscopic data in this region it can be used to estimate the noise in the "occupied" spectral region as has been pointed out by Connes.[Ref. IV-5] This does not imply that only this method is used to measure system noise.

It is now possible to proceed with the signal to noise computation. Assume a background limited detector on the interferometer with $D^* = 5 \times 10^{10}\text{cm Hz}^{1/2}\,\text{W}^{-1}$, a $\pi/9$ field of view and an area $A = 10^{-3}\text{cm}^2$. Then

$$\text{NEP} = \frac{\sqrt{A\Delta f}}{D^*} = 2.66 \times 10^{-11}\text{W}$$

where we have assumed a $\Delta f = 1775$Hz from the spectral range of interest and the parameters of our interferometer. It has been shown that the noise in the spectrum, N_s, is related to the noise in the interferogram N_I[Ref. IV-6] by,

$$N_s = \sqrt{\frac{L\Delta x}{2}\,N_I} = 1.06 \times 10^{-13}(\text{W/cm})$$

where $L = 0.25$cm (resolution = 4cm^{-1}), $\Delta x = 1.2656 \times 10^{-4}$cm and N_I is the NEP as calculated above. The above expression is appropriate for a single-sided interferogram. For a double-sided interferogram we pick up a factor of $\sqrt{2}$, and furthermore the best resolution required is about three resolution widths so we can integrate over these three elements and pick up a further factor of $\sqrt{3}$. Thus,

$$N_s(\sim 12\text{cm}^{-1}\ \text{element}) = 4.32 \times 10^{-14}\ \text{watts}.$$

To estimate a signal for comparison with the noise we assume a particle of radius, $r = 0.5\mu m$ and emissivity $\epsilon = 1$. This corresponds to about the smallest carbon particle size to be investigated in this project and will give a reasonably conservative estimate of the expected signal. Furthermore, assume the solid angle over which radiation is collected, $\Omega = \pi/9$ steradians, and the transmittance or efficiency of the interferometer is $f = 0.4$. Then the detected particle flux is,

$$N_p = A\epsilon\Omega f N_B(T),$$

where $A = \pi r^2$, the effective emitting particle area, and $N_B(T)$ is the blackbody radiance at temperature T. The above expression was evaluated for a range of temperatures (400 to 900°K) for the spectral element 400 to 412cm^{-1} which again should lead to a conservative estimate since for the temperatures considered this wavenumber region lies on the longer wavelength side of the blackbody radiance function. With these assumptions Table IV-3 was constructed. For the various particle temperatures listed in the first column, the second column gives the integrated (ν = 400 to 412cm^{-1}) signal-to-noise ratio for a single interferogram. The third column gives the number of coadded interferograms required to increase the signal-to-noise ratio to 100 in this same spectral element. The fourth column gives the time required to measure this number of interferograms. The table indicates that if the temperature of the emitting particle could be changed quickly, and the detector noise were the limiting noise source, the data could be gathered in ten minutes or somewhat longer, the extra time being used to obtain background interferograms. The S/N and related numbers given above are optimistic, especially for the lower temperatures, since no account has been given to the ~ 300°K bath in which the emitting particle will probably be immersed. To suppress unwanted signals due to radiation from the 300°K surroundings in this apparatus,

Table IV-3. Computed signal-to-noise for 0.5μm particle at various temperatures (ν = 400 to 412cm^{-1})

T (K)	Signal-to-Noise Ratio one interferogram	n, Number of Interferograms to achieve S/N = 100	Time to Obtain n interferograms (minutes)
400	6	277	4.6
500	10	100	1.7
600	13	59	1.0
700	16	39	0.7
800	20	25	0.4
900	24	17	0.3

a modulated signal is sent to the interferometer used to make spectral measurements. The chopping frequency must be significantly greater than the electrical frequencies corresponding to the wavelength region of interest. For the scan speeds of our Michelson interferometers used to obtain spectral data, the highest frequency of interest is $\sim$ 2kHz. The chopper operates at $\sim$ 8kHz and thus adequate sampling is achieved. However, a background problem still exists.

The infrared image of the radiating particle is focused on a chopper blade in the present apparatus. The modulated signal consists of the particle emission, plus emission from the particle surroundings, minus the emission of the chopper blade. Ideally, the emission for the particle surroundings and the chopper blade would be identical so that when no hot particle is present and the chopper is running, there will be no AC signal. However, if the blade and the background are at different temperatures, there will be a residual AC background which must be distinguished from the signal due to particle emission.

In order to estimate the severity of this background problem, the following analysis was carried out. Using the optical parameters of the particle emissivity apparatus, a number of curves were generated for frequencies between 500 and 2500cm^{-1} (20 to 4μm) and are shown in Figure IV-20. Consider first the upper dashed curve. It is the spectral flux density (watts/cm^{-1}) of the residual background signal if the temperature, T_H, of the particle surroundings were 300°K and the temperature, T_B, of the chopper blade were 301°K. The next lower dashed curve is for T_H = 300°K and T_B = 300.2°K, a temperature difference of 0.2°K. The lowest dashed curve is for T_H = 80°K and T_B = 85°K. The solid curves are the spectral flux density (watts/cm^{-1}) collected by the particle emissivity apparatus from a black 2μm radius particle for the indicated temperatures T_p. For the case T_p = 1000°K and $T_B - T_H$ = 0.2°K the particle signal is comfortably above the background signal. However, for a particle whose temperature, T_p = 500°K,

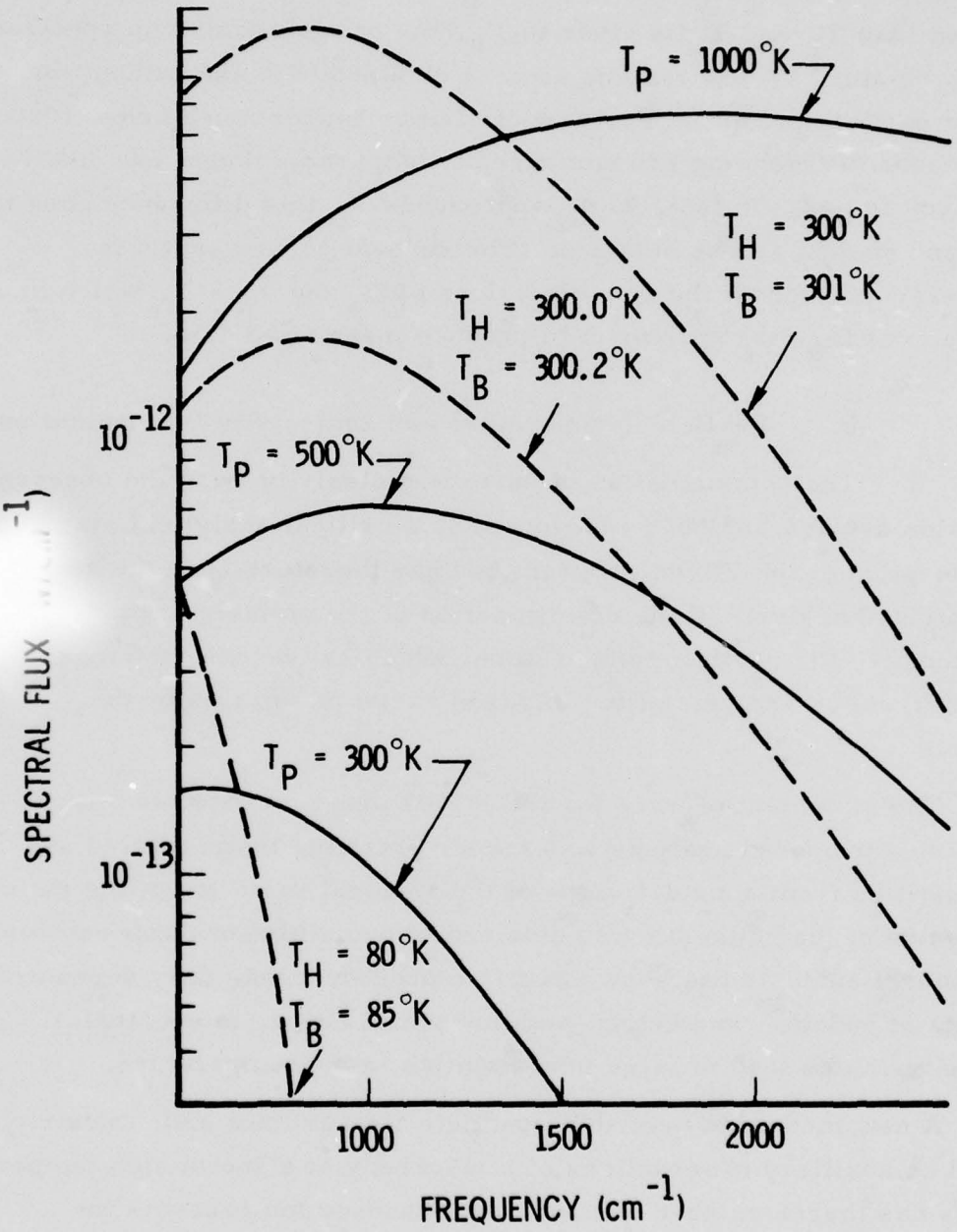

Figure IV-20. Particle and background spectral fluxes for various temperatures.

the background signal is significantly higher than the particle signal up to 1500cm^{-1} ($\sim$ 6.6μm). As long as T_p is at least a few hundred K greater than T_B and T_H is close to T_B, the particle emission spectrum can be obtained by differencing spectra obtained with and without the heated particle present. For particle temperatures much below 1000°K this means differencing two numbers of comparable magnitude and thus accuracy is lost. In fact, as T_p approaches T_B this difference goes to zero and no data can be obtained. The several curves shown in Figure IV-20 suggest the specific values of T_p and $T_B - T_H$ which must be achieved for the experiment to produce meaningful data.

b. Particle Temperature and Emissivity Determination

The determination of particle emissivity from the observed radiation spectra has been recognized as a critical analytical step since the inception of the POPM program and has therefore been the subject of continued analysis. The determination of the emissivity implies a knowledge of the particle temperature, which can be obtained most simply from an analysis of the infrared radiation emitted by the particle.

The statement of work for the POPM program dated 14 June 1974 contains a proposed analysis scheme for obtaining temperatures and emissivities from considerations of the spectral variation of the ratio of spectra of the same particle obtained at two different temperatures. Subsequent analysis has shown that this procedure was very dependent on data at 500cm^{-1} and below, and that small errors in spectral intensity values lead to large uncertainties in the temperature.

A new method to determine particle temperature and emissivity based on auxiliary observations of a blackbody at a known high temperatures has therefore been devised. This subsection presents the details of this data analysis method.

(1) Particle Emissivity Determination

Neglecting the background contribution (for which we shall be able to correct), the intensity of radiation as seen by a spectroscopic device (in our case a Michelson interferometer) can be written,

$$J_p(\nu, T_p)\, d\nu = \frac{\pi \epsilon_p(\nu, T_p)\, C_1 r_p^2 \nu^3 f(\nu)\, d\nu}{e^{\frac{hc\nu}{kT_p}} - 1} \qquad \text{(IV-4)}$$

where

$\epsilon_p(\nu, T)$ = emissivity of the particle which in general may be a function of ν, and T,

C_1 = first radiation constant,

r_p = radius of the particle,

$f(\nu)$ = function of ν accounting for instrumental transmission, detector efficiency, and atmospheric absorption,

h = Planck's constant,

c = velocity of light,

k = Boltzmann's constant,

ν = wavenumber of radiation ($= \lambda^{-1}$), and

T_p = particle temperature.

For a blackbody radiation source a similar equation may be written except by definition $\epsilon_{BB}(\nu, T) \equiv 1$, and in practice manufacturers claim to achieve $\epsilon_{BB}(\nu, T) > 0.995$. The blackbody radiance is

$$J_B = - \frac{\pi C_1 r_B^2 \nu^3 f(\nu)\, d\nu}{e^{\frac{hc\nu}{kT_B}} - 1} \qquad \text{(IV-5)}$$

where r_B is the radius of the circular aperture of the blackbody radiating to the outside world.

Dividing equation IV-4 by equation IV-5 we obtain

$$\frac{J_p}{J_B} = \epsilon_p(\nu, T_p) \frac{r_p^2}{r_B^2} \frac{\left(e^{\frac{hc\nu}{kT_B}} - 1 \right)}{\left(e^{\frac{hc\nu}{kT_p}} - 1 \right)} \qquad \text{(IV-6)}$$

J_p and J_B will be measured experimentally, r_B and T_B are known. The radius of the particle r_p will be determined experimentally by measuring the scattered light as a function of scattering angle. Solving for $\epsilon_p(\nu, T_p)$,

$$\epsilon_p(\nu, T_p) = \frac{J_p r_B^2}{J_B r_p^2} \frac{\left(e^{\frac{hc\nu}{kT_p}} - 1 \right)}{\left(e^{\frac{hc\nu}{kT_B}} - 1 \right)} \qquad \text{(IV-7)}$$

Note that by dividing a particle emission spectrum by a blackbody emission spectrum we obtain an expression for $\epsilon_p(\nu, T_p)$ directly, providing T_p can be obtained.

The accuracy of the determination of ϵ_p depends critically on the determination of the particle temperature. Let the error in T_p be ΔT_p, then

$$\frac{\Delta\epsilon_p}{\Delta T_p} = -\frac{J_p r_B^2}{J_B r_p^2} \frac{e^{\frac{hc\nu}{kT_p}}}{\left(e^{\frac{hc\nu}{kT_B}} - 1\right)} \frac{hc\nu}{kT_p^2}$$

and using equation IV-7

$$\frac{\Delta\epsilon_p}{\epsilon_p} = -\frac{e^{\frac{hc\nu}{kT_p}}}{\left(e^{\frac{hc\nu}{kT_p}} - 1\right)} \frac{hc\nu}{kT_p} \frac{\Delta T_p}{T_p}$$

Thus the fractional error in ϵ_p equals the fractional error in T_p multiplied by a function of the form $xe^x/(e^x - 1)$, where $x = hc\nu/kT_p$. The minus sign indicates the errors run counter to each other. If T_p is overestimated, ϵ_p will be underestimated and vice versa. Note that the relationship is a function of ν/T_p alone. In the particle emissivity experiment $\nu_{min} \sim 400 cm^{-1}$ ($\lambda = 25 \mu m$) and $T_p(max) \sim 2200^\circ K$. Therefore $x_{min} \sim 0.26$. A plot of x versus $xe^x/(e^x - 1)$ out to $x = 7$ is shown in Figure IV-21. As x approaches zero $xe^x/(e^x - 1)$ goes to 1. Thus, for a given percentage error in T_p the error in ϵ_p for small ν/T_p will be of the same order as $\Delta T_p/T_p$. From the graph Table IV-4 was constructed for a one percent error in T_p at various temperatures and radiation frequencies. The above analysis should be used with caution in that the error propagated into ϵ_p by an error in T_p may not always be the most important. For instance, even a "black" 500°K particle will not radiate much power in the $5000 cm^{-1}$ ($\lambda = 2 \mu m$) region, and therefore the determination of ϵ_p may be governed more by how well J_p is determined rather than T_p. However, when the S/N in J_p is sufficiently high, the error in the determination of ϵ_p will be largely governed by the error in T_p. Therefore, even if J_p has a small uncertainty, fractional errors in T_p will result in fractional errors from two to ten times larger in ϵ_p.

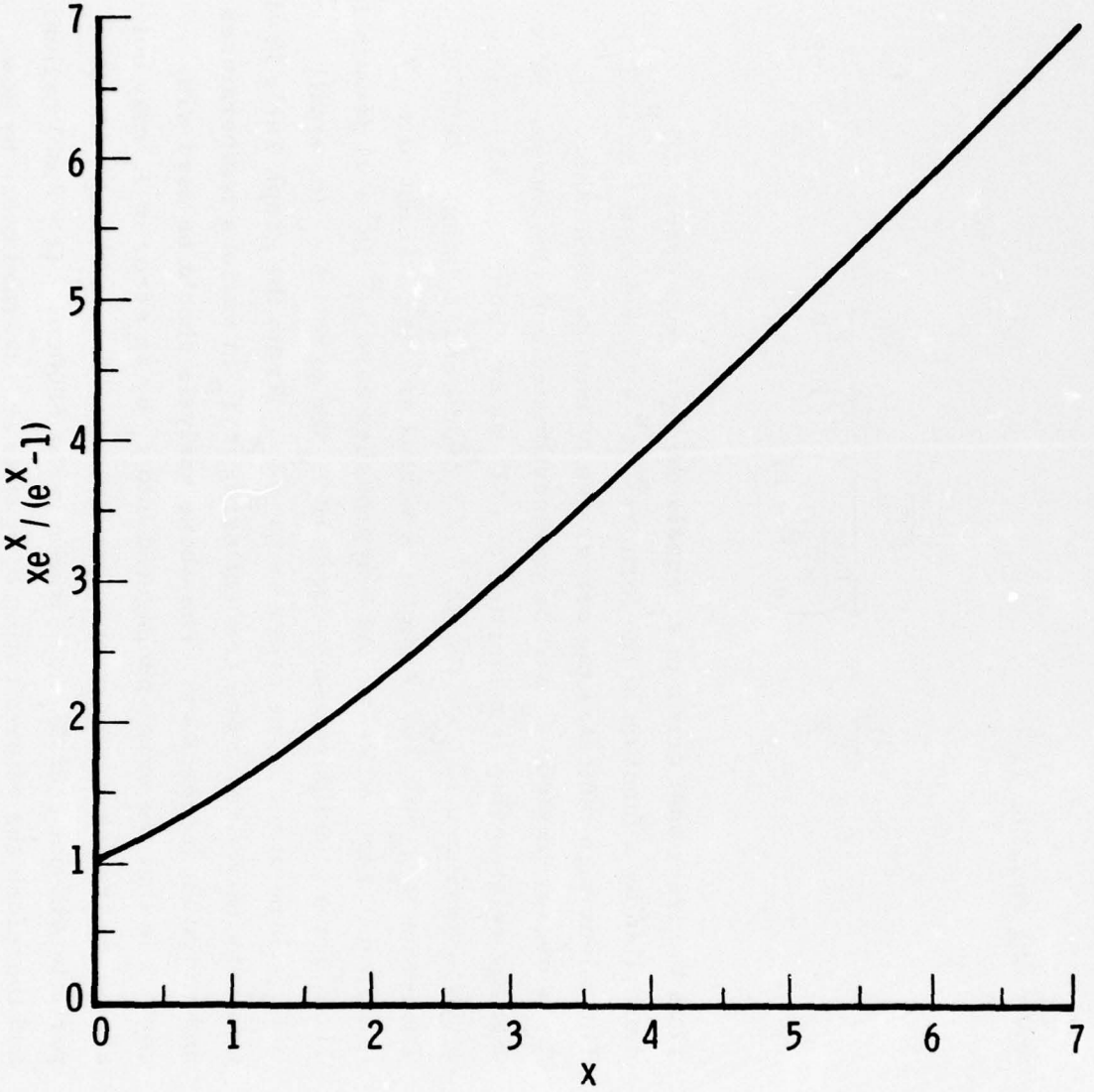

Figure IV-21. The function $xe^x/(e^x-1)$ plotted as a function of x.

Table IV-4. Error in ϵ_p for a one percent error in T_p.

ν =	$500cm^{-1}$	$1500cm^{-1}$	$2500cm^{-1}$	$5000cm^{-1}$
λ =	$20\mu m$	$6.7\mu m$	$4.0\mu m$	$2.0\mu m$
$\Delta\epsilon_p/\epsilon_p$ / $T_p(^\circ K)$				
500	1.9%	4.3%	7.2%	14.4%
1000	1.4%	2.4%	3.7%	7.2%
1500	1.3%	1.9%	2.6%	4.8%
2000	1.2%	1.6%	2.2%	3.7%

(2) Determination of T_p

The reliable determination of T_p is central to the successful determination of $\epsilon_p(\nu, T_p)$. If $\epsilon_p(\nu, T_p)$ is reasonably well behaved, (the meaning of "reasonably well behaved" will become apparent further in this section) in one or more fairly broad wavenumber regions for which $\nu/T_p \geq 3.5(\text{cmK})^{-1}$, then T_p can be determined.

Recalling equation IV-6, and putting all the knowns on the left side of the equation, we can define a $K(\nu)$

$$\frac{J_p r_B^2}{J_B r_p^2}\left(\frac{hc\nu}{e^{kT_B}-1}\right)^{-1} = \epsilon_p(\nu, T_p)\left(\frac{hc\nu}{e^{kT_p}-1}\right)^{-1} \equiv K(\nu)$$

All the quantities on the left are known, therefore $K(\nu)$ is known. Now in the high wavenumber end of the spectrum, where $\nu/T_p \geq 3.5(\text{cmK})^{-1}$ so that $\exp\left[\frac{hc\nu}{kT_p}\right] \gg 1$, we have

$$K(\nu) = \epsilon_p(\nu, T_p)e^{-hc\nu/kT_p}, \text{ or}$$

$$\ln K(\nu) = \ln\epsilon_p(\nu, T) - \frac{hc\nu}{kT_p} \qquad \text{(IV-8)}$$

If ϵ_p is a constant over some wavenumber interval for which $\nu/T_p \geq 3.5(\text{cmK})^{-1}$, then a plot of $\ln K(\nu)$ versus ν will be a straight line whose slope is $-hc/kT_p$, thus T_p will be determined. Obviously, the wider the interval(s) the more accurately T_p will be determined.

Except in the region of sharp absorption bands (and therefore probably emission bands) the emissivity would be expected to be a slowly varying function of ν. For example, let us assume over some wavenumber interval

$$\epsilon_p(\nu, T_p) = a(1 - b\nu) \qquad \text{(IV-9)}$$

such that b is small enough so that

$$\epsilon_p(\nu, T_p) = a(1 - b\nu) \simeq ae^{-b\nu}$$

then

$$\ln\epsilon_p = \ln a - b\nu$$

and equation IV-8 would become

$$\begin{aligned} \ln K(\nu) &= \ln a - b\nu - \frac{hc\nu}{kT_p} \\ &= \ln a - \frac{hc\nu}{k}\left(\frac{1}{T_p} + \frac{bk}{hc}\right) \end{aligned} \qquad \text{(IV-10)}$$

Obviously, b must be very much less than T_p^{-1} if T_p is to be determined accurately. For example, if T_p lies in the range 800°K to 1500°K and $\epsilon_p \sim 0.3$ (average in a $1000cm^{-1}$ range somewhere between 4000 and $8000cm^{-1}$), variation of ϵ_p of three to six percent as given by equation IV-7, would still allow T_p to be determined to about one percent. Particle emissivities have not been measured, but bulk emissivities of the materials of interest show approximately this variation.

Consider now the emission spectrum of a particle measured at two temperatures T_{p1} and T_{p2}. Taking the ratio of these spectra we obtain

$$\frac{J_p(\nu, T_{p2})}{J_p(\nu, T_{p1})} = \frac{\epsilon_p(\nu, T_{p2})}{\epsilon_p(\nu, T_{p1})} \frac{\left(e^{\frac{hc\nu}{kT_{p1}}} - 1\right)}{\left(e^{\frac{hc\nu}{kT_{p2}}} - 1\right)}$$

and for ν/T_{p1} and $\nu/T_{p2} \geq 3.5(\text{cmK})^{-1}$ we have

$$\frac{J_p(\nu, T_{p2})}{J_p(\nu, T_{p1})} = \frac{\epsilon_p(\nu, T_{p2})}{\epsilon_p(\nu, T_{p1})} \, e^{\frac{hc\nu}{k}\left[\frac{1}{T_{p1}} - \frac{1}{T_{p2}}\right]}$$

and therefore

$$\ln\left[\frac{J_p(\nu, T_{p2})}{J_p(\nu, T_{p1})}\right] = \ln\left[\frac{\epsilon_p(\nu, T_{p2})}{\epsilon_p(\nu, T_{p1})}\right] + \frac{hc\nu}{k}\left(\frac{1}{T_{p1}} - \frac{1}{T_{p2}}\right) \qquad \text{(IV-11)}$$

If the ratio of the emissivities is a constant then the above expression is the equation for a straight line whose slope is

$$\frac{hc}{k}\left(\frac{1}{T_{p1}} - \frac{1}{T_{p2}}\right)$$

(3) Particle Radiance Data Reduction

The preceding analysis suggests a procedure for obtaining particle temperatures from the particle emission spectra. We will obtain spectra at a number of unknown temperatures and blackbody emission spectra at a number of known temperatures. It appears that four temperatures will be adequate; ~ 2000, 1600, 1200 and 800 °K. The signal-to-noise ratios for these spectra are anticipated to be much greater than for the particle emission spectra. Rho (ρ) curves of the type

$$\rho_{pB} = \frac{J_{(\text{particle})}}{J_{(\text{blackbody})}}$$

will be generated and $\ln \rho_{pB}$ versus ν will be examined in the 2000 to 4000cm^{-1} interval for straight line behavior.* In a similar fashion ρ curves of the type

$$\rho_{pp} = \frac{J(\text{particle}, T_1)}{J(\text{particle}, T_2)}$$

will be generated and examined for straight line behavior of $\ln \rho_{pp}$ versus ν. In order to simplify the notation, define

X_i = reciprocal of the temperature of a blackbody at temperature T_i, and

Y_j = reciprocal of the temperature of a particle at temperature T_j.

Each physically acceptable straight line plot based on two spectra results in a slope, M_{ji}, proportional to the difference between the reciprocals of the temperatures associated with the two spectra for which the logarithmic ratio has been plotted. The result of all the possible spectral ratios is a system of equations of the form:

$$X_i - Y_j = M_{ij} \qquad \text{(IV-12)}$$

$$Y_k - Y_e = M_{ke} \qquad \text{(IV-13)}$$

The X's and M's are known, and the Y's are to be determined. Since more than one segment of the spectra may be employed, possibly yielding multiple values of M for the same spectra, the Y's will

---

*The noise level in the experimental data is determinable (see Section IV-B.4.a). Criteria can therefore be set up to determine if $\ln \rho_{pB}$ is a straight line within the known signal-to-noise.

probably be over determined. This can be combined with additional a priori knowledge to improve the accuracy of the Y's (and thus temperatures determined). The ordering of the particle temperatures will be known since the highest laser power should correspond to the highest temperature, the second highest laser power to the second highest temperature, and so on. Equations of the type of IV-12 determine the Y's temperature. Equations of the type of IV-13 can be used, along with the ordering information from laser powers to determine if the correct slope value has been used in the type IV-12 equations.

Once T_p for a particle emission spectrum is determined, the emissivity can then be obtained from the ratio of the particle spectrum to a suitable blackbody spectrum times the calculable expressions shown in equation IV-7.

5. Samples for Particle Emissivity Studies

The materials and size ranges for particles of interest for emissivity measurements in the present program are: Carbon, having a diameter from 0.1 to 1.0μm; magnesia (MgO), zirconia (ZrO_2), and alumina (Al_2O_3) having diameters from 1 to 25μm. The study was restricted to spherical particles to facilitate the comparison of measured emissivity with computed values.

a. Materials

(1) Carbon

Pure solid carbon exists in three stable forms. The two crystalline forms are graphite and diamond and the third is quasi-graphitic and known as carbon black. Our main concern here is with carbon black since that is the form of material loaded into rocket motors and most probably the form in which it is present in rocket exhausts.

Carbon black in the size range of interest for the particle emissivity experiment is produced by the thermal decomposition of natural gas in the absence of air or flame and is called thermal black. Carbon blacks display two-dimensional crystallinity. They consist of well developed graphite platelets stacked roughly parallel to one another but random in orientation about the normal to the layers. When carbon black is heated, the growth of the quasi-graphitic parallel layer groups begins at about 1000°C. In the larger carbon black powders such as thermal black, three-dimensional graphitic structure is detected after heating to 3000°C. In the finer carbon blacks, a three-dimensional graphitic structure apparently never evolves. Thermal blacks have negligible oxygen content, and hydrogen present is from the hydrocarbon raw material and is distributed throughout the particle. The finer carbon blacks can have appreciable oxygen present on the surface of each particle. The oxygen and hydrogen combine with surface carbon atoms and form a variety of surface complexes. On heating carbon black progressively from 600 to 1500°C, decomposition products of these surface compounds are evolved as CO_2, CO and H_2.

In air, serious oxidation of carbon probably begins around 500°C. This probably does not effect the surface chemistry, however, since all the products of oxidation are gaseous. Oxidation will cause a small particle to eventually be converted entirely to the gas phase.

(2) Magnesia

The chemical properties of magnesium oxide vary considerably with the purity of the material. MgO prepared in the temperature range from 400 to 900°C rehydrates readily even in cold water. Fused magnesium oxides are virtually insoluble in water except in extremely fine powders. Because of the rapid hydration brought about by the presence of impurities, it is essential to obtain as pure MgO as possible.

MgO crystallizes from the liquid in the face centered cubic system. As with Al_2O_3 there is only one stable crystal form of pure MgO in the range from room temperature to the melting point at 2800°C.

(3) Zirconia

ZrO_2 exists stably at ordinary temperatures as monoclinic crystals. Transformation between monoclinic and tetragonal symmetry occurs at about 1200°C. This transformation is accompanied by a large change in volume, about 7.5 percent. This gives rise to cracks and failures in crystals and in ceramic bodies cycled through this temperature. This can be circumvented by inducing the zirconia to crystallize in the cubic system, through the influence of certain dissolved oxides.

All natural zirconium ores contain hafnium. Concentrations vary from about two percent to somewhat more. The process of removing this hafnium is expensive, and the zirconium dioxide powder used to load rocket motors most probably contains hafnium. Impure zirconia costs about $2.15/lb, while zirconia of comparable size and purity, but with only 25ppm of hafnium costs about $500/lb. There does not seem to be any compelling need to use this costly grade; so the ZrO_2 materials studied in this experiment are designated "pure", when in fact they contain two percent hafnium.

(4) Alumina

α-Al_2O_3 crystallizes from the liquid in the rhombohedral system. This is also the only stable form of pure anhydrous Al_2O_3 at all temperatures from room temperature to the melting point at 2040°C. Because of this, there is no difficulty in insuring that all forms of pure solid Al_2O_3 will have the same crystal structure in these experiments. It is produced industrially by solidification of molten alumina, from a sintering process in the temperature range

from 1300 to 1700°C, and also by calcination at a sufficiently high temperature (1100 to 1300°C) of the other forms of alumina. There are a great many stable forms of aluminum oxide when mixed with hydroxyl groups to produce the so-called hydrated aluminas. It is necessary, therefore, to obtain as pure a form of Al_2O_3 as possible since a number of impurities can cause rapid hydration of α-Al_2O_3.

b. Spheroidal Sample Preparation

(1) Carbon

Carbon powders are available as amorphous carbon, graphite and diamond. Diamond is not available in spherical form nor is it possible to produce it in that form. This results from the fundamental crystal structure of this material which imposes flat surfaces on the particle. The primary interest of this program, in any case, is in amorphous carbon, that being the form of the material most probably present in rocket exhaust.

The powders of spherical particles that we have obtained are of very high purity and meet the size requirements. The Kreka Corporation supplied us with amorphous carbon particles that are almost perfect spheres in the 1.5 to 8μm range and are 99.9 percent pure (Figure IV-22). For the 0.3 to 0.8μm particle size range, the Huber and Vanderbilt Corporations supplied us with powders that are mostly spherical and are 99 percent pure.

(2) Metal Oxides

Abundant sources of these materials in powder forms are available in a wide assortment of sizes. However, no suppliers of any of these materials can claim capability of providing spherical particles. Conversations with manufacturers of plasma arc heaters, on the other hand, revealed that it is possible to form spherical particles by melting the powders in a plasma spray.

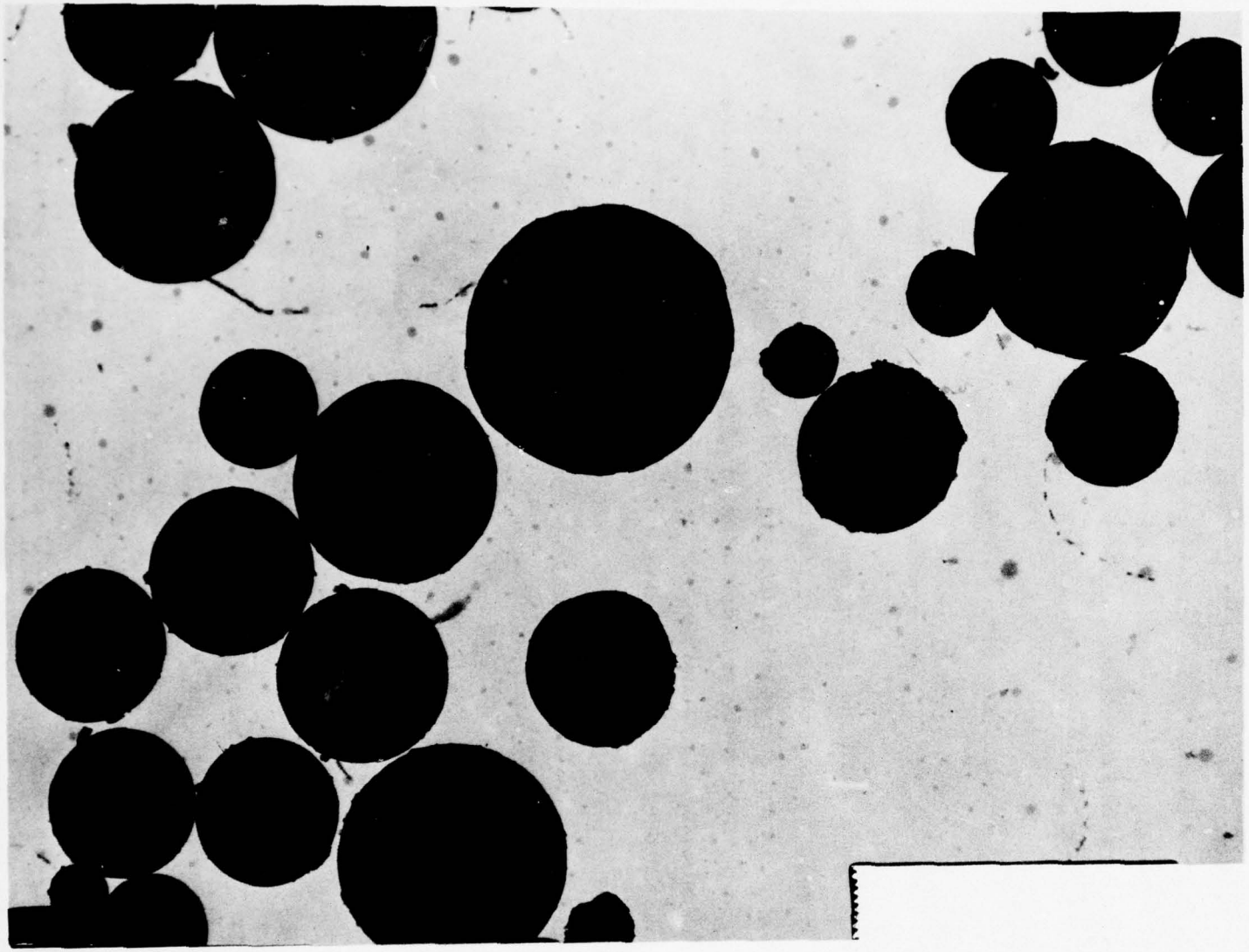

Figure IV-22. Amorphous carbon particles with diameters ranging from 1.5 to 8μm.

Plasmadyne Corporation of Anaheim, California has successfully generated spheres of Al_2O_3 and ZrO_2 in the size range from 20 to 80μm. Photomicrographic studies of these alumina and zirconia powders show that while spheres do indeed exist, the yield of spheres is only about ten percent. Apparently, this process functions in such a way as to convert particles to spheres in only over a fairly narrow range of particle masses. Larger particles do not melt completely and smaller particles evaporate and subsequently recondense as many very small particles. Plasmadyne has not been successful in converting MgO to spheres. Tafa Industries of Bow, New Hampshire claim to be able to produce spheres in the size range of 2 to 20μm from any one of the three oxides of interest. Therefore, it would seem that if these companies were supplied with the proper sized powders that spherical particles could be obtained.

The Aerospace Corporation is capable of supplying these companies with a narrow range of particle sizes, as we are equipped with a Donaldson particle classifier that separates any range of particles desired from powders with a large size distribution.

Several sources for these oxides were contacted, photomicrographic studies of many samples were made and the powders that could meet the program requirements, after classification and spheroidization were chosen.

(a) Magnesia

We have procured three powders that together meet all of the requirements of the experiment after classification and spheroidization: Fisher Chemical M51-75617, Kaiser Chemical 325 mesh, Ventron 325 mesh. No attempt, as yet, has been made to classify or spherisize these particles.

(b) Zirconia

Two powders have been located which, after classification and spheroidization will meet the requirements: Fisher Chemical; 2-83, ML/B, 2x120/8404. No attempt, as yet, has been made to classify or spherisize these particles.

(c) Alumina

The size range from 7-9μm of the Fisher alumina A-591 was separated using the classifier and sent to Tafa Corporation for spheroidization. This attempt failed; the powder agglomerated and could not be plasma sprayed. However, by using their own Al_2O_3 powders as a starting material, Tafa Corporation was able to supply Aerospace with spherical particles, "Ionarc" Al_2O_3-320 and 400. These particles have a size distribution from 4-20μm and 15-30μm, respectively, and are shown in Figure IV-23.

C. SUMMARY, DISCUSSION AND RECOMMENDATIONS

Particles of all four materials of interest in this study have been levitated and maintained in place while being irradiated with intense 1.06μm Nd:YAG laser radiation.

A method of analyzing the spectral emission data has been derived and is presented in this report. The emissivity depends on finding the particle temperature. A procedure for doing this is presented which depends on finding a spectral region, $\nu > 2000 cm^{-1}$, in which the emissivity does not vary rapidly with frequency over a sufficient frequency interval that a slope can be determined. In view of the computed particle emissivities shown in Section III, this condition may not be met for some of the materials of interest.

Samples of all the materials are available in the size range required for the particle experiments. Spherical particle samples of Al_2O_3 and carbon are available.

Figure IV-23. Aluminum oxide particles that have been spherisized by melting powders in a plasma spray.

Due to the problems encountered in simultaneously levitating and irradiating particles, no infrared radiation has been observed from the hot particles within the period covered by this report.

We believe that significant evidence exists that the experiment is possible and recommend that it be continued. Specifically, we recommend the following approach:

(1) Use an infrared detector with the required collection optics to observe the infrared radiation from the hot particle. This will provide a demonstration of the feasibility of the overall experiment.

(2) Measure the particle emission spectrum with a Michelson interferometer spectrometer. The optics should be configured so that calibration spectra from a high temperature blackbody can also be obtained. The emissity spectrum will then be deduced by the methods outlined in this section, or an improvement of these procedures.

SECTION IV. REFERENCES

IV-1. M. E. Whitson, Jr., "Handbook of the Infrared Optical Properties of Al_2O_3, Carbon, MgO and ZrO_2," The Aerospace Corporation Report TR-0075(5548)-2, (SAMSO Report TR-75-131), Vols. I and II, 4 June 1975.

IV-2. N. A. Lange, Handbook of Chemistry, 9th Edition, Handbook Publishers, Sandusky, Ohio, 1956.

IV-3. D. Mergerian, "Optical Properties of Infrared-Transparent Solids at Elevated Temperatures," Proc. I.R.I.S. 4, 146 (1959).

IV-4. D. A. Gryvnak and D. E. Burch, "Optical and Infrared Properties of Al_2O_3 at Elevated Temperatures", J. Opt. Soc. Am. 55, 625-629 (1965).

IV-5. J. Connes and P. Connes, "Near-Infrared Planetary Spectra by Fourier Spectroscopy. I. Instruments and Results," J. Opt. Soc. 56, 896 (1966).

IV-6. J. M. Dowling, "Signal and Noise in Two-Beam Interferometry," Applied Optics 6, 1580 (1967).

This page left blank on purpose.

SECTION V

SUMMARY AND RECOMMENDATIONS

The evaluation of the reliability of using bulk refractive index data to calculate infrared particle emissivity has been the basic motivation for the POPM program. In this report we have shown that particle emissivity calculations from bulk data may indeed be very unreliable. This emphasizes the need for continued efforts to directly determine infrared particle emissivity. To this end an apparatus has been assembled which levitates and simultaneously heats single particles. Analytical means have been derived to determine emissivities from experimental spectral radiance measurements. The significant achievements in each of the areas covered in this report and leading to the general conclusions stated above are summarized in this section. For a more detailed discussion consult the appropriate section of this report.

A. BULK EXPERIMENT

A device was designed and constructed for the measurement of the spectral reflectance of polarized infrared radiation by plane surfaced samples at room temperature, and higher, for a range of incidence angles. The originally planned inversion of the Fresnel equations for various angles to obtain the complex refractive index was found to provide ambiguous results. The refractive index data were therefore obtained by either classical dispersion analysis, or Kramers-Kronig analysis, of the reflectivity data obtained at the fixed incidence angle of 45 degrees.

Reflectivity data between ~ 4.5 and $25\mu m$ have been obtained and analyzed to determine n and k for Al_2O_3, MgO and ZrO_2 at room temperature and a temperature $\sim 600^{\circ}K$. Similar measurements for carbon have been made only at $300^{\circ}K$.

In general, the present refractive index data fall within, or near the range of values given in the literature, which are mostly room temperature values. The values at higher temperatures behave qualitatively as expected, the reststrahl lattice frequencies moving slightly to lower frequencies, with an increase in bandwidth.

As error analysis of the carbon data has been made indicating errors of five to ten percent in n and k for most of the refractive index data, and higher uncertainties for other values, notably for $k \lesssim 0.05$. Direct reflectivity measurements are not well suited to determine small values of k. As discussed previously, transmissivity measurements or total attenuated reflectivity measurements are capable of measuring k down to 10^{-4}, or less.

The temperatures for which data are presented here are below those thought typical of particles in applications. The measurements were limited by sample heater failure, which we do not believe to be a major limitation.

The continued bulk measurement program should incorporate the following improvements to the basically operational bulk experiment.

(1) Improve the thermal contact between the heater and sample so that sample temperatures in excess of 1000 °K may be achieved.

(2) Improve the chopping system in the experiment to provide more efficient chopping. This should improve the signal-to-noise ratio by at least a factor of three to five and thus lower the errors in reflectivity measurements.

(3) Determine theoretically if 45 degrees is the optimum incidence angle for refractive index determination.

(4) Devise a technique complementary to the present reflectance technique to determine accurately low values of k, especially for heated samples.

B. PARTICLE EMISSIVITY COMPUTATIONS

The emissivities expected for spherical particles of a variety of radii have been calculated by Mie theory from complex refractive indices determined in the bulk refractive index measurements program. These calculations indicate the emissivity of small particles depends critically on parameters which are very likely to change markedly between bulk and particle conditions.

The calculations show emissivities greater than unity which are caused by expected resonance effects between vibration modes of the particle and the infrared radiation.

The emissivities are critically dependent on size.

The emissivities are strong functions of frequency in the spectral range corresponding to the reststrahl bands in the bulk material. In this same spectral region the interaction between particle size and refractive index is strong, complicated and difficult to predict without a full Mie theory analysis for particles in the resonant frequency size range. The reader is reminded of the Al_2O_3 particle emissivity spectra presented in Section III as an example.

In the spectral region of wavelength short with respect to particle size and where low values of k occur, the emissivity depends directly on the value of k. See Figures III-27 and III-28 for example.

The observed emissivity of particles large compared with the wavelength of radiation and away from the reststrahl regions is expected to be different than the computed emissivity because of the dependence of emissivity on k and the liklihood that values of k in particles will differ significantly from bulk values due to imperfections in the particles. This result of the theoretical calculations emphasizes the importance of observing experimentally the emission from single particles.

The theoretical analysis effort should be continued to determine the effects of particle non-sphericity and surface roughness on the emissivity of particles.

C. PARTICLE EMISSIVITY EXPERIMENT

An experimental apparatus has been designed and constructed which has demonstrated the capability to levitate and simultaneously irradiate with Nd:YAG laser radiation single particles of Al_2O_3, C, MgO and ZrO_2. Analysis indicates the observed laser intensities should be sufficient to heat the particles to temperatures approaching the melting point of Al_2O_3.

Analytical procedures have been devised to determine the emissivity of the particles from observed spectral measurements of the intensity of the emitted radiation, providing a spectral region of nearly uniform particle emissivity can be found in the 2000-8000cm^{-1} region.

The difficult problem of simultaneously levitating and irradiating a particle was solved shortly before the close of the time period covered by this report. Therefore, no thermal energy from a single particle has been observed.

The continued single particle emissivity experiment should incorporate the following steps:

(1) Detect thermal radiation from a laser heated levitated particle. This will provide an empirical demonstration of the feasibility of the experiment.

(2) Incorporate the fast scanning Michelson interferometer and high temperature calibration source into the experimental apparatus to measure the spectral dependence of the emitted radiation.

(3) Determine from the emission measurements the emissivity of small spherical particles and compare with the theoretically computed emissivity values.

(4) Extend the measurements on single particles to non-spherical shapes and other materials.

D. GENERAL CONCLUSIONS AND RECOMMENDATIONS

The computed emissivity of small particles can be expected to differ widely from the observed emissivity, based on computations presented in Section III and summarized above. This provides a partial answer to the fundamental question to which the POPM program has been addressed. This analytically derived answer should be verified by empirical single particle observations.

We recommend that in the near future the highest priority in the POPM program should be given to the single particle emissivity experiment. A lower priority should be given to the theoretical analysis of non-spherical shapes. At this time the bulk refractive index is also of low priority, but in the more distant future bulk data will be required to analyze the then available single particle data. Therefore the improvements in this bulk experiment outlined above should be implemented on the basis of non-interference with the particle experiment.

THE IVAN A. GETTING LABORATORIES

The Laboratory Operations of The Aerospace Corporation is conducting experimental and theoretical investigations necessary for the evaluation and application of scientific advances to new military concepts and systems. Versatility and flexibility have been developed to a high degree by the laboratory personnel in dealing with the many problems encountered in the nation's rapidly developing space and missile systems. Expertise in the latest scientific developments is vital to the accomplishment of tasks related to these problems. The laboratories that contribute to this research are:

Aerophysics Laboratory: Launch and reentry aerodynamics, heat transfer, reentry physics, chemical kinetics, structural mechanics, flight dynamics, atmospheric pollution, and high-power gas lasers.

Chemistry and Physics Laboratory: Atmospheric reactions and atmospheric optics, chemical reactions in polluted atmospheres, chemical reactions of excited species in rocket plumes, chemical thermodynamics, plasma and laser-induced reactions, laser chemistry, propulsion chemistry, space vacuum and radiation effects on materials, lubrication and surface phenomena, photosensitive materials and sensors, high precision laser ranging, and the application of physics and chemistry to problems of law enforcement and biomedicine.

Electronics Research Laboratory: Electromagnetic theory, devices, and propagation phenomena, including plasma electromagnetics; quantum electronics, lasers, and electro-optics; communication sciences, applied electronics, semiconducting, superconducting, and crystal device physics, optical and acoustical imaging; atmospheric pollution; millimeter wave and far-infrared technology.

Materials Sciences Laboratory: Development of new materials; metal matrix composites and new forms of carbon; test and evaluation of graphite and ceramics in reentry; spacecraft materials and electronic components in nuclear weapons environment; application of fracture mechanics to stress corrosion and fatigue-induced fractures in structural metals.

Space Sciences Laboratory: Atmospheric and ionospheric physics, radiation from the atmosphere, density and composition of the atmosphere, aurorae and airglow; magnetospheric physics, cosmic rays, generation and propagation of plasma waves in the magnetosphere; solar physics, studies of solar magnetic fields; space astronomy, x-ray astronomy; the effects of nuclear explosions, magnetic storms, and solar activity on the earth's atmosphere, ionosphere, and magnetosphere; the effects of optical, electromagnetic, and particulate radiations in space on space systems.

THE AEROSPACE CORPORATION
El Segundo, California

. . .